Probing the top-quark coupling to the photon through the cross-section measurement of $t\bar{t}\gamma$ production in pp collisions with the ATLAS detector

Dissertation
zur
Erlangung des Doktorgrades (Dr. rer. nat.)
der
Mathematisch-Naturwissenschaftlichen Fakultät
der
Rheinischen Friedrich-Wilhelms-Universität Bonn

von
Mazuza Ghneimat
aus
Hebron, Palestinian territories

Bonn, 2018

Dieser Forschungsbericht wurde als Dissertation von der Mathematisch-Naturwissenschaftlichen Fakultät der Universität Bonn angenommen und ist auf dem Hochschulschriftenserver der ULB Bonn `http://hss.ulb.uni-bonn.de/diss_online` elektronisch publiziert.

1. Gutachter: Priv.-Doz. Dr. Markus Cristinziani
2. Gutachterin: Prof. Dr. Jochen Dingfelder

Tag der Promotion: 17.05.2018
Erscheinungsjahr: 2018

Acknowledgements

I would like to acknowledge everyone who has supported me during my educational career, by one mean or another.

I would like to express my gratitude to my advisor PD Dr. Markus Cristinziani for accepting me to join his research group. Thanks for his patience, support, guidelines and fruitful discussions, that all qualified this work to be completed. I would also like to thank the European Research Council for their financial support. I also thank the council of Bonn-Cologne Graduate School (BCGS) for offering a one-year step program, financing the first year of my PhD.

Special thanks to Dr. Julien Caudron, Dr. Liza Mijović and Dr. Vadim Kostyukhin, for their direct supervision, close discussions and frequent feedbacks, I have learned and built many skills from them. I would especially thank my current and former group members: Nello Bruscino, Carlo Gottardo, Sebastian Heer, Evan Machefer, Omer Oğul Öncel, Arshia Ruina, Andrea Sciandra, Kaven Yau Wong. I appreciate very much their great help and support in the technical aspects of the work and the social ones. Indeed their presence and talks make the environment more friendly and enjoyable to work.

Many thanks to the analysis team in Siegen and Göttingen Universities. Without their contribution, the work would have not been completed. Many thanks to everyone at CERN contributed to this analysis.

I will not forget to thank my dear and inspiring friends all over the world, and my inspiring Palestinian colleagues and teachers at CERN or at home. I thank all of them for checking my progress, their encouragement, their advice and for telling me all the way: "You can do it!"

My words will not be enough to express how much I am grateful to my parents, sisters, brothers, and every supportive member of my family. I would definitely have not reached to this point without their trust, prayers, love, support, motivation and the list is long. Thank you very much for being part of my life!

Contents

CHAPTER 1

Introduction

The Standard Model (SM) describes the physics of particles that form the building blocks of matter. The model has been very successful to describe a very large amount of experimental data.

The heaviest elementary particle in the SM is the top quark. It was discovered by the CDF and DØ collaborations in 1995 [1, 2]. Since the discovery, the top-quark properties have been studied extensively by the ATLAS and CMS experiments [3, 4], the two large general-purpose detectors at the Large Hadron Collider (LHC) [5]. The distinctive properties of the top quark, and its numerous possible interactions, provide many handles to test the SM predictions and to explore new phenomena. For example, due its heavy mass, the top quark decays quickly, before it forms a bound state, and thus it behaves as a free quark. This offers great opportunities for in-situ studies of quarks. Furthermore, its heavy mass suggests that its Yukawa coupling to the last discovered SM particle, the Higgs boson [6–8], is very close to unity. Therefore, the top quark plays an important role in physics scenarios with a strongly coupled Higgs sector.

Despite the great success of the SM theory to describe many physical phenomena, it does not provide solutions for some significant issues. For instance, the hierarchy problem, where the mass of the Higgs boson receives large quantum loop corrections. The corrections give rise to a Higgs mass in the order of the Planck scale (10^{19} GeV). However, the discovered Higgs boson has a very small mass compared to the Planck scale. This implies the need of loop cancellations, in order to keep the Higgs mass small. The cancellations could be due to new physics, that is not described by the SM. The unique value of the top-quark coupling to the Higgs boson indicates that the largest loop corrections are due to the top quark. Hence, extensions of the SM are expected to couple strongly to the top quark and modify its various couplings to the SM particles. Thus, measurements of top-quark couplings with high precision are crucial to test the SM.

The top-quark coupling to the photon can be directly probed through the cross-section measurement of top-quark pair production in association with a photon ($t\bar{t}\gamma$) [9, 10]. Deviations in the measured spectrum of certain observables from the SM prediction might point to anomalous dipole moments of the top quark [11–16]. Such deviations could be observed by measuring the cross section differentially, as a function of the photon transverse momentum p_{T}, for example. Therefore, in this thesis, the top-quark coupling to the photon is probed through the cross-section measurement of the $t\bar{t}\gamma$ production.

Two measurements are described in this work. For both, proton–proton collision data collected by the ATLAS detector is used. The first measurement is performed at a centre-of-mass energy of 8 TeV and published in Ref. [17]. The cross section is measured in the single-lepton channel, where one of the two W bosons resulting from the decay of the top-quark pair decays leptonically, and the other W boson decays into a pair of light quarks. The second analysis is performed at $\sqrt{s} = 13$ TeV [18]. The higher centre-of-mass energy and the higher luminosity provide a larger amount of data, which allow the cross section to be also measured in the dilepton channel (the two W bosons decay leptonically). The dilepton channel has a smaller branching ratio than the single-lepton channel. It is the first time that $t\bar{t}\gamma$ production is measured in the dilepton channel. The dilepton channel is nicely characterised by the low expected background processes. The inclusive and differential cross sections are measured using both data periods, 8 TeV and 13 TeV, employing maximum-likelihood fits [19]. The likelihood fits are performed in a fiducial phase-space region that is chosen to be as close as possible to the selection requirements applied in the analysis. The likelihood function is slightly different in the two analyses due to the different input discriminators. The fits exploit the shape differences of input discriminators between the signal and background processes. At 8 TeV, the isolation property of the photons is exploited in the fit, and the differential cross section is measured using a simple bin-by-bin approach. For the 13 TeV analysis, a neural network is developed to separate signal from background processes, and a more advanced technique to measure the differential cross section is used. Furthermore, the Effective Field Theory (EFT) approach [13–16] is employed to search for new physics beyond the Standard Model, at 13 TeV. My key contributions to the 13 TeV analysis have been through the cross-section measurement in the dilepton channel and the EFT interpretation, and therefore they will be described in greater detail.

The rest of this thesis is organised as follows. The second, third and fourth chapters explain the inputs to both analyses. Differences are highlighted when present. In Chapter 2, an overview of the Standard Model, focusing on the top-quark and photon sectors, is provided. The LHC machine, the ATLAS detector, and the principles of particle detection, are described in Chapter 3. Chapter 4 presents the data used in the two analyses, the simulated samples, the definitions of the final-state objects in the $t\bar{t}\gamma$ channel, and the common techniques to measure the cross section. The first analysis at 8 TeV is summarised briefly in Chapter 5, including theoretical predictions, event selections, background estimation, methods to extract the cross section, systematic uncertainties affecting the measurement and, finally, results. Chapter 6 is devoted to the 13 TeV analysis, and has a similar structure to the previous one, but with more details. The unfolding procedure to extract the differential cross section is also explained in this chapter. A search for anomalous top-photon coupling at 13 TeV is presented in Chapter 7. Chapter 8 provides a summary of the two analyses and an outlook for future work. Finally, Appendices A – G are added, in order to provide relevant details for some topics presented in the main body of this thesis.

CHAPTER 2

The production of $t\bar{t}\gamma$ in the Standard Model and beyond

This chapter introduces the Standard Model of particle physics. It describes briefly the fundamental particles, their properties and interactions, focusing on photons, top quarks and their coupling to each other. The top-photon coupling is studied through the top-quark pair production in association with a photon. Theoretical predictions and experimental evidence of $t\bar{t}\gamma$ production in the SM are presented. Furthermore, a search for the $t\bar{t}\gamma$ production beyond the SM within the effective field theory framework is introduced.

2.1 Introduction to the Standard Model

The Standard Model of particle physics [20–25] describes the basic building blocks of matter in the universe and their interactions. The constituents of matter are classified into three types: two particle types of spin-1/2, called fermions, and known as leptons and quarks, and a third type of spin-1, called gauge bosons or force carriers, which mediate the interactions of the other particles. Three charged leptons exist: the electron (e), the muon (μ), and the tau (τ) lepton. Their corresponding neutrinos are also described by the model, and are known as ν_e, ν_μ and ν_τ. Each quark and each lepton has its own anti-particle of the same mass and lifetime, but with opposite values of the additive quantum numbers such as the electric charge, the magnetic moment, the baryon and lepton numbers. There are six flavours of quarks: up (u), down (d), charm (c), strange (s), bottom (b) and top (t). Each quark carries a fractional number of the electric charge, and has three different colour states: red, green and blue. All quarks, with the exception of the top quark, form composite particles, called hadrons, which are colourless.

Leptons and quarks are arranged into three generations; each generation is made of two quarks or two leptons, with an increase of their masses from one generation to the next, except for the neutrinos, which are nearly massless in all generations. The fundamental particles and their properties are presented in Table 2.1. Quarks and leptons interact via four fundamental forces: the strong force, which is mediated by gluons, the weak force, which is mediated by the massive Z and W bosons, the electromagnetic force, which is mediated by the massless photon (γ), and the gravitational force which is mediated by the graviton. The forces and their mediators are summarised in Table 2.2. The generation of particle masses and their interactions are presented in the following sections.

Particles		Generation			Charge/$\|e\|$
		First	Second	Third	
Leptons		e	μ	τ	-1
	mass [GeV]	0.511×10^{-3}	0.106	1.777	
		ν_e	ν_μ	ν_τ	0
	mass [GeV]	≈ 0	≈ 0	≈ 0	
Quarks		u	c	t	2/3
	mass [GeV]	2.2×10^{-3}	1.27	173.2	
		d	s	b	-1/3
	mass [GeV]	4.7×10^{-3}	96×10^{-3}	4.18	

Table 2.1: The fundamental fermions and their main properties [26].

Interaction	Mediator	Charge/$\|e\|$	Mass [GeV]
Strong	Gluon	0	0
Electromagnetic	γ	0	0
Weak	$W^\pm$	± 1	80.4
	Z	0	91.2
Gravitational	Graviton	0	0

Table 2.2: The fundamental forces and their mediators [26].

2.2 Particle interactions

In 1967, Glashow, Weinberg and Salam [23–25] proposed a unified electroweak gauge theory, which describes the electromagnetic and weak interactions. The gauge theory is a product of two gauge groups, $\mathrm{SU}(2)_L \otimes \mathrm{U}(1)_Y$ with massless fermions and exchanging gauge bosons. The $\mathrm{SU}(2)_L$ group is related to the weak interaction with generators of the weak isospin, represented by 2×2 Pauli matrices (σ_a), with a = 1,2,3, where the subscript L indicates that only the left-handed particles are involved in the interaction. The second gauge group is $\mathrm{U}(1)_Y$, which represents the electromagnetic interaction, with the weak hyper-charge Y, as a generator of the group, defined as $Y = 2(Q - I_3)$, where Q is the charge of the particle and I_3 is the third component of the weak isospin.

At that time, the SM theory described all gauge interactions but failed to describe the mass spectrum: the local $\mathrm{SU}(2)_L \otimes \mathrm{U}(1)_Y$ gauge invariance forbids massive fermions and gauge bosons. In order to accommodate for massive particles, the theory postulates two complex scalar fields. The mechanism of generating masses of particles in the presence of a scalar field is called the Brout-Englert-Higgs mechanism [27–29]. The masses of the particles are a consequence of the electroweak symmetry breaking (see Section 2.3). However, the theory could not predict the mass of the Higgs boson, while an upper bound of the order of 1 TeV is derived from unitarity conditions. Indirect bounds on the Higgs mass were determined from the electroweak precision tests [30]. The Higgs particle was discovered in 2012 by both the ATLAS and CMS collaborations at the LHC [6, 7]. The most recent combined measurement of the Higgs mass, performed by the two collaborations, is found to be 125.09 ± 0.21(stat.) ± 0.11(syst.) GeV [8].

The Lagrangian density that describes the fermion fields is written as

$$\mathcal{L} = i\bar{\psi}\gamma^\mu\partial_\mu\psi - m\bar{\psi}\psi, \tag{2.1}$$

where the most general Lorentz invariant mass term for fermions is written as

$$\begin{aligned} m_f\bar{\psi}\psi &= m_f(\bar{\psi}_R + \bar{\psi}_L)(\psi_R + \psi_L) \\ &= m_f(\bar{\psi}_R\psi_L + \bar{\psi}_L\psi_R). \end{aligned} \tag{2.2}$$

However, such terms are not allowed in the SM Lagrangian since ψ_L (left-handed, a member of an isospin doublet of $I = \pm 1/2$) and ψ_R (right-handed, isospin singlet of $I = 0$) transform differently under local gauge transformation as

$$\begin{aligned} \psi_L \rightarrow \psi'_L &= e^{i\alpha(x)T + i\beta(x)Y}\psi_L, \\ \psi_R \rightarrow \psi'_R &= e^{i\beta(x)Y}\psi_R, \end{aligned} \tag{2.3}$$

where $\alpha(x)$ and $\beta(x)$ are arbitrary, real-valued functions of space-time x_μ. T and Y are the generators of the groups $SU(2)_L$ and $U(1)_Y$.

The requirement of the invariance under the local gauge transformation ($\phi \rightarrow \phi' = e^{ieQ\alpha(x)}\phi$) is achieved by replacing the partial derivative with a covariant derivative: $\partial_\mu \rightarrow \mathcal{D}_\mu = \partial_\mu - ieQA_\mu$, and the introduction of a new vector field A with a very specific transformation property: $A_\mu \rightarrow A'_\mu = A_\mu - ieQ\partial_\mu\alpha$. The covariant derivative transforms then as $D_\mu \rightarrow D'_\mu = e^{ieQ\alpha(x)}D_\mu$.

Thus, the full Lagrangian density function that describes the electroweak interaction, and satisfies the local gauge invariance, is given by

$$\mathcal{L}_{\text{EW}} = \bar{\psi}(i\gamma^\mu D_\mu - m)\psi - \frac{1}{4}F^{\mu\nu}F_{\mu\nu}, \tag{2.4}$$

where $F^{\mu\nu}$ is the electromagnetic field strength tensor, which is defined as $F^{\mu\nu} = \partial_\mu A_\nu - \partial_\nu A_\mu$. The interaction between the fermion field and the new field A_μ (photon field) is described by the term

$$-ieQ_f\bar{\psi}\gamma^\mu A_\mu\psi, \tag{2.5}$$

with a fermion charge of Q_f.

In addition to the electroweak interaction, there is also the strong interaction between quarks which is mediated by eight massless gluons and given by the $SU(3)_C$ gauge group. The subscript C refers to the colour symmetry. The Lagrangian density of the quark fields can be initially written as

$$\mathcal{L}_{\text{QCD}} = \bar{q}_j(i\gamma^\mu\partial_\mu - m)q_j. \tag{2.6}$$

The quark fields transform under the SU(3) local gauge invariance as $q(x) \rightarrow q'(x) = e^{-\alpha_a(x)\frac{\lambda_a}{2}}q(x)$, where λ_a are 3×3 matrices, the so-called Gell-Mann matrices, which represent the generators of the gauge group SU(3), with $a = 1, 2, ..., 8$. The partial derivative should be replaced by the covariant derivative as in the electroweak sector. Therefore, a gluon field tensor is required and defined by $G_a^{\mu\nu} = \partial_\mu G_a^\nu - \partial_\nu G_a^\mu - g_s f^{abc}G_b^\mu G_c^\nu$, where f^{abc} are the fine structure constants of the SU(3) group, G_a^ν is the gluon field, and g_s is the strong coupling constant. Consequently, the Lagrangian density in Equation 2.6 changes to

$$\mathcal{L}_{\text{QCD}} = \bar{q}_j(i\gamma^\mu D_\mu - m)q_j - \frac{1}{4}G^a_{\mu\nu}G_a^{\mu\nu}. \tag{2.7}$$

The full gauge symmetry of the SM is a product of three gauge groups described above,

$$\mathrm{G_{SM}} = \mathrm{SU}(3)_C \otimes \mathrm{SU}(2)_L \otimes \mathrm{U}(1)_Y, \tag{2.8}$$

with massless fermions and gauge bosons.

2.3 Masses of fermions and gauge bosons

The spontaneous symmetry breaking mechanism is introduced in order to allow the masses of fermions and gauge bosons in the SM Lagrangian. In general, the mechanism can be described by introducing a scalar ϕ with the field potential $V(\phi)$. The minimum of the potential $< \phi >$ is chosen in a certain way to break the symmetry. Masses of particles are generated as a consequence of the coupling of their fields associated with broken symmetries to that scalar field. The expansion of the scalar field $\phi(x)$ around the minimum is given by

$$\phi(x) = < \phi > + H(x), \quad \text{and} \quad < \phi > = \frac{1}{\sqrt{2}} \begin{pmatrix} 0 \\ v \end{pmatrix}, \tag{2.9}$$

where v is the absolute value of the scalar field at the minimum of the ϕ potential, the so-called vacuum expectation value which has a value of 246 GeV, and $H(x)$ is the physical scalar Higgs field.

The SM Lagrangian should be modified to accommodate the mass terms. Accordingly, the full SM Lagrangian is expressed as

$$\mathcal{L}_{\mathrm{SM}} = \mathcal{L}_{\mathrm{SM}}^{\mathrm{gauge}} + \mathcal{L}_{\mathrm{SM}}^{\mathrm{Yukawa}} + \mathcal{L}_{\mathrm{SM}}^{\mathrm{EWSB}}. \tag{2.10}$$

The first term, $\mathcal{L}_{\mathrm{SM}}^{\mathrm{gauge}}$, describes the coupling between fermions and gauge fields, and the self-coupling of the gauge fields. The full term is not described here, since it is not of interest in the context of the masses of particles. The Feynman vertices for the self-coupling of the gauge fields are shown in Figure 2.1.

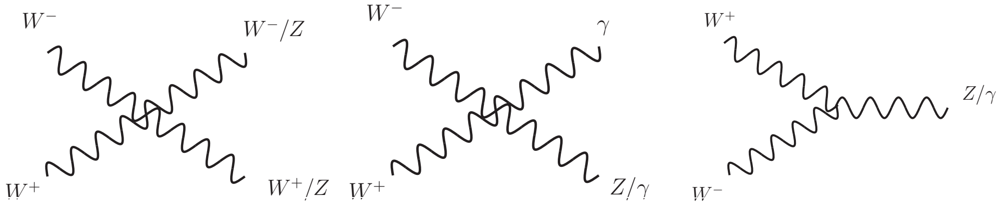

Figure 2.1: The Feynman vertices for the self-coupling gauge fields.

The second term, $\mathcal{L}_{\mathrm{SM}}^{\mathrm{Yukawa}}$, describes the Yukawa coupling of fermions to the SM Higgs, and is given by

$$\mathcal{L}_{\mathrm{SM}}^{\mathrm{Yukawa}} = \lambda_e \bar{e}_R L \phi + \lambda_u \bar{u}_R^\alpha Q^\alpha \phi + \lambda_d \bar{d}_R^\alpha Q^\alpha \phi + h.c, \tag{2.11}$$

where L is the left-handed field of the fermion field doublet, $L = \begin{pmatrix} \nu_L \\ e_L \end{pmatrix}$, and Q is the left-handed quark field doublet, and defined as $Q^\alpha = \begin{pmatrix} u_L^\alpha \\ d_L^\alpha \end{pmatrix}$, α is the colour index, and ϕ is defined in Equation 2.9. By plugging ϕ in Equation 2.11, the Yukawa term transforms as

$$\mathcal{L}_{\mathrm{SM}}^{\mathrm{Yukawa}} = \frac{1}{\sqrt{2}}[\lambda_e v \bar{e}_R L + \lambda_u v \bar{u}_R^\alpha Q^\alpha + \lambda_d v \bar{d}_R^\alpha Q^\alpha] + \text{other terms of } H + h.c., \tag{2.12}$$

such that the mass of fermions is given by $m_f = \frac{v\lambda_f}{\sqrt{2}}$, and f refers to the fermion type. Hence, the Yukawa coupling (λ) to the Higgs field is linearly proportional to the fermion mass.

The last term, $\mathcal{L}_{\mathrm{SM}}^{\mathrm{EWSB}}$, describes the masses of gauge bosons:

$$\mathcal{L}_{\mathrm{SM}}^{\mathrm{EWSB}} = (\mathcal{D}_\mu \phi)^\dagger (\mathcal{D}^\mu \phi) - V(\phi), \tag{2.13}$$

where

$$\begin{aligned} \mathcal{D}_\mu &= \partial_\mu + i g_s G_\mu^A T_A^3 + i g W_\mu^a T_a^2 + i g' B_\mu Y, \qquad (2.14) \\ \mathcal{D}_\mu \phi &= \partial_\mu \phi + i g W_\mu^a \frac{\sigma_a}{2} \phi + i g' B_\mu \frac{1}{2} \phi, \end{aligned}$$

and G_μ^A is associated to the SU(3)$_C$ group, W_μ^a are three gauge fields associated to the SU(2)$_L$ group, and σ_a are the generators of this group. B_μ is the gauge field associated to the U(1)$_Y$ group, Y is the generator of the group U(1)$_Y$, g and g' are the weak and the electromagnetic coupling constants, respectively. The last two couplings are related to each other by the electroweak mixing angle θ_W (Weinberg angle) and the electrical charge e:

$$\sin\theta_W = \frac{g'}{\sqrt{g'^2 + g^2}}, \tag{2.15}$$

$$\tan\theta_W = \frac{g'}{g}, \tag{2.16}$$

$$e = g \sin\theta_W = g' \cos\theta_W, \tag{2.17}$$

$$\tag{2.18}$$

where θ_W has been determined experimentally [26]:

$$\sin^2\theta_W = 0.23116 \pm 0.00013. \tag{2.19}$$

In order to obtain the masses of the gauge bosons, the kinetic term of the Lagrangian is used together with $< \phi >$:

$$\begin{aligned} (\mathcal{D}_\mu < \phi >)^\dagger (\mathcal{D}^\mu < \phi >) &= |(i g W_\mu^a \frac{\sigma_a}{2} + i g' B_\mu \frac{1}{2}) < \phi > |^2 \qquad (2.20) \\ &= \frac{v^2}{8}[g^2((W_\mu^1)^2 + (W_\mu^2)^2) + (g W_\mu^3 - g' B_\mu)^2]. \end{aligned}$$

The charged vector boson, W_μ^-, its complex conjugate, and the vector boson Z_μ, are defined as the following:

$$W_\mu^\pm = \frac{W_\mu^1 \pm W_\mu^2}{\sqrt{2}}, \tag{2.21}$$

$$Z_\mu = \frac{gW_\mu^3 - g' B_\mu}{\sqrt{g^2 + g'^2}}. \tag{2.22}$$

If these vector bosons are inserted in Equation 2.20, the expression changes to

$$\begin{aligned}(\mathcal{D}_\mu < \phi >)^\dagger (\mathcal{D}^\mu < \phi >) &= \frac{v^2 g^2}{4} W_\mu^+ W^{\mu -} + \frac{v^2}{4}(g^2 + g'^2) Z_\mu Z^\mu \\ &= M_W^2 W_\mu^+ W^{\mu -} + M_Z^2 Z_\mu Z^\mu,\end{aligned} \tag{2.23}$$

where the masses of the gauge bosons are calculated as $M_W = gv/2$, and $M_Z = \sqrt{g^2 + g'^2} v/2$. The masses of these bosons are related to each other by the electroweak mixing angle:

$$\frac{M_W}{M_Z} = \cos\theta_W. \tag{2.24}$$

Since Equation 2.20 is transformed to Equation 2.23, it can be concluded that three generators of the electroweak symmetry $\mathrm{SU}(2)_L \times \mathrm{U}(1)_Y$ are spontaneously broken with the field vacuum expectation value. As a result, masses of three gauge bosons ($W^\pm$, Z) are generated. The $\mathrm{U}(1)_Y$ generator remains unbroken and the photon remains massless. The $\mathrm{SU}(3)_C$ symmetry is also not broken.

2.4 The photon

The photon is a spin-one particle and electrically neutral. It does not interact with the Higgs field (shown in Section 2.3), and therefore it is a massless particle. The photon mediates all the electromagnetic interactions. For example, the Bhabha scattering $e^+e^- \to e^+e^-$ can occur through the exchange of a photon between a positron and an electron, as shown in Figure 2.2.

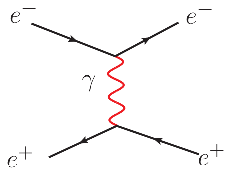

Figure 2.2: An example of a Feynman diagram for the Bhabha scattering.

In the SM, photons can be directly produced through quark–antiquark annihilation, gluon–gluon fusion or Compton scattering processes ($qg \to q\gamma$). Examples of Feynman diagrams are shown in Figure 2.3. The indirect production of photons occurs through the fragmentation of coloured high transverse momentum partons,[1] or from the decay of unstable particles such as the neutral pion (π^0)[2] which decays mainly into a pair of photons. Furthermore, photons can be radiated from charged particles with high transverse momenta. Examples of the indirect photon production are shown in Figure 2.4.

In collider experiments, the diphoton production occurs dominantly through quark–antiquark annihilation and gluon–gluon fusion via a quark-loop. Examples of measurements of the diphoton production cross section can be found in Ref. [31, 32]. The inclusive photon production with a jet[3] is dominated by the $qg \to q\gamma$ process, and an example measurement of its cross section can be found in Ref. [33].

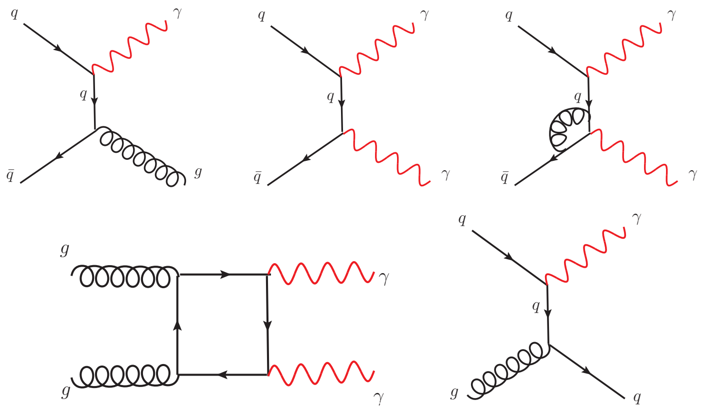

Figure 2.3: Representative Feynman diagrams for the direct photon production through: $q\bar{q}$ annihilation (top), gg fusion (bottom-left), Compton scattering (bottom-right).

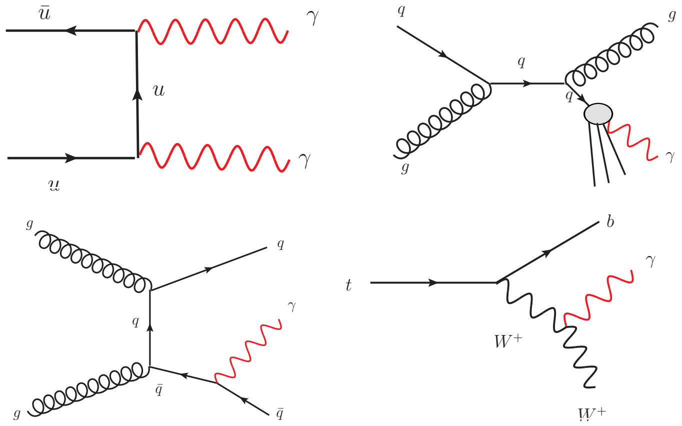

Figure 2.4: Representative Feynman diagrams for the indirect photon production from: neutral pion decay (top-left), quark fragmentation (top-right), and charged particle radiation (bottom).

---

[1] Transverse momentum is the component of the momentum in the transverse plane.

[2] π^0 is a composite state of a quark and antiquark of the same flavour ($u\bar{u}$), a so-called meson. The charged pions consist of a quark and an antiquark of different flavours, such as the π^-, which consists of $\bar{u}d$.

[3] A jet is a collimated stream of particles produced through the hadronisation of quarks and gluons. Jets will be described in Section 4.4.

2.5 The top quark

The top quark is the weak isospin partner of the bottom quark, and has a third component of the weak isospin of $I_3 = +1/2$. Given its large mass of 173.34 ± 0.76 GeV [34], the top quark decays quickly, before it forms a bound state, so that it can only be detected via its decay products. This feature allows the study of top-quark spin polarisation and the correlation between spins. The total decay width of the top quark is calculated to be ≈ 1.5 GeV [26], and is given by the following formula at leading order (LO)[4]:

$$\Gamma_t^{\mathrm{LO}} = \frac{G_F}{8\pi\sqrt{2}} m_t^3 (1 - \frac{m_W^2}{m_t^2})^2 (1 + 2\frac{m_W^2}{m_t^2}), \tag{2.25}$$

where $G_F = \frac{\sqrt{2}g^2}{8m_W^2}$, m_t is the top-quark mass and m_W is the mass of the W boson. The lifetime of the top quark is expected to be 5×10^{-25} s [26]. The top-quark mass is generated by its Yukawa coupling to the Higgs boson

$$\lambda_t = \frac{\sqrt{2}m_t}{v} \tag{2.26}$$

and has a value very close to one.

2.5.1 Top-quark production

The top quark can be mainly produced either in pairs of top and anti-top ($t\bar{t}$) or as a single quark. The production cross section of the single-top quark is about two to three times smaller than the $t\bar{t}$ production cross section. The process of quark-antiquark annihilation ($q\bar{q} \to t\bar{t}$) was the dominant production mode of $t\bar{t}$ at the Tevatron. In contrast, the gluon-gluon fusion ($gg \to t\bar{t}$) forms approximately 90% of the production cross section of $t\bar{t}$ at the LHC, at a centre-of-mass energy of 13 TeV at LO. The remaining fraction is produced through the quark-antiquark annihilation process. The contributions from qg and $\bar{q}g$ scattering at the LHC are considered at next-to-leading order (NLO). The corrections with real emission of gluons and virtual loops to the LO production processes are also added at NLO.

The single-top production occurs mainly through three electroweak processes; the t-channel production ($ub \to dt$ or $\bar{d}b \to \bar{u}t$) which is the dominant (expected 70% of the total cross section), the associated production of the top quark with a real W boson (Wt-channel: $gb \to Wt$), and finally the s-channel production ($u\bar{d} \to t\bar{b}$). Most recently, an evidence for the associated production of the top quark with a real Z boson has been obtained by the ATLAS collaboration at the LHC [35]. The production cross section of top quarks is given by

$$\sigma = \sum_{j,k}^{\text{partons}} \int_0^1 \int_0^1 dx_j dx_k f_j(x_j, \mu_{\mathrm{F}}^2) f_k(x_k, \mu_{\mathrm{F}}^2) \hat{\sigma}(x_j x_k s, \mu_{\mathrm{F}}, \alpha_S(\mu_{\mathrm{R}})). \tag{2.27}$$

The probability of a parton j to carry a fraction x_j of the proton's momentum is given by $f_j(x_j, \mu_{\mathrm{F}}^2)$, which is called the Parton Distribution Function, PDF. The infrared[5] and collinear[6] divergences are

---

[4] The leading order interactions are represented by the lowest order Feynman diagrams in perturbative QCD and QED. An example of top-quark pair production at LO is shown in Figure 2.6. For the next-to-leading order diagrams, extra contributions with virtual loop corrections or gluon emissions are added to the LO diagrams.

[5] Infrared divergences occur if massless particles with vanishing momenta are radiated from other particles.

[6] Collinear divergences occur when massless are particles radiated at very small angles.

absorbed by the PDF. The factorisation scale in the PDF, μ_F, is the energy scale which separates the parton-parton (hard) scattering processes from processes that occur at long distances and low energies. The hard scattering processes occur at high energies and short distances. Their cross section, $\hat{\sigma}$, is a function of μ_F, the strong coupling constant $\alpha_S(\mu_\mathrm{R})$, and the partonic centre-of-mass energy squared ($x_j x_k s$, where s is the proton–proton centre-of-mass energy squared). The re-normalisation scale, μ_R, is introduced in the calculation, in order to cancel the ultraviolet divergences[7] that could arise in the NLO calculations. Thus, the cross section of any process is expressed as the hard scattering cross section weighted by the PDF integrated over all partons' momenta and summed over all partons' types.

The expected and measured production cross sections as a function of the centre-of-mass energies are shown in Figure 2.5. Both, the $t\bar{t}$ production at the LHC and the Tevatron and the single-top production at the LHC, are shown in the figure. The calculations are performed at next-to-next-to-leading order (NNLO) including the next-to-next-to-leading logarithm (NNLL) soft-gluon re-summation [36–40]. The most recent cross-section measurements of $t\bar{t}$ production at $\sqrt{s}$ = 13 TeV have relative uncertainties at the level of ∼ (4 – 5)% [41, 42].

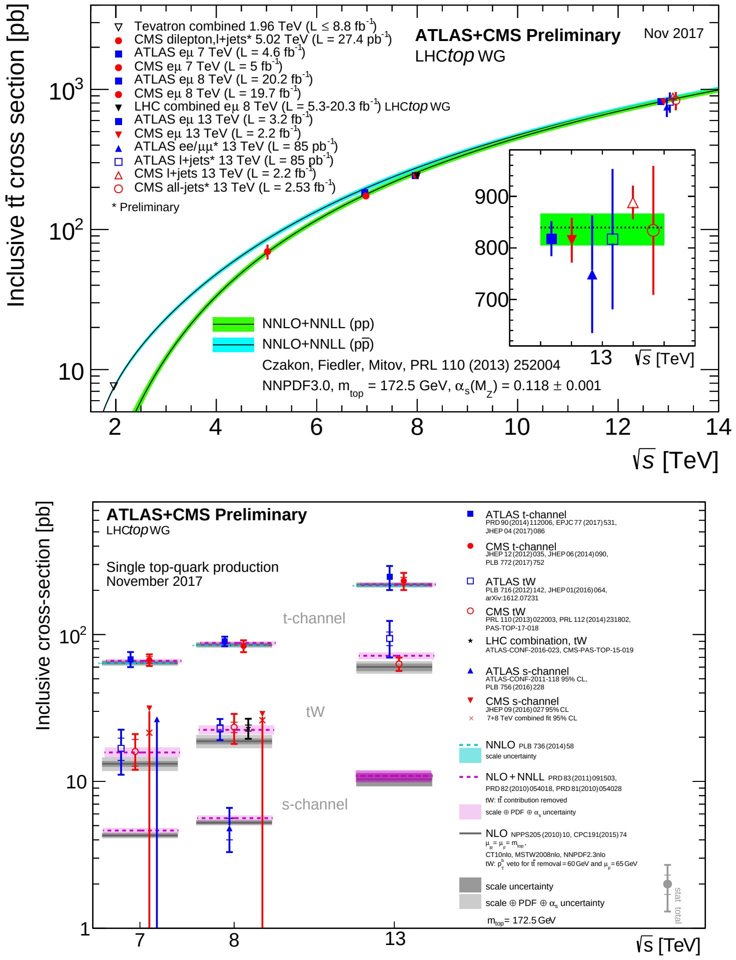

Figure 2.5: The measured production cross section at the LHC and Tevatron compared to the SM expectations as a function of the centre-of-mass energies ($\sqrt{s}$) [43] for $t\bar{t}$ (top), and for single top at the LHC (bottom).

---

[7] Ultraviolet divergences occur if particle momenta in virtual corrections approach infinity.

2.5.2 Top-quark decay

The top quark decays in 99.8% of the cases into a W boson and a b-quark. This is a consequence of the Cabibbo-Kobayashi-Maskawa (CKM) matrix [26]. Each element of the CKM matrix describes the coupling of two quarks to a W boson. The matrix element $|V_{tb}|^2$ is very close to one. The other decays of the top quark into a W boson and a d- or s-quark are strongly suppressed, since the other matrix elements, $|V_{td}|^2$ and $|V_{ts}|^2$, are small. The W boson then decays into a quark and anti-quark of different types, or it could decay into a lepton and its anti-neutrino. For the top-pair production, both W bosons decay into quarks with a branching fraction of 0.46, the so-called fully hadronic channel, whereas in the lepton+jets channel (also known as single-lepton channel) one W boson decays hadronically and the other decays leptonically with a branching fraction of 0.30. The smallest branching fraction of 0.04 is given by the dilepton channel, where both W bosons decay leptonically. The previous numbers do not include the decay of the τ-lepton. In contrast, the branching fractions change to 0.56 if the hadronic decay of the τ-lepton is included in the fully hadronic channel, and change to 0.35 and 0.064 if the leptonic decay of the τ-lepton is included in the lepton+jets and the dileptonic channels, respectively. The three decay channels are shown in Figure 2.6.

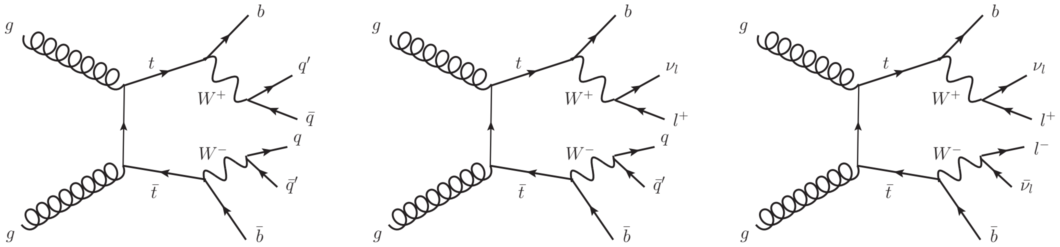

Figure 2.6: LO representative Feynman diagrams for $t\bar{t}$ production and its decay to the fully hadronic channel (left), single-lepton channel (middle) and dilepton channel (right).

2.5.3 Top-quark coupling

The unique value of the top-quark coupling to the Higgs boson (Equation 2.26) suggests the important role that the top quark could play in physics beyond the SM. Extensions of the SM, such as technicolor [44] or other scenarios with a strongly coupled Higgs sector are expected to couple strongly to the top quark and modify its SM couplings. The couplings of the top quark to the SM bosons (γ, Z, W, H) can be directly probed through the cross-section measurements of the associated top-quark production with these bosons [17, 45–49]. Some processes, which involve top-quark loops, could provide indirect probes of the top-quark couplings. For example, the flavour changing neutral current process of the rare decay of the B meson, $b \to s\gamma(Z)$, could indirectly probe the coupling of the top quark to the photon or to the Z boson [50]. Other rare decays of B (e.g., $B_s \to \mu^+\mu^-$) and of K mesons (e.g., $K_L \to \pi^0\nu\bar{\nu}$) also provide indirect probes of the top-quark coupling to the Z boson [51].

2.6 Associated top-quark pair production with a photon in the Standard Model

In this analysis, the $t\gamma$-coupling is probed directly through the cross-section measurement of the associated top-quark pair production with a photon. The interaction between top quarks and photons is predicted by the SM and given by the Lagrangian term defined in Equation 2.5. Hence, the SM vertex of the electromagnetic coupling of top quark to a photon ($t\gamma$-coupling vertex) is given by

$$\Gamma_\mu = -ieQ_t\gamma_\mu. \tag{2.28}$$

The cross-section measurement of $t\bar{t}\gamma$ can be also directly used to obtain the electric charge of the top quark; the production cross section of $t\bar{t}\gamma$ is directly proportional to the square of the top-quark electric charge. The possibility of the existence of an exotic top quark with an electric charge of $Q_t = -4/3$ has been ruled out by the ATLAS collaboration at the LHC [52].

The $t\bar{t}\gamma$ process can be represented with the same diagrams of $t\bar{t}$ production and decay (see Figure 2.6), with an additional photon radiated from any charged particle in the production or the decay of $t\bar{t}$. Photons can be radiated directly from the top quark itself or from the initial partons which interact to give the top-quark pair, the latter is referred as the Initial State Radiation, ISR. Furthermore, photons can be radiated from the charged decay products of the top quark, this is known as the Final State Radiation, FSR. In this thesis, processes of photons emitted from off-shell top quarks or ISR are referred as “radiative top-quark production”, while processes of photons emitted from other sources are referred as “radiative top-quark decay”. The two types of radiation are shown in Figure 2.7. In order to obtain a precise measurement of the $t\gamma$-coupling, a separation between photons emitted from top and from other sources is required. However, it is experimentally not possible to separate completely the two. A reduction of photons that are not radiated from top quarks can be achieved by applying some kinematic requirements on the $t\bar{t}\gamma$ events. For example, photons radiated from top quarks or any initial parton are expected to be highly separated from leptons of the decay products, in the η-ϕ space.

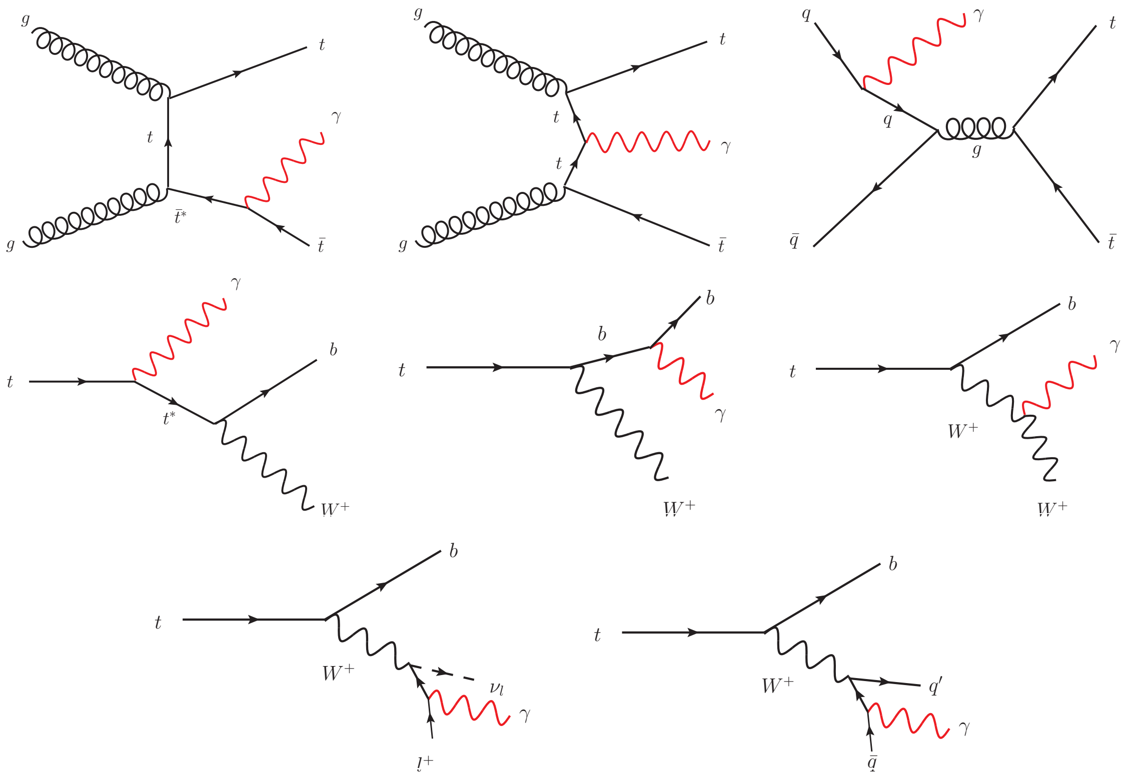

Figure 2.7: LO representative Feynman diagrams for the radiative top-quark production (top), and the radiative top-quark decay (centre and bottom). The star sign indicates an off-shell particle.

2.6.1 Theoretical prediction

The published theoretical predictions of the $t\bar{t}\gamma$ production cross section at LO and NLO in QCD corrections, are performed at a centre-of-mass energy of 14 TeV [53]. This calculation extends the results of Ref. [54] performed in the approximation of stable top quarks, whereas the calculation of Ref. [53] allows for the decay of top quarks. It includes photon radiation from the production and the decay of the $t\bar{t}$ system. Examples of the lowest order diagrams of $t\bar{t}\gamma$ production through gluon–gluon fusion and quark anti–quark annihilation processes are shown earlier in Figure 2.7 (top). The QCD corrections, which are considered in the NLO calculations, include the emission of a real gluon from the previous mentioned processes. The contributions from processes with real parton emission ($q(\bar{q})g \to t\bar{t}\gamma q(\bar{q})$) and virtual loop corrections are also added in the NLO calculations. Examples of the last two contributions are shown in the same Figure 2.8 (bottom-left and bottom-right).

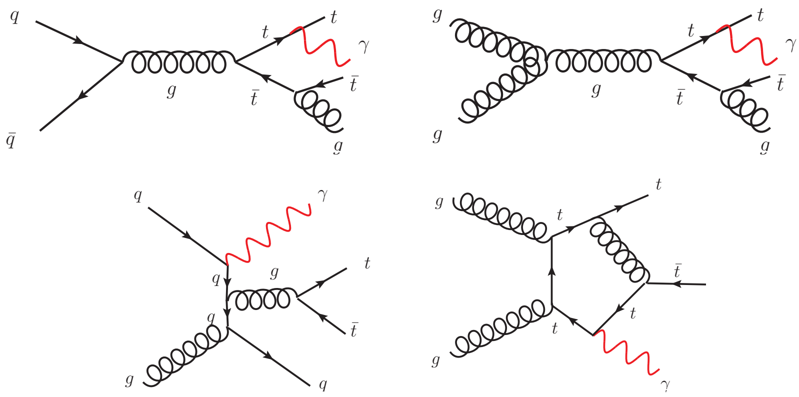

Figure 2.8: NLO representative Feynman diagrams for the radiative top-quark production with real gluon emission in $q\bar{q}$ annihilation process (top-left), real gluon emission in gg fusion process (top-right), real parton emission in qg process (bottom-left) and with virtual loop correction in gg fusion process (bottom-right). More diagrams can be found in Ref. [54].

The method of generalised D-dimensional unitarity [55] extended to massive particles [56] and the dipole formalism are used respectively to calculate one-loop virtual amplitudes and real emission corrections. Top quarks are treated in the narrow width approximation with all spin correlations retained. The hadronic decays of W bosons into two families of light quarks, are considered, and always treated as massless. The W bosons are considered in their mass-shells and no QCD radiative corrections to the hadronic decays are considered. The strong coupling constant is evaluated using one- and two-loop running with five massless flavours. A fine structure constant of $\alpha_{QED} = 1/137$ is used to describe the emission of real photons.

Both types of radiative top-quark decay and production are involved in the calculations. All photons are required to have a minimum transverse momentum of 20 GeV in order to avoid infrared divergences, in addition to some other generic requirements described in the same Ref. [53]. The kinematic distributions of the photons' transverse momenta and the η-ϕ distance between the photon and the hardest b-jet[8] are shown in Figure 2.9, for the the radiative top-quark production and decay. At photon momenta above 60 GeV, photons are mostly emitted from top-quark production. Another set of requirements known as "radiation-in-the-decay suppression", RDS, is applied in addition to the previous generic selections, in order to have observables that are sensitive to the electromagnetic couplings of the top quark. The

---

[8] Jets are reconstructed from stable particles using the anti-k_T algorithm ($R = 0.4$) [57]. b-jets are jets initiated by b-quarks.

RDS exploits the b-jet kinematics in the event, and reduces contributions from the radiative top-quark decay. As a result the NLO cross section is reduced by roughly a factor of three. The new kinematic distributions with the extra RDS requirements are shown in Figure 2.10.

The calculated cross sections at LO and NLO are found to be different. The ratio of the NLO to the LO cross section is called the k-factor. The re-normalisation and factorisation scales largely affect the NLO calculations due to the additional qg channel at NLO. The nominal calculation is made by setting both the re-normalisation and factorisation scales equal to the top-quark mass. The effect of the scale variations by a factor of two or a half around the nominal value is considered as an uncertainty to the theoretical prediction. An uncertainty of approximately 20 (30)% at NLO (LO) around the nominal cross-section value is estimated for the specific calculations in Ref. [53].

Similar dedicated calculations for a centre-of-mass energy of 8 TeV and 13 TeV are also performed [58], but with different selections, adjusted to match the requirements applied in the simulation of the $t\bar{t}\gamma$ process in this thesis. This will be described in later sections (Section 5.1.1 and Section 6.1.1). The NLO cross section is predicted to be 885 ± 13 fb and 2258 ±12 fb in the single-lepton channel at a centre-of-mass energy of 8 TeV and 13 TeV. In the dilepton channel, it is predicted to be 174 ± 13 fb and 439 ± 12 fb at a centre-of-mass energy of 8 TeV and 13 TeV, with uncertainties due to the scale variations.

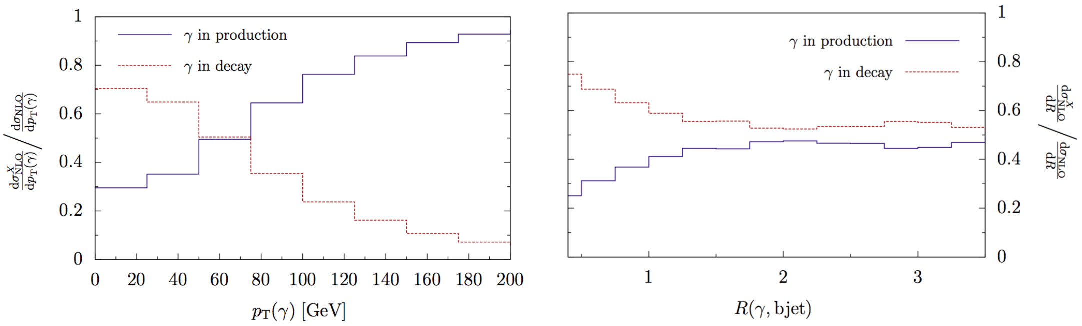

Figure 2.9: Distributions of the photon transverse momentum (left) and the η-ϕ distance between the photon and the hardest b-jet (right) in the single-lepton channel, for both, the radiative top-quark decay (red) and the radiative top-quark production (blue) [53].

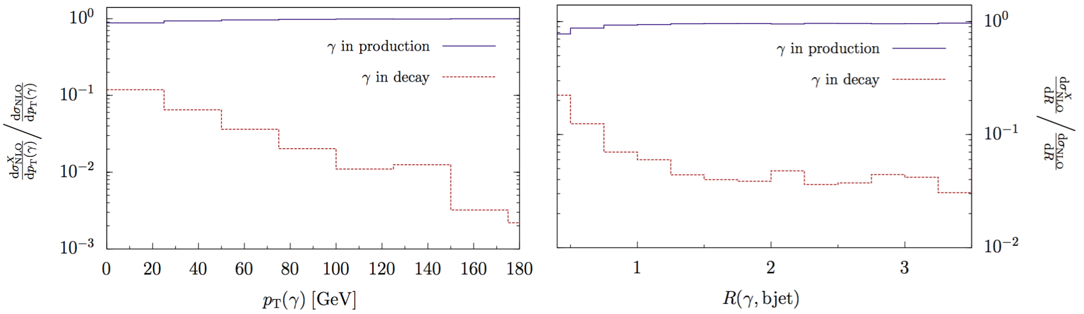

Figure 2.10: Distributions of the photon transverse momentum (left) and the η-ϕ distance between the photon and the hardest b-jet (right) in the single-lepton channel, after applying the RDS requirements, for both, the radiative top-quark decay (red) and the radiative top-quark production (blue) [53].

2.6.2 Experimental evidence

The production cross section of $t\bar{t}\gamma$ was first explored by the CDF collaboration at the Tevatron [59], in proton–antiproton collisions with a data luminosity of 6.0 fb^{-1} at a centre-of-mass energy of $\sqrt{s}$ = 1.96 TeV. It was measured as 180 ± 70 (stat.) ± 40 (syst.) ± 10 (lumi.) fb with a significance of 3.0σ, in agreement with the SM theoretical prediction within uncertainties [54]. The ATLAS collaboration at the LHC has measured the cross section for the first time using data of proton–proton collisions at $\sqrt{s}$ = 7 TeV, with a luminosity of 1.04 fb^{-1}, and then with a luminosity of 4.59 fb^{-1}. The measured cross sections were found to be of 2.0 ± 0.5 (stat.) ± 0.7 (syst.) pb with a significance of 2.7σ [60], and 63 ± 8 (stat.) $^{+17}_{-13}$ (syst.) fb with a significance of 5.3σ [61], respectively. Later, the CMS and ATLAS collaborations at the LHC performed cross section measurements at $\sqrt{s}$ = 8 TeV, with luminosities of 19.7 fb^{-1} and 20.2 fb^{-1}, respectively. The two cross sections, measured in different fiducial regions, were found to be 127 ± 27 fb for CMS [45] and 139 ± 7 (stat.) ± 17 (syst.) fb for ATLAS [17]. The results are in agreement with the SM prediction at NLO [53]. All of the previous mentioned results were obtained in the single-lepton channel of the top-quark pair decay (see Figure 2.6).

The measurement by ATLAS at $\sqrt{s}$ = 8 TeV in the single-lepton channel, will be described in this thesis, as well as a cross-section measurement at $\sqrt{s}$ = 13 TeV.

2.7 Associated top-quark pair production with a photon beyond the Standard Model

The top quark is important in the search for new physics. Deviations from the SM could appear as anomalous top couplings. For the search of physics beyond the SM, there are usually two methods to choose among. The two methods quantify the accuracy with which the new physics is excluded in the case if new physics did not appear. The first method is to specifically extend the physics of the SM. For example, a general form of the Lorentz decomposition of the $t\gamma$-vertex in Equation 2.28 can be written as following [62, 63]:

$$\Gamma_\mu^V(q^2) = -ie[\gamma_\mu(F_1^V(q^2) + \gamma_5 F_3^V(q^2)) + \frac{i\sigma_{\mu\nu}q^\nu}{2m_t}(F_2^V(q^2) + \gamma_5 F_4^V(q^2))], \tag{2.29}$$

where q^2=s is the Mandelstam variable associated to the square of the centre-of-mass energy. F_1^V = 2/3 is the form factor for the $t\gamma$-vector coupling, and F_3^V=0 is the form factor for the axial coupling. F_2^V and F_4^V are the magnetic and the electric-dipole moment form factors, respectively. At the SM tree-level, those two factors are zeros. The F_2^V gets a non-zero value at one-loop quantum corrections, while the F_4^V, which is the CP-violating term, receives the non-zero value at three loops. Deviations from these SM expectations when measuring the F_2^V and F_4^V could indicate new physics beyond the SM.

The other method is a model-independent approach, which is independent of any specific extension of the SM, and can be used to flexibly study any physics beyond the SM. For searches at the LHC, the second method is mostly useful in the situation where the new heavy states are beyond the energy reach of the LHC and reveal themselves only as anomalous interactions among the SM particles. An example of the model-independent method is the Effective Field Theory approach [12–16], which describes low-energy physics effects originated at a higher energy scale. The physics of the SM is considered as low energy physics, which occurs at energies much less than the new physics scale, Λ. The new physics is an extra correction to the SM physics, and suppressed by two powers of inverse Λ. The new physics could be new particles, or extra space-time dimensions, or a new effect on the top coupling which appears as anomalous top couplings in the search of this thesis, or could be any other new physics.

In the effective field approach, the effect of new physics can be parametrised by adding operators of higher orders to the SM Lagrangian, as shown in Equation 2.30. Each operator has a coefficient of the inverse power of the scale, Λ, and all operators of the higher-order dimension (dimension-six operators are used here) satisfy the gauge symmetry of the SM, $G_{\text{SM}} = \text{SU}(3)_C \otimes \text{SU}(2)_L \otimes \text{U}(1)_Y$. Thus, the SM physics is recovered in the limit of $\Lambda \to \infty$. The strength of the new physics coupling to the SM particles is described by the dimensionless coefficients C_i.

$$\mathcal{L}_{\text{eff}} = \mathcal{L}_{\text{SM}}^{(4)} + \sum_i \frac{C_i}{\Lambda^2} O_i^{(6)} + ..., \tag{2.30}$$

where $\mathcal{L}_{\text{SM}}^{(4)}$ is the SM part of the Lagrangian and the second term contains the dimension-six operators. The ellipsis accounts for higher order terms, but those terms are even more suppressed than the dimension-six operators and are therefore neglected. Indeed, in collider physics, the dimension-six operators are the dominant terms [14]. The effect of the operators on the inclusive cross section can be described as

$$\sigma_{\text{eff}} = \sigma_{\text{SM}} + \sum_i \frac{C_i}{\Lambda^2} \sigma_i^{(1)} + \sum_{i \leq j} \frac{C_i C_j}{\Lambda^4} \sigma_{ij}^{(2)}, \tag{2.31}$$

where σ_{SM} is the SM cross section, $\sigma_i^{(1)}$ is the cross section of the interference between diagrams with the operator O_i vertex and the SM diagrams, $\sigma_{ij}^{(2)}$ is the cross section of the quadratic term of the operator O_i when $i = j$; otherwise it corresponds to the interference of two diagrams with one EFT vertex each. For the $t\bar{t}\gamma$ production, three operators, given in Equation 2.32, can be affected by new physics: the O_{tB} and O_{tW} operators, which represent the couplings to the weak hypercharge and isospin gauge bosons, that create the electroweak dipole moment, and the O_{tG} operator, which represents the coupling to gluons and creates the chromomagnetic dipole moments.

$$\begin{aligned} O_{tW} &= \lambda_t g_w (\bar{Q}\sigma^{\mu\nu}\tau^I t)\tilde{\phi} W_{\mu\nu}^I, \\ O_{tB} &= \lambda_t g_Y (\bar{Q}\sigma^{\mu\nu} t)\tilde{\phi} B_{\mu\nu}, \\ O_{tG} &= \lambda_t g_s (\bar{Q}\sigma^{\mu\nu} T^A t)\tilde{\phi} G_{\mu\nu}^A, \end{aligned} \tag{2.32}$$

where λ_t is the top-Yukawa coupling constant, g_w, g_Y and g_s are the SM coupling constants, $\sigma^{\mu\nu} = \frac{i}{2}[\gamma^\mu, \gamma^\nu]$, Q is the left-handed quark doublet of the third generation, t is the right-handed top quark, ϕ ($\tilde{\phi} = \epsilon\phi^*$, $\epsilon = i\tau^2$) is the Higgs field, and τ^I and T^A are the generators of the SU(2) and SU(3) groups, respectively.

Representative Feynman diagrams for the EFT vertices and the corresponding operators are shown in Figure 2.11.

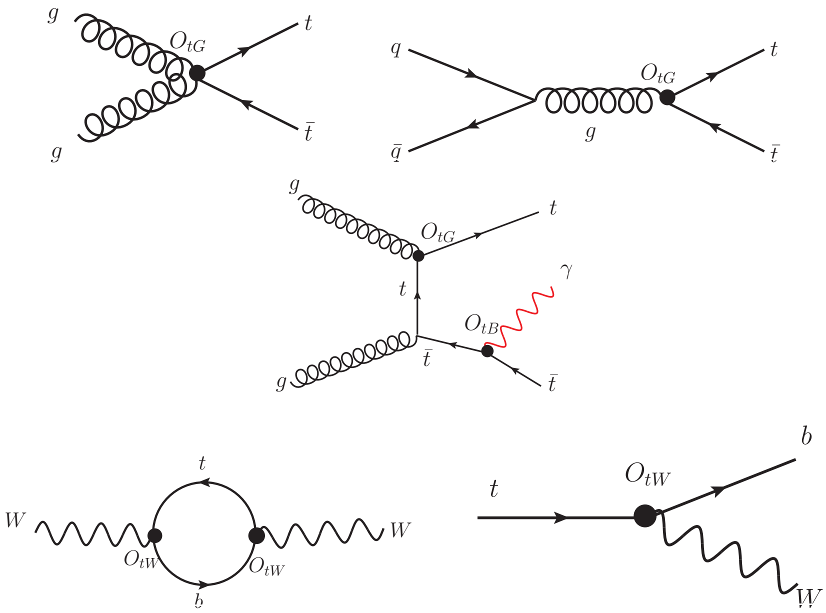

Figure 2.11: Feynman diagrams for the EFT vertices in top-quark production and decay. The black dots represents dimension-six vertices.

CHAPTER 3

The Large Hadron Collider and the ATLAS detector

3.1 The Large Hadron Collider

The Large Hadron Collider [5] is a circular particle accelerator designed to study the smallest known particles, and search for the unknowns. The LHC has a circumference of 27 km and is located about 100 m beneath the ground. Inside the accelerator, two beams of either protons or lead ions circulate in opposite directions, and travel at speeds close to that of light. The two beams gain energy with each lap, when the beams reach the required energy, they are made to collide and a lot of particles are produced as a result.

The accelerator is designed to collide protons at a centre-of-mass energy of 14 TeV, and an instantaneous luminosity of 10^{34} cm^{-2}s^{-1}, providing a bunch collision rate of 40 MHz. Each bunch consists of of 10^{11} protons. The time interval between the interactions is at least 25 ns. The beams are kept on circular paths by the aid of around 1232 dipole magnets. In order to minimise the number of lost particles and maximise the chances of interaction, an additional 392 quadrupole magnets are employed to keep the beams focused. The accelerator can also collide heavy ions at a centre-of-mass energy up to 2.8 TeV and a luminosity of 10^{27} cm^{-2}s^{-1}.

3.1.1 Experiments at the LHC

The collision of protons can occur in four points, the largest two experiments of those points are: ATLAS (A Toroidal LHC Apparatus) and CMS (Compact Muon Solenoid) which are general purpose detectors designed to search for new physics phenomena and perform precision measurements in particle physics. The other two colliding points are LHCb and ALICE. The LHCb (Large Hadron Collider Beauty) studies the beauty quark to investigate the differences between matter and anti-matter. ALICE (A Large Ion Collider) explores the formation of quark-gluon plasma in collisions of heavy ions. In addition to the four colliding experiments, there are few other smaller size experiments shown in Figure 3.1 and described in Ref. [5].

3.1.2 Luminosity at the LHC

The instantaneous luminosity $\mathcal{L}$ describes the instantaneous number of interactions per second, per unit area. Hence, the higher value of $\mathcal{L}$, the higher is the number of collisions. The number of events at the LHC is given by

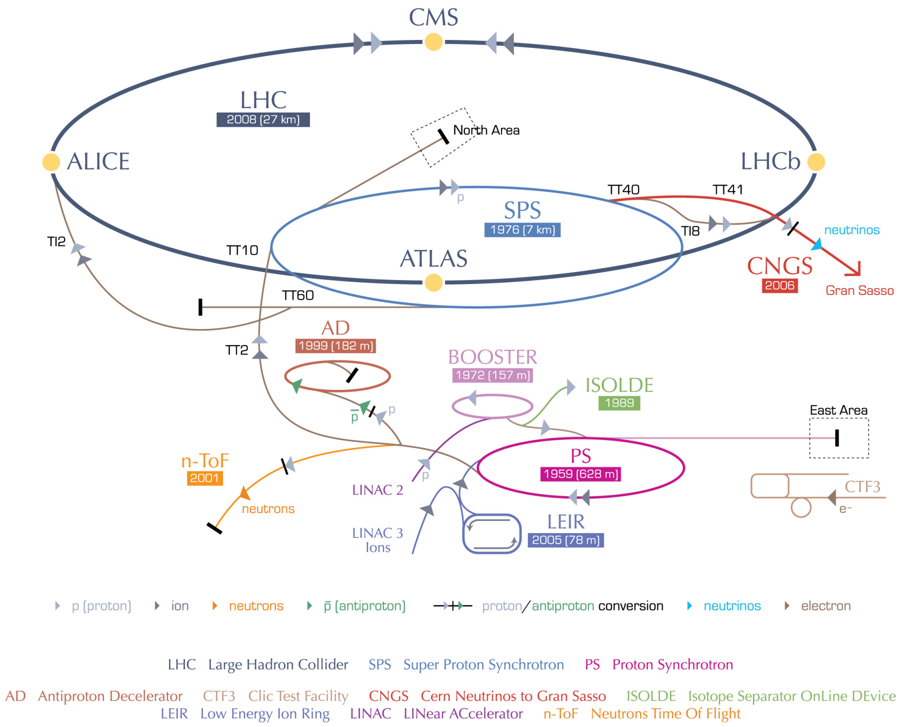

Figure 3.1: The layout of the CERN accelerator complex [64].

$$N_{\text{events}} = L\sigma_{\text{events}}, \tag{3.1}$$

where L is the integrated luminosity which is defined as the integral of the delivered luminosity over time. It has the inverse unit of the cross section and usually is given in fb^{-1}:

$$L = \int \mathcal{L} dt. \tag{3.2}$$

The instantaneous luminosity $\mathcal{L}$ (Equation 3.3) is proportional to the number of particles per bunch N_b, the number of bunches per beam n_b, and the revolution frequency f_{rev}. The other factors that appear in Equation 3.3 are the relativistic gamma factor γ_r, ϵ_n is the normalised transverse beam emittance, β^* is the amplitude function at the interaction point, and F is the geometric luminosity reduction factor due to the crossing angle at the interaction point.

$$\mathcal{L} = \frac{N_b^2 n_b f_{\text{rev}} \gamma_r}{4\pi\epsilon_n\beta^*} F. \tag{3.3}$$

High luminosity of 10^{34} cm^{-2}s^{-1} is provided for the two experiments ATLAS and CMS, while the other two interaction regions have lower nominal luminosities of the order of 10^{32} cm^{-2}s^{-1} for LHCb and 10^{30} cm^{-2}s^{-1} for ALICE. By the end of the proton–proton run for 2011, ATLAS and CMS have each received around 5.6 fb^{-1} of integrated luminosity at a centre-of-mass energy of 7 TeV. Increasing the beam energy to 4 TeV has lead to a total luminosity per experiment of roughly 23 fb^{-1}in 2012 (Run I of the LHC). The centre-of-mass energy has reached 13 TeV (Run II of the LHC) in 2015 and 2016 for a total delivered luminosity of around 43.1 fb^{-1}, and expected to reach 120 fb^{-1} by the end of 2018 before the long shut-down of the LHC.

3.2 Basic principles of particle detection

Particles resulting from proton–proton collisions interact with the medium they are traversing, and produce secondary particles. The secondary particles also interact with the medium and produce others [65–68]. Unstable particles can decay immediately or travel some distance in the medium and decay afterwards. The average distance that a particle travels before it decays is given by $\beta\gamma c\tau$[1], where τ is the lifetime of the particle and $\beta\gamma$ is the boost factor. The trajectory of the primary particle and its momentum can be established by observing the particle itself, or the decay products and the secondary particles. If a charged particle is moving perpendicular to a magnetic field B, its transverse momentum p_T is related to the curvature of its trajectory R by the following formula[2]:

$$p_\text{T} \approx 0.3 \cdot B \cdot R, \tag{3.4}$$

where p_T is measured in GeV, B in Tesla and R in meters. Oppositely charged particles bend in opposite directions. The successive interactions of the primary particle and the newly produced particles can result in showers of particles with energy deposit in the medium. The energy deposit can be transferred into a measurable quantity, hence the energy of the initial particle will be known (calorimetry [69]). The most dominant interactions that lead particles to lose their energies in matter are described in this section. Electrons, muons and photons are used as examples for particles that interact via the electromagnetic force, and produce electromagnetic showers, and hadrons as examples for particles that interact via the strong force and produce hadronic showers.

Electrons of energies in the range [200 keV – few 10 MeV] lose their energies via ionisation (governed by the Bethe-Bloch equation). For higher energies electrons lose their energy via Bremsstrahlung. In the ionisation process, part of the electron energy is used to eject an electron from atoms that were hit by the initial electron. Bremsstrahlung occurs when an electron of high energy decelerates in the Coulomb field of a nucleus, and the change in its energy appears in the form of a photon. The energy loss via Bremsstrahlung is proportional to the energy of the electron. For a particle of mass M, other than the electron, Bremsstrahlung is suppressed by a factor of $\approx 1/M^2$. For instance, muons with energies above 1 TeV lose their energy mainly via Bremsstrahlung, while it is negligible for smaller energies, and thus the ionisation process becomes the dominant energy loss mode. The radiation length, X_0[3], of the muon is much larger than that of the electron. Therefore, additional apparatus for muon detection is usually added at some larger distances (see e.g. Section 3.3.5). On the other hand, photons undergo different types of interactions with matter. For photons with energies less than 100 keV, the energy loss occurs dominantly via the photoelectric effect, where the photon energy is transferred to an electron of an atom which is hit by the photon. The energy is used to liberate the electron, if it is sufficient: as a result, the photon disappears completely. If the photon energy is between 100 keV and 1 MeV, the elastic collision between a photon and an electron is the dominant mode of the energy loss. This process is known as

---

[1] $\beta = \frac{|\vec{p}|}{E}$ and $\gamma = \frac{E}{m}$, where E is the energy of the particle, m is the particle mass, $|\vec{p}|$ is the Cartesian momentum and related to p_T by $|\vec{p}| = p_\text{T} \cosh\eta$ if the beam of particles is moving along the z-axis as in the ATLAS detector (η is defined in Section 3.3.1).

[2] Derived by equating the Lorentz magnetic force to the centripetal force ($QvB = \frac{mv^2}{R}$), and using the correct units. The particle momentum $p_\text{T} = mv$, v and Q are the velocity and the electric charge of the particle, respectively.

[3] For the Bremsstrahlung loss, the radiation length can be defined as the medium thickness where the energy of the particle reduces by a factor e.

Compton scattering. In this type of processes, the photon transfers part of its energy to the recoiling electron. Finally, the pair production dominates at photon energies above 1 MeV, where electron-positron pairs are produced[4].

An electromagnetic shower develops by a series of electromagnetic interactions of the primary particle and the newly produced particles. For example, an electron with E_0 loses half of its energy after one radiation length via Bremsstrahlung. The Bremsstrahlung photon can undergo an electron-positron pair production and gives its energy to the pair. The initial electron loses the second half of its energy after two radiation lengths, by radiating other Bremsstrahlung photon. The procedure continues until the energy per particle at a specific depth reaches a critical point. The critical point is the energy value where no further radiation is possible, and the energy loss via ionisation becomes dominant for the electrons. The remaining particles continue losing their energy slowly until they are finally absorbed. The depth of the shower grows logarithmically with the energy. The transverse and longitudinal shower dimensions are characterised by the radiation length. The spread of the shower in the transverse direction is mainly due to the opening angle between electrons and positrons, multiple scattering of electrons and positrons away from the shower axis, and also due to contributions from the emitted Bremsstrahlung photons.

Hadrons lose their energy mainly by nuclear interactions (the strong force) which takes the form of breakups of nuclei, nuclear excitations, or nucleon evaporations. If an energetic hadron hits a very heavy nucleus, the nucleus can be broken up and the fragments expel their excess neutrons. Large numbers of neutrons are consequently produced (this process of neutron production is called spallation). When a high energetic hadron interacts with one or more nucleons within the nucleus, new hadrons can be produced. For example, if a nucleus is hit by a proton of a few GeV, 90% of the produced hadrons are pions. A nucleus, which absorbed a hadron or was hit by an energetic hadron, is left in an excited state. The de-excitation occurs through the emission of photons.

The hadronic shower develops in a similar way to the electromagnetic shower, where hadrons interact with matter and produce secondary hadrons. The secondary hadrons interact and produce more hadrons. The longitudinal and transverse shower sizes are characterised by the nuclear absorption length, λ_I[5], which is much larger then the radiation length for the electromagnetic showers. For instance, a value of $\lambda_I = 85.7$ cm is compared to $X_0 = 14$ cm for liquid Argon [65]. Therefore, hadronic showers are longer and wider than electromagnetic showers and hence hadronic calorimeters are designed to be larger than electromagnetic calorimeters.

The combination of different detectors is required to identify all kinds of particles of all types of interactions. A summary example of particle interactions with the different components of the ATLAS detector is sketched in Figure 3.2. The components will be described in the following sections. From the figure, it can be observed that different particles travel different distances across the detector, and leave signatures in different places depending on the type of interactions they undergo. In addition to the energy deposits in the calorimeters, charged particles leave tracks in the tracking detectors. Those detectors are used to provide precise position and track parameter measurements (see Section 3.3.3). Furthermore, the detectors can be used to measure the amount of energy deposit per unit distance, in order to provide useful information about the type of the interacting particle [70].

---

[4] The intensity of a photon beam is reduced by a factor e at $x = \frac{9}{7X_0}$. In other words, the number of unconverted photons reduces according to $e^{-\frac{7x}{9X_0}}$.

[5] The mean free path that a hadronic particle travels before it undergoes a nuclear interaction. $\lambda_I \approx 35A^{1/3}$ gm/cm^2 where A is the atomic number of the medium.

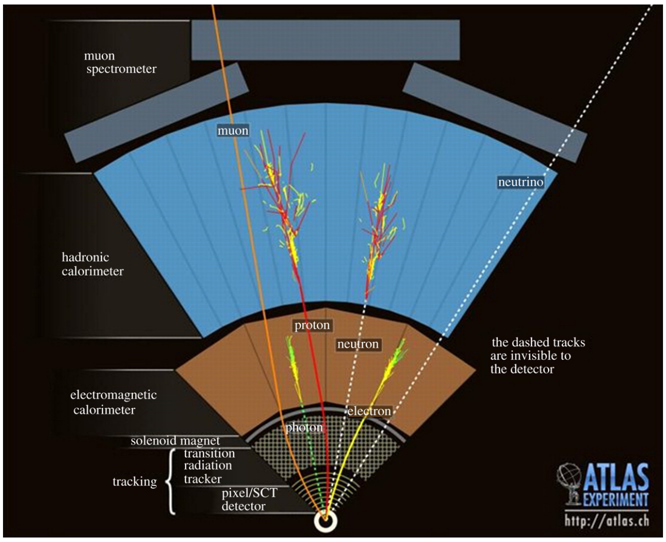

Figure 3.2: Particle interactions with different layers of the ATLAS detector [71].

3.3 The ATLAS detector

The ATLAS experiment [3] is a general purpose detector, one of the collision points of the LHC, and is forward-backward symmetric with respect to the interaction point. The detector has a length of 44 m, a height of 25 m and a weight of around 7000 tonnes.

ATLAS is composed of four major parts shown in Figure 3.3; the inner detector (ID), which is designed to track electrically charged particles and measure their momenta. The muon spectrometer (MS) identifies the muons and measures their kinematics. The magnet systems: a solenoidal magnet outside of the inner detector provides a 2 T magnetic field for the inner detector, and the toroid magnet located in the muon system bends the charged particle trajectories. The calorimetric system, which is used to measure the energy deposits of particles passing the detector.

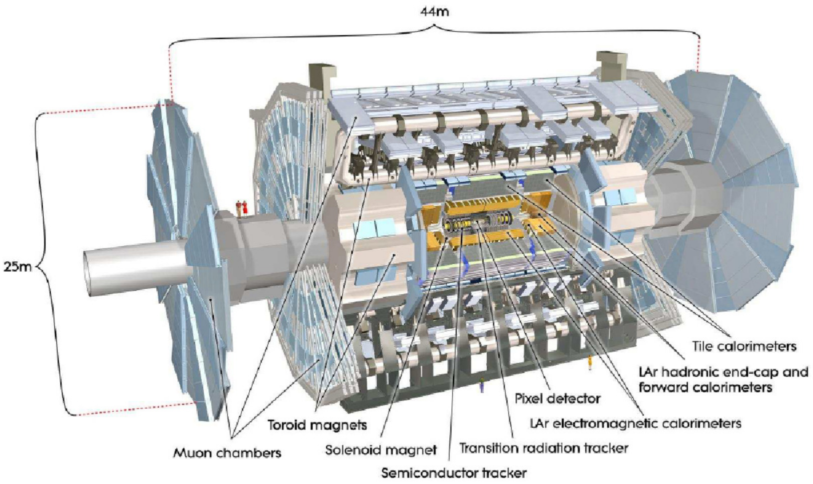

Figure 3.3: An overview of the ATLAS detector and its main components [3].

3.3.1 ATLAS coordinate system

The coordinate system of the ATLAS detector, which is illustrated in Figure 3.4, can be described as follows: the beam travels along the z-axis, while the x-y plane is transverse to the beam direction. The point (0,0) is the interaction point, the positive x-axis is pointing from the interaction point to the centre of the LHC ring, and the positive y-axis is pointing upwards. The azimuthal angle ϕ corresponds to the angle between the x-axis and the projection of a direction on the transverse plane. The polar angle θ is the angle with respect to the z-axis.

Using the mentioned coordinate system, several kinematic variables can be defined (see Figure 3.5) to detect and identify the interactions. The main variables are defined as follows:

- The particle momenta p_x, p_y and p_z are defined along the x-, y- and z-axis, respectively.
- The transverse momentum p_{T} is the projection of the particle momentum on the x-y plane:

$$p_{\mathrm{T}} = \sqrt{p_x^2 + p_y^2}. \tag{3.5}$$

- The pseudorapidity η is a parametrisation of the polar angle θ, as given in Equation 3.6. The pseudorapidity approaches the rapidity y in the limit of a massless particle in Equation 3.7. The difference in the pseudorapidity of two particles is invariant under Lorentz boosts along the z-axis.

$$\eta = -\ln[\tan(\frac{\theta}{2})]. \tag{3.6}$$

$$\eta = \frac{1}{2}\ln\frac{E + p_z}{E - p_z}. \tag{3.7}$$

- The ΔR is the η-ϕ distance between particles:

$$\Delta R = \sqrt{\Delta\eta^2 + \Delta\phi^2}. \tag{3.8}$$

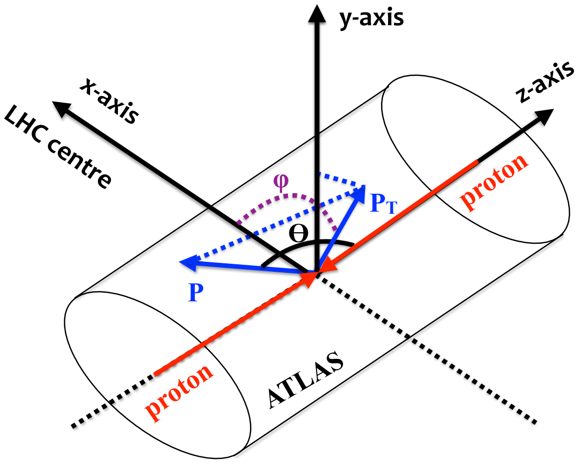

Figure 3.4: The right-handed coordinate system of the ATLAS detector.

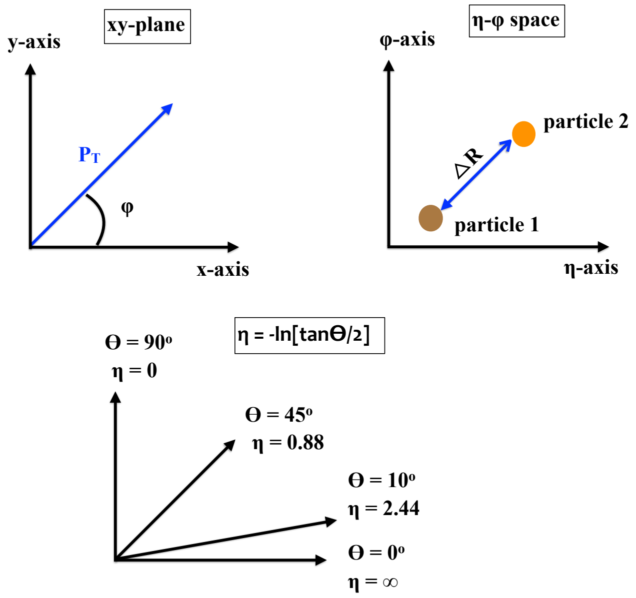

Figure 3.5: An illustration of some measured quantities at the ATLAS detector.

3.3.2 Magnetic field

Two magnetic field systems are employed at the ATLAS detector, with the purpose of identifying and bending charged particles in the inner detector and the muon spectrometer. The two systems are kept cooled using liquid helium, and operated at a temperature of 4.7 K.

The first system is a solenoid magnetic field which creates a homogeneous magnetic field of 2 T, parallel to the beam axis and is located between the inner detector and the electromagnetic calorimeter. The system consists of aluminum, copper and a niobium-titanium alloy. The second system is a toroid magnet, consists of one barrel toroid located in the central calorimeter, and two end-cap toroids installed at each end of the barrel toroids. Each toroid is composed of eight superconducting coils, made of the same material as of the solenoid magnets. The system provides a magnetic field of up to 4 T orthogonal to the muon trajectories. An illustration of the magnetic field system at ATLAS is shown in Figure 3.6.

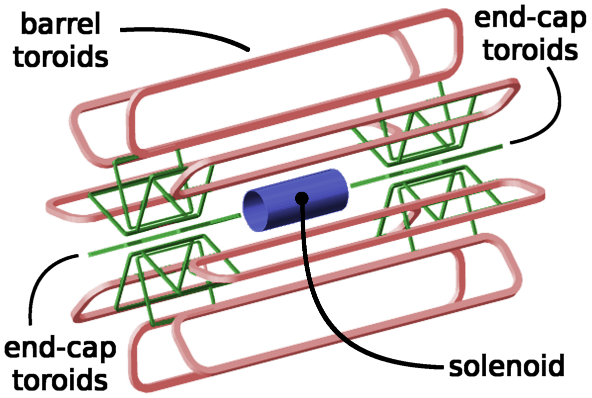

Figure 3.6: The magnetic field system at the ATLAS detector [72].

3.3.3 The inner detector

The ATLAS Inner Detector (ID) is responsible for reconstructing the tracks of particles crossing the detector. It provides a coverage in pseudorapidity of $|\eta| < 2.5$, a length of ±3.5 m and a radius of 1.15 m, embedded within a cylindrical envelope.

The ID is composed of three sub-detectors (see Figure 3.7), providing a resolution for the transverse momentum of 1% for tracks with $p_T > 0.5$ GeV. The silicon pixel detector, which is the nearest to the beam-line, provides the most precise position measurement. It consists of a barrel made of three concentric cylinders around the beam axis, and two end-cap regions with three disks each. The pixel size is $50 \times 400\ \mu\text{m}^2$. The pixel detector allows to identify particles with long lifetimes, such as b-hadrons, with a high precision. The closest layer to the beam pipe was the B-layer in Run I of the LHC, which is positioned at a radius of 50.5 mm. It provides a precise measurement of the track impact parameters and the secondary vertices from the b-hadron decay. A new B-layer, the so-called Insertable B-Layer (IBL), was inserted for Run II at a radius of 33 mm from the beam axis, in 2014 [73–75]. The new pixel layer provides an additional space point very close to the interaction point, which keeps the performance of the tracking while the older B-layer continues to degrade.

The second sub-detector is the Semi-Conductor Tracker (SCT). The SCT comprises four micro-strip layers in the barrel and nine disks in the end-cap region. The SCT employs two sets of strips with a relative rotation of 40 mrad to measure all coordinates, and uses a micro-strip sensor pitch of 80 μm. The SCT provides extra accuracy to the vertex and the impact parameter measurements together with the pixel detector. The last component of the ID is the Transition Radiation Tracker (TRT). The TRT provides measurements in the r-ϕ plane by means of straw drift tubes. The tubes are filled by a Xe-based gas mixture. When a particle passes the gaseous mixture, it produces transition radiations. The intensity of the radiation is proportional to the Lorentz factor of the incoming particle, which allows the discrimination of ultra-relativistic electrons from other heavier hadronic particles. The barrel of the TRT is composed of 73 layers of straws interleaved with fibres, with r-ϕ resolution of 130 μm, while the end-cap is made of 160 straw planes interleaved with foils.

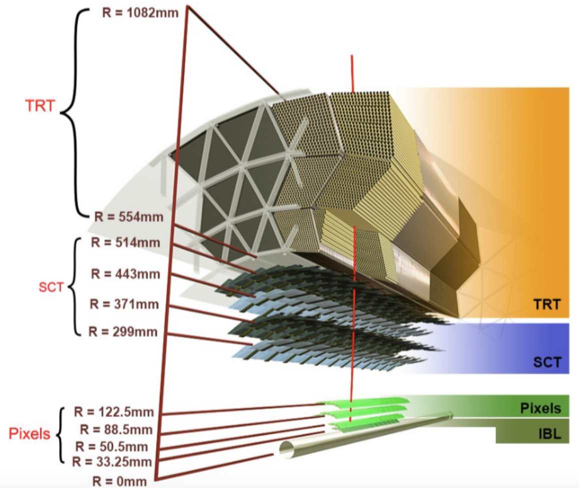

Figure 3.7: The Pixel, SCT and TRT sub-detectors of the ID. The new insertable B-layer is also shown [74].

Track reconstruction

Particles crossing the detector interact with the detector material and leave hits in the pixel and the SCT detectors[6]. A tracking algorithm [76] combines the hits from the pixel and SCT detectors, and tries to correctly associate hits with tracks. A Kalman filter [77] is employed to reject or add hits to the track. Sometimes, two tracks or more share the same hits. Therefore, a χ^2 fit [78] is performed, and the tracks fullfiling a certain selection criterion are chosen. The criterion is based on the track quality fit (χ^2 per degree of freedom), number of found hits, number of missing hits and shared hits. The selected fitted tracks are extended into the TRT, and the fit is repeated using the full information provided by the three detectors; pixel, SCT and TRT. More details about the track reconstruction can be found in Ref. [76].

3.3.4 Calorimeter

The Electromagnetic Calorimeter (ECAL) and the Hadronic Calorimeter (HCAL) are the two main calorimetric systems of the ATLAS detector. Each calorimeter consists of different layers with different thickness to cover all types of interactions that could occur within the detector layers, hence the pattern recognition and energy measurements can be improved. A schematic view of the ATLAS calorimetric system is shown in Figure 3.8.

The ECAL measures the energy of particles interacting via the electromagnetic force such as electrons, photons and positrons (see Section 3.2). Those particles lose their energy fast and do not reach to the second calorimeter. The central ECAL is of an accordion-geometry design made from lead/liquid-argon (LAr) detectors. The detectors consist of two half barrels that cover the region $|\eta| < 1.475$, and two end-caps, that cover the region $1.375 < |\eta| < 2.3$. Between the barrel and the end-cap, in the region $1.37 < |\eta| < 1.52$, there is a free space for cables and services for the inner detector. The region is called the "crack " or the transition region. The interactions happen in two parts of the system: the lead which acts as an absorber and the liquid-Argon (LAr) which acts as an active medium. Particles interact with the lead layers, low and high energetic electrons, positrons and gammas are produced as a result. The high energetic particles penetrate through the medium and create more secondary particles with lower energies, the particle production continues until all the incident particle energy is absorbed. The secondary generated particles create ionisation while interacting with the LAr. The negatively charged ions drift through the LAr, to be collected on the electrodes, which create an electric signal to be analysed. The energy of the original particles can be determined from the amount of the energy and the charge deposited through the path of passing particles.

In the region $|\eta| < 2.47$ which is devoted to precision measurements, the electromagnetic calorimeter is divided to three sampling layers, longitudinal in shower depth, that vary for their different granularity in the η direction. The first layer, the so-called front or strip layer, is segmented with strips along the η direction. It provides discrimination between single photon showers and two overlapping showers coming from the decays of neutral hadrons, mostly π^0 and η mesons. The middle layer collects most of the energy deposited in the calorimeter by photon and electron showers, while the back one is used to correct for leakage of high-energy showers beyond the EM calorimeter. The energy lost by electrons and photons before reaching the calorimeter is corrected by a pre-sampler detector, which is a separate thin LAr layer (11 mm). The pre-sampler covers the pseudorapidity range of $0 < |\eta| < 1.8$ and provides a shower sampling in front of the active ECAL.

The HCAL is located behind the ECAL, and designed to provide energy measurements of particles

---

[6] The pixel detector is designed to measure 4 hits per track in the barrel region and 5 hits per track in the end-caps. Its initial Run I design allowed to measure only 3 hits per track in the barrel region. The SCT detector is designed to measure 8 hits per track in the central region and 9 hits per track in the end-caps, considering two sides per layer.

interacting via the strong force such as neutrons (see Section 3.2). It covers the range $|\eta| < 4.9$. The HCAL contains three types of detector technologies: the tile calorimeter (TileCal) where the plastic scintillator operates as an active medium, and iron as an absorber. The LAr hadronic end-cap calorimeter uses the LAr as an active medium and the copper as an absorber. It covers the range of $1.5 < |\eta| < 3.2$. The last technology is the LAr forward calorimeter, it covers the range of $3.1 < |\eta| < 4.9$. The forward calorimeter is exposed to high level of radiation, and is important to measure events with forward jets. For example, events induced by vector boson fusion processes [79].

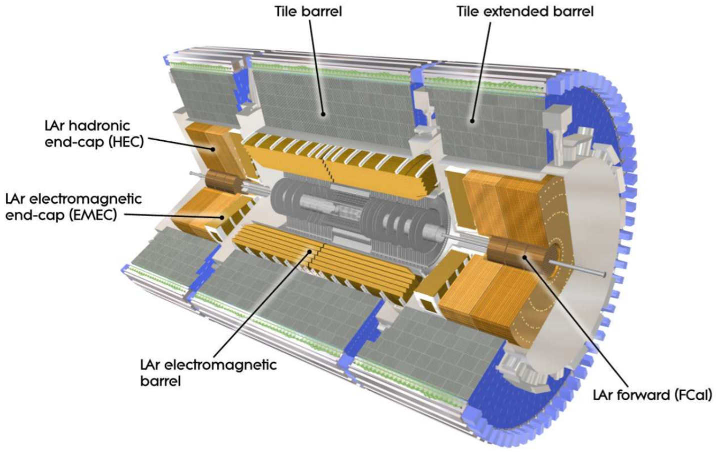

Figure 3.8: A schematic view of the ATLAS calorimeter system [3].

3.3.5 Muon spectrometer

The Muon Spectrometer (MS) forms the outermost layer of the ATLAS detector, and is designed to detect muons. It covers the region $|\eta| < 2.7$. The MS contains a collection of trigger and tracking chambers to provide a stand-alone measurement of the muon transverse momentum with a precision of approximately 10% for tracks with $p_{\mathrm{T}} > 1$ TeV. The chambers and the other components of the muon spectrometer are shown in Figure 3.9.

Muons are heavy charged particles, compared to electrons, therefore muons pass through the whole entire detector, while leaving signatures in the inner tracking detector and muon spectrometer, and small amounts of energy deposit in the ECAL and the HCAL. The muon deflection occurs in the magnetic fields generated by the three large air-core toroids, hence the momentum can be determined. The Monitored Drift Tubes chambers (MDT) function as proportional counters that can be used for precise timing measurements over most of the η range. The coordinates of tracks can be determined by measuring the time that the muon takes to pass through the medium and to interact with the traversed gases in the drift tubes. The multi-wire proportional chambers, Cathode-Strip Chambers (CSCs), cover the region $2.0 < |\eta| < 2.7$. The chambers are filled with a gas mixture of argon and carbon dioxide. They are employed in the forward region due to the high flux of particles. The CSCs provide high-rate-safe measurements, using the induced-charge distribution.

The triggering system in the MS consists of two components that cover the $|\eta| < 2.4$ range: the Thin Gap Chambers (TGC) which are multi-wire chambers filled with gases, and the Resistive Plate Chambers (RPC) which consist of charged parallel plates with a separation of 2 mm from each other and a gas filled gap in between. The system is used to measure both the η and the ϕ coordinates of the muon tracks. The trigger chambers also provide bunch-crossing identification and complement the measurement of the MDTs and the CSCs.

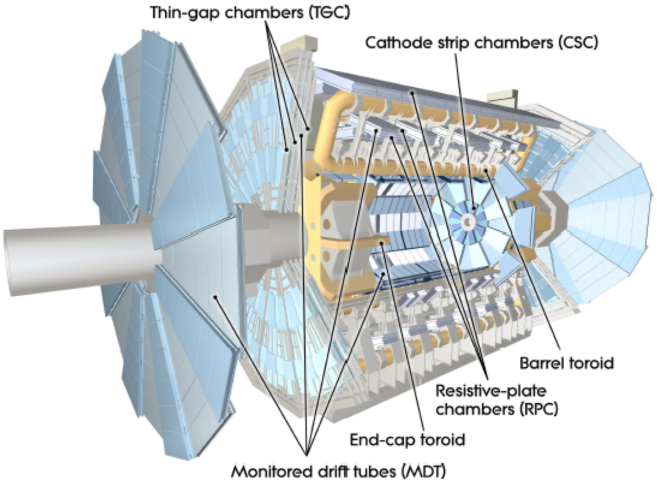

Figure 3.9: A schematic view of the muon spectrometer at the ATLAS experiment [3].

3.3.6 Trigger and data acquisition system

Millions of collisions happen per second at the ATLAS detector, many of them do not carry any useful information for physics and few are of interests for the research purposes. However, the computing capability of the ATLAS detector cannot save every single collision information, therefore a trigger system is employed to classify events and choose only the interesting ones. The trigger system consists of three levels: the Level-1 trigger is a hardware-based trigger and selects high p_{T} objects. It takes the information from the MS to select muons, and the information from the calorimeter to select electrons, photons, jets, taus decaying into hadrons and also large missing transverse energies. It reduces the event rate down to 75 kHz, and is able to take the decisions within 2.5 μs. The Level-2 trigger analyses the region of interests that are provided by Level-1 for each event. It uses information about the η-ϕ position and the energy. Level-2 reduces the event rate to 3.5 kHz, in an average processing time of 40 ms per event. The last level is the event filter, it provides an offline and high-level triggering (HLT) in order to decide for the final events to be recorded. It uses the full data information from the calorimeter, the muon chamber and the inner detector to refine the trigger selections. The HLT decreases the event rate down to 400 Hz. It usually processes each event in about 4 seconds.

CHAPTER 4

Ingredients for the cross-section measurements of $t\bar{t}\gamma$ production

Two cross section measurements of the top-quark pair production in association with a photon are performed separately using the data collected by the ATLAS detector, at a centre-of-mass energy of 8 TeV and 13 TeV. At 8 TeV, the cross section is measured in the single-lepton channel [17]. The measurement is summarised in Chapter 5. The 13 TeV analysis is performed in both, the single-lepton and the dilepton channels [18]. Since I was the main analyser in the cross-section measurement in the dilepton channel, it will be describe in the remaining chapters in greater detail.

This chapter presents the data collected by ATLAS and the Monte Carlo (MC) simulation samples, which are used in the two analyses. The definition of the final-state objects in the $t\bar{t}\gamma$ process, the definition of the measured cross sections, and the likelihood function, which are common for both analyses, are also described.

4.1 Data collected by ATLAS

The first analysis uses the data delivered by ATLAS at $\sqrt{s} = 8$ TeV between April 4th and December 16th of the year 2012; this corresponds to a recorded total integrated luminosity of 21.3 fb^{-1} [80]. The data is classified into eleven periods, according to the running condition parameters, for example the number of protons per bunch. The data is then filtered by the so-called Good Run List (GRL), which ensures that the beam and detector conditions are qualified to provide good data for the physics analyses. The final certified GRL corresponds to a total integrated luminosity of 20.3 fb^{-1}. The data is divided into two streams depending on the applied triggers; the egamma stream which uses the single-electron triggers or the muon stream which uses the single-muon triggers.

The second cross-section measurement uses the data collected at a centre-of-mass energy of 13 TeV, in the period between August and November of the year 2015, and the period of April to October of the year 2016 [81, 82]. A total integrated luminosity of 3.9 fb^{-1} (35.5 fb^{-1}) was recorded in 2015 (2016). This provides a GRL data of 3.2 fb^{-1} (33.3 fb^{-1}) in 2015 (2016).

The total luminosities delivered, recorded and passing GRL requirements as a function of time, are shown in Figure 4.1 for the year 2012, and Figure 4.2 for the years 2015 and 2016. The mean number of interactions per bunch crossing during proton–proton collisions for different luminosities are shown in Figure 4.3.

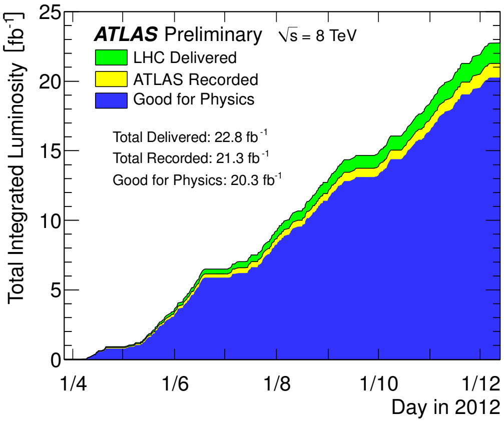

Figure 4.1: The total integrated luminosity delivered in green, recorded by ATLAS in yellow, and certified to be good for data analysis in blue, in the year of 2012 [80].

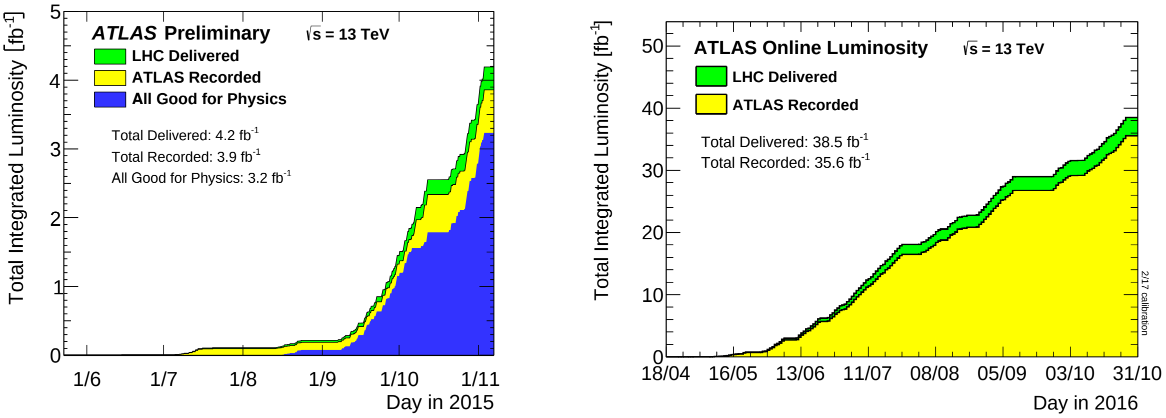

Figure 4.2: The total integrated luminosity delivered in green, recorded by ATLAS in yellow, and certified to be good for data analysis in blue, in the year of 2015 (left) and 2016 (right) [82]

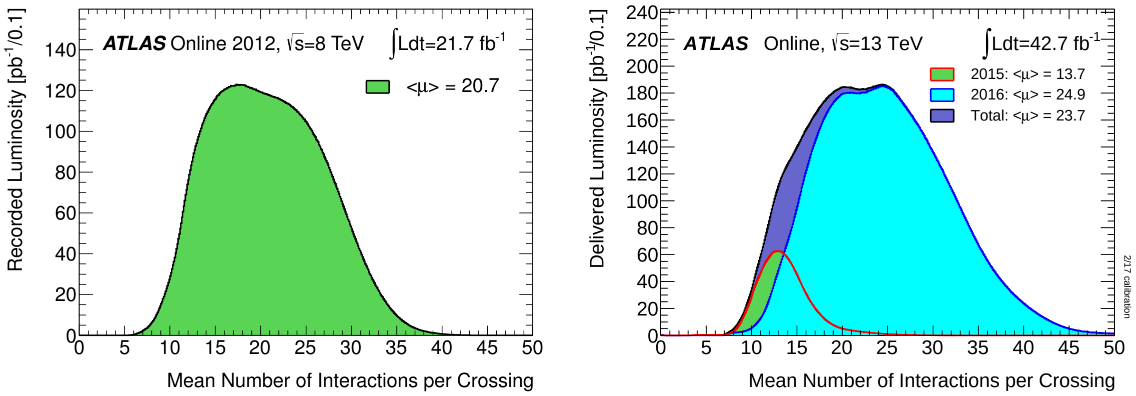

Figure 4.3: The average number of interactions per bunch crossing during proton–proton collisions at $\sqrt{s}$ = 8 TeV(left) [80], and $\sqrt{s}$ = 13 TeV for the 2015 and 2016 runs (right) [82], at the ATLAS detector .

4.2 Monte-Carlo simulation

The data collected by the ATLAS detector is compared to a theoretical model. The comparison provides an understanding of the physics process, and might indicate the existence of new physics beyond the SM. The limitations in the theory model could be also observed by comparing it to the data. In order to do the comparison, Monte Carlo simulation is used to model the proton–proton collisions. In rare proton–proton collisions, the partons inside the proton interact with each other and produce new particles. The probability of a parton to carry a fraction x of the proton momentum at a given energy scale Q, is described by the parton distribution function [83–89]. An example of the CTEQ6L1 PDF set [83, 84] is shown in Figure 4.4.

The first step in simulating every physics process, which results from the proton–proton interactions, is the generation of the hard-scattering process (parton-level generation). The parton-level generators are used to generate the matrix-element of the process. The generators compute the parton-parton interactions at a fixed number of partons in the final state. The choice of the generator depends on the process of interest. Two types of generators are available: the process-specific generators, an example is the Alpgen generator [90]. The other type are the arbitrary-process generators, which are designed to generate any tree-level process, some examples are MadGraph [91–94], Sherpa [95] or Powheg-Box [96, 97]. The MadGraph generator is used to model the signal sample in this analysis, thus it will be described briefly in Section 4.2.1.

Extra radiations from the initial state or the final state can be photons or gluons, where gluons split into other gluons or into quark-antiquark pairs, leading to the so-called parton shower (PS). At an energy scale of 1 GeV, all partons start to combine and form colourless states. The process is called hadronisation. The remnant partons in the proton interact to produce underlying events. The decay of long-lived particles is also simulated. The PS and what follows from hadronisation and other interactions are modelled and added to the hard scatter-process by different MC generators from the parton-level ones, such as Pythia [98–100]. The additional electromagnetic radiations in the fragmentation process are also simulated with the dedicated generator Photos [101, 102]. Non-physical parameters, called tunes, are calibrated using the experimental data and used together with the PS generators. The MC generator tunes are optimised to produce a reasonable description of the measured observables. In this thesis, the minimum bias events, which are generated with Pythia 8 [99, 100] and A2 tune [103], are overlaid to model the in-time pile-up and out-time pile-up[1] on top of the hard process. The pile-up distribution is re-weighted to match the data. Finally the interaction of all final state particles with the detector are simulated using Geant 4 [104]. The generation process of a simulated event is schematically described in Figure 4.5.

4.2.1 The MadGraph generator

The MadGraph generator is designed to do an automated computation of the tree-level and the one-loop amplitudes for any process with all possible diagrams. The generation process starts by defining the exact initial and final state of the desired process, and choosing its order in QCD and QED. MadGraph generates all possible Feynman diagrams, and run specific routines to calculate the amplitudes of all diagrams. The generator has the power to generate the Feynman diagrams and do the calculations for hundreds of diagrams in seconds. The generator can be then used to calculate the cross sections or the decay width. It can also be used for the event generation using the MadEvent package [105].

---

[1] The in-time pile-up are the additional proton–proton collisions which occur during the same bunch crossing as the collisions of interest. The out-time pile-up are the additional proton–proton collisions which occur during bunch crossing just before and after the collision of interest.

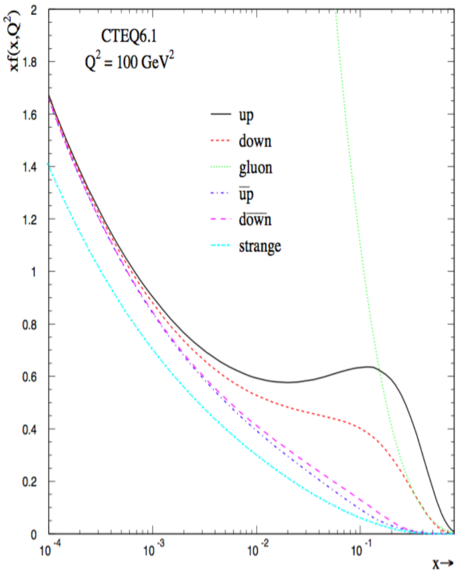

Figure 4.4: The PDF distributions from the CTEQ6L1 for different partons, at Q^2 of 100 GeV^2 [84].

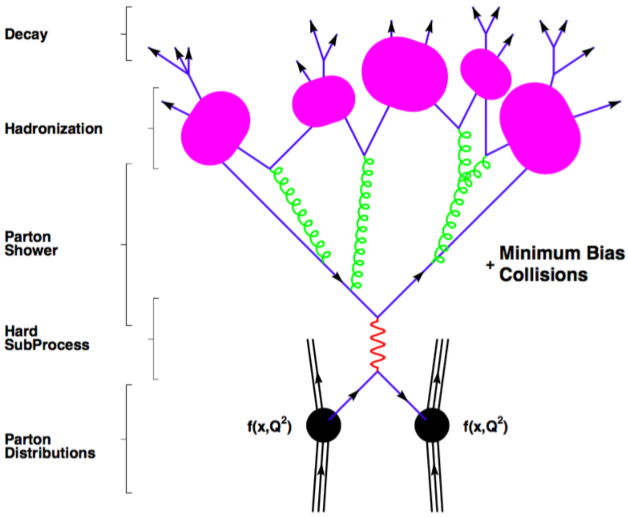

Figure 4.5: A pictorial representation of the event generation process [84].

The latest version of MadGraph is v5 [92, 93]. The earlier version v4 [94] is written in Fortran, and uses the HELAS routines [106] in order to calculate the amplitudes, whereas MadGraph v5 is fully written in Python. The new version is able to compute the Lagrangian of any process defined by the user, including those defined for new physics beyond the SM for any renormalisable or effective theory implemented in FeynRules [107] via the UFO interface [108]. The calculation of the amplitudes occurs through the ALOHA package [109]. MadGraph v5 performs the full automation and optimisation of the NLO computations in the SM and beyond. The latest version computes larger number of tree-level processes than the previous version, and it supports more flexible output formats in Fortran, C++, and Python, and dedicated matrix element output for Pythia 8 [100].

4.3 Signal and background modelling

The term signal refers to the $pp \to t\bar{t}\gamma$ production, including the subsequent decay of $t\bar{t}$ into the single-lepton or the dilepton channel (see Section 2.5.2). Many SM processes emulate the same final state as the signal, these processes are called backgrounds. All simulated samples for the signal and backgrounds are processed through the full ATLAS detector simulation [110] based on Geant 4 [104].

4.3.1 Signal modelling

The $t\bar{t}\gamma$ signal sample is simulated with the MadGraph generator described in Section 4.2.1. MadGraph v4 [94] is used at 8 TeV, while MadGraph5_aMC@NLO [92] is used at 13 TeV.

Both, single-lepton and dilepton channels are generated, and all the final state particles are calculated in the matrix element ($\ell\nu_\ell qq'b\bar{b}\gamma$, $\ell\nu_\ell\ell\nu_\ell b\bar{b}\gamma$). The charged lepton ℓ can be an electron, a muon or a tau, and q stands for any light-quark (u, d, c, s). Leptons and light-quarks result from the decay of the two W bosons, where the two bosons result from the decay of the top-quark pair. The photon γ is radiated from any charged particle in the final state, or from the W-boson. It can be also radiated from any charged particle in the initial state (see Figure 2.7).

In the MC generation process, two schemes are considered for including the b-quark in the initial state. The five-flavour scheme (5FS), which allows the b-quark to be part of the initial state quarks as well as the final state quarks, with its mass is set to zero. The second scheme is the four-flavour scheme (4FS), where the b-quark is massive and not considered as one of the quarks in the proton but has its own category as a final state particle. A summary of the two schemes and the masses of the considered quarks is given in Table 4.1. The particular choice of the b-quark mass is made to be consistent with the chosen PDF set. The 8 TeV sample uses the 4FS with the CTEQ6L1 (LO) PDF set [83]. For the 13 TeV analysis, I performed a check to compare the two schemes in terms of changing the shapes of the photon observables, as shown in Figure 4.6. This check is performed by generating privately a small number of events with exactly the same settings but a different scheme. Since no significant shape difference is observed, both schemes are suitable for the signal generation. However, the 5FS is chosen in order to harmonise this setting with other recent ATLAS analyses, for examples the $t\bar{t}$ [46] and the $t\bar{t}$+V [111] analyses. The signal sample uses the NNPDF2.3LO set [86, 89]. Since q is defined according to the chosen scheme in MadGraph, any requirement on q does not include the b-quark in the 4FS, whereas it does in the 5FS. This is shown in Figure 4.6, by looking at the first bin, where the ΔR between the photon and any q is required to be larger than 0.2.

Scheme		light-quarks	b-quark
4FS	category	ISQ and FSQ	own category in the final state
	mass [GeV]	0	4.7
5FS	category	ISQ and FSQ	ISQ and FSQ
	mass [GeV]	0	0

Table 4.1: A comparison of the quark definitions between the two MC flavour schemes. ISQ refers to an initial state quark, and FSQ refers to a final state quark.

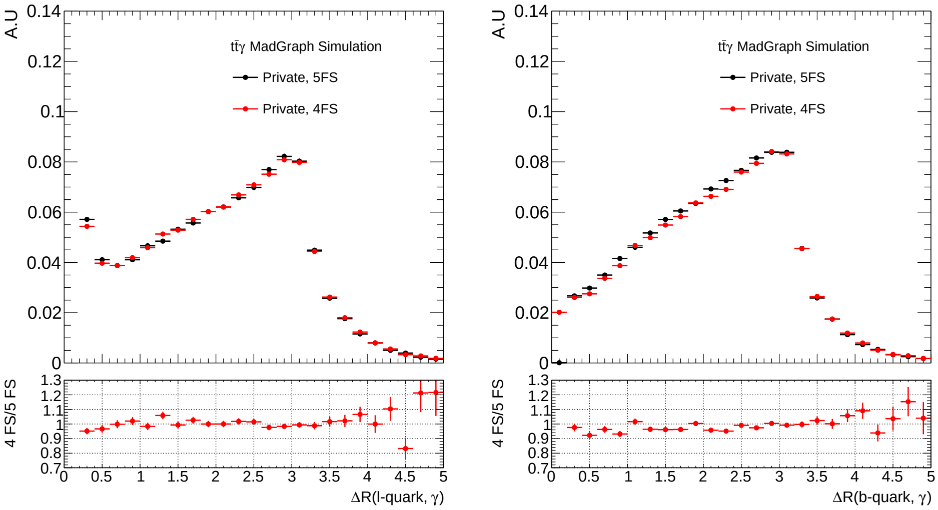

Figure 4.6: Distribution of the ΔR between the photon and any light-quark (left), and between the photon and any b-quark (right). Privately simulated sample with the four-flavour scheme in red is compared to a sample simulated with the five-flavour scheme in black. Plots are normalised to unit area.

The renormalisation and the factorisation scales are set the same and equal to twice of the top mass ($\mu_R = \mu_F = \mu = m_t$ = 172.5 GeV) at 8 TeV. For the 13 TeV sample, a similar check to the flavour scheme is performed by choosing a dynamic scale (the sum of the transverse momenta of the final state particles divided by two) [112] for privately produced samples. The sample is compared with an ATLAS simulated MC sample of a fixed scale choice ($\mu = 2m_t$). No significant differences are observed in the shape of the photon variables, as shown in Figure 4.7. However, since the previous mentioned ATLAS analyses [46, 111] use the dynamic scale, a harmonisation with those analyses is also preferred for the $t\bar{t}\gamma$ sample.

The parton showering, the fragmentation and underlying event modeling are simulated using Pythia 6 [98] which uses the Perugia2011C tune [113] at 8 TeV, while simulated using Pythia 8 [100] together with the A14 tune [114] at 13 TeV. The systematic uncertainties due to the fragmentation modelling is estimated using an alternative parton showering generator, Herwig 6.520 [115] with Jimmy 4.31 [116] are used at 8 TeV, and Herwig 7 [117] is used at 13 TeV.

In order to avoid infrared and collinear singularities, a set of kinematic requirements are imposed. The photon transverse momentum is required to be larger than 15 GeV (a minimum value of 10 GeV is required at 8 TeV), and the absolute value of the photon pseudorapidity is required to be smaller than 5.0. The transverse momentum of at least one charged lepton and the absolute value of the pseudorapidity are requested to be larger than 15 GeV and smaller than 5.0 respectively. Photons separated from any charged lepton or any quark with $\Delta R > 0.2$ are selected. Since the b-quark is not considered in the quark definition at 8 TeV, the latter selection is not applied to the b-quark.

The expected cross section for the $t\bar{t}\gamma$ production calculated by MadGraph, with the requirements above, is found to be 1.19 pb and 4.63 pb at 8 TeV and 13 TeV, respectively. The ratio of photons emitted from the initial state partons or from the top quark, compared to all emitted photons in the samples is found to be 0.25 (0.26) at 8 (13) TeV. In order to increase these ratios, i.e., to enhance the sensitivity to the top-photon coupling, further requirements are applied, as will be described in Section 5.2 and Section 6.2 for the 8 TeV and 13 TeV analyses, respectively.

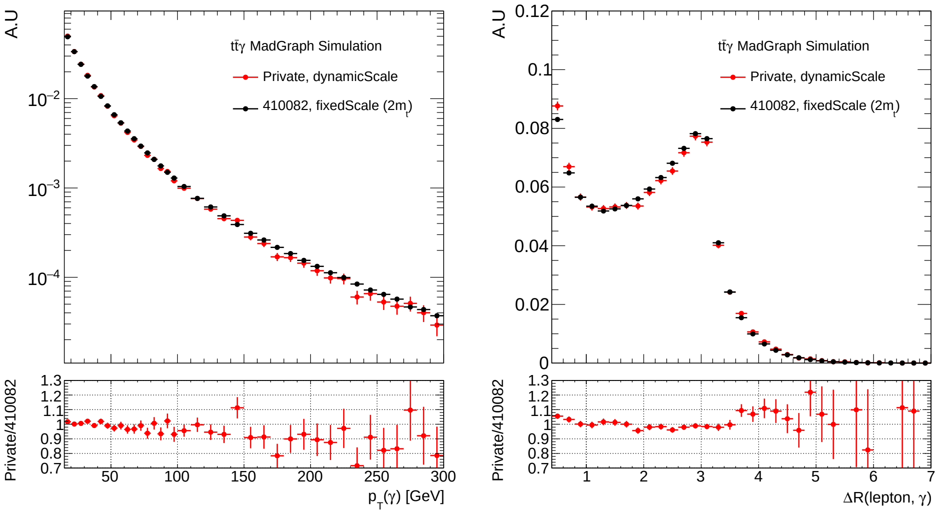

Figure 4.7: Distributions of the photon transverse momentum (left), and the ΔR between the photon and any lepton (right). Privately simulated sample with a dynamic scale choice in red is compared to an ATLAS simulated sample with a fixed scale choice in black. Plots are normalised to unit area.

4.3.2 Background modelling

Specific generators have been used to simulate each background process. Top-quark pairs are generated with the NLO matrix-element generator, Powheg-Box [96, 97] interfaced to Pythia for parton showering and hadronisation. The CT10 PDF set [87] is used at 8 TeV, and the NNPDF3.0NLO set [88] is used at 13 TeV. The main background of fake photons from hadronic-jets in the dilepton channel is estimated from the $t\bar{t}$ production at 13 TeV, since the contribution of this background is found to be very small. An alternative $t\bar{t}$ sample generated with Sherpa [95] is used for systematic uncertainty evaluation. The $t\bar{t}$ sample at 8 TeV is used to validate the data-driven methods of backgrounds in the single-lepton channel.

Backgrounds with additional prompt photon emission are simulated with different MC generators. The productions of W- and Z-bosons + γ are simulated using Sherpa and the CT10 PDF set, generated with up to three jets and massless b-/c-quarks. The contributions from these processes are normalised to the LO cross sections from Sherpa without any further re-weighing. Other vector boson production samples (W- and Z-bosons + jets) are used to estimate the backgrounds from hadronic-jets, at 13 TeV. The samples are simulated with Sherpa, using the NNPDF3.0NLO set. Due to the mismodelling of the heavy flavour decay in the $W + \gamma$ Sherpa sample, a systematic uncertainty is estimated using the W+jet production at 8 TeV. The latter is modelled with the Alpgen 2.14 generator [90] interfaced to Pythia.

The single top quark t-, s- and Wt-channel samples are produced by the Powheg-Box generator [118, 119] with the CT10(NLO) PDF set. The parton shower and hadronisation are done by Pythia with the Perugia2012 tune [113]. The samples are normalised to their NNLO theoretical cross sections [120–122].

The WW-, WZ- and ZZ-diboson samples are simulated using the Sherpa generator at 13 TeV, and Herwig [115] at 8 TeV. Both samples use the CT10(NLO) PDF set. Those processes contribute mainly to backgrounds with the emission of prompt photons.

4.4 Object definitions

The main final-state objects of the $t\bar{t}\gamma$ process are electrons, muons, photons, jets and neutrinos. The basic principle of identifying these objects is based on their track signatures left in the inner detector for the charged particles and the energy deposition in the calorimeter. The neutrino, which passes the detector with no signature, is recognised by the missing transverse momentum $\not{E}_{\mathrm{T}}$ which can be calculated by the momentum conservation law. The exact definition of each object and how it is implemented in the software of the two analyses are described in this section.

- Electrons

  Electrons are identified from the energy deposition in the central ECAL, with tracks in the ID pointing to them [123–125]. The electron candidate is required to have a transverse momentum of $p_{\mathrm{T}} > 25$ GeV, and an absolute pseudorapidity of the electromagnetic energy cluster in the calorimeter less than 2.47, excluding the transition region of the ECAL, $1.37 < |\eta_{\mathrm{cl}}| < 1.52$, where η_{cl} is the pseudorapidity of the electromagnetic energy cluster, measured with respect to the geometric centre of the detector. A tight cut-based quality criterion [124] is used to identify the electrons of the 8 TeV analysis, with a requirement on the transverse impact parameter (d_0) to be less than 1 mm. A tight likelihood-based quality criterion [125] is applied for the 13 TeV analysis. The d_0^{sig}[2] is required to be less than 5 and a longitudinal impact parameter of $|z_0 \sin\theta| < 0.5$ mm.

  Electrons are required to be isolated, in order to reduce contributions from background electrons originating from jets. Two quantities are used to measure the isolation of the electrons at 8 TeV:

---

[2] The transverse impact parameter significance is defined as $d_0^{\mathrm{sig}} = |d_0|/\sigma_{d_0}$, where σ_{d_0} is the uncertainty on the transverse impact parameter d_0.

the ECAL isolation ($E_{\mathrm{T}}^{\mathrm{cone20}}$) which is the energy sum of the cells within a cone of size $\Delta R = 0.2$ around the electron direction, excluding the cells associated to the electron clusters. The second isolation is the tracking isolation ($p_{\mathrm{T}}^{\mathrm{cone30}}$) which is the sum of the transverse momenta of all the tracks in a cone of size $\Delta R = 0.3$ around the electron direction, excluding the tracks associated to the electron candidate. Both isolations have an efficiency of 90%. A tracking and ECAL isolation criteria that depend on p_{T} and η are applied at 13 TeV [125], a result of an isolation efficiency of 95% for electrons of $p_{\mathrm{T}} > 25$ GeV and 99% for electrons of $p_{\mathrm{T}} > 60$ GeV is achieved.

- Muons

  Muons are reconstructed by matching the tracks in the MS to the tracks from the ID [126, 127]. If the tracks from the MS and the ID are matched, a combined fit is performed and a combined muon object is formed. The muon candidate is required to have a $p_{\mathrm{T}} > 25$ GeV, and $|\eta| < 2.5$. Tight muons [128] are required at 8 TeV, and a longitudinal impact parameter $|z_0 \sin\theta| < 2.0$ mm is required. Muons are identified by medium identification criterion [127] at 13 TeV. The d_0^{sig} and $|z_0 \sin\theta|$ are requested to be less than 3.0 and 0.5 mm respectively.

  A tracking isolation requirement is used at 8 TeV [129]. The isolation is defined to remove muons from the heavy flavour decays. The tracking isolation is based on the ratio of the sum of the tracks p_{T}, excluding the muon, in a cone of variable size $\Delta R = 10\ \mathrm{GeV}/p_{\mathrm{T}}\ (\mu)$, to the p_{T} of the muon. The ratio is requested to be smaller than 0.05. An isolation efficiency of 97% is found for prompt muons from $Z \rightarrow \mu\mu$ decays. The isolation criterion at 13 TeV [130] is based on the tracking and the topological clusters in the calorimeter, which depends on p_{T} and η.

- Photons

  The reconstruction of photons [131, 132] starts with forming a set of seed clusters of size $\Delta\eta \times \Delta\phi = 0.075 \times 0.123$, and $p_{\mathrm{T}} > 2.5$ GeV. The seeds are formed by using the sliding-window algorithm [133]. The reconstructed tracks from the ID are matched to the seed clusters. A converted photon to an electron-positron pair is reconstructed, if two oppositely-charged tracks collinear at the production vertex, or one track that does not have any hits in the innermost pixel layer, are found to be compatible with the electron hypothesis in the TRT and matched to the seed cluster. If the cluster is not matched to any reconstructed tracks or to a production vertex, an unconverted photon candidate is reconstructed. Approximately 96% of prompt photons with $E_{\mathrm{T}} > 15$ GeV are reconstructed as photon candidates. The remaining 4% are incorrectly reconstructed as electrons. The reconstruction efficiency reduces to 90% for E_{T} around 1 TeV due to the lower efficiency to reconstruct photon conversions.

  Photons are required to have a $p_{\mathrm{T}} > 15$ (20) GeV for the 8 (13) TeV analyses, within an acceptance of $|\eta_{\mathrm{cl}}| < 2.37$, excluding the region $1.37 < |\eta_{\mathrm{cl}}| < 1.52$. Photons are identified by a tight identification criterion [131], that is based on the fractional energy deposited in the HCAL and the shower shape variables in the ECAL (see Section 3.3.4 for HCAL and ECAL description), as described in Table 4.2. Two criteria are introduced in Table 4.2 for comparison; the loose and tight criteria. The loose criterion is based only on the energy deposited in the HCAL and the shower shapes in the middle layer of the ECAL. The tight criterion employs all the shower shape variables in the middle and the strip layers of the ECAL, and the energy deposits in the HCAL. Tight photons are required to deposit only a small fraction of their energy in the HCAL, and required to have a lateral shower shape consistent with that expected from a single electromagnetic shower. The shower shape variables can be used to distinguish prompt photon sources from fake photon sources (hadronic fakes). The hadronic fakes are mainly photons produced from a hadron decaying into a pair of photons, or with a smaller contribution, from hadrons mis-identified as photons, produced in jet fragmentation. The pair of photons makes a single cluster in the calorimeter which tends to be broader than the cluster of a single photon. The fine η granularity of the ECAL strips is generally sufficient to discriminate between the two clusters. Moreover, photons resulting from hadron decays tend to have a larger leakage in the HCAL than prompt photons. At 8 TeV, the photon identification efficiency reaches 50–65% (45–55%) for unconverted (converted) photons at $E_\mathrm{T} \approx 10$ GeV and 95–100% at $E_\mathrm{T} \geq 100$ GeV. For the 13 TeV analysis, efficiencies of 53–64% (47–61%) at $E_\mathrm{T} \approx 10$ GeV and 88–92% (96 -98%) at $E_\mathrm{T} \geq 100$ GeV, for unconverted (converted) photons, are achieved.

Photons at 13 TeV are required to be isolated with the FixedTightCut working point [130]. This working point applies both the calorimetric and the tracking isolations. The sum of the tracks energy in a cone of size $\Delta R = 0.4$ around the photon candidate ($E_\mathrm{T}^\mathrm{cone40}$) is required to be less than $0.022 \times p_\mathrm{T}\,(\gamma) + 2.45$ GeV, and the ratio of the sum of the tracks transverse momenta in a cone of size $\Delta R = 0.2$ to the photon momentum ($p_\mathrm{T}^\mathrm{cone20}/p_\mathrm{T}$) should be less than 0.065. The isolation criteria reduce significantly the hadron sources of photons, due to the very distinguished isolation distributions of the hadronic fakes. Since the hadronic fakes are expected to originate from hadrons produced in the hadronisation process, many track activities could occur around the hadronic-fake candidate during this process, which will be considered in the calculation of the isolation variable, if present within the isolation cone. Thus, their final isolation distribution is expected to be wider than the distribution of the prompt photons as they are not expected to have such activities. This behaviour is clarified in Section 5.4 and 6.2. No isolation requirement is imposed at 8 TeV due to the different measurement strategy that employs the shape of the track isolation variable ($p_\mathrm{T}^\mathrm{cone20}$). The two strategies will be explained in Section 5.4 and Section 6.5.

- Jets

The hadronisation of quarks and gluons produces many new particles that could collimate as a group and form a jet. Jets deposit their energy in the electromagnetic calorimeter, therefore jets can be reconstructed from the topological clusters in the calorimeter. The anti-k_t algorithm [57] is used to reconstruct a jet. From the topological clusters, the algorithm defines a distance measure between two objects d_{ij}, and a distance between the object and the beam d_{iB}. The two distances are calculated as follows:

$$d_{ij} = \min(k_{t_i}^{-2}, k_{t_j}^{-2}) \frac{\Delta_{ij}^2}{R^2}, \tag{4.1}$$

$$d_{iB} = k_{t_i}^{-2}, \tag{4.2}$$

where $\Delta_{ij}^2 = (y_i - y_j)^2 + (\phi_i - \phi_j)^2$, R is the radius parameter which sets the relative distance where jets are resolved from each other as compared to the beam. k_{t_i}, y_i, and ϕ_i are the transverse momentum, the rapidity and the azimuth of an object i, and similarly for object j. The algorithm works as follows:

- If the smallest entry is d_{ij}, the two objects i and j are combined into a new object, and the list is updated.
- If the smallest entry is d_{iB}, the object i is labelled as a jet and removed from the list.
- The procedure is repeated until no objects are left.

Topological clusters (jets) are calibrated to the electromagnetic energy scale [134]. The calibration

Category	Name	Description	Loose	Tight
Acceptance	–	$\lvert\eta\rvert < 2.37$, with $1.37 < \lvert\eta\rvert < 1.52$ excluded	yes	yes
Hadronic leakage	R_{had_1}	Ratio E_{T} in the first sampling layer of the hadronic calorimeter to E_{T} of the EM cluster (used over the range $0.8 < \lvert\eta\rvert < 1.37$)	yes	yes
	R_{had}	Ratio E_{T} in the hadronic calorimeter to E_{T} of the EM cluster ($0.8 < \lvert\eta\rvert < 1.37$)	yes	yes
EM middle layer	R_η	Ratio of 3×7 to 7×7 cell energies in the $\eta \times \phi$ plane	yes	yes
	w_{η_2}	Lateral width of the shower: lateral width of the shower in the second layer of the EM calorimeter, using cells in a window $\eta \times \phi = 3 \times 5$	yes	yes
	R_ϕ	Ratio of 3×3 to 3×7 cell energies in the $\eta \times \phi$ plane	no	yes
EM strip layer	w_{s3}	Shower width calculated from three strips around the strip with maximum energy deposit	no	yes
	w_{stot}	Total lateral shower width: shower width in η in the first layer of the EM calorimeter using cells in a window $\Delta\eta \times \Delta\phi = 0.065 \times 0.2$ corresponding approximately to 20×2 strip cells in $\eta \times \phi$	no	yes
	F_{side}	Energy outside the core of the three central strips but within seven strips divided by the energy within the three central strips	no	yes
	ΔE	Difference between the energy associated with the second maximum in the strip layer and the energy reconstructed in the strip with the minimum value found between the first and the second maxima ($\Delta E = 0$ when there is no second maximum)	no	yes
	E_{ratio}	Ratio of the energy difference associated with the largest and second largest energy deposits to the sum of these energies ($E_{\mathrm{ratio}} = 1$ when there is no second maximum)	no	yes

Table 4.2: The different variables used in the loose and the tight photon identification procedure [131, 132].

is performed using a MC based correction factor which depends on the jet p_{T} and η. This method partially corrects the jet energy response and reduces fluctuations due to the non-compensating nature of the ATLAS calorimetry. Jets in this analysis are reconstructed with the anti-k_t algorithm of radius $R = 0.4$, and required to have a $p_{\mathrm{T}} > 25$ GeV and $\lvert\eta\rvert < 2.5$. In order to reduce the contribution from pile-up jets and enhance the selection of hard-scatter jets, the fraction of the total transverse momentum of the jets associated tracks that are contributed by tracks (JVF) from the primary vertex (PV) [135] is required to be larger than 0.5 at 8 TeV, while a jet-track association algorithm, called jet vertex tagger (JVT) [136], is used at 13 TeV, requiring the jet vertex tagger discrimininat to be larger than 0.59 for jets with $p_{\mathrm{T}} > 60$ GeV and $\lvert\eta\rvert < 2.4$.

- *b*-tagged jets

  Jets initiated by *b*-quarks are called *b*-jets. Several algorithms are being used in ATLAS to identify *b*-jets [137]. During the fragmentation process, a *b*-quark forms a *b*-hadron which decays via the electroweak interaction, and thus a *b*-jet contains charged tracks coming from the decay of the *b*-hadron and tracks produced in the *b*-parton showering. The dominant decay modes of a *b*-hadron are characterised by the transition of a *b*-quark to a *c*-quark, followed by the *c*-hadron decay (see Figure 4.8). *b*-hadrons have relatively long lifetimes (e.g.~1.5 ps for the B^0 meson), travelling a long distance before they decay. For example, a *b*-hadron with $p_{\mathrm{T}} = 40$ GeV travels an average distance of $\beta\gamma c\tau = 3.4$ mm in the transverse direction before it decays. Charmed hadrons' lifetimes are smaller, e.g. 1.0 ps for the $D^\pm$ meson and 0.4 ps for the D^0 meson, but they can also travel significant distances at high energies. The displaced vertices resulting from the b-hadron and subsequent c-hadron decays provide a strong signature for a b-quark jet. These vertices can be explicitly reconstructed and their properties can be used to construct b-jet identification algorithms (b-tagging), that are able to separate jets likely to contain b-hadrons from jets containing light or c-hadrons.

The Single Secondary Vertex Finder algorithm (SSVF) [138, 139] reconstructs the displaced b- and c-hadron decay vertices, the secondary vertices (SV), inside a jet. The SSVF takes a list of tracks as input. The tracks undergo a selection procedure that includes requirements on the number of the track hits, the impact parameters and the tracks' p_{T}. Every possible two-track vertex is then formed. In order to remove vertices resulting from hadronic interactions, crossing of tracks or vertices from K_s and Λ decays, the two-track vertices are requested to pass a set of requirements. The final selected two-track vertices are then merged into a final single secondary vertex. More details about the SV reconstruction procedure can be found in Appendix A and Ref. [139]. I have been working on improving the performance of the SSVF [139, 140]. Before the start of Run II, the SVF algorithm was upgraded to accommodate the new pixel detector layer, the IBL [73], and to increase the vertex reconstruction efficiency and reduce the fake-vertex rate[3] for high p_{T} and high $|\eta|$ jets. A comparison between the initial settings of the SSVF and the improved settings is shown in Figure 4.9, and detailed in Appendix A. The new settings have increased significantly the rejection power of the SSVF to remove fake vertices. The SV reconstruction efficiency for b-jets of 80% is achieved in the central region of the detector, with c-jet and light-jet efficiencies of 30% and <5%. This efficiency reaches a maximum for jets with a transverse momentum of 80 GeV, as it can be seen in the figure.

The list of reconstructed secondary vertices and their properties are propagated to the SV-based b-tagging algorithms [137]. Multivariate approaches such as neural networks or boosted decision trees (BDT) [141] can handle the output of the individual algorithms and combine them to achieve the highest possible b-tagging efficiency. For example, the ATLAS b-tagging algorithm MV2 [140, 142] uses kinematic and topological information provided by the SV finder, together with information provided by several other algorithms, as input to a dedicated BDT algorithm.

The MV1 [137] algorithm is used to tag b-jets at 8 TeV. The working point of 70% with $p_{\mathrm{T}} > 20$ GeV and $|\eta| < 2.5$ in simulated $t\bar{t}$ events is chosen, which corresponds to a light-jet rejection factor of 140. The MV2c10 [140] algorithm is used at 13 TeV, with a working point of 77% and a a light-jet rejection factor of 134.

- Missing transverse momentum

  The missing transverse momentum ($\not{E}_{\mathrm{T}}$ or $E_{\mathrm{T}}^{\mathrm{miss}}$) [143] is calculated from the calibrated and corrected physics objects; electrons, muons, photons and jets. Those objects deposit energy in different components of the detector, thus the x-, y-components of the $E_{\mathrm{T}}^{\mathrm{miss}}$ are the sum of three elements: the energy deposit in the calorimeter, the energy in the muon spectrometer and the energy loss in the cryostat:

$$\not{E}_{x,y} = \not{E}_{x,y}^{\mathrm{Calo}} + \not{E}_{x,y}^{\mathrm{Muon}} + \not{E}_{x,y}^{\mathrm{Cryo}}, \tag{4.3}$$

  where $\not{E}_{x,y}^{\mathrm{Calo}}$ is the vectorial sum of all topological clusters (TopoClus) in the calorimeter which is defined as the sum of the energy of all particles in the calorimeter except for the muons. The $\not{E}_{x,y}^{\mathrm{Muon}}$

---

[3] Unrelated tracks could be occasionally close to each other in space to be wrongly considered as coming from a displaced vertex, a so-called fake vertex.

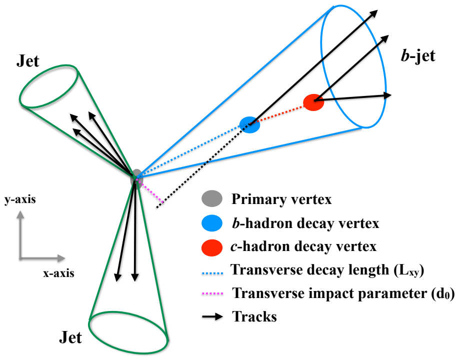

Figure 4.8: A schematic view of the displaced vertices in a *b*-jet.

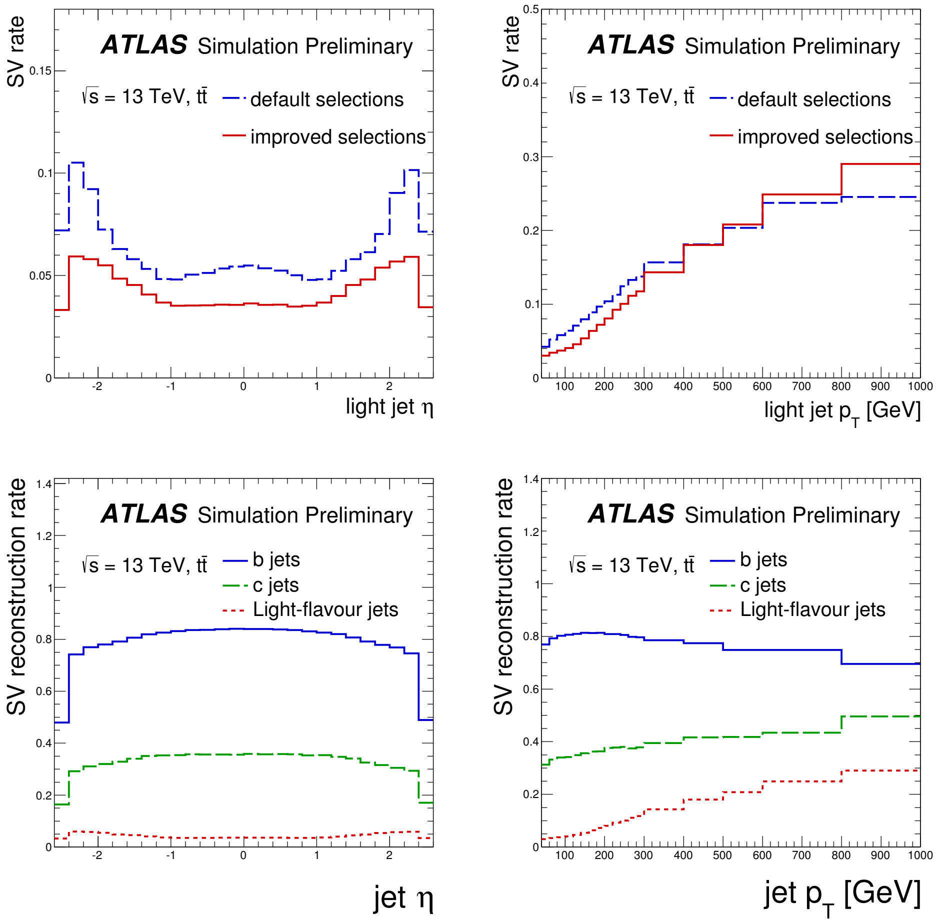

Figure 4.9: The fraction of fake vertices in light-flavour jets, as a function of the jet η (top-left), and the jet p_{T} (top-right). The initial settings of the SSVF in blue are compared to the improved settings in red. The bottom panel shows the secondary vertex reconstruction efficiencies for the three jet flavours, *b*-jet in blue, *c*-jet in green, and fake vertices are shown in red for light-flavour jet, as a function of the jet η (left), and the jet p_{T} (right) [140].

is the sum of the muons energy measured by the muon spectrometer. The different components in Equation 4.3 are expressed as

$$\not{E}^{\text{Calo}}_{x,y} = -\sum_{\text{TopoClus}} E_{x,y}, \tag{4.4}$$

$$\not{E}^{\text{Muon}}_{x,y} = -\sum_{\text{Muons}} E_{x,y}, \tag{4.5}$$

$$\not{E}^{\text{Cryo}}_{x,y} = -\sum_{\text{Cryo}} E_{x,y}, \tag{4.6}$$

Since the $E_{x,y}$ should be reconstructed from the calibrated objects, it should be refined by replacing the initial cell energies with the calibrated objects. If cells are associated to more than one object, the highest p_{T} one is taken. If the cell is not associated to any high-p_{T} object, it is then grouped in the CellOut term. If jets have small momenta 10 GeV $< p_{\text{T}} <$ 20 GeV, they are grouped into the soft jet component:

$$\not{E}_{x,y} = \not{E}^{\text{Electron}}_{x,y} + \not{E}^{\text{Photon}}_{x,y} + \not{E}^{\text{Jet}}_{x,y} + \not{E}^{\text{SoftJet}}_{x,y} + \not{E}^{\text{Muon}}_{x,y} + \not{E}^{\text{CellOut}}_{x,y}. \tag{4.7}$$

Finally, the total missing transverse momentum is the quadrature sum of the x-, y-components:

$$\not{E}_{\text{T}} = \sqrt{\not{E}_x^2 + \not{E}_y^2}, \tag{4.8}$$

- Objects overlap removal

  Double counting of reconstructed objects could occur when the same energy deposits in the electromagnetic calorimeter, or the same tracks in the inner detector are used to reconstruct two different objects. In order to avoid that, and thus reducing background contributions from misidentified objects or leptons that are likely originating from heavy flavour hadron decays, an overlap procedure is performed in the following order. Electron and muon candidates that are sharing the same tracks in the inner detector are removed. Jets which are close to an electron within $\Delta R < 0.2$ are discarded. The electron is removed if one of the remaining jets is found within a cone of $\Delta R = 0.4$ around the electron. In order to reduce the mis-identification of muons as jets, jets found within a ΔR distance of 0.4 around a muon are discarded if they have less than three associated tracks, otherwise the muon is removed in order to suppress muons originating from heavy-flavour decays. Background photons from mis-identified electrons or muons as photons are reduced by discarding photons that are within a distance of $\Delta R < 0.4$ from the remaining electron or muon candidates. Finally, all jets within a cone of size $\Delta R = 0.1$ (0.4) around the remaining photons are not considered in the 8 (13) TeV analyses.

4.5 Cross-section definitions

The inclusive fiducial and differential cross sections are measured for both run campaigns (8 TeV and 13 TeV) using a maximum-likelihood fit. The likelihood function is slightly different in the two analyses due to the different input parameters, as will be described in the coming chapters.

4.5.1 Fiducial cross section

The cross section is measured in a fiducial phase-space region of the detector, defined after the hadronisation and showering processes. This measurement in simulation is referred as “particle level”, as opposed to the “generator level”, where the hadronisation and showering processes are not simulated, and to the “reconstruction level”, which corresponds to the expected reconstruction that will be observed with data (see Section 4.2). The fiducial region is chosen to be as close as possible to the region defined at reconstruction level. This is done to ensure that the extrapolation from the observed data to the fiducial phase space is as model-independent as possible, ideally depending only on detector effects. The selections at reconstruction level are applied to objects defined in Section 4.4, and will be explained in Section 5.2 and Section 6.2. The particle-level objects and the fiducial selections will be described in Section 5.4 and Section 6.5, for the 8 TeV and 13 TeV analyses, respectively. There is also a larger phase space; the so-called total phase space. This is already defined at generator level, when the signal samples are simulated, as described earlier in Section 4.2.

An illustration of the different phase spaces, total, fiducial and reconstructed, are shown in Figure 4.10. The corresponding numbers of events falling into each phase-space region are also shown.

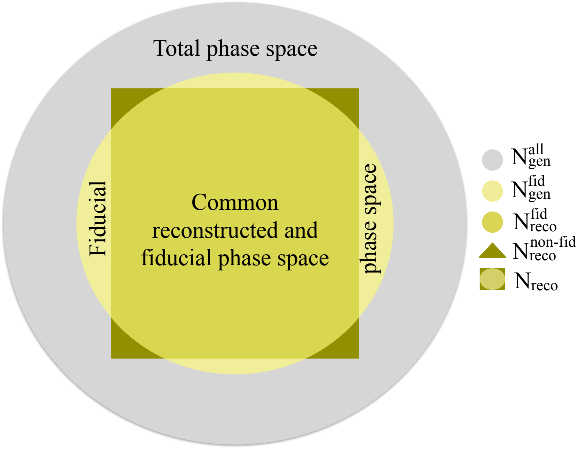

Figure 4.10: An illustration of the different phase spaces; total, fiducial and reconstructed phase space, with the corresponding number of events falling into those regions.

The numbers shown in Figure 4.10 are used to extract different factors, which can be used to calculate the fiducial cross section as follows:

- ϵ is the fraction of generated signal events that are reconstructed in the fiducial region:

$$\epsilon = \frac{N^{\text{fid}}_{\text{reco}}}{N^{\text{fid}}_{\text{gen}}}, \tag{4.9}$$

  where $N^{\text{fid}}_{\text{reco}}$ is the number of signal events generated in the fiducial region and passing the selections at reconstruction level, and $N^{\text{fid}}_{\text{gen}}$ is the number of signal events generated in the fiducial region.

- f_{mig} is the fraction of events selected at reconstruction level but not generated in the fiducial region:

$$f_{\text{mig}} = \frac{N^{\text{non-fid}}_{\text{reco}}}{N_{\text{reco}}}, \tag{4.10}$$

where N_{reco} is the number of all events passing the selections at reconstruction level.

- C is the correction factor of the signal, and defined as the ratio between events at reconstruction level and events generated in the fiducial region (see Equation 4.11). The correction factor is useful to account for events migrated to the fiducial region, where events can be mis-reconstructed with wrong kinematics. For example, photons of $p_{\mathrm{T}} < 15$ GeV can be reconstructed with $p_{\mathrm{T}} > 15$ GeV due to the detector resolution. This can be seen from the second equality in Equation 4.11.

$$C = \frac{N_{\mathrm{reco}}}{N_{\mathrm{gen}}^{\mathrm{fid}}} = \frac{\epsilon}{1 - f_{\mathrm{mig}}}, \tag{4.11}$$

where ϵ is given in Equation 4.9 and f_{mig} is given in Equation 4.10.

- A is the detector acceptance and is defined as the fraction of events that pass the fiducial selection out of all events generated in the signal sample. It is given by

$$A = \frac{N_{\mathrm{gen}}^{\mathrm{fid}}}{N_{\mathrm{gen}}^{\mathrm{all}}}. \tag{4.12}$$

The fiducial cross section of channel j is calculated using the acceptance of the detector defined earlier in Equation 4.12:

$$\sigma_j^{\mathrm{fid}} = A \cdot (\sigma^{\mathrm{tot}} \cdot B_j) = \frac{N - N_b}{C \cdot L}, \tag{4.13}$$

where,

- A is the detector acceptance defined in Equation 4.12.
- σ^{tot} is the $t\bar{t}\gamma$ production cross section in the total phase space.
- B_j is the branching ratio of $t\bar{t}\gamma$ decay mode, either single lepton or dilepton.
- N is the number of data events passing the fiducial selection.
- N_b is the number of background events estimated to be in the observed data.
- L is the integrated luminosity.
- C is the correction factor defined in Equation 4.11.

4.5.2 Differential cross section

The total and fiducial cross section can be measured as a function of any observable of interest, in a specific channel, the so-called differential cross sections, which are calculated by the following equations:

$$\sigma_{i,j}^{\mathrm{tot}} = \sigma_i^{\mathrm{tot}} \cdot B_j = \frac{N_i - N_{b,i}}{A_i \cdot C_i \cdot L}, \tag{4.14}$$

$$\sigma_{i,j}^{\mathrm{fid}} = A_i \cdot (\sigma_i^{\mathrm{tot}} \cdot B_j) = \frac{N_i - N_{b,i}}{C_i \cdot L}, \tag{4.15}$$

where each i corresponds to a different bin of the histogram of the observable of interest. C_i and A_i are the correction and acceptance factors in each bin:

$$A_i = \frac{N^{\text{fid}}_{\text{gen},i}}{N^{\text{all}}_{\text{gen},i}}, \tag{4.16}$$

$$C_i = \frac{N_{\text{reco},i}}{N^{\text{fid}}_{\text{gen},i}}. \tag{4.17}$$

To measure a differential cross section, a simple bin-by-bin approach is used for the 8 TeV analysis, as given in Equation 4.15. A more advanced technique, the iterative Bayesian method, is employed for the 13 TeV analysis to benefit from the larger amount of data. The method will be explained in Section 6.6.

4.5.3 Likelihood function

The cross-section measurement is based on a fit maximising the likelihood [19], which is performed to the observed data, within a chosen fiducial volume. The likelihood function is written as a product of two function types; Poisson functions $P(N_{i,j}|N^s_{i,j} + \sum_b N^b_{i,j})$, and Gaussian functions $G(0|\theta_t, 1)$ of unit width:

$$\mathcal{L} = \prod_i \prod_j P(N_{i,j}|N^s_{i,j} + \sum_b N^b_{i,j}) \times \prod_t G(0|\theta_t, 1). \tag{4.18}$$

The Poisson functions represent the probability to observe N data events given the expected number of signal and total background events N^s and N^b in bin i of the discriminant distribution of channel j. The discriminator is chosen based on its power to separate the signal from the background processes. The Gaussian function $G(0|\theta_t, 1)$ models the different systematic uncertainties t, where θ_t is the parametrisation of the systematic uncertainty t.

The number of post-fit signal events $N^s_{i,j}$ is related to the SM expectation and expressed in terms of the so-called signal strength μ:

$$N^s_{i,j} = \mu_j \cdot N^{\text{SM}}_{s,j} \cdot f_{i,j}, \tag{4.19}$$

where $f_{i,j}$ is the fraction of events falling into bin i of the discriminator of channel j, and μ_j is the ratio of the total number of observed signal events (N^{obs}_s) to the total predicted number (N^{SM}_s) in channel j:

$$\mu_j = \frac{N^{\text{obs}}_{s,j}}{N^{\text{SM}}_{s,j}}. \tag{4.20}$$

The number of signal events and the fiducial cross section of channel j are related to each other by the following:

$$N^s_{i,j} = L \cdot \sigma^{\text{fid}}_j \cdot C_j \cdot f_{i,j}, \tag{4.21}$$

For the differential cross-section measurement, the likelihood in Equation 4.18 runs over the bin index k of the chosen observable:

$$\mathcal{L} = \prod_i \prod_j \prod_k P(N_{i,j,k}|N^s_{i,j,k} + \sum_b N^b_{i,j,k}) \times \prod_t G(0|\theta_t, 1). \tag{4.22}$$

The uncertainty on the fiducial cross section is defined by the profile likelihood ratio λ_s in Equation 4.23. The ratio is evaluated and used to determine uncertainties on the cross section within a 68% confidence level:

$$\lambda_s(\sigma_{\mathrm{j}}^{\mathrm{fid}}|\mathrm{DIS}) = \frac{\mathcal{L}(\sigma_{\mathrm{j}}^{\mathrm{fid}}, \hat{\hat{\theta}}|\mathrm{DIS})}{\mathcal{L}(\hat{\sigma}_{\mathrm{j}}^{\mathrm{fid}}, \hat{\theta}, |\mathrm{DIS})}, \tag{4.23}$$

where quantities with double hats are the values that maximise the likelihood given a fixed value of σ_j^{fid}, and called the conditional maximum likelihood estimation of the parameters, the single hats are the unconditional maximum likelihood estimation of the parameters, and DIS is the discriminant distribution. The profile likelihood ratio is evaluated within the RooFit/RooStats framework [144, 145].

CHAPTER 5

Cross-section measurement of $pp \rightarrow t\bar{t}\gamma$ at 8 TeV

The analysis at a centre-of-mass energy of 8 TeV is performed in the single-lepton channel (see Section 2.5.2), where the lepton can be either an electron or a muon, including those produced from the leptonic decay of a τ-lepton. My main contributions to this analysis were: the NLO k-factor calculations explained in Section 5.1, the estimation of backgrounds due to events with electrons misidentified as photons and events with prompt photons, which are described in Section 5.3, and the systematic uncertainties due to the signal modelling, described in Section 5.5.

The $t\bar{t}\gamma$ signal sample is generated at leading-order using MadGraph (see Section 4.3), and theory calculations are performed at next-to-leading order in QCD. The ratio of the prediction at NLO to the LO is used to scale the MadGraph simulation. As the signal sample is scaled everywhere in the analysis, this chapter introduces first the theoretical calculations in Section 5.1. The other parts of the analysis are described in the remaining sections.

5.1 Theory prediction

The LO MadGraph sample shall be normalised to the best available higher-order theory calculations. This allows for the best comparison of the $t\bar{t}\gamma$ prediction to the measured data. The higher QCD corrections to the production of $t\bar{t}$ in association with a hard photon are first calculated in Ref. [53] at a centre-of-mass energy of $\sqrt{s} = 14$ TeV (see Section 2.6.1). Similar calculations at $\sqrt{s} = 8$ TeV are performed in the single-lepton channel (e, μ) at LO and NLO [58]. The CTEQ6L1 (CT10) PDF sets are used for the LO (NLO) calculations. The renormalisation and factorisation scales are set to m_t ($\mu_\mathrm{R} = \mu_\mathrm{F} = \mu = m_t$). Calculations are repeated varying the scales by a factor of 2 simultaneously around the nominal value. Another set of calculations is performed by fixing $\mu = m_t$ and varying the used PDF to the NNPDF3.0NLO [88] or the MSTW2008 [85] PDF sets. The variations are estimated as uncertainties on the nominal calculation.

5.1.1 Leading-order cross section

The nominal LO MadGraph calculation is compared to the LO theory prediction. In order to do the comparison, the same phase-space region used in the theory calculation is defined for the generated event kinematics from MadGraph. Exactly one lepton with $p_\mathrm{T} > 15$ GeV and $|\eta| < 5$ is required. For the theory calculation, the jets are reconstructed from stable particles using the anti-k_t algorithm ($R = 0.4$), and are considered if they have $p_{\mathrm{T}} > 10$ GeV and $|\eta| < 5$. For the study using MadGraph, the selection is defined at parton level, i.e., the quarks are used instead of the clustered jets. Consistently, only quarks with $p_{\mathrm{T}} > 10$ GeV and $|\eta| < 5$ are considered. The final state photon is required to have a $p_{\mathrm{T}} > 10$ GeV and $|\eta| < 5$. The photon is also required to be separated from jets and leptons with $\Delta R(\text{jet}, \gamma) > 0.2$ and $\Delta R(\ell, \gamma) > 0.5$ respectively.

The LO cross section obtained from MadGraph after applying the selections described above, $\sigma^{\mathrm{LO,sel}}_{t\bar{t}\gamma}$, can be written as

$$\sigma^{\mathrm{LO,sel}}_{t\bar{t}\gamma} = \frac{N^{\mathrm{gen,sel}}_{t\bar{t}\gamma}}{N^{\mathrm{gen,all}}_{t\bar{t}\gamma}} \times \sigma^{\mathrm{LO}}_{t\bar{t}\gamma}, \tag{5.1}$$

where

- $N^{\mathrm{gen,sel}}_{t\bar{t}\gamma}$ is the number of events at generator level after applying the phase-space requirements used in the theoretical calculation.
- $N^{\mathrm{gen,all}}_{t\bar{t}\gamma}$ is the number of generated single-lepton events in the $t\bar{t}\gamma$ MC sample.
- $\sigma^{\mathrm{LO}}_{t\bar{t}\gamma}$ is the LO cross section of the generated $t\bar{t}\gamma$ sample in the single-lepton channel.

The cross sections calculated by Equation 5.1 are compared with the theoretical prediction at scales of m_t and $2m_t$, as summarised in Table 5.1. The distributions of the photon p_{T} are also compared and shown in Figure 5.1. The small observed differences are possibly due to small differences in the setting of some electroweak parameters between MadGraph and the theory calculation, as shown in Table 5.2. Since MadGraph at LO reproduces well the LO theory results, the k-factor used for the MadGraph generation at LO can be extracted using the NLO theory and the LO MadGraph calculations.

Calculation	$\sigma(\mu = m_t)$ [fb]	$\sigma(\mu = 2m_t)$ [fb]
Theory	606.36	458.55
MadGraph	616.38	465.14

Table 5.1: A comparison between the LO cross sections predicted by theory and those obtained from MadGraph calculations in the single-lepton channel at scales of m_t and $2m_t$.

Calculation	G_F [GeV^{-2}]	W-decay width [GeV]	top-decay width [GeV]
Theory	1.16637×10^{-5}	2.14	1.48
MadGraph	1.12677×10^{-5}	1.98	1.41

Table 5.2: The different electroweak parameters used in theory and MadGraph calculations.

5.1.2 Next-to-leading order k-factor

The NLO k-factor is defined as the ratio of the NLO cross section to the LO cross section calculated by MadGraph in the same phase space used for the theoretical prediction. The scale of $\mu = 2m_t$ is used for the LO MadGraph. For the NLO theory calculation, the k-factor as a function of the scale is checked

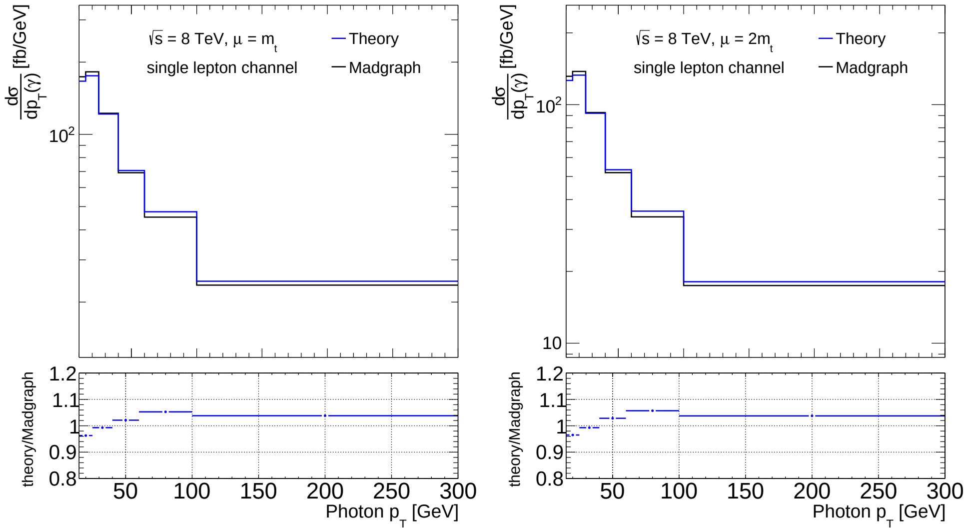

Figure 5.1: Distributions of the differential cross section as a function of the photon transverse momentum p_{T}, at a scale of $\mu = m_t$ (left) and $\mu = 2m_t$ (right) in the single-lepton channel. The distributions are normalised to the same area. Theory calculations are shown in blue and MadGraph calculations in black.

and the scale with a small perturbative correction is chosen [58]. Thus, a scale of $\mu = m_t$ is used for the calculation. The NLO k-factor as a function of the photon p_{T} and η is shown in Figure 5.2.

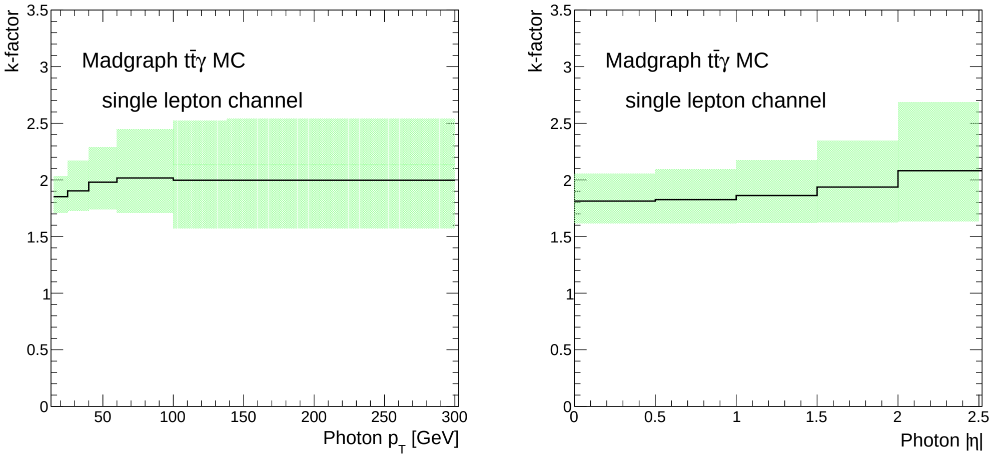

Figure 5.2: Distributions of the k-factor as a function of the photon transverse momentum p_{T} (left) and the photon absolute pseudorapidity $|\eta|$ (right). The shaded area corresponds to the scale variation by a factor of two around the central value used for the NLO calculations. Photons are selected according to the requirements applied in the theory calculation in the single-lepton channel.

The average k-factor is calculated by weighting the binned k-factor shown in Figure 5.2 with the p_{T}-spectrum of the selected photons in MadGraph:

$$\bar{k} = \frac{\sum_i [k_i \times N_i^{\text{gen,sel}}]}{\sum_i N_i^{\text{gen, sel}}}, \tag{5.2}$$

where k_i is the k-factor in the i-th p_{T} bin and $N_i^{\text{gen, sel}}$ is the number of selected photons in the same i-th p_{T} bin after applying the theory requirements.

A $\bar{k}$ of 1.90 ± 0.25 ± 0.12 is estimated in the single-lepton channel. The first uncertainty in the k-factor is due to the scale variation, and the second uncertainty is due to the variation of the PDF set used. An alternative method is used to calculate the k-factor at 13 TeV, as will be described in Section 6.1. It has been verified that the two methods are in agreement within uncertainties, in the single-lepton channel.

5.2 Event selection

The $t\bar{t}\gamma$ single-lepton channel is characterised by the presence of an isolated lepton with a high p_{T} and large missing transverse momentum, originating from the leptonic decay of the W boson, two light-jets, resulting from the hadronic decay of the other W boson, two jets identified as originating from b-quarks produced from the decay of the top-quark pair, and a high-p_{T} photon emitted either from the top-pair production or the decay products of $t\bar{t}$ (see Figure 2.7).

Since leptons from the decay of top quarks are expected to be energetic, a high transverse momentum threshold is required. Events are asked to pass a single-lepton trigger. The trigger requires at least one lepton to have a $p_{\mathrm{T}} > 24$ GeV with an isolation requirement (see Section 4.4 for the isolation requirement), or a $p_{\mathrm{T}} > 60$ (34) GeV but independent of the isolation, for the electron (muon). Exactly one reconstructed lepton with $p_{\mathrm{T}} > 25$ GeV and $|\eta| < 2.5$, and matched to one of the previously mentioned triggers, is required to be present in a $t\bar{t}\gamma$ candidate. In order to suppress multijet background events, the missing transverse momentum is required to be larger than 20 GeV, and the sum of $E_{\mathrm{T}}^{\mathrm{miss}}$ and the transverse mass of the W boson, $m_{\mathrm{T}}(W)$[1], is required to be larger than 60 GeV. Since the multijet background is expected to be larger in the electron channel, a higher $E_{\mathrm{T}}^{\mathrm{miss}}$ threshold is imposed. Both, $E_{\mathrm{T}}^{\mathrm{miss}}$ and $m_{\mathrm{T}}(W)$, are required to be larger than 30 GeV. Due to the fact that multijet events are typically balanced in the transverse plane, the presence of large $E_{\mathrm{T}}^{\mathrm{miss}}$ provides a good discrimination between multijet events and $E_{\mathrm{T}}^{\mathrm{miss}}$ from neutrinos. The $m_{\mathrm{T}}(W)$ requirement also discriminates between events with true W bosons, multijet or Z+jets production. In order to reduce several background contributions, mainly from the W+jets background, at least four reconstructed jets with $p_{\mathrm{T}} > 25$ GeV and $|\eta| < 2.5$ are required, where at least one of them is required to be tagged as a b-jet. The same requirements on jets are made in both channels.

Exactly one photon with $p_{\mathrm{T}} > 15$ GeV and $|\eta_{\mathrm{cl}}| < 2.37$, excluding the region $1.37 < |\eta_{\mathrm{cl}}| < 1.52$, is required to be present in each event. In order to suppress photons radiated from the decay products of the top quarks, the photon is required to be displaced from leptons in the η-ϕ space, with a $\Delta R > 0.7$. To reduce background from jets misidentified as photons, events with jets within a cone of $\Delta R = 0.5$ around the selected photon candidate are discarded. Finally, the background from Z+jets with an electron misidentified as a photon is reduced in the electron channel, by requiring the invariant mass of the electron and the photon to be outside a 5 GeV window around the Z mass, i.e., $m_{e\gamma} < 86$ GeV or $m_{e\gamma} > 96$ GeV.

The number of data events passing the above selections are found to be 1256 and 1816 candidates in the electron and muon channels, respectively. The number of expected signal events selected from the $t\bar{t}\gamma$ simulation is estimated to be 440 ± 90 and 720 ± 140 in the electron and the muon channels, respectively. The number of data candidates passing the various selections is presented in Table 5.3.

The event selection aims to reduce the number of events with photons radiated from the decay products of $t\bar{t}$, in order to enhance the sensitivity to the electroweak coupling of top quarks to the photon. Table 5.4

---

[1] $m_{\mathrm{T}}(W)$ is the transverse mass of the W boson decaying leptonically, and calculated as $m_{\mathrm{T}}(W) = \sqrt{(E_{\mathrm{T}}^{\ell} + E_{\mathrm{T}}^{\mathrm{miss}})^2 + (\vec{p}_{\mathrm{T}}^{\,\ell} + \vec{p}_{T}^{\,\mathrm{miss}})^2}$.

summarises the fraction of events with one photon emitted from the radiative production sources or the radiative decay sources of $t\bar{t}$, before and after applying the full event selections described above. The sources are also split according to the initial state particles that interact to produce the top-quark pair; either via gluon–gluon (gg) fusion or quark–antiquark ($q\bar{q}$) annihilation.

Requirement	Muon channel	Electron channel
Initial number of events	705 961 000	712 788 000
Trigger	218 114 000	222 497 000
Trigger Match	103 495 000	85 735 100
At least four jets	510 571	467 423
$E_{\mathrm{T}}^{\mathrm{miss}}$	446 636	321 982
$m_{\mathrm{T}}(W)$	409 136	263 659
At least one b-tagged jet	211 073	135 133
At least one photon with $\|\eta(\gamma)\| < 1.37$ or $\|\eta(\gamma)\| > 1.52$	3 788	2 831
$p_{\mathrm{T}}\ (\gamma) > 15$ GeV	2 644	2 128
Exactly one photon	2 591	2 101
$\|m_{e\gamma} - M_Z\| > 5$ GeV	2 591	1 894
$\Delta R(\mathrm{jet}, \gamma) > 0.5$	2 023	1 546
$\Delta R(\ell, \gamma) > 0.7$	1 816	1 256

Table 5.3: Data event yields for the electron and muon channel selections.

Source	Initial state	Before selection	After selection
Radiative production	gg	10.5	29.5
	$q\bar{q}$	14.2	33.1
Radiative decay	gg	57.5	28.6
	$q\bar{q}$	17.8	8.8

Table 5.4: The fractions in percentages (%) of events with photons emitted from the radiative production or the radiative decay sources of $t\bar{t}$ out of all selected, classified into gg or $q\bar{q}$ initial state events. The fractions are compared before and after applying the $t\bar{t}\gamma$ event selection in the single-lepton channel.

5.3 Background estimation

The main source of background processes in the single-lepton channel are $t\bar{t}$ events with one hadronic-fake candidate. This candidate is either a hadron misidentified as a photon, or a photon originating from a hadron decay. The background is derived from a control region defined in data, chosen to be enriched with hadronic fakes. The region is constructed with very loose selections compared to the signal region (defined in Section 5.2), where few requirements are imposed to define the control region. The photon is required to fail at least one of the four photon identification criteria that are constructed using the shower-shape variables from the first layer of the ECAL (see Table 4.2). This requirement is imposed since the hadronic-fake candidate is expected to have a broader shower profile than a prompt photon, and the fine granularity of the first layer in η is able to differentiate between the two shower profiles. For example, a meson decaying into two photons, is expected to have two maxima in the clustering energy in the ECAL, thus it will have a broader shower profile. The hadronic-fake candidate is required to be displaced from the electrons with a $\Delta R > 0.1$, in order to prevent events with an electron misidentified as a photon to enter the control region. At least fours jets are required similarly as in the signal region.

Contrary to the hadronic fakes, multijet events with the emission of a prompt photon and one jet misidentified as a lepton, a so-called fake lepton, are found to be a small background source in the single-lepton channel. The same event selections as in the signal region are applied to a control region in data with a loosened identification criterion of one lepton. Weights derived using the matrix method [146] in data are applied to the selected events, to obtain contributions from events with fake leptons. A total of 7.5 ± 3.6 and 8.3 ± 5.2 events is estimated in the electron and muon channels, respectively.

The other background processes are described in the following sections.

5.3.1 Electrons misidentified as photons

Events with an electron misidentified as a photon are the second largest source of backgrounds after the hadronic fakes. Both, electrons and photons deposit their energies in the ECAL, producing similar clusters. Photons are distinguished by the electromagnetic clusters only, while charged tracks are associated to the clusters of the electron candidates. However, electrons with poorly reconstructed tracks, can be misidentified as photons. If activities are happening very close to the photon direction, they may produce tracks pointing to the electromagnetic clusters; as a result the reconstructed electrons can be misidentified as converted photons.

This background contribution is mainly the result of dileptonic processes where one electron is misidentified, dominantly from dileptonic $t\bar{t}$ events (ee or $e\mu$), followed by a smaller contribution from Z bosons decaying into an electron-positron pair. The contribution of events with electrons misidentified as photons is estimated with a fully data-driven method. The probability for an electron to fake a photon (fake rate, FR) is calculated using two control regions: One region is enriched with $Z \to e^+e^-$ and the other is enriched with events reconstructed as $Z \to e$ + fake γ events. The electron with the highest p_{T} is called the tag, and is asked to have a $p_{\mathrm{T}} > 25$ GeV and to fulfill the tight identification criteria with calorimetric ($E_{\mathrm{T}}^{\mathrm{cone20}}$) and tracking ($p_{\mathrm{T}}^{\mathrm{cone30}}$) isolation requirements [124] (see Section 4.4). The second electron in the first region and the photon in the second region are required to have a $p_{\mathrm{T}} > 15$ GeV: both objects are called the probe. The signal photon requirements described in Section 5.2 are applied to the probe objects.

The fake rate is calculated as a function of the photon p_{T} and the pseudorapidity. It is obtained by the ratio of number of $Z \to ee$ events to the number of $Z \to e$ +fake-γ events. The two numbers in the ratio are determined by applying a fit to the invariant mass distribution of the tag and the probe objects using a sum of a Crystal-Ball [147] and a Gaussian function. The Crystal-Ball function describes the Z-mass peak and the mass resolution, while the Gaussian function is used to describe the background events, mainly events with jets misidentified as electrons or photons. The fit is performed in the invariant mass range [70, 110] GeV.

The number of events with an electron misidentified as a photon is calculated by applying the fake rate to any electron that could fake a photon in a modified signal region (SR′). The region SR′ is defined in a very similar way to the signal region defined in Section 5.2, except that the requirement of one photon is replaced by the requirement of one electron that is fulfilling the same kinematic requirements as the photon. Hence, the number of events with a non-isolated probe electron faking a photon is given by

$$N^{\mathrm{fakes}}_{e\to\gamma} = N^{\mathrm{SR}'}_{e_i^T e_j^P} \cdot \mathrm{FR}_j, \tag{5.3}$$

while for an isolated tag electron faking a photon, the number is given by

$$N^{\text{fakes}}_{e\to\gamma} = N^{\text{SR}'}_{e^T_i e^P_j} \cdot \text{FR}_i \cdot \frac{\epsilon^{iso}_j}{\epsilon^{iso}_i}, \tag{5.4}$$

where $N^{SR'}_{e^T_i e^P_j}$ is the number of events in the modified signal region, T and P refer to the tag and probe electrons respectively, FR_i is the fake rate in the i-th η-p_{T} bin, and ϵ^{iso}_i is the isolation efficiency of the i-th electron. The efficiency correction in Equation 5.4 compensates for the isolation requirement of the tag electron, where the fake rate is estimated for non-isolated probe objects.

Isolation of the probe electron

The tight isolation criterion applied to the tag electron in SR′, is checked for the probe object in four different cases. The first is by applying both the calorimetric and the tracking isolation requirements, or applying one of the isolation at a time, for the second and third case, or none of them is applied in the fourth case. The different isolation options and the final yields are summarised in Table 5.5. Since the number of events with electrons faking photons is found to be similar in all checks, the isolation requirements are not applied for the probe electron to obtain a modified signal region. Furthermore, the cross-section measurement is based on fitting the isolation variable, $p_{\text{T}}^{\text{cone20}}$, as will be described in Section 5.4. Therefore it is not preferred to impose requirements on this variable.

The yields of events with an electron misidentified as a photon is estimated to be 340 ± 4 and 306 ± 6 in the electron and the muon channels, respectively.

Isolation	Electron channel	Muon channel
No isolation	340 ± 4	306 ± 6
Calorimetric and tracking isolation	332 ± 4	300 ± 6
Calorimetric isolation	338 ± 4	304 ± 6
Tracking isolation	338 ± 4	302 ± 6

Table 5.5: Yields of events with an electron misidentified as a photon, after applying different isolation requirements to the probe electron in the modified signal region. Only statistical uncertainties are shown.

5.3.2 Prompt photons

Several processes produce the same final state as $t\bar{t}$ with the emission of a prompt photon. These processes include the $W\gamma$ + jets, $Z\gamma$ + jets, single-top and diboson production with an additional photon. Due to the expected small contributions from single-top and diboson processes, no dedicated samples with photon emissions calculated in the matrix element are generated. Therefore, the only source of photons in the simulation is the QED radiation, which is simulated with Photos [101, 102]. This source contributes to the other backgrounds with prompt photons, in addition to the matrix-element photons. Only the Wt- and t-channels are considered in the single-top production, while the contribution from the s-channel is found to be negligible.

All those backgrounds are estimated from their corresponding simulations described in Section 4.3. Events are selected using the same $t\bar{t}\gamma$ event selection (Section 5.2). In order to avoid the double counting of backgrounds from electrons misidentified as photons or photons originating from hadron decays, truth information is used to remove such contributions from the prompt photon sources. The $W\gamma$ + jets, $Z\gamma$ + jets are normalised to their LO cross sections. The event yields of all prompt photon sources are summarised in Table 5.6. The associated errors are statistical uncertainties only. Since the expected cross section of the $W\gamma$ + jets is larger than the one estimated from data due to the mismodelling of the heavy flavour decay in SHERPA samples, the event yield of the $W\gamma$ + jets production is scaled later (not in Table 5.6) by a factor of 0.69 ± 0.16, which is derived from a control region in data [148]. This scale factor is applied to its prediction from simulation.

Process	Electron channel	Muon channel	Combined
$W\gamma$ + jets	94.2 ± 6.7	126.7 ± 8.0	220.9 ± 10.4
$Z\gamma$ + jets	35.4 ± 2.3	37.5 ± 2.3	73.0 ± 3.2
Single top + γ	13.3 ± 3.1	18.9 ± 3.7	32.2 ± 4.9
Diboson + γ	2.2 ± 0.6	1.8 ± 0.5	4.0 ± 0.8

Table 5.6: The expected event yields of background processes with a prompt photon. The numbers are estimated from simulation and normalised to the total integrated luminosity of 20.2 fb^{-1}. The statistical uncertainties are shown.

5.4 Analysis strategy

In order to measure the number of $t\bar{t}\gamma$ signal events and consequently the $t\bar{t}\gamma$ cross section, a likelihood fit to the observed data, is applied. The fit is performed in a fiducial volume described below. An efficient discriminator between signal and background events is required as input to the likelihood function in Equation 4.18. The tracking photon isolation variable $p_{\mathrm{T}}^{\mathrm{cone20}}$ (also called $p_{\mathrm{T}}^{\mathrm{iso}}$), which will be described in Section 5.4.2, is chosen for that purpose.

5.4.1 Definition of the fiducial phase space

The fiducial cross section can be calculated by Equation 4.13, in a fiducial region defined at particle level, in a very similar way to the region defined at reconstruction level, which is described earlier in Section 5.2. The particle-level objects are defined as follows:

- Leptons: Electrons and muons with $p_{\mathrm{T}} > 10$ GeV and $|\eta| < 2.7$ are corrected to account for possible collinear soft-photon emissions: all photons not originating from a hadron decay and found within $\Delta R < 0.1$ around the lepton are considered as bremsstrahlung, and therefore are combined to the lepton momentum. Those photons are then removed from further considerations. The p_{T} of the combined object is required to be larger than 25 GeV and $|\eta|$ is required to be less than 2.5.

- Jets: Jets are reconstructed with the anti-k_{t} clustering algorithm with a radius parameter of $R = 0.4$. All stable particles (lifetime > 3×10^{11} s), with the exception of the above selected leptons and photons used to define the leptons, are considered in the jet clustering. Jets are required to have a $p_{\mathrm{T}} > 25$ GeV and $|\eta| < 2.5$.

- b-jets: A b-jet is defined if a b-hadron with $p_{\mathrm{T}} > 5$ GeV is found within a $\Delta R = 0.3$ from the jet axis described above.

- Photons: Photons are required not to originate from a hadron decay, and to have $E_{\mathrm{T}} > 15$ GeV and $|\eta| < 2.37$.

The double counting of objects is avoided by applying the following requirements: jets are removed if found within a $\Delta R < 0.2$ around an electron or within a $\Delta R < 0.1$ around a photon. The muon is removed if found within a $\Delta R < 0.4$ around any remaining jet. The electron is discarded if ΔR between the electron and any remaining jet is found within the range of [0.2, 0.4].

The above defined objects are required to pass the event selections described in Section 5.2, except for the requirements on $E_{\mathrm{T}}^{\mathrm{miss}}$, $m_{\mathrm{T}}(W)$ and $m_{e\gamma}$ which are removed, in order to have a common phase space for the electron and muon channels.

The differential cross section is measured as a function of the photon p_{T} and $|\eta|$ in the defined fiducial region and using Equation 4.17. Five bins in photon p_{T} and five bins in $|\eta|$ are considered.

5.4.2 Templates

Several isolation variables can be defined for the photon using the tracking or the calorimetric information. However, the tracking isolation variable is chosen as a discriminator in the likelihood fit. The calorimetric information is not preferred because of its dependency on the photon η, due to the variable amount of material in the calorimeter, whereas the $p_{\mathrm{T}}^{\mathrm{cone20}}$ variable does not have that dependency. It also has a good discriminating power against the main background in the single-lepton channel (i.e. the hadronic fakes). The $p_{\mathrm{T}}^{\mathrm{cone20}}$ variable is defined by the scalar sum of the transverse momenta of all the tracks which have a p_{T} larger than 1 GeV and within a cone of size $\Delta R = 0.2$ around the photon candidate. The longitudinal impact parameter of the track should be smaller than 1 mm to reduce contributions from pile-up events. The shape of the isolation distribution of the prompt photons is different from that of the hadronic fakes, as already explained in Section 4.4, due to the many activities that could happen around the hadronic-fake candidate. The tracks produced in these activities could be considered in the calculation of the isolation variable if exist within the isolation cone. The difference can be seen clearly in Figure 5.3. The figure describes the isolation shape of the prompt photons estimated in the $t\bar{t}\gamma$ signal sample compared to the shape of the hadronic fakes obtained from a simulated $t\bar{t}$ sample. The signal photons are peaking at very low values of the variable, while a broader distribution is observed for the hadronic fakes. A better description of the hadronic-fake shape is extracted using a data-driven technique that will be described later.

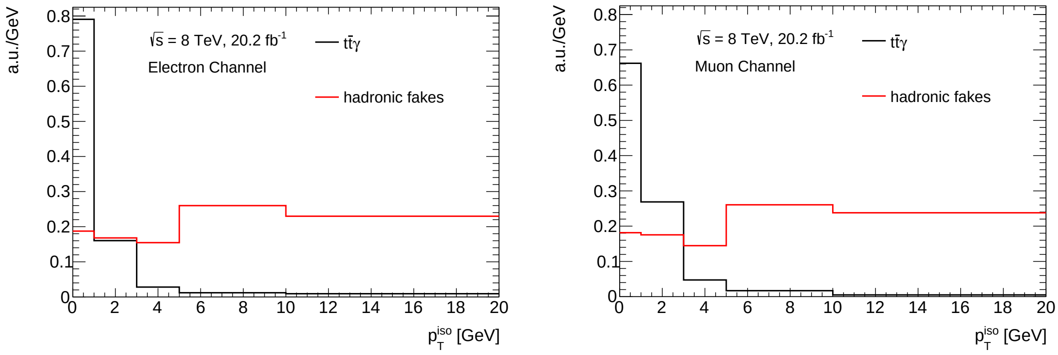

Figure 5.3: Distributions of the tracking isolation variable in the electron (left) and the muon (right) channel, for the prompt photons estimated from $t\bar{t}\gamma$ simulation in black, compared to fake photons from hadrons in $t\bar{t}$ simulation in red. Histograms are normalised to unit area.

According to the photon source, three templates are defined and used in the fit. The first template is derived for the prompt photons obtained in the signal region defined in Section 5.2. It also describes the prompt photon backgrounds introduced in Section 5.3.2. The second template is defined for the hadronic fakes, and is obtained from two control regions in data. The template is initially derived from the loose control region described in Section 5.3. This template is then scaled with weights derived from a second control region in data. The second region is defined in a similar way to the signal region but replacing the nominal photon selection by one photon that fails to satisfy at least one of the tight identification criteria (Table 4.2). The weights are calculated in five p_{T} bins, the same as used in the differential measurement, and in two bins of $|\eta|$ ($|\eta| < 1.80$ and $1.80 < |\eta| < 2.37$). The scaled template is used in the fit. The third template is used to describe events with an electron misidentified as a photon, which is estimated as explained in Section 5.3.1. The multijet background is described by a template that is merged with the signal template since the source of photons is prompt. Its template is derived based on the likelihood fit to the $p_{\mathrm{T}}^{\mathrm{cone20}}$ distribution of the weighted multijet events, using the prompt photons and the hadronic-fake templates. The normalisation of the first two templates (prompt and hadronic fakes) are left as free parameters in the likelihood fit, while for the last template, the normalisation is fixed to the data-driven estimate of the number of events with an electron misidentified as a photon. The three templates used in the fit are shown in Figure 5.4.

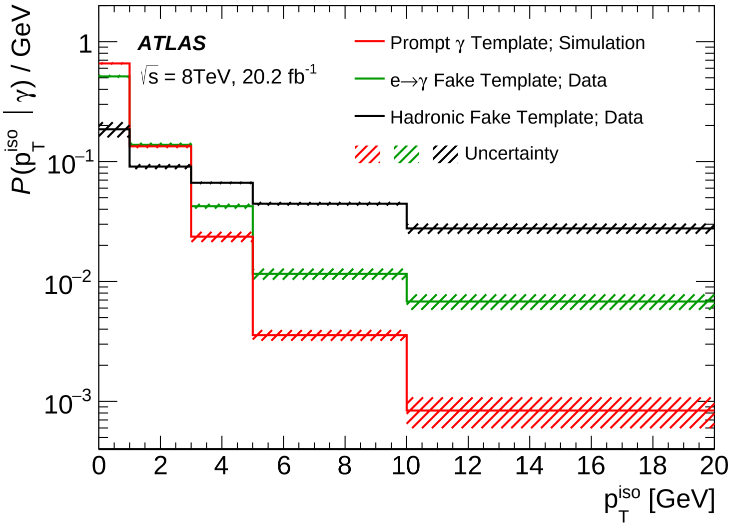

Figure 5.4: The $p_{\mathrm{T}}^{\mathrm{iso}}$ templates for the inclusive cross-section measurement for prompt photons, hadronic fakes and electron fakes [17]. The template for signal photons is taken from simulation, while the other two templates are derived from data. The distributions are normalised to unity and the last bins contain the overflows. The shaded bands show the total uncertainty (will be described in Section 5.5) in each template.

5.4.3 The likelihood fit

The difference in the shape of the $p_{\mathrm{T}}^{\mathrm{cone20}}$ variable between signal and background events is exploited in the fit of the isolation distribution to data using the likelihood function defined in Equation 4.18. Thus, the Poissons function of Equation 4.18 represent the probability to observe N data events given the expected number of signal and total background events N^s and N^b in bin j of the $p_{\mathrm{T}}^{\mathrm{cone20}}$ distribution of bin i in the p_{T} or $|\eta|$ distribution. For the fiducial measurement, only one bin is considered, while 5 bins are included for the differential measurement, and the systematic uncertainties are treated as correlated in all bins. The number of signal events in terms of the fiducial cross section is given by Equation 4.21. The post-fit event yields for the signal and background processes is presented in Section 5.6.

5.5 Systematic uncertainties

Several systematic uncertainties could affect the measured cross section. These include the signal and background modelling, the experimental uncertainties and the template-related uncertainties. The systematic variations are obtained by changing the settings of the corresponding source. The likelihood fit described above is repeated for each systematic variation, and the corresponding shifted fit result is compared to the result where the nominal setting is used. The difference between the two results is taken as an uncertainty on the measured cross section.

5.5.1 Signal and background modelling

- The effect of changing the particular choice of the renormalisation and factorisation scales in the signal sample is estimated by varying the μ_{R} and μ_{F} simultaneously by a factor of 2 around the central value ($\mu_{\mathrm{R}} = \mu_{\mathrm{F}} = \mu = 2m_t$) of the nominal MadGraph signal sample. The effect of this variation can be understood by first comparing the event kinematics produced with the same setup as the nominal sample, except for the scale, to the kinematics generated from the nominal sample. The comparison is shown in Figure 5.5. The final variation samples are generated with the full ATLAS detector simulation [110], and used to evaluate the uncertainty. A total uncertainty due to this variation of 0.6% is estimated on the measured cross section.

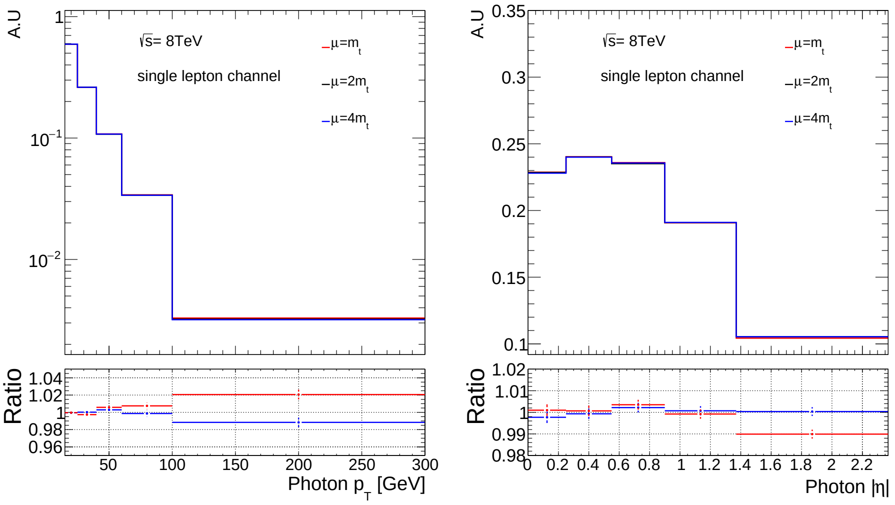

Figure 5.5: Distributions of the photon p_{T} (left), and the photon $|\eta|$ (right), for events generated using the MadGraph generator with different factorisation scales, compared to the nominal sample with a scale of $\mu = 2m_t$. Statistical uncertainty is shown.

- The uncertainty on the parton shower modelling and the hadronisation in the signal sample is estimated by comparing the nominal signal sample generated using MadGraph and showered by Pythia 6 to a MadGraph sample showered by Herwig 6.520 [115] with Jimmy 4.31 [116]. A result of 0.6% uncertainty on the inclusive cross section is calculated. Different Pythia 6 tunes corresponding to higher or lower levels of initial- and final-state radiation, with respect to the nominal settings, are compared. This result in an uncertainty of 2.2% on the inclusive cross section.
- The PDF, color reconnection, underlying event and QED uncertainties are checked in a $t\bar{t}$ sample, as the effect is expected to be similar as for $t\bar{t}\gamma$ production. The effect of their variations on the

isolation variable of the prompt photons is found to be negligible, and therefore those sources are not considered and no dedicated $t\bar{t}\gamma$ samples with those variations were produced. The comparison with a lower level of color reconnection or higher level of multiple parton interactions than the nominal settings of the $t\bar{t}$ sample are shown in Figure 5.6.

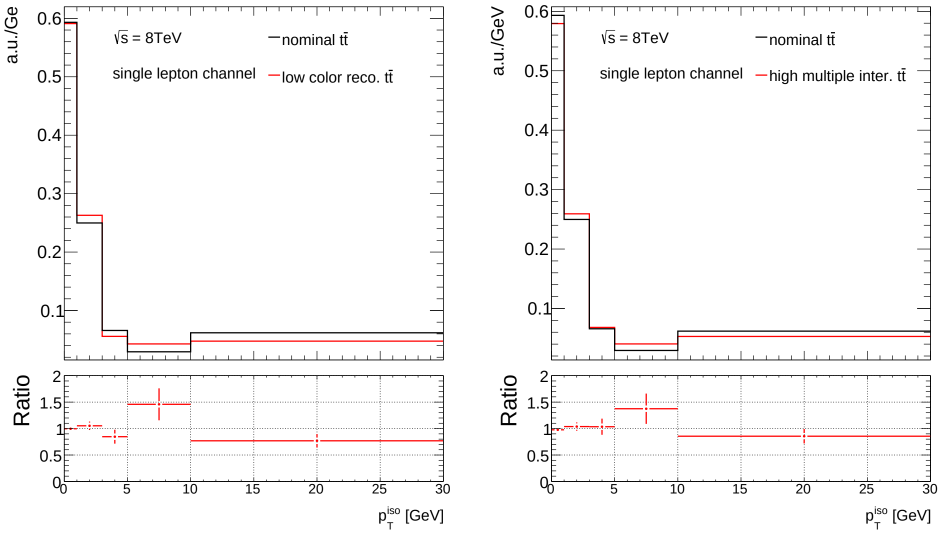

Figure 5.6: Distributions of the isolation variable of the prompt photons estimated in a $t\bar{t}$ sample, generated with lower color re-connection (left), higher multiple parton interactions (right), and compared to the nominal sample shown in black.

- The uncertainty in the normalisation of the $Z\gamma$ + jets, single top + γ, and diboson + γ backgrounds is assumed to be 48% in the four-jet bin from the Berends–Giele scaling [149]. This results in an uncertainty of 2.8% and 1.2% on the measured cross section, for the $Z\gamma$+jets and single top + γ backgrounds respectively, whereas the effect on the inclusive cross section is found to be negligible for the diboson + γ background. For the W+jets, a total uncertainty of 4% on the inclusive cross section is estimated when comparing data with different predictions from Sherpa and Alpgen. The uncertainty on the fake rate for events with an electron misidentified as a photon is estimated to be 6.1% on the inclusive cross section. The latter uncertainty is estimated by varying the choice of the range and the function used in the fit performed to the ee and $e\gamma$ invariant mass distributions, in order to calculate the fake rate.

5.5.2 Experimental uncertainties

The experimental uncertainties are mainly related to the reconstruction, identification and triggers of the final-state particles, namely leptons, photons, jets and $E_{\mathrm{T}}^{\mathrm{miss}}$. In addition, uncertainties related to the pile-up and the integrated luminosity are considered. All the uncertainties affect both the signal and background processes. The leading experimental uncertainty is found to stem from the jet energy scale (JES) [150]. This uncertainty is evaluated from different sources. The dominant are found to be due to uncertainties in the modelling, the amount of pile-up, and the jet flavour composition. Each source is varied independently and summed in quadrature to give a 4.9% total uncertainty on the inclusive cross section.

The uncertainty in the integrated luminosity is calculated to be 1.9%, from a calibration of the luminosity scale derived from beam-separation scan [151]. This results in an uncertainty of 2.1% on the measured cross section. Two sources of photon-related uncertainties are considered. The first uncertainty arises from the scale factors derived to correct for the detector mismodelling, and defined as the ratio between the photon identification efficiencies estimated in data and those obtained from simulation [131]. The effect of varying the scale factors is studied and has an impact of 1.2% on the inclusive cross section. The second source is the photon energy scale uncertainty [152], which results in an uncertainty of 0.7% on the inclusive cross section. For electrons (muons), scale factors derived as the ratios between lepton reconstruction, identification and energy scales obtained from simulation to those obtained from data [124, 126]. The effect of varying the scale factors has an uncertainty of 1.2% (1.4%) on the measured cross section.

5.5.3 Template uncertainties

The uncertainty in the hadronic-fake template is mainly caused by the prompt photon contamination. The amount of prompt photon leakage varies by varying the number of the shower variables that the hadronic-fake candidate is required to fail. The template is modified by requiring the fake photon to fail all the four shower shape variables, instead of failing at least one of them. The likelihood fit is repeated using the new template, and an uncertainty of 6.1% on the measured cross section is estimated on the measured cross section. The template of events with an electron misidentified as a photon is modified by changing the requirements in the determination of the fake rate. This result in an uncertainty of 6.1% on the measured cross section.

5.6 Results

A likelihood fit to the track isolation distribution is performed in data. A total of 3072 events are observed in data. The post-fit event yields for the signal and background processes are presented in Table 5.7. The distribution of the track isolation variable after the fit is shown in Figure 5.7.

Process	$t\bar{t}\gamma$	Hadronic fakes	$e \to \gamma$ fake	$W\gamma$ + jets	$Z\gamma$ + jets	Single top + γ	Multijet + γ	Diboson + γ	Data
Event yield	1060 ± 130	1020 ± 90	710 ± 90	160 ± 40	73 ± 32	32 ± 15	16 ± 6	5.1 ± 2.4	3072

Table 5.7: The post-fit event yields for the signal and background processes for the $t\bar{t}\gamma$ fiducial cross-section measurement in the single-lepton channel. The statistical and systematic uncertainties are shown.

The measured fiducial cross section in the single-lepton channel is found to be

$$\sigma_{\text{sl}}^{\text{fid}} = 139 \pm 7\ (\text{stat.}) \pm 17\ (\text{syst.})\ \text{fb} = 139 \pm 18\ \text{fb},$$

in agreement with the SM NLO prediction of 151 ± 24 fb [53]. The measured differential cross section as a function of the photon p_{T} and $|\eta|$ is shown in Figure 5.8, which is also compared to its theoretical prediction, and found to be in good agreement.

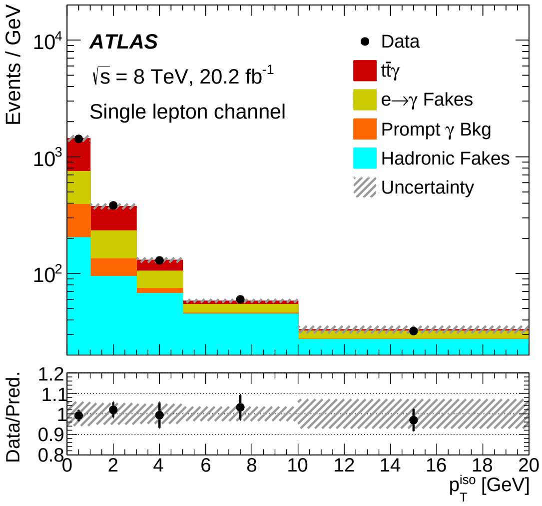

Figure 5.7: The post-fit track isolation distribution for the inclusive cross-section measurement [17]. The last bin includes the overflow. The uncertainty band includes all uncertainties.

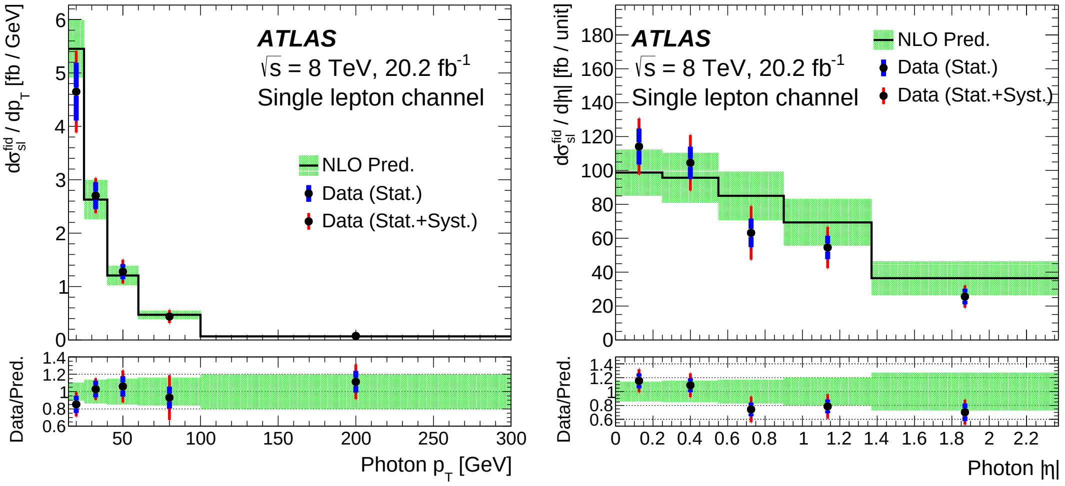

Figure 5.8: The measured differential cross section in the photon p_{T} and $|\eta|$ [17] compared to the corresponding theoretical prediction [53].

CHAPTER 6

Cross-section measurement of $pp \to t\bar{t}\gamma$ at 13 TeV

The cross-section measurement of $t\bar{t}\gamma$ production is performed in the dilepton channel at $\sqrt{s} = 13$ TeV. Both inclusive and differential cross sections are measured in a fiducial phase space close to the selection requirements. The inclusive fiducial cross section is measured using the maximum-likelihood fit [19] as in the 8 TeV analysis [17], but with different input parameters. The differential cross section is measured by employing the iterative Bayesian method, instead of the simple bin-by-bin approach used in the 8 TeV measurement. The cross section is measured in bins of photon p_{T}, $|\eta|$, minimum $\Delta R(\ell, \gamma)$, $\Delta\eta(\ell, \ell)$ and $\Delta\phi(\ell, \ell)$. In this chapter, the fit for the inclusive measurement is described briefly, while the remaining parts are explained in more details, emphasizing my personal contributions to this analysis.

6.1 Theory prediction

Similar calculations as performed at 14 TeV [53] (see Section 2.6.1) are repeated at $\sqrt{s} = 13$ TeV in the dilepton channel, at LO and NLO [58]. The NNPDF sets [86, 88] and the renormalisation and factorisation scales of $\mu_{\mathrm{R}} = \mu_{\mathrm{F}} = \mu = m_t$ are used for the nominal setting. Calculations are repeated for two sets of variations. The first set is obtained by varying the scales μ_{R} and μ_{F} by a factor of 2 simultaneously around the nominal choice. The used PDF set is changed to the CT10 [87] or the MMHT2014 [89] PDF set, for the second set of variations.

Following the strategy explained in Section 5.1 at 8 TeV, the nominal LO MadGraph prediction is compared to the LO theory prediction in Section 6.1.1. Both predictions are used to calculate the NLO k-factor in Section 6.1.2. In this section, two k-factors are estimated. The first one follows the calculation at 8 TeV, while the second is estimated in a region that is very close to the fiducial region (described in Section 6.5). The second k-factor is used to scale the MadGraph prediction of the $t\bar{t}\gamma$ sample.

6.1.1 Leading-order cross section

The phase-space region for the calculation and the MadGraph prediction is defined in the following. Two leptons, where at least one of them has a $p_{\mathrm{T}} > 15$ GeV and $|\eta| < 5$, are required. For the calculation, jets are reconstructed from stable particles using the anti-k_t algorithm ($R = 0.4$), while in MadGraph, quarks are used, instead of clustered jets. Jets in theoretical calculations and quarks in MadGraph are required to have $p_{\mathrm{T}} > 10$ GeV and $|\eta| < 5$. The final state photon is required to have a $p_{\mathrm{T}} > 15$ GeV, $|\eta| < 5$, and to be separated from jets and leptons with $\Delta R(\text{jet}, \gamma) > 0.2$ and $\Delta R(\ell, \gamma) > 0.5$, respectively.

The LO cross section calculated by MadGraph, after applying the selections described above, is obtained using Equation 5.1. The cross sections computed in this way are compared to the theoretical calculation in Table 6.1, using a fixed scale of $2m_t$ or a dynamic scale (see Section 4.3.1). It can be seen that the difference between the two calculations is less than 2%. Having shown that MadGraph at LO reproduces well the LO theory results, the k-factor used for a MadGraph generation at LO can be extracted from a comparison of the LO and NLO theory calculations, as described in the next section.

Calculation [fb]	$\mu = 2m_t$	Dynamic scale
Theory	227.7	276.2
MadGraph	232.3	279.9

Table 6.1: A comparison of the LO cross section obtained from theory calculations to those obtained from MadGraph in the dilepton channel, using fixed and dynamic scales.

6.1.2 Next-to-leading order k-factor

Two calculations for the NLO k-factor are performed. The first one follows the method employed in the 8 TeV analysis, and uses the cross sections estimated in the previous section. The dynamic scale is set for the LO calculation (Table 6.1), which is the same scale used for the LO MadGraph signal sample (Section 4.3.1). The scale $\mu_F = \mu_R = m_t$ is set for the NLO calculation. The NLO predictions are shown differentially in Figure 6.1 and inclusively in Table 6.2. The k-factor is found to be $1.59 \pm 0.20 \pm 0.03$. The first uncertainty is due to the scale variation of the NLO calculations by a factor of 2 around the central value ($\mu = m_t$), while the second uncertainty is due to the PDF variation. The k-factor as a function of the photon p_T is shown in Figure 6.2.

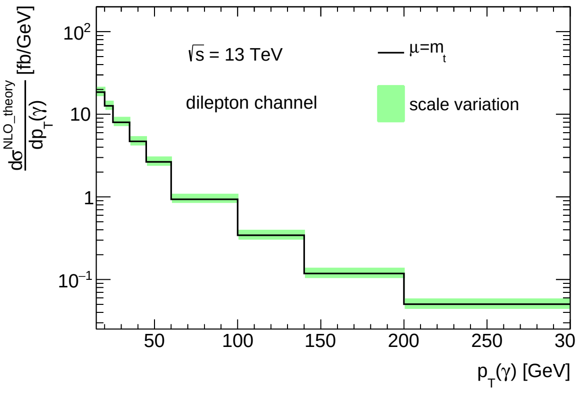

Figure 6.1: The differential NLO theoretical cross section as a function of the photon transverse momentum p_T in the dilepton channel, applying the selections described in Section 6.1.1. The uncertainty band is the scale variation by a factor of 2 around nominal.

Table 6.2: The inclusive NLO theoretical cross section in the dilepton channel, for different scale choices, applying the requirements described in Section 6.1.1.

Scale	NLO theory cross section [fb]
$2m_t$	386.3
m_t	439.2
$0.5m_t$	495.2

The second k-factor is calculated using tighter requirements than the selections described above. The tight requirements are defined to be very close to the selections in the fiducial region (described in Section 6.5). The selections are summarised in the following. Each event is required to have exactly

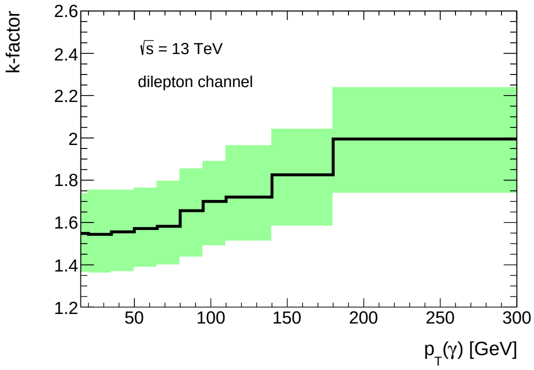

Figure 6.2: The k-factor distribution as a function of the selected photon transverse momentum p_{T}, in the dilepton channel. The shaded area is due to the NLO scale variation by a factor of two around the central value used for the NLO calculations.

one photon with $p_{\mathrm{T}} > 20$ GeV and $|\eta| < 2.37$, exactly two leptons with $p_{\mathrm{T}} > 25$ GeV and $|\eta| < 2.5$, and at least two jets with $p_{\mathrm{T}} > 25$ GeV and $|\eta| < 2.5$. The event is discarded if the distance between the photon and any jet, or the distance between any lepton and any jet is found to be less than 0.4. Photons are required to be separated from leptons with $\Delta R(\ell, \gamma) > 1.0$. The requirement on the number of jets demands a more accurate definition of the jets than the partonic quarks in the MadGraph calculation. Therefore, jets and all other final-state objects are defined at particle level in MadGraph, in contrast to the parton-level objects which were used in the first calculation of the k-factor. The particle-level objects will be described in Section 6.5.

Using the above requirements, the k-factor is estimated as the ratio of the NLO calculation to the LO cross section calculated by MadGraph, and found to be 1.97. The uncertainty in the k-factor as estimated for the first k-factor is not expected to differ significantly, thus its calculation is not repeated here. The k-factor of 1.97 is chosen to scale the LO $t\bar{t}\gamma$ sample in this analysis, since it is estimated in a region that is very similar to the region where the cross-section measurement is performed. The differential k-factor are extracted in photon p_{T} and $|\eta|$ bins, as shown in Figure 6.3, and used to scale their LO predictions, whereas the inclusive k-factor is used to scale all other distributions.

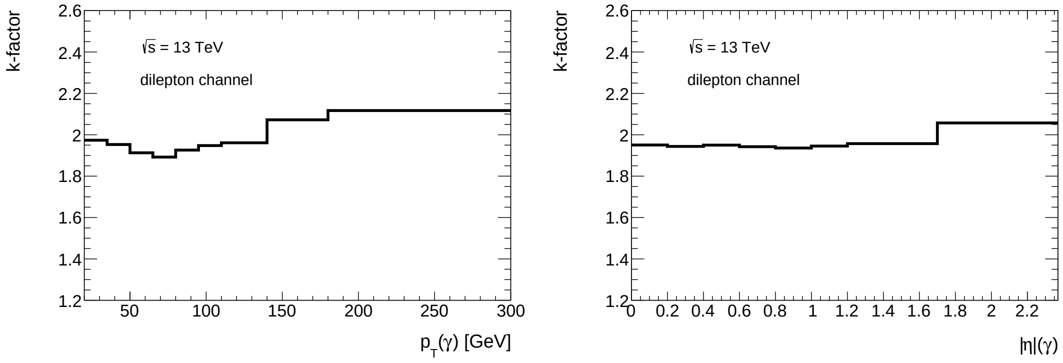

Figure 6.3: The k-factor distribution as a function of the photon p_{T} (left) and the photon $|\eta|$ (right), estimated using particle-level objects at LO in the dilepton channel.

6.2 Event selection

The signal region selection is chosen to be similar to the baseline $t\bar{t}$ dilepton selection (see e.g. Ref. [41]), with the additional requirement of one reconstructed photon.

The $t\bar{t}\gamma$ dilepton channel is characterised by the presence of two leptons. At least one lepton should be triggered by one of the triggers described in Table 6.3 [125, 153]. The triggers are split according to the data period used in this analysis (2015 and 2016). At least one electron (muon) trigger amongst the described triggers should be fired for the ee ($\mu\mu$) channel, while at least one electron trigger or a muon trigger is fired for the $e\mu$ channel. In order to be consistent with the trigger requirement, the minimum reconstructed p_{T} of the highest p_{T} lepton is required to be 27.5 GeV for the 2016 selection and 25 GeV for the 2015 selection. At least one of the selected leptons in the event should be matched to reconstructed objects from the fired trigger. The two leptons are required to have opposite charges, $|\eta| < 2.5$, and an invariant mass ($m_{\ell\ell}$) larger than 15 GeV. In order to reduce background contributions from Z+jets and $Z+\gamma$ events in the same-flavour channels (ee and $\mu\mu$), a requirement on the $m_{\ell\ell}$ value to be outside the mass range [85,95] GeV is applied. Events with at least two reconstructed jets of $p_{\mathrm{T}} > 25$ GeV and $|\eta| < 2.5$ are selected. A $t\bar{t}\gamma$ candidate is characterised by the presence of exactly one isolated photon with $p_{\mathrm{T}} > 20$ GeV and $|\eta_{\mathrm{cl}}| < 2.37$, excluding the region $1.37 < |\eta_{\mathrm{cl}}| < 1.52$. The isolation requirement, as described in Section 4.4, is imposed in order to reduce the hadronic-fake background. Its importance will be shown later in this section. Both the tracking ($p_{\mathrm{T}}^{\mathrm{cone20}}$) and calorimetric isolation ($E_{\mathrm{T}}^{\mathrm{cone40}}$) properties are employed for this requirement. Since part of the lepton energy is carried by the photon, if emitted from leptons, a requirement on the invariant mass of the two leptons and the photon candidate ($m_{\ell\ell\gamma}$) is made similarly to the invariant mass of the two leptons, in the ee and $\mu\mu$ channels.

An additional set of requirements on the missing transverse momentum in the same-flavour channels, the number of b-tagged jets, the distance between the photon and any lepton, $\Delta R(\ell, \gamma)$, and the distance between the photon and any jet, $\Delta R(\mathrm{jet}, \gamma)$, are optimised in the next section. The optimisation is performed within the following defined range for each variable:

- $E_{\mathrm{T}}^{\mathrm{miss}}$ in a range of [0, 70] GeV.
- The number of b-tagged jets in a range of [0, 2].
- $\Delta R(\ell, \gamma)$ in a range of [0.4, 1.0].
- $\Delta R(\mathrm{jet}, \gamma)$ in a range of [0.4, 1.0].

Year	Electron trigger	Description	Muon trigger	Description
2015	`HLT_e24_lhmedium_L1EM20VH`	$p_{\mathrm{T}} > 24$ GeV, $E_{\mathrm{T}} > 20$ GeV and medium ID	`HLT_mu20_iloose_L1MU15`	$p_{\mathrm{T}} > 20$ GeV for the combined muon, $E_{\mathrm{T}} > 15$ GeV for each muon and loose ID
	`HLT_e60_lhmedium`	$p_{\mathrm{T}} > 60$ GeV and medium ID	`HLT_mu50`	$p_{\mathrm{T}} > 50$ GeV for the combined muon
	`HLT_e120_lhloose`	$p_{\mathrm{T}} > 120$ GeV and loose ID		
2016	`HLT_e26_lhtight_nod0_ivarloose`	$p_{\mathrm{T}} > 26$ GeV, variable E_{T} selection and tight ID	`HLT_mu26_ivarmedium`	$p_{\mathrm{T}} > 26$ GeV for the combined muon, variable E_{T} selection for each muon and medium ID
	`HLT_e60_lhmedium_nod0`	$p_{\mathrm{T}} > 60$ GeV and medium ID	or `HLT_mu50`	$p_{\mathrm{T}} > 50$ GeV for the combined muon
	`HLT_e140_lhloose_nod0`	$p_{\mathrm{T}} > 140$ GeV and loose ID		

Table 6.3: The lepton triggers considered in the event selections. The identification (ID) criteria are described in Ref. [125, 153].

6.2.1 Selection optimisation

The event selections described above are optimised in order to minimise the total uncertainty on the expected cross section, reducing the background contributions in the signal region. This strategy follows the method described in Ref. [154]. Background processes that will be described in Section 6.3, are estimated based on their simulations (see Section 4.3.2). The expected cross section σ is given by the following equation:

$$\sigma = \frac{N_{\text{data}}^{\text{expected}} - N_{\text{bkg}}}{\epsilon \cdot \mathcal{L}} = \frac{(N_{\text{sig}} + N_{\text{bkg}}) - N_{\text{bkg}}}{\epsilon \cdot \mathcal{L}} \tag{6.1}$$

where $\mathcal{L}$ is the integrated luminosity, $N_{\text{data}}^{\text{expected}}$ is the expected number of signal and background events ($N_{\text{sig}} + N_{\text{bkg}}$), and ϵ is the selection efficiency, which is defined as the ratio of number of selected signal events to the initial number of events before selection:

$$\epsilon = \frac{N_{\text{sig}}}{N_{\text{sig}}^{\text{initial}}}. \tag{6.2}$$

The statistical uncertainty of the expected cross section is derived using the error propagation as follows:

$$\begin{aligned}\Delta\sigma_{\text{stat}} &= \sqrt{(\frac{\Delta(N_{\text{sig}} + N_{\text{bkg}})}{\epsilon \cdot \mathcal{L}})^2 + (\frac{\Delta N_{\text{bkg}}}{\epsilon \cdot \mathcal{L}})^2} &(6.3)\\ &= \sqrt{(\frac{\sqrt{N_{\text{sig}} + N_{\text{bkg}}}}{\epsilon \cdot \mathcal{L}})^2 + (\frac{\sqrt{N_{\text{bkg}}}}{\epsilon \cdot \mathcal{L}})^2} \\ &= \frac{\sqrt{N_{\text{sig}} + N_{\text{bkg}}}}{\epsilon \cdot \mathcal{L}}, &(6.4)\end{aligned}$$

where the background component of the statistical uncertainty ($\sqrt{N_{\text{bkg}}}$) is expected to be very small, and thus is neglected. For the selection optimisation, the total systematic uncertainty is calculated by

$$\Delta\sigma_{\text{sys}} = \sqrt{(\frac{\Delta N_{\text{bkg}}}{\epsilon \cdot \mathcal{L}})^2 + (\sigma \cdot \frac{\Delta\mathcal{L}}{\mathcal{L}})^2 + (\sigma \cdot \frac{\Delta\epsilon}{\epsilon})^2}, \tag{6.5}$$

where the following set of systematic uncertainties are considered:

- Background modelling: All background processes are estimated from their MC predictions described in Section 4.3. An uncertainty of 10% is applied to the total event yield of all backgrounds.
- Luminosity uncertainty: An uncertainty of 2.1% is used. The uncertainty is estimated following the method described in Ref. [151]. It affects the nominal event yield of the signal and all backgrounds.
- Efficiency uncertainty:
  - b-tagging, jet, leptons, and $E_{\text{T}}^{\text{miss}}$ uncertainties: Uncertainties estimated in the $t\bar{t}$ differential cross-section measurement performed in the $e\mu$ channel [41] are assumed.
  - Photon identification uncertainty: The uncertainty is estimated by varying the scale factors defined as the ratio of the photon identification efficiencies obtained in data to those obtained in simulation [132]. The variations are implemented as event weights in the signal sample. Therefore, the uncertainty affects the estimation of the signal efficiency defined in Equation 6.2.

The total uncertainty on the expected cross section is the quadrature sum of the statistical and systematic uncertainties derived above:

$$\Delta\sigma = \sqrt{(\Delta\sigma_{\mathrm{stat}})^2 + (\Delta\sigma_{\mathrm{sys}})^2}. \tag{6.6}$$

The optimisation is conducted for each variable independently from the other. For the optimisation of a specific selection, all others are set to their lowest value in their specified range. A special case is made for optimising the number of b-tagged jets. For this optimisation, a requirement on the missing transverse momentum of $E_{\mathrm{T}}^{\mathrm{miss}} > 30$ GeV is applied, to reduce background contributions from prompt photon sources (see Figure 6.4). The latter reduces the background uncertainty on the expected cross section.

A minimum of the total uncertainty on the expected cross section at $E_{\mathrm{T}}^{\mathrm{miss}} = 30$ GeV is observed in the ee and $\mu\mu$ channels, as shown in Figure 6.4. The distribution of the missing transverse momentum for signal and background processes is shown in the same figure. A threshold of 30 GeV is able to get rid of a large fraction of background contributions, thus it is chosen for the event selection.

The optimisation of the number of b-tagged jets is shown in Figure 6.5. The statistical uncertainty is dominant. The total uncertainty indicates a minimum at a point of at least one or at least two b-tagged jets. However, a requirement of at least one b-tagged jet is preferred to enhance data statistics.

The result of optimising the distance between jets and photons is shown in Figure 6.6. No specific value of the distance minimises the total uncertainty, in any of the three channels. Hence, no further selection is applied. In this variable and the other distance $\Delta R(\ell, \gamma)$ (described below), the requirement at a value of 0.4, which can be observed in the distributions, arises from the object-level selection where jet-photon and lepton-photon overlap removals are required, as described in Section 4.4.

Finally, the $\Delta R(\ell, \gamma)$ selection is shown in Figure 6.7. The statistical uncertainty is dominant for this variable, while no clear minimum of the total uncertainty is observed. However, a requirement of $\Delta R(\ell, \gamma) > 1.0$ is chosen. This selection is preferred to enhance the radiative top-quark production over the radiative top-quark decay. Photons emitted from the final-state objects or from the W boson are expected to be close to these objects, as can be seen in Figure 6.8. In the figure, the fractions of the two types of radiation are estimated from the $t\bar{t}\gamma$ sample, based on their truth information, and shown as a function of the distance between the photon and any lepton (top), and as a function of the minimum $\Delta R(\ell, \gamma)$ (bottom). A differential cross-section measurement in bins of the latter variable is planned. Therefore, its not preferred to cut further on $\Delta R(\ell, \gamma)$.

As a summary, the total uncertainty on the expected cross section is reduced by imposing the following: a requirement of at least one b-tagged jet in the three channels, a minimum missing transverse momentum of 30 GeV in the ee and $\mu\mu$ channels, and a value larger than 0.4 for the two distances variables; $\Delta R(\mathrm{jet}, \gamma)$ and $\Delta R(\ell, \gamma)$. The optimised selections are required in the signal region, with the exception of $\Delta R(\ell, \gamma)$, which is required to be larger than 1.0.

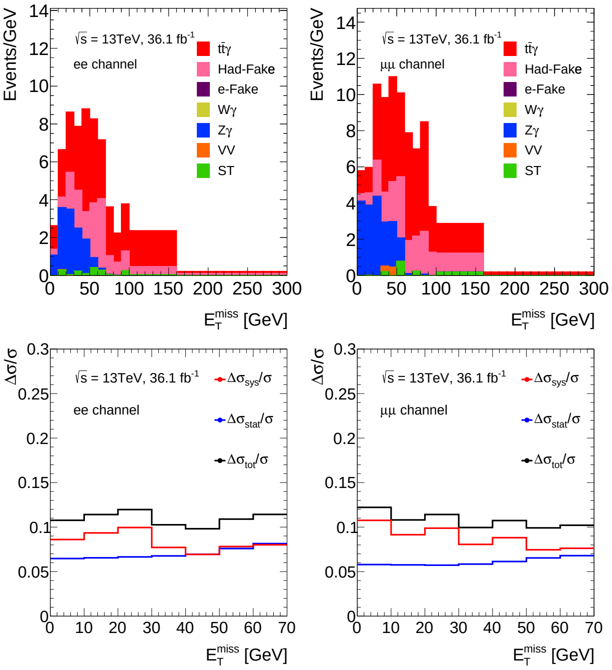

Figure 6.4: Distributions of the missing transverse momentum (top). The uncertainty on the expected cross section as a function of this variable (bottom), in the *ee* (left) and $\mu\mu$ (right) channels. The systematic uncertainty is shown in red, the statistical uncertainty in blue and the total uncertainty in black. Had-Fake refers to the hadronic-fake background, VV to the diboson background and ST to the single-top background.

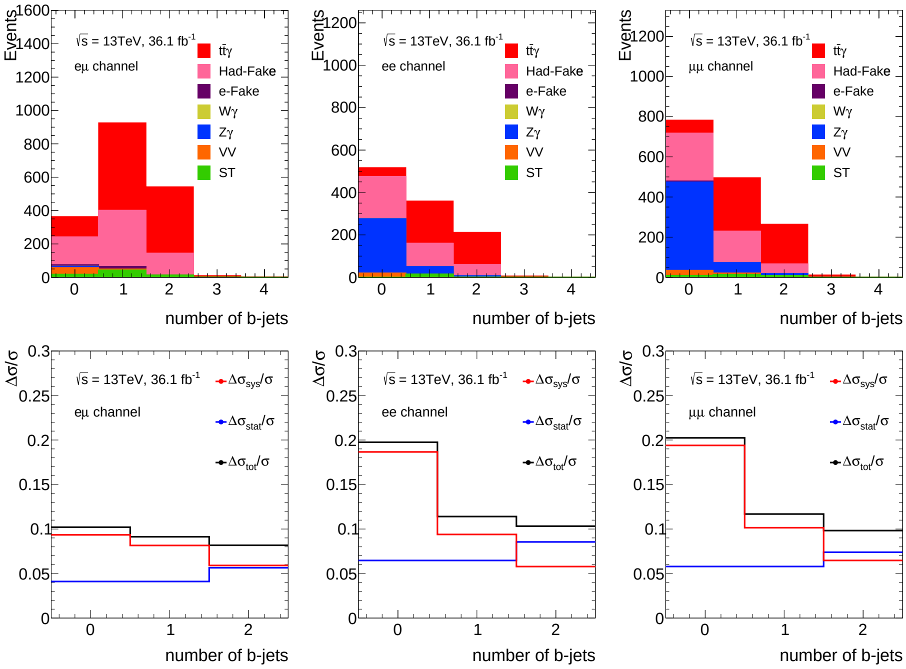

Figure 6.5: Distributions of the number of b-tagged jets (top). The uncertainty on the expected cross section as a function of this variable (bottom), in the $e\mu$ (left), *ee* (centre) and $\mu\mu$ (right) channels. The systematic uncertainty is shown in red, the statistical uncertainty in blue and the total uncertainty in black. Had-Fake refers to the hadronic-fake background, VV to the diboson background and ST to the single-top background.

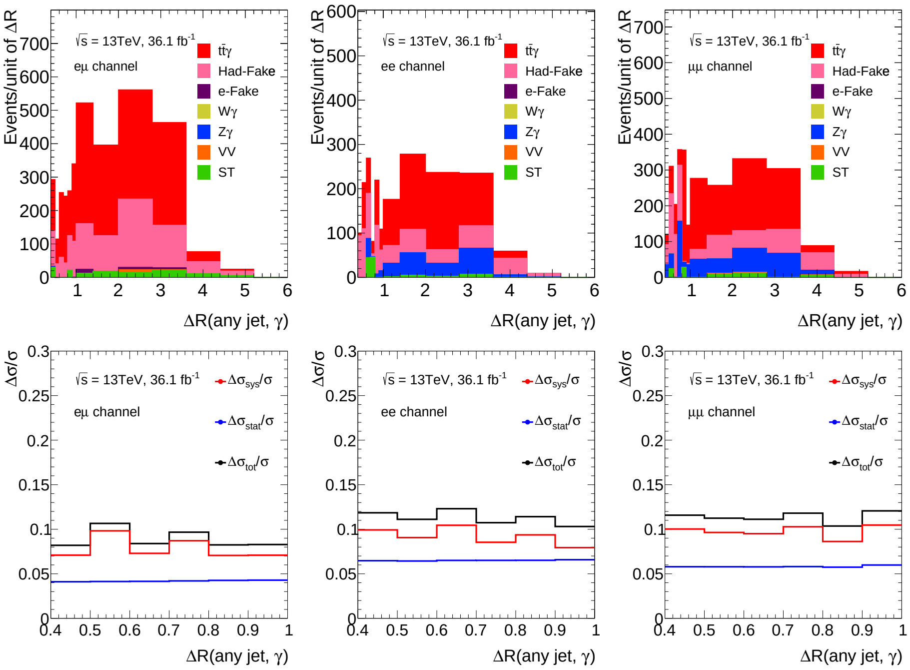

Figure 6.6: Distribution of the distance between the photon and any jet (top). The uncertainty on the expected cross section as a function of the variable (bottom), in the $e\mu$ (left), ee (centre) and $\mu\mu$ (right) channels. The systematic uncertainty is shown in red, the statistical uncertainty in blue and the total uncertainty in black. Had-Fake refers to the hadronic-fake background, VV to the diboson background and ST to the single-top background.

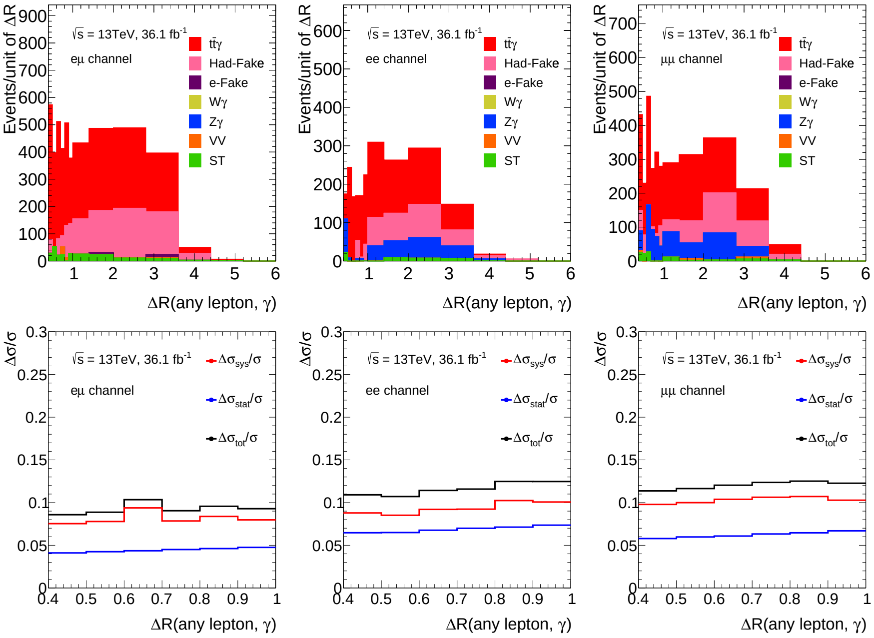

Figure 6.7: Distribution of the distance between the photon and any lepton (top). The uncertainty on the expected cross section as a function of this variable (bottom), in the $e\mu$ (left), ee (centre) and $\mu\mu$ (right) channels. The systematic uncertainty is shown in red, the statistical uncertainty in blue and the total uncertainty in black. Had-Fake refers to the hadronic-fake background, VV to the diboson background and ST to the single-top background.

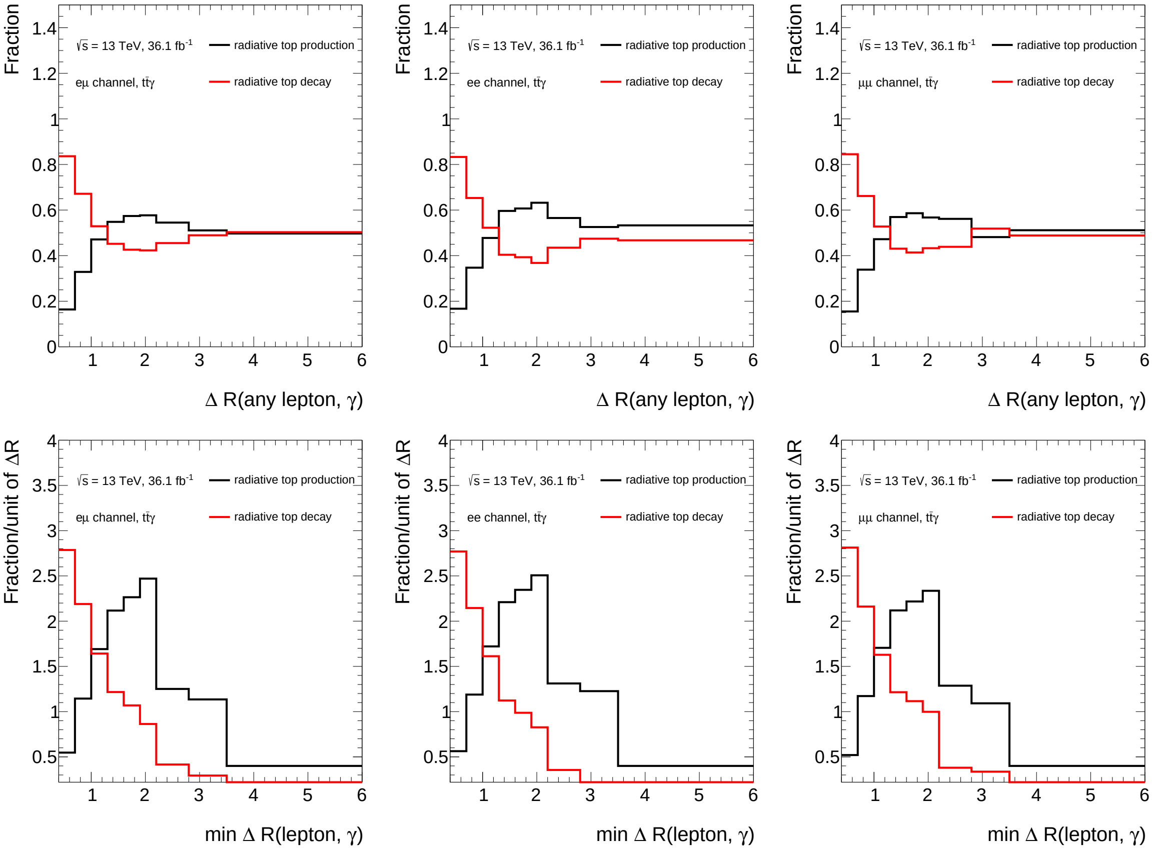

Figure 6.8: Fractions of photons radiated from the initial-state particle or the top quark in black, and photons radiated from the W boson or any final-state particle in red, as a function of the ΔR between the photon and any lepton (top), and the minimum ΔR between the photon and the lepton (bottom), in the $e\mu$ (left), ee (centre) and $\mu\mu$ (right) channels. Both types of radiation are estimated from the $t\bar{t}\gamma$ sample. Distributions in the bottom panel are normalised to the bin width for better shape comparison.

Photon isolation

The importance of the choice of the isolation can be understood by comparing distributions of the tracking and the calorimetric isolation variables (described in Section 4.4) before and after applying the isolation requirements; $p_{\mathrm{T}}^{\mathrm{cone20}}/p_{\mathrm{T}} < 0.065$ and $E_{\mathrm{T}}^{\mathrm{cone40}} < 0.022 \times p_{\mathrm{T}}\ (\gamma) + 2.45$ GeV. The distributions are obtained after applying all the event selections described above, and shown in Figure 6.9. The W+γ background process is removed from the figures due to its negligible contribution. From the figures, it can be observed that most of the background photons are less isolated than the signal photons. A large fraction of these backgrounds is rejected with the isolation requirements.

6.2.2 Event selection summary

The full $t\bar{t}\gamma$ selections are listed in Table 6.4 for the combined 2015 and 2016 data, with the corresponding event yield for each selection.

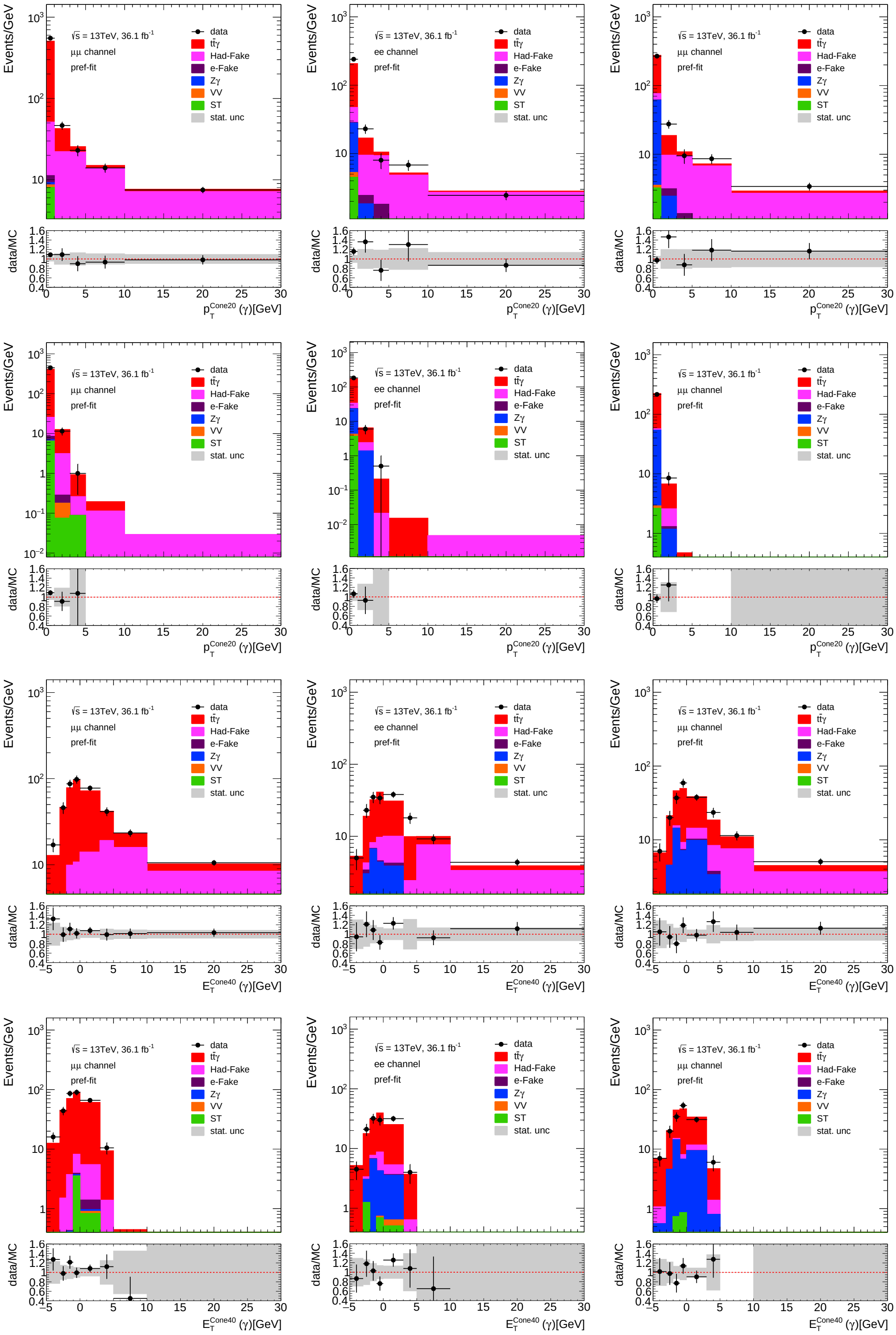

Figure 6.9: Distributions of the $p_{\mathrm{T}}^{\mathrm{cone20}}$ variable before (first row) and after (second row) applying the isolation requirement. Distributions of the $E_{\mathrm{T}}^{\mathrm{cone40}}$ variable before (third row) and after (fourth row) applying the isolation requirement, in the $e\mu$ (left), ee (centre) and $\mu\mu$ (right) channels. All background processes are estimated based on simulations and will be described in Section 6.3. Had-Fake refers to the hadronic-fake background, VV to the diboson and ST to the single-top background. Only the statistical uncertainty is shown.

Selection	$e\mu$	ee	$\mu\mu$
Initial number of events	1 528 814 900	1 528 814 900	1 528 814 900
Good run list	1 491 862 870	1 491 862 870	1 491 862 870
Trigger	933 534 934	435 241 872	498 707 759
Number of electrons or muons ($p_{\mathrm{T}} > 25$ (27.5) GeV) ≥ 1	544 768 707	b 435 241 872	498 707 759
Number of muons (electrons/muons) ($p_{\mathrm{T}} > 25$ (27.5) GeV) $\geq 1(1/1)$ $e\mu$ (ee/ $\mu\mu$)	23 363 214	264 040 516	246 565 835
Number of electrons (electrons/muons) ($p_{\mathrm{T}} > 25$ GeV) ≥ 1 (2/2) $e\mu$ (ee/ $\mu\mu$)	319 729	12 392 393	19 805 540
Trigger match	319 606	12 392 367	19 805 366
Number of muons (electrons/muons) ($p_{\mathrm{T}} > 25$ GeV) $= 1$ (2/2) $e\mu$ (ee/ $\mu\mu$)	318 037	12 390 072	19 801 961
Number of electrons (muons/electrons) ($p_{\mathrm{T}} > 25$ GeV) $= 1$ (0/0) $e\mu$ (ee/ $\mu\mu$)	315 891	12 388 456	19 799 585
Opposite sign of leptons	307 098	12 299 970	19 797 478
Invariant mass of the two leptons > 15 GeV	305 504	12 274 775	12 977 209
Number of photons ($p_{\mathrm{T}} > 15$ GeV) ≥ 1	3 356	142 638	1 217 400
Exactly one photon ($p_{\mathrm{T}} > 20$ GeV)	1 441	30 661	47 044
Isolated photon	1 340	19 368	29 824
At least two jets ($p_{\mathrm{T}} > 25$ GeVand $\lvert\eta\rvert < 2.5$)	916	3 247	4 193
At least one b-tagged jet	766	731	890
$m_{\ell\ell}$ not in [85,95] GeV	766	550	654
$m_{\ell\ell\gamma}$ not in [85,95] GeV	766	432	488
$E_{\mathrm{T}}^{\mathrm{miss}} > 30$ GeV	766	330	362
$\Delta R(\ell, \gamma) > 1.0$	473	196	233

Table 6.4: The event yields after each selection for the combined 2015 and 2016 data.

6.3 Background estimation

The dilepton channel receives small contributions from background photons. The different-flavour channel has the highest purity, with a signal-to-background ratio of ~12, as already shown in Table 6.8. The main background source in the $e\mu$ channel stems from hadronic fakes, produced mainly in dileptonic $t\bar{t}$ events. For the ee and $\mu\mu$ channels, Z+γ events with a prompt photon emission are the main background. Small contributions are expected in all channels from single-top and diboson productions, or from single-lepton $t\bar{t}$ events with one jet misidentified as a lepton (fake lepton). Events with an electron misidentified as a photon ($e \to \gamma$ fake, or e-Fake) are also few. All backgrounds are estimated from their simulation, using samples described in Section 4.3.2. The estimation is performed by applying the event selections described in Section 6.2. Photons are classified according to their truth information. The hadronic-fake background is scaled by a factor derived from a control region in data, in the single-lepton channel of $t\bar{t}\gamma$ [18]. Since the source of the fake photon is expected to be similar in the single-lepton and dilepton channels, the same scale factor derived in the single-lepton channel is applied. The scale factor is calculated in η-p_{T} slices, and separately for converted and unconverted photons, as presented in Table 6.5.

The modelling of the Z+γ process is checked in Section 6.3.1. The fake-lepton background is described in Section 6.3.2.

6.3.1 Validation region for Z+γ

The heavy-flavour modelling of Z+γ production is checked in the same-flavour channels, where the Z+γ events are found to be the dominant background. The check is performed in different validation regions (VRs). The non-Z+γ contributions are estimated from their predictions in simulation. The VRs are defined in a similar way to the signal region (Section 6.2), with the exception of certain selections that are made different in order to have enriched Z+γ VRs. The different selections are as follows: the invariant mass of the two leptons is required to be in a mass window of [60, 100] GeV, and there are no requirements on the number of jets nor on the missing transverse momentum. In the first validation

Conversion type	η-p_{T} bin	Scale factor
Converted	$\lvert\eta\rvert < 0.60$	1.52 ± 0.17 (stat.) $^{+0.56}_{-0.50}$ (syst.)
	$0.60 < \lvert\eta\rvert < 1.37$, $20 < p_{\mathrm{T}} < 30$	1.74 ± 0.27 (stat.) $^{+0.78}_{-0.90}$ (syst.)
	$0.60 < \lvert\eta\rvert < 1.37$, $p_{\mathrm{T}} > 30$	1.00 ± 0.14 (stat.) $^{+0.48}_{-0.49}$ (syst.)
	$1.52 < \lvert\eta\rvert < 2.37$, $20 < p_{\mathrm{T}} < 50$	1.71 ± 0.26 (stat.) $^{+0.70}_{-0.91}$ (syst.)
	$1.52 < \lvert\eta\rvert < 2.37$, $p_{\mathrm{T}} > 50$	0.79 ± 0.22 (stat.) $^{+0.46}_{-0.36}$ (syst.)
Unconverted	$\lvert\eta\rvert < 0.60$, $20 < p_{\mathrm{T}} < 30$	2.36 ± 0.35 (stat.) $^{+0.79}_{-0.92}$ (syst.)
	$\lvert\eta\rvert < 0.60$, $p_{\mathrm{T}} > 30$	1.37 ± 0.18 (stat.) $^{+0.76}_{-0.64}$ (syst.)
	$0.60 < \lvert\eta\rvert < 1.37$, $20 < p_{\mathrm{T}} < 30$	1.72 ± 0.25 (stat.) $^{+0.48}_{-0.82}$ (syst.)
	$0.60 < \lvert\eta\rvert < 1.37$, $p_{\mathrm{T}} > 30$	1.33 ± 0.23 (stat.) $^{+0.44}_{-0.84}$ (syst.)
	$1.52 < \lvert\eta\rvert < 2.37$	3.15 ± 0.48 (stat.) $^{+1.34}_{-1.37}$ (syst.)

Table 6.5: The hadronic-fake scale factors calculated in η-p_{T} (in GeV) bins for converted and unconverted photons, derived in the single-lepton channel [18], and applied to the dilepton channel. The statistical and systematic uncertainties (described in Section 6.7) are shown.

region, VR1, the number of b-tagged jet is required to be 0. This requirement reduces contributions from $t\bar{t}\gamma$ signal, while enhancing contributions from hadronic fakes and other backgrounds. Exactly one b-tagged jet is required to be present in the second validation region, VR2. With this selection, the heavy-flavour jet modelling is checked in a region with b-tagged jets. A requirement of at least one b-tagged jet is imposed for VR3. With this selection, the VR3 is the closest to the $t\bar{t}\gamma$ signal region. The event yields in the validation regions are summarised in Table 6.6. The table also shows scale factors derived as the ratio of the observed Z+γ to the expected Z+γ production. These factors can be used to scale the expected Z+γ in case mismodelling is observed, and calculated as

$$\mathrm{SF} = \frac{\text{data} - \text{non-}Z\text{+}\gamma}{Z\text{+}\gamma}, \tag{6.7}$$

where non-Z+γ is the sum of all expected contributions: hadronic fakes, electrons misidentified as photons, $t\bar{t}\gamma$, diboson+γ and single top + γ. From Table 6.6 it can be seen that the Z+γ process is well modelled in VR2 and VR3. A selected set of distributions in VR1 are shown in Figure 6.10 in the ee and $\mu\mu$ channels. Additional distributions are shown in Appendix B.

Channel		Z+γ	hadronic-fakes	$e \to \gamma$ fake	$t\bar{t}\gamma$	diboson + γ	single top + γ	data	data/MC	SF
VR1 (0 b-tag)	$\mu\mu$	$16\,920 \pm 133$	$1\,262 \pm 152$	27.30 ± 2.51	67.11 ± 2.00	85.42 ± 4.40	5.08 ± 1.12	19 684	1.07 ± 0.01	1.08 ± 0.02
	ee	$11\,472 \pm 110$	803 ± 127	42.68 ± 3.80	47.52 ± 1.62	75.86 ± 4.40	4.91 ± 1.24	12 829	1.03 ± 0.01	1.03 ± 0.02
VR2 (1 b-tag)	$\mu\mu$	525.46 ± 31.86	34.09 ± 6.59	1.04 ± 0.43	161.40 ± 3.04	0.73 ± 1.55	4.35 ± 1.02	685	0.94 ± 0.05	0.92 ± 0.09
	ee	376.40 ± 27.96	26.07 ± 3.44	2.48 ± 0.81	127.34 ± 2.84	3.44 ± 0.98	3.49 ± 1.00	500	0.93 ± 0.05	0.89 ± 0.11
VR3 (at least 1 b-tag)	$\mu\mu$	549.07 ± 32.38	44.16 ± 9.55	1.28 ± 0.49	276.65 ± 3.21	0.97 ± 1.56	4.86 ± 1.11	839	1.05 ± 0.04	0.93 ± 0.08
	ee	406.10 ± 31.48	33.89 ± 4.23	2.69 ± 0.84	216.70 ± 3.00	3.59 ± 0.98	5.18 ± 1.30	625	0.94 ± 0.04	0.90 ± 0.10

Table 6.6: The observed number of events as well as its expected composition in the Z+γ VRs. The errors include only the statistical uncertainty.

6.3.2 Fake-lepton background

For this type of background, the source of photons is prompt but one of the leptons is of non-prompt origin or is a fake lepton. Events with one prompt lepton and one fake lepton are determined with the help of a control region, defined in the same way as the signal region described in Section 6.2, except that the opposite-sign two leptons condition is replaced by a same-sign condition. The same MC samples described in Section 4.3 are used to estimate this background. Fake leptons are classified using truth

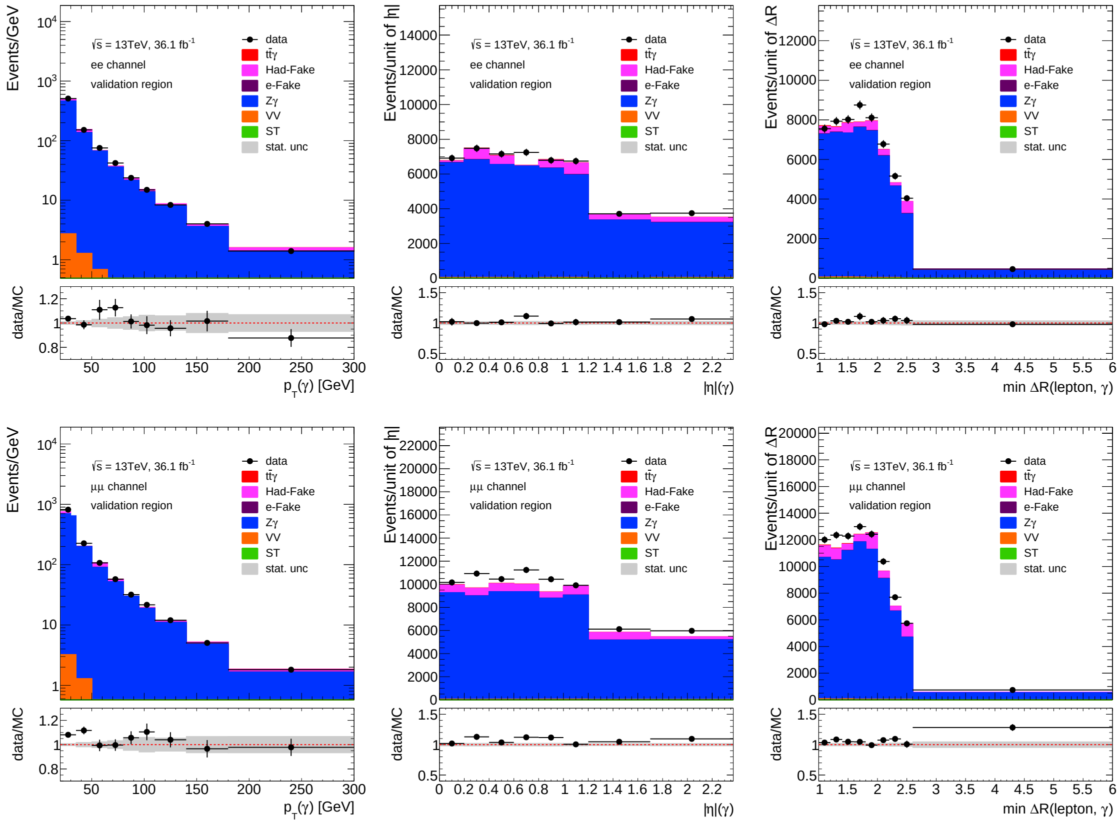

Figure 6.10: A selection of pre-fit distributions in the VR1, in the ee (top) channel and $\mu\mu$ (bottom) channel. Only statistical uncertainties are included.

information. Most leptons in the same-sign region are of prompt origin, as described in Table 6.7. Real leptons originating from the decay of a pion or a kaon, or fake leptons from misidentified objects contribute to a very small extent. The main process leading to the latter contribution is single-lepton $t\bar{t}$ with an extra fake lepton. The number of same-sign data events, after subtracting the expected prompt events, is used as an estimate of the fake-lepton background. The number is found to be small in the signal region, hence, this source of background is neglected.

Component	$e\mu$	ee	$\mu\mu$
Prompt lepton	5.8 ± 1.3	7.6 ± 1.5	0.1 ± 0.1
Heavy flavour	1.9 ± 1.0	$< 10^{-3}$	0.5 ± 0.4
Other	0.5 ± 0.3	$< 10^{-3}$	$< 10^{-3}$
Data	17	3	2

Table 6.7: The number of events in the same-sign region in data, and the expected number of events with two prompt leptons or events with at least one fake lepton estimated from simulation (Other), or at least one lepton of heavy flavour origin. The numbers are normalised to the total integrated luminosity of 36.1 fb^{-1}. Only statistical uncertainties are given.

6.4 Event yield in the signal region

The signal region is defined by imposing the requirements optimised in Section 6.3 and summarised in Table 6.4. A total of 902 events is observed in data, and 721 ± 7 expected $t\bar{t}\gamma$ events are estimated from simulation in the combined dilepton channels (referred as dilepton channel). The signal and background composition in the signal region is presented in Table 6.8 and shown in Figure 6.11. Additional distributions, broken down by channel, can be found in Appendix C. All backgrounds are estimated based on simulations as described in Section 6.3, except for the hadronic-fake background, which is scaled by a data-driven scale factor.

Process	$e\mu$	ee	$\mu\mu$	combined
$t\bar{t}\gamma$	401.47 ± 5.20	145.21 ± 2.97	173.95 ± 3.15	720.63 ± 6.77
hadronic fakes (Had-Fake)	25.64 ± 3.40	8.62 ± 1.75	9.29 ± 1.99	43.55 ± 6.29
$e \to \gamma$ fake (e-Fake)	1.07 ± 0.71	0.46 ± 0.27	0.24 ± 0.54	1.77 ± 0.93
$Z+\gamma$	0.52 ± 0.27	21.69 ± 3.85	53.73 ± 13.65	75.94 ± 14.10
single top + γ (ST)	6.72 ± 1.36	3.66 ± 1.18	2.64 ± 0.82	13.02 ± 1.98
diboson + γ (VV)	0.30 ± 0.22	0.56 ± 0.24	0.35 ± 0.22	0.76 ± 0.48
data	473	196	233	902

Table 6.8: The pre-fit event yields in the three dilepton channels. The combined yield is also presented. Only statistical uncertainties are shown.

6.5 Analysis strategy

6.5.1 Fiducial cross section

In order to measure the fiducial cross section given in Equation 4.13, a fiducial phase space is defined at particle level, which reflects both the acceptance of the ATLAS detector and the selections imposed on the reconstructed objects. The particle-level objects are defined in a very similar way as in the 8 TeV analysis (see Section 5.4.1). The definitions are summarised as follows:

- Leptons: The considered leptons are corrected to account for possible collinear soft photon emission: all photons not originating from a hadron decay and found within a $\Delta R < 0.1$ around the lepton, are combined to the lepton momentum. Those photons are then removed from further consideration. A transverse momentum larger than 25 GeV and $|\eta| < 2.5$ are required for the combined object.

- Jets: Jets are reconstructed with the anti-k_t algorithm with a radius parameter of $R = 0.4$. All stable particles ($\tau > 3 \times 10^{11}$ s), except for the above selected leptons and photons used to define the leptons, are considered in the jet clustering. Jets are required to have a $p_T > 25$ GeV and $|\eta| < 2.5$.

- b-jets: The particle-level jet is tagged as a b-jet by the "ghost matching" procedure [155, 156]: truth information are used to select B-hadrons with $p_T > 5$ GeV, the momenta of these hadrons are rescaled to infinitesimal values, and then the hadrons are introduced to the jet clustering algorithm. A clustered particle-level jet, which contains a rescaled B-hadron, is considered to be ghost-matched to a B-hadron and thus tagged as a b-jet.

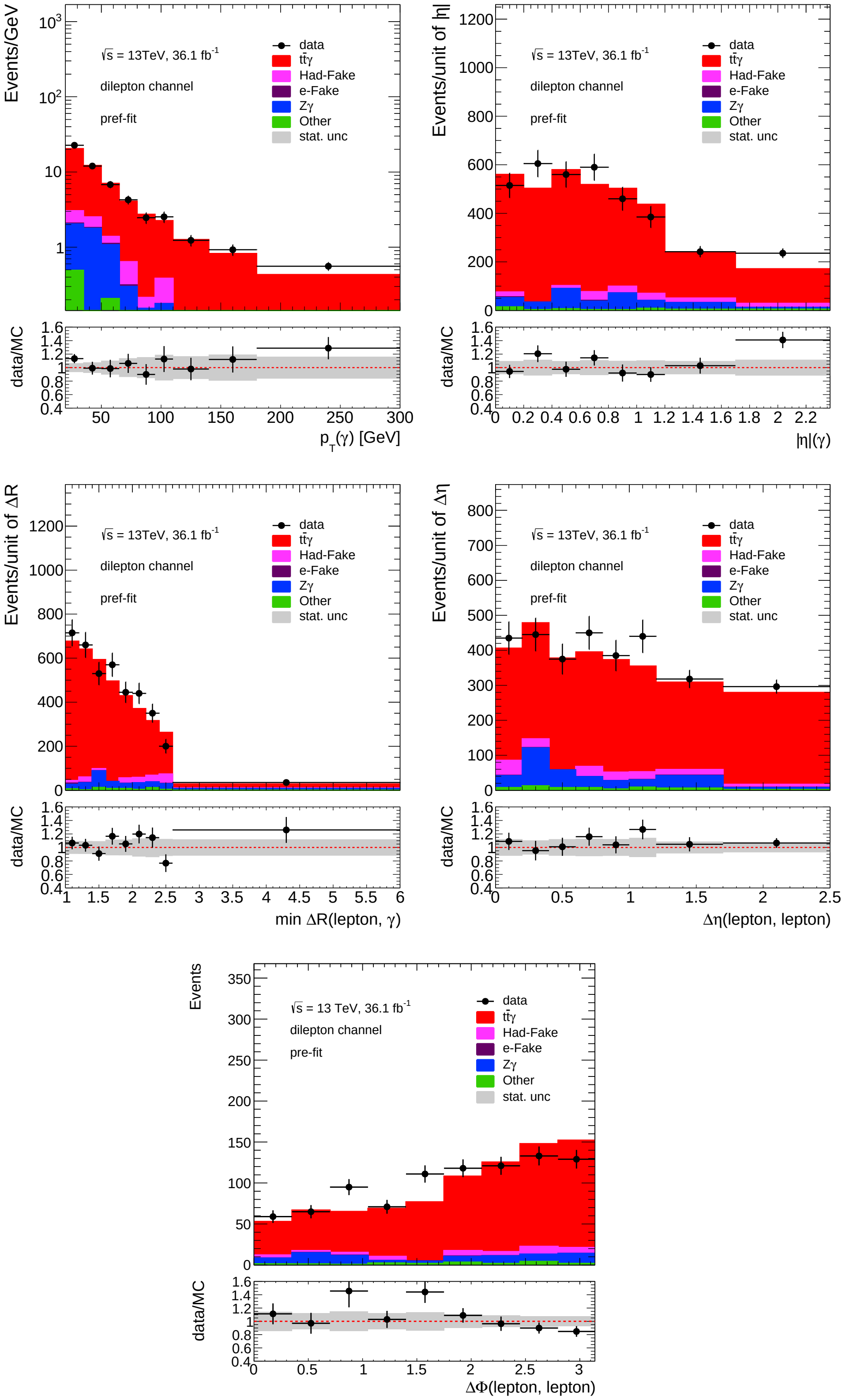

Figure 6.11: A selection of pre-fit distributions in the dilepton channel. All background processes are estimated based on simulations, as will be explained in Section 6.3. Only statistical uncertainties are shown.

- Photons: Photons are required not to originate from a hadron decay, to have $E_{\mathrm{T}} > 20$ GeV and $|\eta| < 2.37$ and to be isolated. The isolation is based on the ratio of the sum of the transverse momenta of all tracks, which are found around the photon in a cone of $\Delta R = 0.3$, to the photon p_{T} is less than 0.1.

In order to avoid double counting of objects, a jet is removed if found within a $\Delta R < 0.4$ around an electron, a muon, or an isolated photon.

The objects at particle level defined above are required to pass the event selections (at reconstruction level) of the signal region described in Section 6.2, except that the $E_{\mathrm{T}}^{\mathrm{miss}}$ and the invariant mass are removed, to have a common phase space between the same- and different-flavour channels. The signal acceptance and the correction factors, which are defined earlier in Equations 4.11 and 4.12, are summarised in Table 6.9.

Channel	Acceptance	Correction factor
$e\mu$	0.47	35.49 ± 0.46
ee	0.24	23.71 ± 0.50
$\mu\mu$	0.24	28.69 ± 0.53
Combined	0.96	30.81 ± 0.29

Table 6.9: The acceptance (due to selected phase space) and correction factor (due to reconstruction) in percentages (%) in the three dilepton channels [18]. Only statistical uncertainties are shown. The error in the acceptance is very small and thus is neglected.

The fiducial cross section is extracted by performing a likelihood fit to the data, employing an event level discriminator (ELD), described below. The likelihood function is defined in Equation 4.18. Therefore, the number of events appearing in that equation are estimated in the i-th bin of the ELD distribution in the j-th channel. The numbers of signal events in Equation 4.21 are re-written as follows:

$$N_{i,j}^{s} = L \cdot \sigma_i \cdot C_i \cdot f_{i,j}^{\mathrm{ELD}}, \tag{6.8}$$

where $f_{i,j}^{\mathrm{ELD}}$ is the fraction of events falling in bin i of the ELD discriminant in the channel j.

The ELD takes the form of a neural network (NN). The NN's architecture is developed and trained using Keras [157] with reconstruction and application of the NN using the LightWeight Neural Network library (or LWTNN) [158]. The training of the NN uses the same samples introduced in Section 4.3, and event selections described in Section 6.2, except that the two jets, the $E_{\mathrm{T}}^{\mathrm{miss}}$ and the invariant mass windows requirements are removed, in order to enhance the amount of events and provide more stable training results. The NN is trained for the combined dilepton channels, using several event variables including: the missing transverse momentum, the number of b-tagged jets, the jet p_{T}, the b-tagging weights, and the minimum distance between the photon and leptons. The input variables are ranked according to their signal-background separation power in Table 6.10. The separation power is defined in the following equation:

$$\mathcal{S} = \frac{1}{2} \sum_{i \in \mathrm{bins}} \frac{(s_i - b_i)^2}{(s_i + b_i)}, \tag{6.9}$$

where s_i and b_i are the number of signal and background events in bin i of the input variable, respectively.

The seven input variables in Table 6.10 are used to construct the output of the NN, in the form of an ELD distribution. The modelling of the inputs is shown in Appendix C. The ELD is used to perform the binned maximum-likelihood fit. The pre- and post-fit distributions of the ELD are shown in Figure 6.12. The contributions from single-top and diboson productions are combined under the category "Other", due to their small importance. Additional post-fit distributions, and the post-fit event yields are presented in Section 6.8.

Variable	Separation(%)
second highest MV2c10 b-tagging weight	13.6
minimum $\Delta R(\ell, \gamma)$	13.4
$E_{\mathrm{T}}^{\mathrm{miss}}$	12.8
p_{T} of leading jet	11.4
number of b-jets	11.0
highest MV2c10 b-tagging weight	10.5
p_{T} of sub-leading jet	7.72

Table 6.10: List of input variables used in the neural network, sorted by separation power.

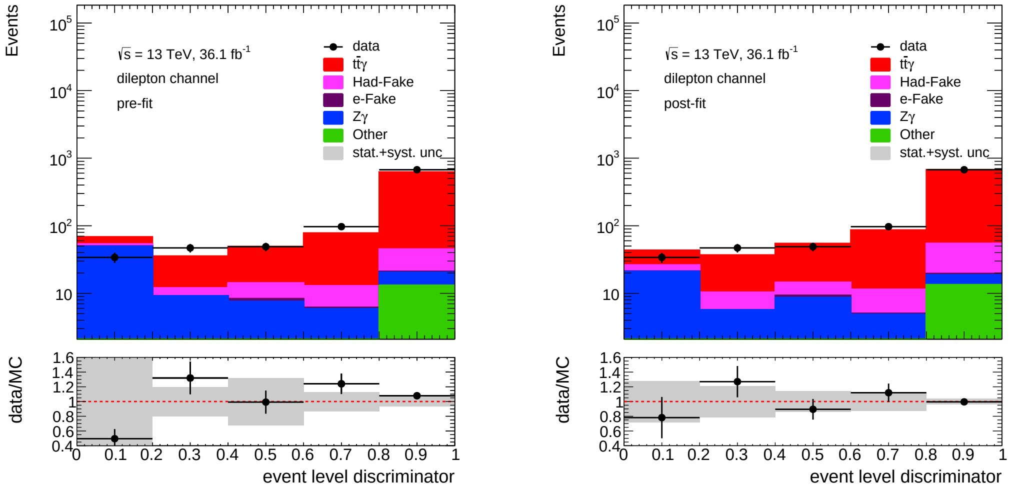

Figure 6.12: The pre-fit (left) and post-fit (right) distributions of the ELD variable in the dilepton channel. The statistical and systematic uncertainties (described in Section 6.7) are shown.

6.5.2 Differential cross section

The differential cross section is measured in bins of photon p_{T}, photon $|\eta|$, minimum distance between the photon and leptons (min $\Delta R(\ell, \gamma)$), η and ϕ differences between the two leptons ($\Delta\eta(\ell, \ell)$, $\Delta\phi(\ell, \ell)$). The different- and same-flavour channels are combined in order to increase the amount of events in the low populated region of the signal distributions. These distributions are obtained from the background-subtracted data distributions, after performing the likelihood fit. The signal distributions are corrected to account for the geometric acceptance of the detector, trigger and reconstruction efficiencies, and for the distribution distortions due to the finite resolution. The correction procedure, which is called unfolding, will be described in Section 6.6. In order to perform the correction, a mapping between the simulation of the physics events and the simulation of the reconstructed events in the detector is required. The mapping, a so-called migration matrix, is constructed using events at particle level which are selected in the previous Section 6.5.1, and events at reconstruction level which are selected in the signal region in Section 6.2. The diagonal of the matrix represents the probability that for each particle-level object within a bin, a reconstructed object exists and falls into the same bin. The particle-level and reconstructed-level objects are defined in Section 6.5.1 and Section 4.4, respectively.

The migration matrices are built from the $t\bar{t}\gamma$ simulation. The binning of the migration matrix is chosen to minimise the signal statistical fluctuation. The choice of binning is made such that the maximum uncertainty in the expected signal is not larger than 20% in each bin of the reconstructed distribution. Moreover, a binning satisfying the above requirement is preferred if rather diagonal migration matrices can be reconstructed. The list of bin borders for photon p_{T} (in GeV) are: {20 – 25 – 35 – 50 – 65 – 80 – 95 – 110 – 140 – 180 – 300]}, for photon $|\eta|$: {0.0 – 0.2 – 0.4 – 0.6 – 0.8 – 1.0 – 1.2 – 1.7 – 2.37}, minimum $\Delta R(\ell, \gamma)$: {1.0 – 1.2 – 1.4 – 1.6 – 1.8 – 2.0 – 2.2 – 2.4 – 2.6 – 6}, $\Delta\eta(\ell, \ell)$: {0 – 0.2 – 0.4 – 0.6 – 0.8 – 1.0 – 1.2 – 1.7 – 2.5}, and for $\Delta\phi(\ell, \ell)$: {0.0 – 0.35 – 0.70 – 1.05 – 1.40 – 1.75 – 2.10 – 2.45 – 3.14}. The statistical uncertainty as a function of the above variables is shown in Figure 6.13, and the bin-by-bin migration matrices are shown in Figure 6.14.

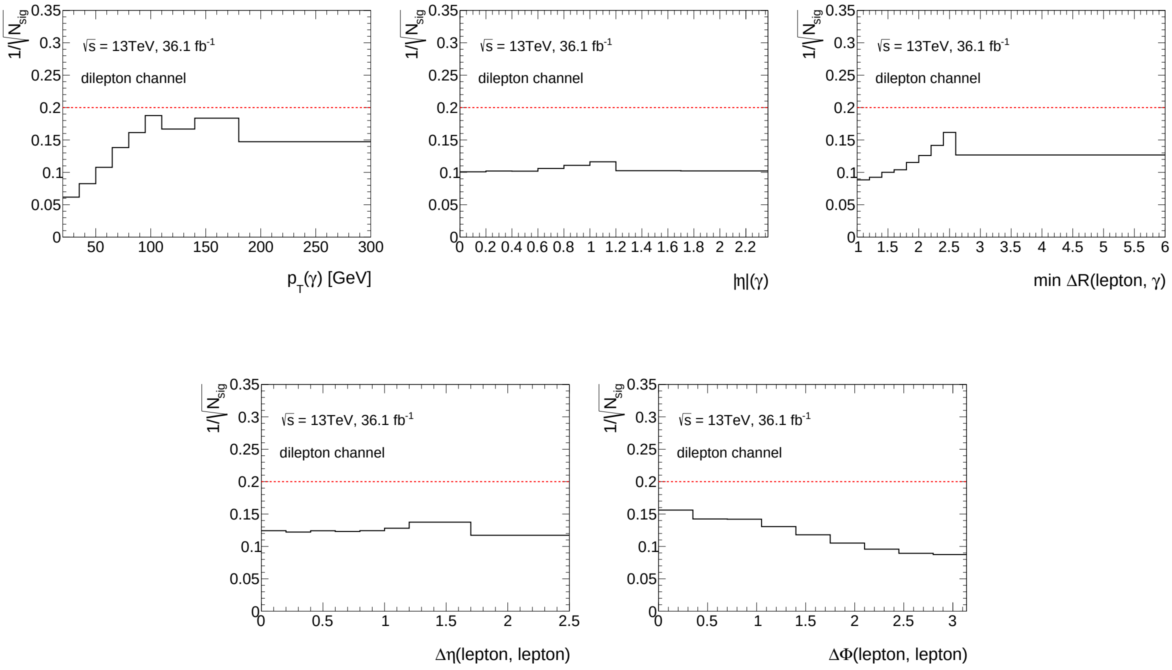

Figure 6.13: The expected signal statistical uncertainty as a function of the photon p_{T} (top-left), the photon $|\eta|$ (top-centre), the minimum $\Delta R(\ell, \gamma)$ (top-right), $\Delta\eta(\ell, \ell)$ (bottom-left) and $\Delta\phi(\ell, \ell)$ (bottom-right), in the dilepton channel. The red line indicates the 20% statistical uncertainty.

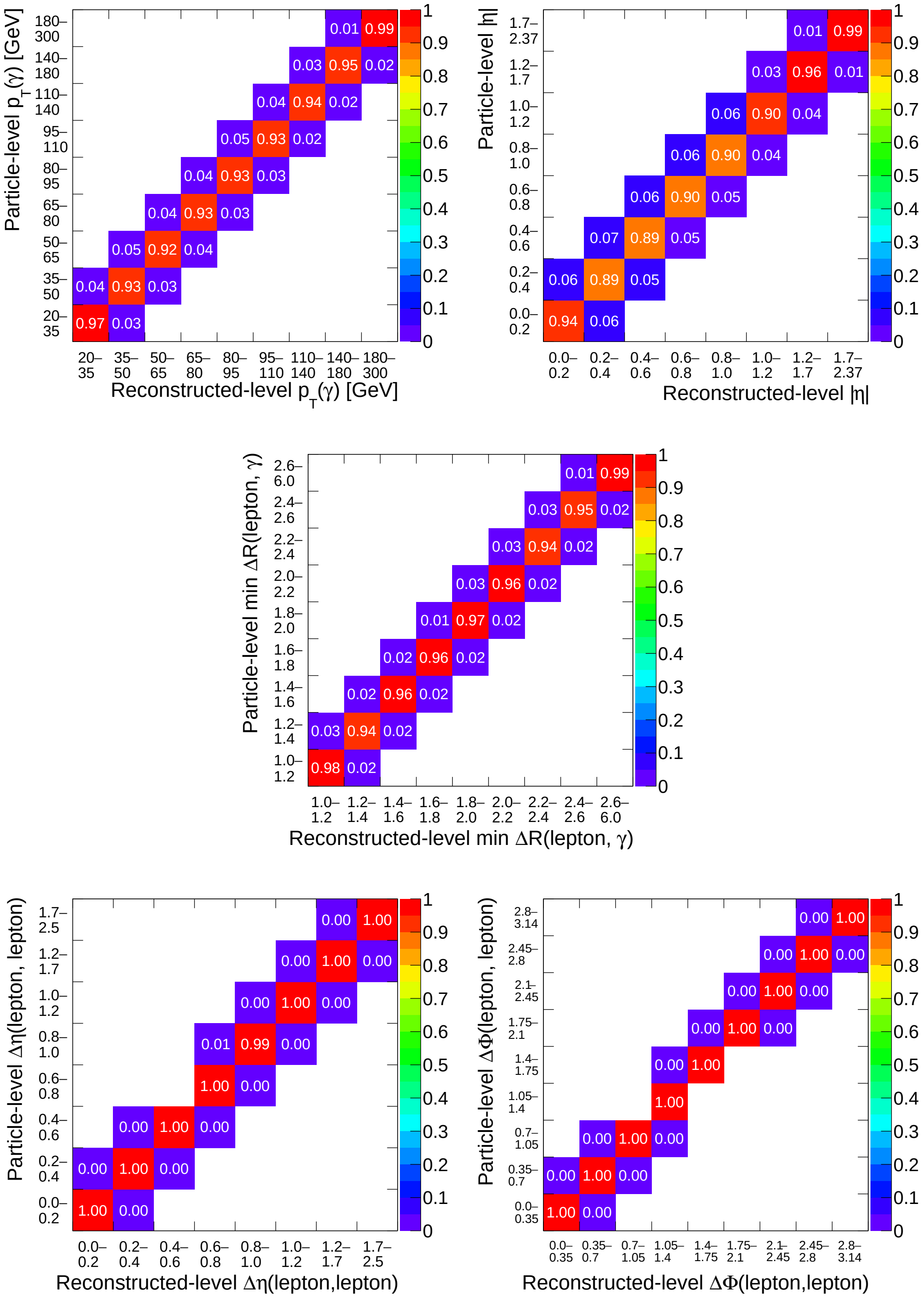

Figure 6.14: The bin-by-bin migration matrix in the photon p_{T} (top-left), the photon $|\eta|$ (top-right), the minimum $\Delta R(\ell,\gamma)$ (centre), $\Delta\eta(\ell,\ell)$ (bottom-left) and $\Delta\phi(\ell,\ell)$ (bottom-right), in the dilepton channel.

To measure the differential cross section, the number of signal events in data is required to be estimated. The number is obtained using the following:

$$N_{\mathrm{sig},j} = N_{\mathrm{data},j} - N_{\mathrm{bkgs},j}, \tag{6.10}$$

where $N_{\mathrm{data,j}}$ and $N_{\mathrm{bkgs},j}$ are the number of selected data and background events in the j-th bin of the spectrum at reconstruction level. The corrected observed spectrum due to possible migration from outside the fiducial region, $N^{\mathrm{corr}}_{\mathrm{sig},j}$, is written as

$$N^{\mathrm{corr}}_{\mathrm{sig},j} = (N_{\mathrm{data},j} - N_{\mathrm{bkgs},j}) \times (1 - f_{\mathrm{mig},j}), \tag{6.11}$$

where $f_{\mathrm{mig},j}$ (defined inclusively in Equation 4.10) is the fraction of signal events migrating from outside the fiducial region into the bin j of the reconstructed distribution. For example, events generated with a true photon $p_{\mathrm{T}} < 20$ GeV can be reconstructed with a $p_{\mathrm{T}} > 20$ GeV due to the detector resolution:

$$f_{\mathrm{mig},j} = \frac{N^{\text{non-fid},j}_{\mathrm{reco},j}}{N_{\mathrm{reco},j}}. \tag{6.12}$$

The differential cross section σ^{diff}_k is related to the observed spectrum by

$$N_{\mathrm{sig},j} = \frac{1}{1 - f_{\mathrm{mig},j}} \times \sum_k (L \times \sigma^{\mathrm{diff}}_k \times \epsilon_k \times M_{kj}), \tag{6.13}$$

where k is the bin index of the observable at particle level (truth), M_{kj} is the bin-by-bin migration matrix, representing the probability of signal events generated in bin k of the truth distribution but observed in bin j of the reconstructed distribution.

By solving Equation 6.13 and using Equation 6.10, the differential cross section can be expressed as

$$\sigma^{\mathrm{diff}}_k = \frac{1}{L} \times \frac{1}{\epsilon_k} \times \sum_j M^{-1}_{jk} \times (N_{\mathrm{data},j} - N_{\mathrm{bkgs},j}) \times (1 - f_{\mathrm{mig},j}), \tag{6.14}$$

where M^{-1}_{jk} is the inversion of the bin-by-bin migration matrix. The inversion is obtained by the iterative Bayesian method (see Section 6.6). The efficiencies of reconstructing and identifying objects used in the analysis are described by ϵ_k, which is the efficiency of signal events generated in bin k of the truth distribution to be reconstructed and selected. The efficiency is defined earlier in Equation 4.9 and can be expressed differentially as

$$\epsilon_k = \frac{N^{\mathrm{fid},k}_{\mathrm{reco},k}}{N^{\mathrm{fid},k}_{\mathrm{gen}}}. \tag{6.15}$$

The efficiency corrected truth spectrum is given by

$$N^{\mathrm{corr}}_{\mathrm{gen},k} = \sum_j M^{-1}_{jk} \times N^{\mathrm{corr}}_{\mathrm{sig},j}. \tag{6.16}$$

From the above equation, the differential cross-section measurement is reduced to the problem of converting the corrected observed spectrum $N^{\mathrm{corr}}_{\mathrm{sig},j}$ to the corrected truth spectrum $N^{\mathrm{corr}}_{\mathrm{gen},k}$ with the inverted migration matrix M^{-1}_{jk}. The inputs to Equation 6.14: $(1 - f_{\mathrm{mig,j}})$ and the inverse of ϵ_k are shown in Figure 6.15.

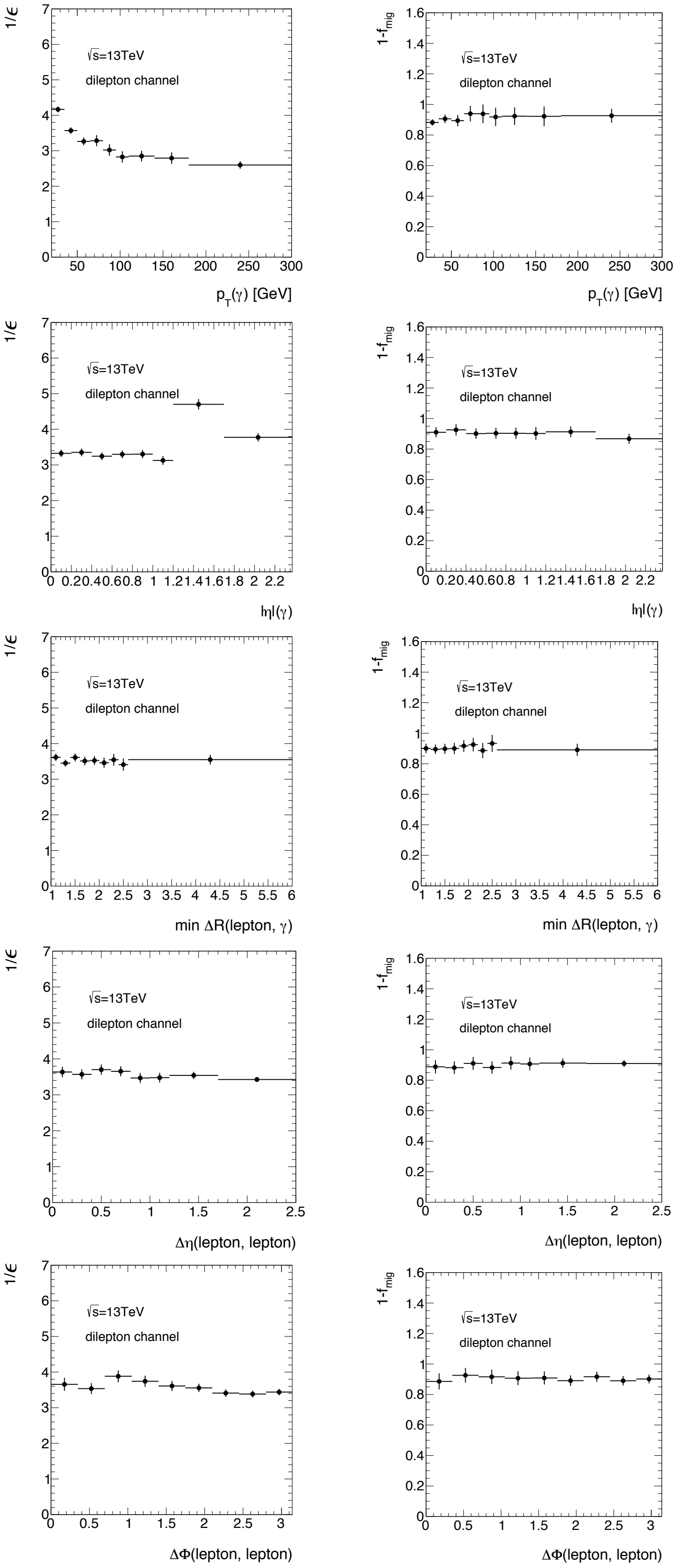

Figure 6.15: The inverse of signal efficiency $1/\epsilon$ (left) and the fraction of non-outside migration ($1 - f_{\text{mig}}$) (right) as a function of the photon p_{T} (first row), the photon $|\eta|$ (second row), the minimum $\Delta R(\ell, \gamma)$ (third row), the $\Delta\eta(\ell, \ell)$ (fourth row) and the $\Delta\phi(\ell, \ell)$ (fifth row), in the dilepton channel.

6.6 Unfolding

The procedure of retrieving the truth spectrum of an observable from the measured spectrum is called unfolding [159, 160]. Here, the measured spectrum is unfolded to the particle level. The unfolding is performed in order to correct for the detector effects due to limited resolution and acceptance; this enables the measured distributions to be compared to the prediction of an existing theory, or to a new theory yet to be developed. Unfolding also enables the comparison with other experiments which could have different migration matrices.

The main difficulty of unfolding is the inversion of the migration matrix, as already mentioned in Section 6.5.2. To invert the migration matrix, various methods have been developed. In this analysis, the iterative Bayesian method (IBS) proposed by D'Agostini [161] is applied, and compared to two other methods: the singular value decomposition (SVD) [162] and the bin-by-bin correction approaches [160], both of them are used as cross-checks. All these methods are implemented in the RooUnfold package [163]. For each of the unfolding methods, the same inputs are used: efficiency, fraction of outside migration, and the bin-by-bin migration matrix, introduced in Section 6.5.2.

Additional information is usually added, in order to regularise the unfolding procedure and to avoid large statistical fluctuations. In the iterative Bayesian method, the additional information appears as a prior information of the bin content. This information is updated after each iteration, as will be described in the following. Concepts of cause and effect from the Bayesian statistics are introduced to invert the migration matrix. The migration matrix can be expressed as

$$M_{kj} = P(E_j|C_k), \tag{6.17}$$

where E means effect, corresponding to the measured values and C means cause, corresponding to the true values. $P(E_j|C_k)$ is the probability to observe an effect in bin j, given a cause in bin k. Its inversion M^{-1}_{jk} is written as

$$M^{-1}_{jk} = P(C_k|E_j), \tag{6.18}$$

which represents the probability for a cause in bin k, given the observation of an effect in bin j. According to Bayes' theorem, $P(C_k|E_j)$ can be written as follows:

$$P(C_k|E_j) = \frac{P(E_j|C_k) \cdot P_0(C_k)}{\sum_l^{n_C} P(E_j|C_l) \cdot P_0(C_l)}, \tag{6.19}$$

where $P_0(C_l)$ is the prior truth distribution, which is obtained from the signal simulation, $P_0(C_k)$ is the new prior distribution gained by the iterative procedure, n_C and l are the number of bins and the bin index of the prior truth distribution, respectively. For the first iteration, the two prior distributions are equivalent and correspond to the first truth distribution from the signal simulation.

Unfolding starts by inverting the migration matrix using the truth distribution as a prior, to derive an unfolded distribution. For the next iteration, the unfolded distribution (from the previous iteration) is used as a prior and the migration matrix is inverted to derive a new unfolded distribution. The procedure is repeated until the unfolded distribution converges to the truth distribution. However, a larger number of iterations does not necessarily mean a better convergence, since the unfolding procedure is affected by the statistical uncertainties of the migration matrix. The number of iterations is chosen based on two criteria that will be described in Section 6.6.2. When the iteration stops, the differential cross section can be derived by solving Equation 6.14.

6.6.1 Pseudo-data

A number of checks are needed in order to confirm that the unfolding procedure is not biased. For this, the bin choice, the number of iterations, and the specific choice of the simulation sample which is used to obtain the truth spectrum are varied. These checks are performed with the help of pseudo-data, where the measured spectrum is replaced by the pseudo-data to be unfolded. The pseudo-data is generated by randomly sampling the $t\bar{t}\gamma$ simulated events into two parts: testing and training. The sampling ensures that an equivalent statistical power of the expected number of observed events is achieved. The training part is used to build the migration matrix, while the testing part is used for unfolding. In total, 100 pseudo-datasets with different random sampling are generated. Sections 6.6.2, 6.6.3 and 6.6.4 are using the same pseudo-datasets.

6.6.2 Optimisation of the number of iterations

The choice of the number of iterations is a compromise between two goals: the first is to have a small difference in all bins between the unfolded results obtained when using different number of iterations (the convergence speed of unfolded results). The second goal is to have a statistical uncertainty which does not change from one iteration to another in a given bin, with no expected bias against any number of iterations (the RMS test).

For the first goal, the migration matrix is built from the training part of the 100 pseudo-datasets described above, whereas the testing part is used to generate another 1000 pseudo-datasets using a Poisson distribution from the reconstructed distribution. This new pseudo-data is unfolded. The number of pseudo-unfolded events in one bin after the next iteration $i + 1$ is compared to the previous number of unfolded events estimated after a given iteration i. The relative difference between the two numbers is calculated and plotted in bins of the photon's variable. The chosen convergence speed requirement consists in requesting a number of iterations that provides a low relative difference, less than 1% in all bins:

$$\frac{N^{\text{unf, i+1}} - N^{\text{unf, i}}}{N^{\text{unf, i+1}}} < 1\%. \tag{6.20}$$

The result of the test is shown in Figure 6.16. From the figure, any number of iterations is enough to have a difference of $< 1\%$ for the $\Delta\phi(\ell,\ell)$, at least two iterations are needed for the three variables, the photon $|\eta|$, the minimum $\Delta R(\ell,\gamma)$ and the $\Delta\eta(\ell,\ell)$, and at least three iterations are needed to have that difference for the photon p_{T}. The number of iterations, which will be used for all variables, will be determined after considering the RMS test.

For the RMS test, the statistical uncertainty on the unfolded pseudo-data is checked. The 100 pseudo-datasets described in Section 6.6.1 are used: the training pseudo-data is used to build the migration matrix, while the pseudo-data of the testing part at reconstruction level is unfolded. The quantity

$$\text{RMS} = \frac{(\text{truth} - \text{unfolded})}{\text{unfolded}} \tag{6.21}$$

is calculated to compare the unfolded reconstruction-level distribution to the pseudo particle-level distribution. The RMS is estimated per bin after each iteration i in the range $1 \leq i \leq 20$. For example, a variable represented by 9 bins, will have 180 different RMS distributions of the 100 pseudo-datasets. Each distribution is fit by a Gaussian function (see e.g. in Appendix D), with a mean value expected to be zero. The mean value of the RMS is shown, in a given bin, as a function of the number of iterations in Figures 6.17 – 6.21 for the photon p_{T}, $|\eta|$, minimum $\Delta R(\ell,\gamma)$, $\Delta\eta(\ell,\ell)$ and $\Delta\phi(\ell,\ell)$, respectively. In the

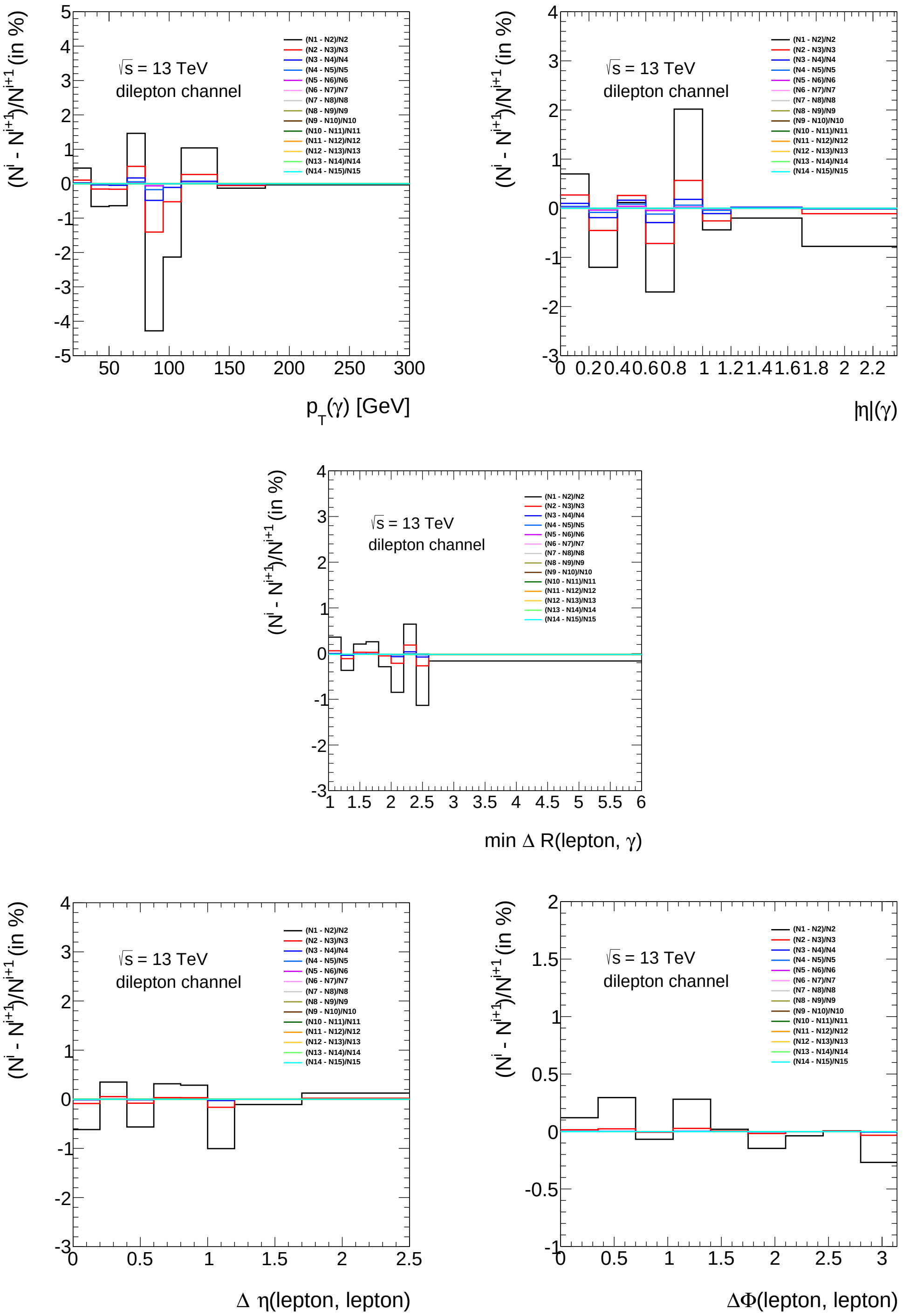

Figure 6.16: The relative difference of the unfolded result between two successive iterations as a function of the photon p_{T} (top-left), the photon $|\eta|$ (top-right), the minimum $\Delta R(\ell, \gamma)$ (centre), the $\Delta\eta(\ell, \ell)$ (bottom-left), and the $\Delta\phi(\ell, \ell)$ (bottom-right), in the dilepton channel.

figures, it can be observed that most of the bins are not biased against any number of iterations, and all bins have a stable statistical uncertainty after one or two iterations.

As both goals are achieved after two or three iterations, three iterations are chosen for the following checks and the final results.

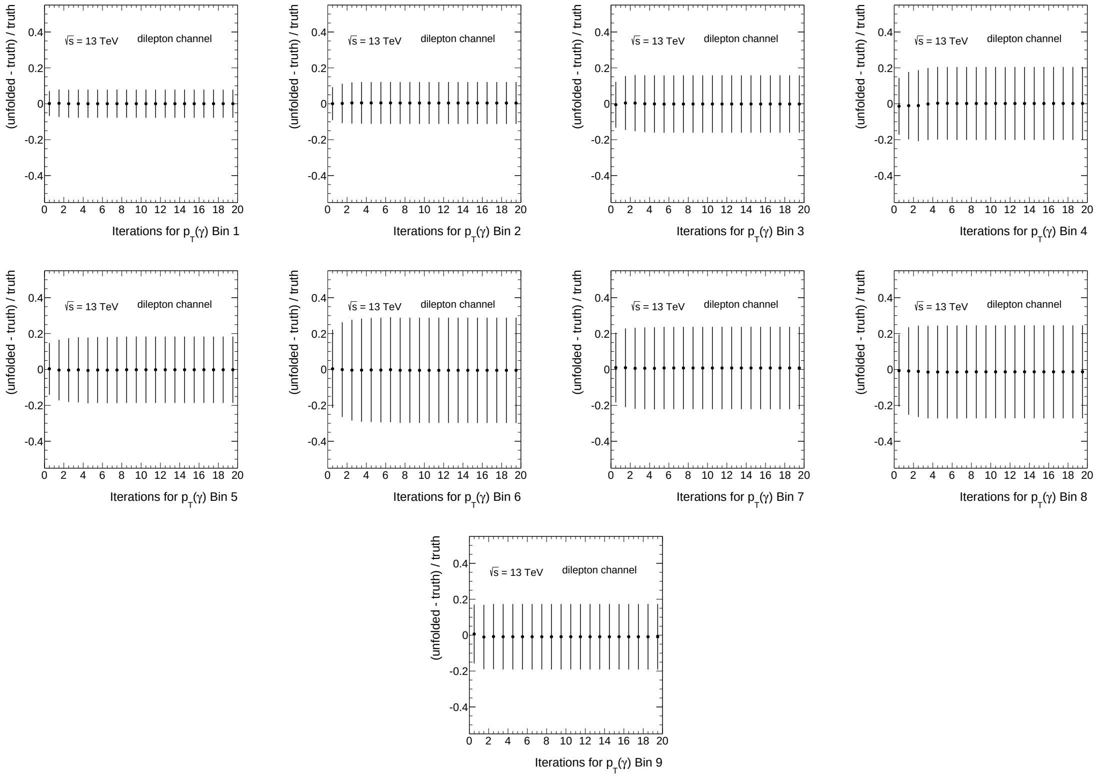

Figure 6.17: RMS as a function of the number of iterations for the 9 bins in photon p_{T}, in the dilepton channel.

6.6.3 Closure test

The closure test is performed to check whether the unfolding procedure can recover the truth spectrum. The 100 pseudo-data distributions of the testing part at reconstruction level are unfolded using the migration matrix built from the training part. The unfolded results are then compared to the particle level from the training part. A perfect closure is observed, as can be seen in Figure 6.22.

6.6.4 Pull test

The binning is initially chosen to have rather diagonal matrices, with low expected statistical uncertainty per bin, as explained in Section 6.5.2. The stability of the bin choice is checked by performing the so-called pull test. The same pseudo-data described in Section 6.6.1 is used and another 1000 pseudo-experiments are built from the reconstruction level in the testing part using the Poisson distribution, and unfolded. The unfolded pseudo-results are then compared to the pseudo particle-level distributions, and pulls are calculated per bin as

$$\text{Pull} = \frac{(\text{truth} - \text{unfolded})}{\sigma_{\text{unfold}}}, \tag{6.22}$$

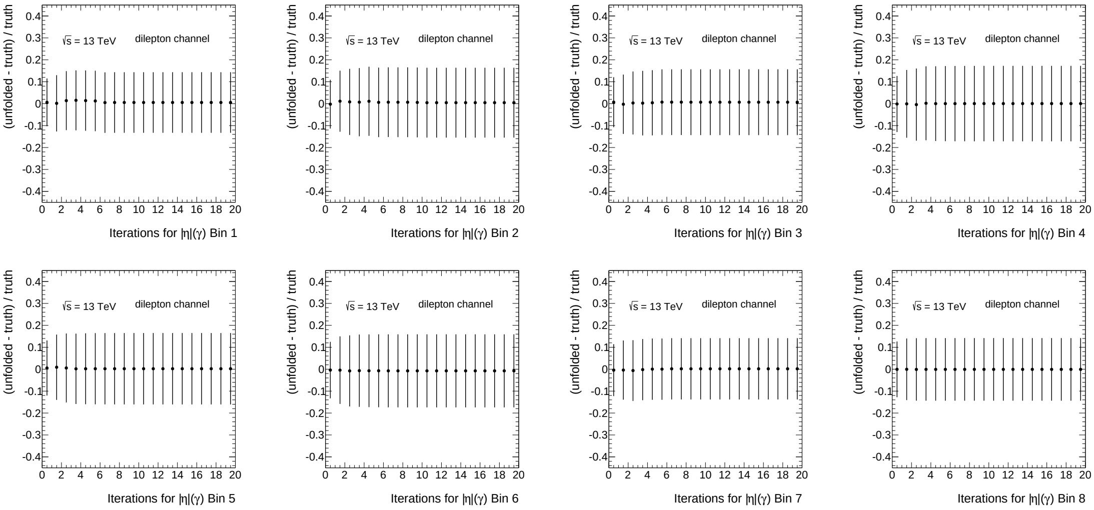

Figure 6.18: RMS as a function of the number of iterations for the 8 bins in photon $|\eta|$, in the dilepton channel.

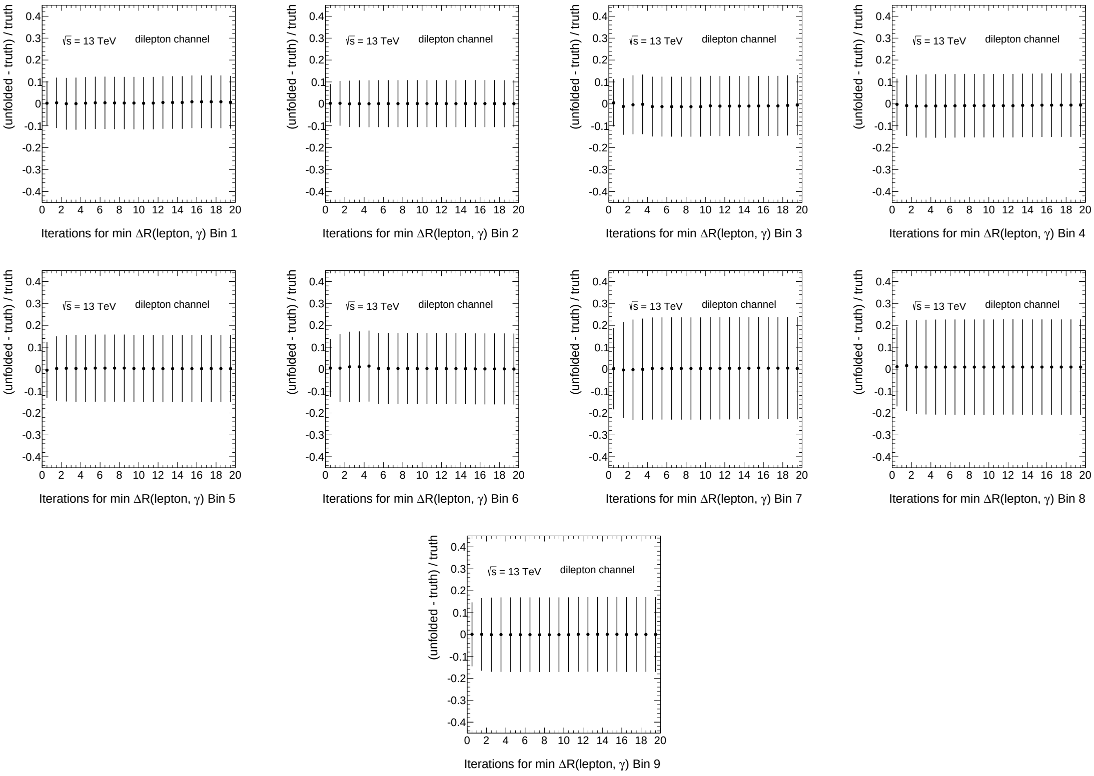

Figure 6.19: RMS as a function of the number of iterations for the 9 bins in minimum $\Delta R(\ell, \gamma)$ in the dilepton channel.

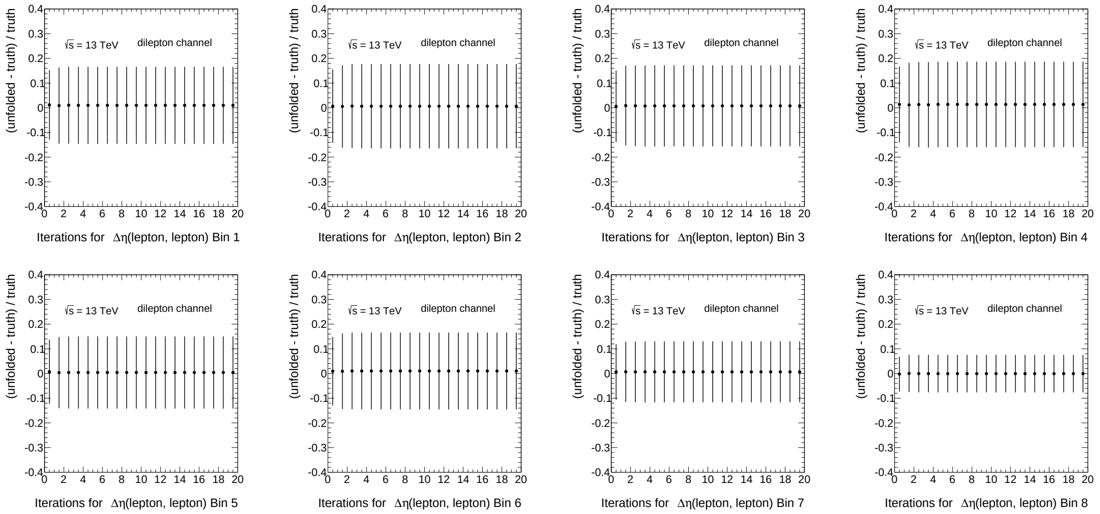

Figure 6.20: RMS as a function of the number of iterations for the 8 bins in $\Delta\eta(\ell, \ell)$ in the dilepton channel.

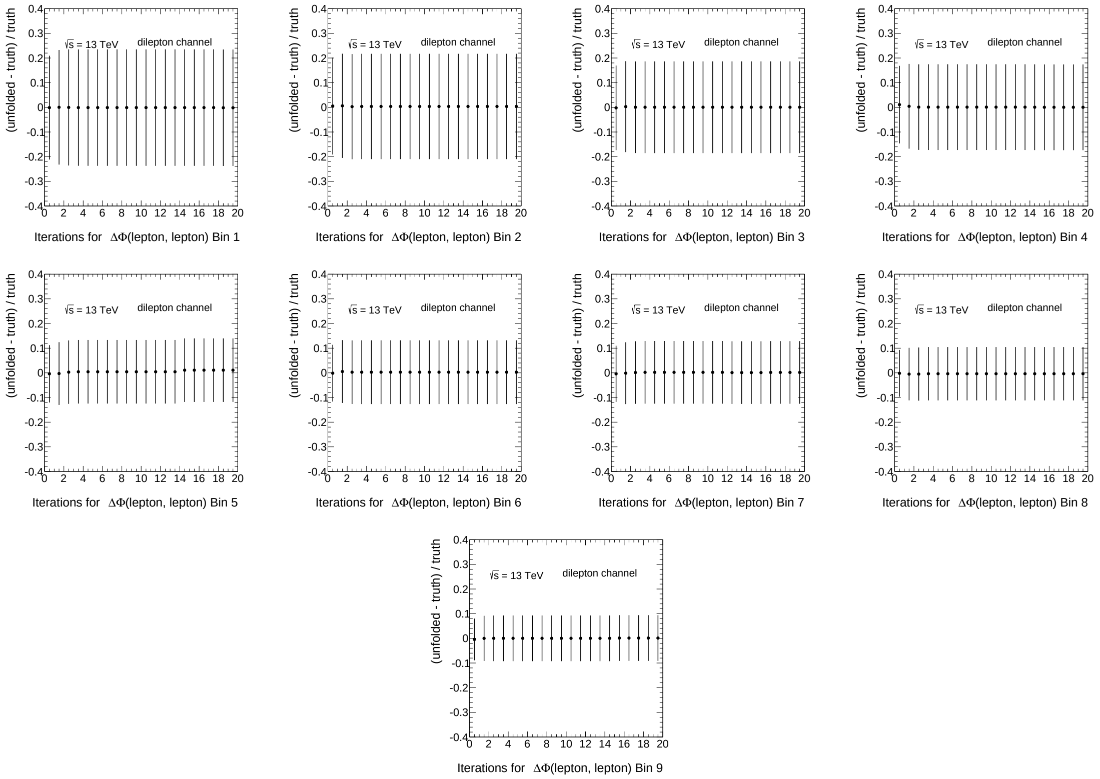

Figure 6.21: RMS as a function of the number of iterations for the 9 bins in $\Delta\phi(\ell, \ell)$ in the dilepton channel.

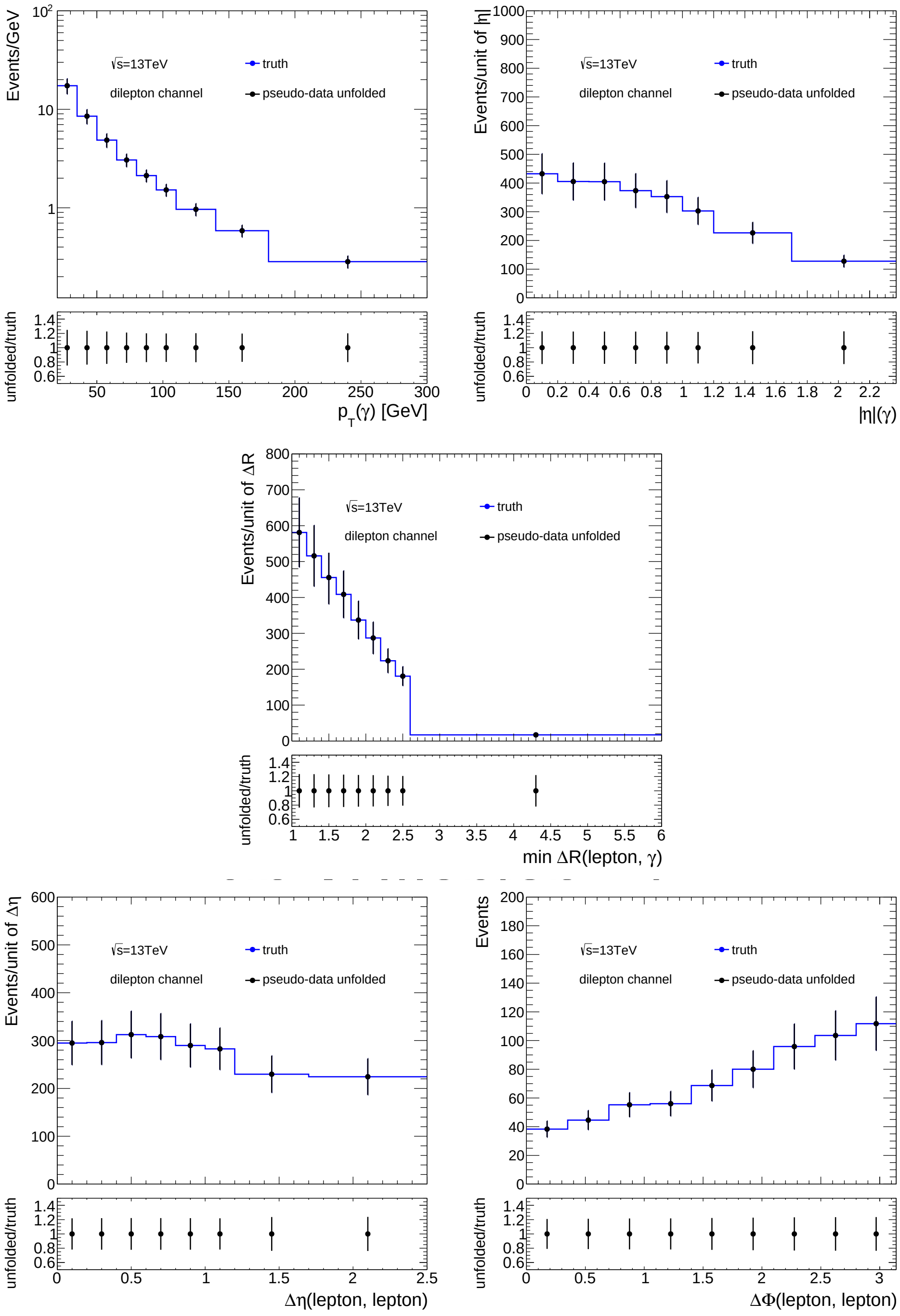

Figure 6.22: The distribution of the unfolded pseudo-data after three iterations (black) compared to the truth distribution (blue), as a function of the photon p_{T} (top-left), the photon $|\eta|$ (top-right), the minimum $\Delta R(\ell, \gamma)$ (centre), the $\Delta\eta(\ell, \ell)$ (bottom-left), and the $\Delta\phi(\ell, \ell)$ (bottom-right), in the dilepton channel.

where σ_{unfold} is the statistical uncertainty on the unfolded results. The pull is fit by a Gaussian function (see Appendix E). It is expected to have a mean value of zero, which indicates no bias, and a width of one, as an indication that the statistical uncertainty is estimated correctly. The pull distributions are shown in Figure 6.23. The figure shows no bias in the bin choice, and the width is consistent with one.

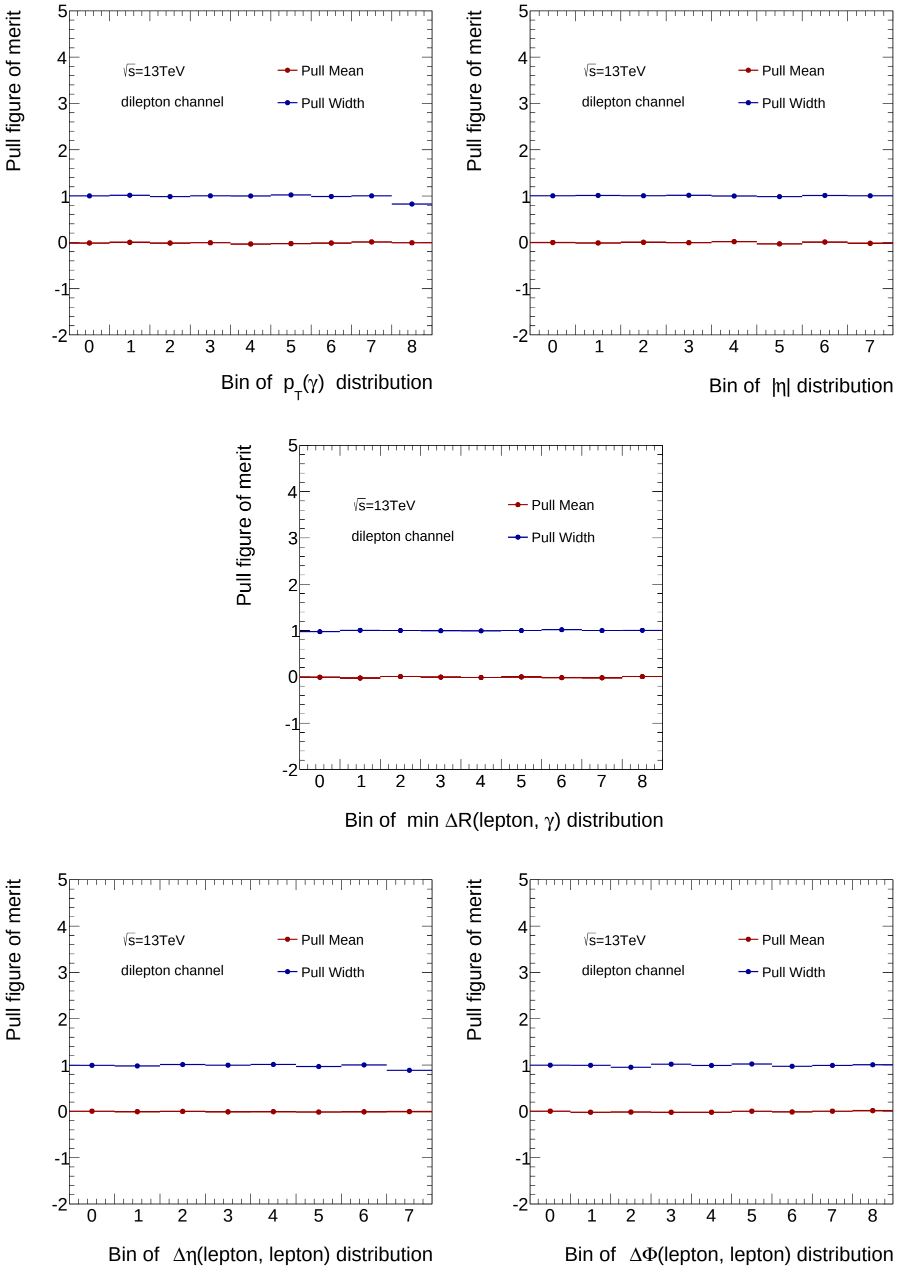

Figure 6.23: The pull test in each bin of photon p_{T} (top-left), photon $|\eta|$ (top-right), minimum $\Delta R(\ell, \gamma)$ (centre), $\Delta\eta(\ell, \ell)$ (bottom-left), and $\Delta\phi(\ell, \ell)$ (bottom-right), in the dilepton channel.

6.6.5 Stress test

A "stress test" is performed in order to verify that the unfolding procedure is not biased to any specific choice of particle-level distributions. In other words, to confirm that the unfolding is able to retrieve any truth distribution if the corresponding reconstructed distribution is unfolded using the nominal migration matrix. The particle-level and reconstruction-level distributions obtained from the nominal sample are reweighted. The reweighted distribution is then unfolded using the nominal inputs from the simulated sample. The unfolded results are compared to the corresponding particle-level distributions. Two different methods to generate weights that modify the shape are used. The first method is based on the observed difference in data with respect to simulation, and corresponds to an up and down variation corresponding to this difference, using $Y = 1$ and $Y = -1$ respectively in the following equation:

$$\text{weight} = 1 + Y \cdot \frac{\text{data}_i - \text{MC}_i}{\text{data}_i} = 1 + Y \cdot \text{Obs}, \tag{6.23}$$

where i refers to the bin index.

The second method corresponds to a linear skewness of the shape. It is given by Equations 6.24 – 6.28. For the photon p_{T}, the photon $|\eta|$, the minimum $\Delta R(\ell, \gamma)$, the $\Delta\eta(\ell, \ell)$, and the $\Delta\phi(\ell, \ell)$, this corresponds to:

$$\text{weight} = 1 + Y \cdot \frac{100 - i_{p_{\text{T}}}(\text{GeV})}{300} = 1 + Y \cdot X, \tag{6.24}$$

$$\text{weight} = 1 + Y \cdot \frac{1.2 - i_{|\eta|}}{2.37} = 1 + Y \cdot X, \tag{6.25}$$

$$\text{weight} = 1 + Y \cdot \frac{1.8 - i_{\Delta R}}{6.0} = 1 + Y \cdot X, \tag{6.26}$$

$$\text{weight} = 1 + Y \cdot \frac{1.2 - i_{\Delta\eta}}{2.5} = 1 + Y \cdot X, \tag{6.27}$$

$$\text{weight} = 1 + Y \cdot \frac{1.75 - i_{\Delta\phi}}{3.14} = 1 + Y \cdot X, \tag{6.28}$$

where Y can be 1, or -1, corresponding to a positive or negative slope, and i is the bin centre. Numbers in the denominator are set to match the upper boundary of the last bin in each distribution, while numbers in the numerator are the starting point of the slope variation, and chosen to be as close as possible to the centre of each variable range.

The results of the two tests are shown in Figure 6.24. The results confirm that the unfolding procedure is able to unfold a modified shape to the correct particle-level shape.

6.6.6 Alternative unfolding methods

Two different unfolding methods, described below, are compared to the iterative Bayesian method: the bin-by-bin and the singular value decomposition approaches.

Bin-by-bin correction method

This method is based on extracting a bin-by-bin correction factor from simulation. The correlation between bins is neglected in this method, thus it is a good approximation only when the bin-to-bin

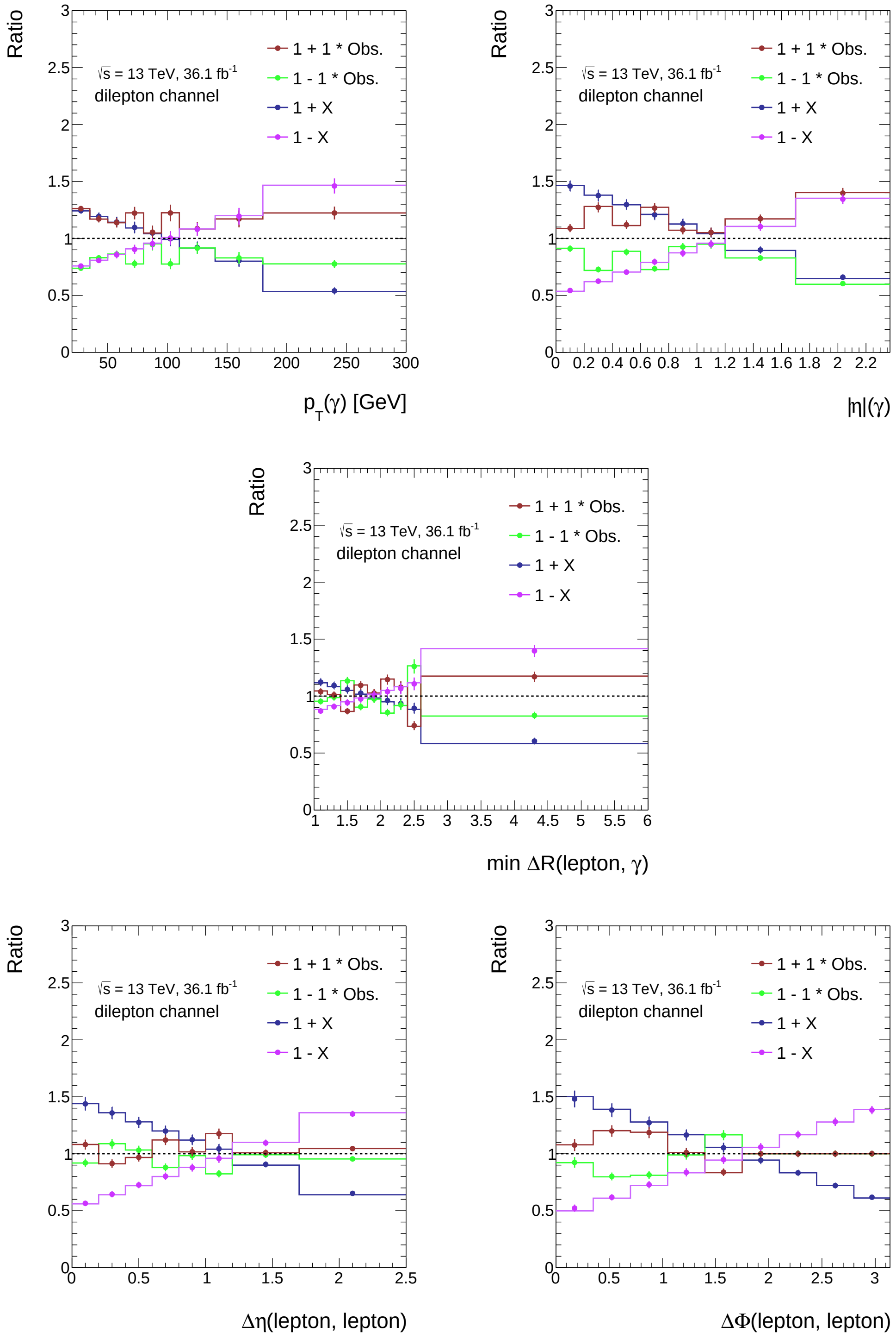

Figure 6.24: The stress test for the photon p_{T} (top-left), the photon $|\eta|$ (top-right), the minimum $\Delta R(\ell, \gamma)$ (centre), the $\Delta\eta(\ell, \ell)$ (bottom-left), and the $\Delta\phi(\ell, \ell)$ (bottom-right), in the dilepton channel. Both, dots and lines, are ratios with respect to the nominal particle level. The dots are the ratio of the unfolded reweighted distributions to the nominal particle-level distribution, while the solid lines are the ratio of the reweighted particle-level distributions to the nominal one. Obs. is defined in Equation 6.23, and X in Equations 6.24 – 6.28.

migration is very small. In this analysis, the bin-bin migration is shown in Figure 6.15 and found not to be negligible (~ 10%) in all variables. The bin-by-bin correction factor is defined as the ratio of number of events at reconstruction-level to the number of particle-level events in each bin, and is obtained from $t\bar{t}\gamma$ simulation; consequently, the correction factor depends significantly on the chosen $t\bar{t}\gamma$ underlying distribution. The unfolded particle-level spectrum is given by the following equation

$$\frac{N_k^{\text{reco}}}{N_k^{\text{part}}} \cdot N_k^{\text{unf,part}} = N_k^{\text{data}} - N_k^{\text{bkgs}}. \tag{6.29}$$

The singular value decomposition method

The singular value decomposition method (SVD) described in Ref. [162] simplifies the inversion process of the migration matrix by decomposing the migration matrix into other matrices:

$$M = US^{-1}V^T, \tag{6.30}$$

where U and V are quadratic orthogonal matrices, and S is a diagonal matrix. Hence, the inverse of the migration matrix can be derived as

$$M^{-1} = VS^{-1}U^T. \tag{6.31}$$

The method also introduces a normalisation term to regularise the solution. The term acts as a cut-off for the large sensitivity of the output to small fluctuations in the input (the noise in the measurement). The regularisation parameters are set to their default values, i.e., number of bins divided by 2. No optimisation of these parameters is performed.

Comparison result

The three different unfolding methods are used to unfold the reconstruction-level distribution, which is estimated from simulation. The different unfolded results are compared to the same truth distribution, as shown in Figure 6.25. From the figure, all methods agree within their statistical uncertainties. The SVD uncertainties are systematically smaller than in the other methods, but they have to be taken as a first approximation, as they strongly depend on the tuning of some of the parameters, while the SVD method implementation was limited to test the unfolded values only and not their uncertainties.

6.7 Systematic uncertainties

The considered systematic uncertainties can be divided in three categories: the signal modelling, the background modelling and the experimental systematics. The latter category is common to both signal and background processes and related to the quality of the detector simulation to describe the detector response in data for each of the reconstructed objects. In this case, uncertainties in the reconstruction and calibration of the physics objects are estimated. The nominal settings correspond to the nominal calibrated objects and nominal modelling of signal and background processes. The systematic variation from nominal is either two-sided or one-sided. For the two-sided systematics, up and down variations around the nominal are obtained. One-sided systematic uncertainties are defined when either both up and down variations have the same sign, that can happen when a variation on one object property affects several selection cuts in different directions, or is defined when the uncertainty has only one variation. If two variations exist, the systematic shifts from nominal are symmetrised by taking the difference between

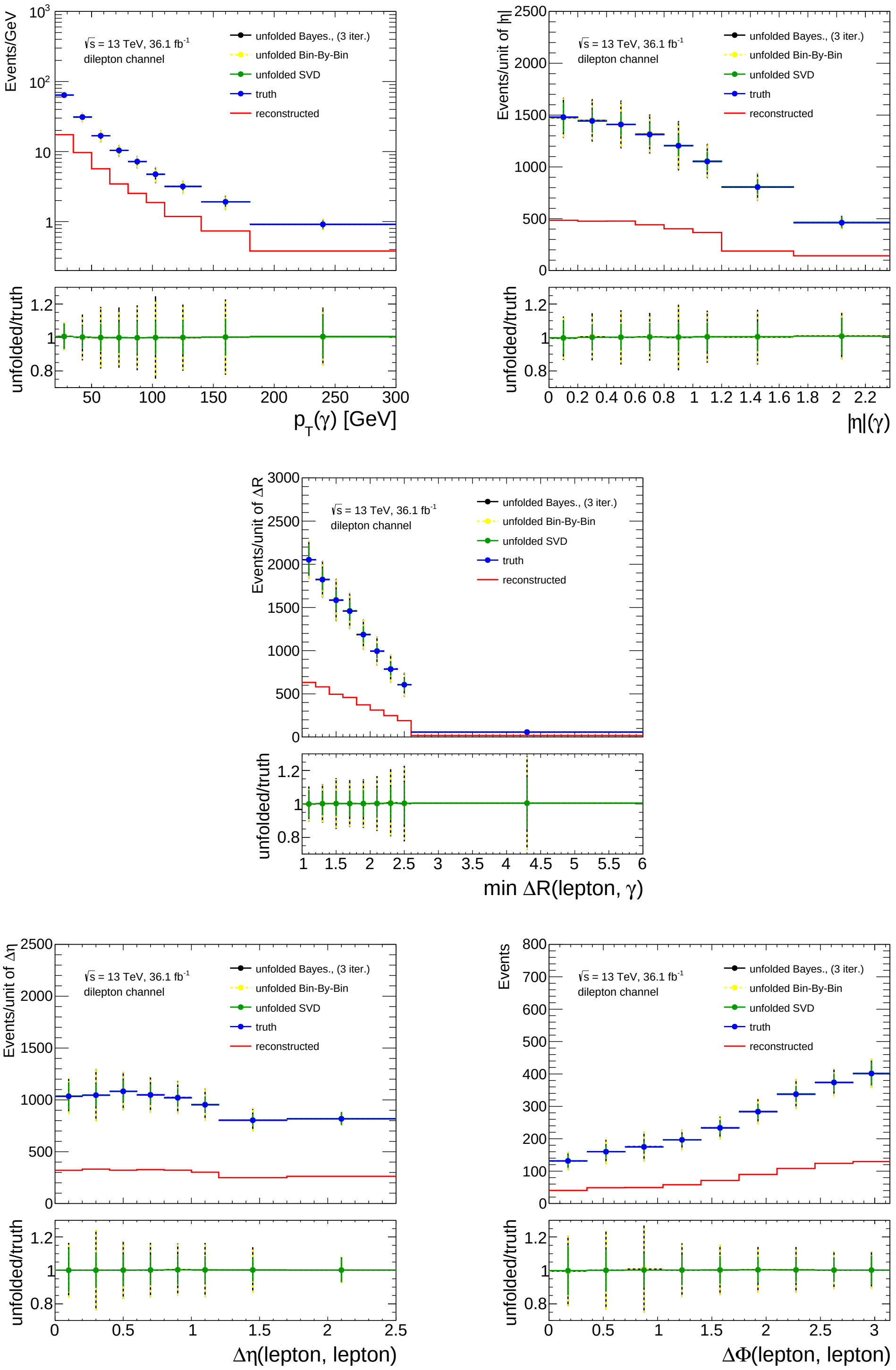

Figure 6.25: The number of unfolded events as a function of the photon p_{T} (top-left), the photon $|\eta|$ (top-right), the minimum $\Delta R(\ell,\gamma)$ (centre), the $\Delta\eta(\ell,\ell)$ (bottom-left), and the $\Delta\phi(\ell,\ell)$ (bottom-right), in the dilepton channel, obtained by the iterative method using three iterations (black), the bin-by-bin (yellow), and the SVD (green). All are compared to the truth distribution (blue), in the ratio plot. The red line is the original reconstructed distribution before unfolding. All distributions are normalised to a luminosity of 36.1 fb^{-1}.

the two variations and dividing by the mean of the variations. This value is then taken as positive (for up) and negative (for down). Thus, the up and down variation is centred around the nominal value. If only one variation exists, the variation is simply mirrored to reflect the supplementary variation.

To propagate the uncertainty to the unfolding framework, the input to be unfolded is shifted with the corresponding systematic variation. The systematic shifts are applied either directly to the physics objects themselves, or as weights of the events. The unfolding is then performed for each shifted input, using the nominal migration matrix which is built from the nominal signal sample. The shifted inputs are obtained after performing the likelihood fit described in Section 6.5.1. The uncertainty is estimated as the difference between the nominal unfolded result and the shifted ones.

6.7.1 Signal modelling

- Renormalisation and factorisation scale choice: The effect of a particular choice of renormalisation and factorisation scales for the signal sample simulation is estimated by varying μ_R and μ_F by a factor of 2 around the central value of the nominal MadGraph signal sample (which uses a dynamic scale). Several configurations are possible; applying simultaneously the variation for the two scales or applying the variation separately, and all of the configurations are tested. The systematic shift is applied as an event weight [164], and the final uncertainty is estimated as the quadrature sum of all variations.

- PDF uncertainty: The PDF uncertainty is evaluated by the 101 variations of the NNPDF2.3LO set [86], implemented as event weights [164]. The variations are either in the up or the down direction. The total PDF uncertainty is estimated by computing the standard deviation of the 100 PDF variations with respect to the central value, where the latter corresponds to the mean of all variations. The calculation is performed using the following equation

$$\Delta X = \sqrt{\frac{1}{N}\sum_{i=1}^{N}(X_i - X_0)^2}, \tag{6.32}$$

  where N=100, X_0 is the mean value, and X_i is the i-th PDF variation for i = [1, 2, ..., 100].

- Initial and final state radiation (ISR/FSR): Two different tunes of Pythia 8, which is used for parton showering, are used to provide two signal samples with lower or higher QCD radiation activities. The new signal samples are compared to the nominal sample generated with MadGraph + Pythia 8 with the nominal A14 tune.

- Uncertainty due to the parton shower and hadronisation: The nominal signal sample generated with MadGraph + Pythia 8 is compared to a sample generated with MadGraph, but using Herwig 7 for the parton shower and hadronisation.

6.7.2 Background modelling

A prior uncertainty of 50% is assumed for the $e \to \gamma$ fake background and backgrounds with a prompt photon. An up and down variation of 1σ around the nominal yield of each background source is calculated. For the hadronic-fake background, which is obtained dominantly from $t\bar{t}$ simulation, several sources of uncertainty are estimated [18]. The uncertainty due to the modelling of the $t\bar{t}$ process is calculated by comparing the nominal $t\bar{t}$ sample generated with Powheg-Box + Pythia 8 to a $t\bar{t}$ sample generated with Sherpa. The uncertainty due to the initial and final state radiations in the simulated $t\bar{t}$

events is estimated by comparing the sample with the nominal A14 tune to $t\bar{t}$ samples generated with different Pythia 8 tunes, corresponding to lower or higher QCD radiation activities. In addition, the modelling of the signal, the $e \to \gamma$ fake and the prompt photon backgrounds affect the hadronic-fake scale factor, estimated in data. These sources are varied to calculate a new scale factor, and the difference with respect to the nominal scale is taken as an uncertainty. This uncertainty is calculated in the single-lepton channel and used in the dilepton channel.

6.7.3 Experimental uncertainties

The experimental uncertainties are mostly related to the physics objects: leptons, photons, jets and missing transverse momentum. Additionally, the uncertainty on the total integrated luminosity affects the total expected yield. All uncertainties, except for the luminosity, are implemented as modified event weights.

- Luminosity: A total systematic uncertainty of 2.1% is assigned to the total luminosity used in this analysis, which is estimated following the method described in Ref. [151], from a preliminary calibration of the luminosity scale derived from beam-separation scans performed in August 2015 and May 2016. The uncertainty is implemented as up and down variations of the nominal yield.

- Pile-up: The uncertainty due to the modelling of pile-up events is evaluated by comparing data and simulated events. The distribution of the average number of pp interactions per bunch crossing, $< \mu >$ in data (see Figure 4.3) is scaled by a factor of 1/1.09 [165]. The differences between the simulated $< \mu >$ distribution and the scaled $< \mu >$ in data are taken as event weights. The uncertainty is evaluated by changing the scale factor from 1/1.09 to 1 (1/1.18) for the up (down) variation.

- Photons: The uncertainty on the identification efficiency is estimated by varying the scale factors derived due to the difference in calculating the efficiency in data and simulation [132]. These scale factors are applied to simulation in order to correct for possible detector mismodelling. The photon energy calibration and the study of its scale and resolution uncertainties are calculated together with the electrons [166] (referred later as E/Gamma scale and resolution).

- Leptons: The uncertainty on lepton efficiency arises due to different efficiencies in the reconstruction, identification and triggering leptons, obtained from simulation to those in data. Thus, scale factors are applied to simulation, and calculated as the ratio of efficiencies estimated in simulation and data. The efficiencies from data are calculated using the tag-and-probe method with $Z \to ee/\mu\mu$ and $J/\psi \to ee$ selections [125, 127]. These scale factors, which are E_{T} and η dependent, are varied to study the impact of lepton efficiency uncertainties on the analysis result. The lepton momentum is corrected using correction factors calculated from dileptonic Z decays.

- Jets: The measurement of jets is affected by the jet energy scale (JES) [167]. The JES is estimated by varying the jet energies according to the uncertainties derived from simulation and in-situ calibration measurements, to correct for the topo-cluster energy and the pile-up effect, for example. The uncertainty is divided into 21 independent components, added in quadrature. The jet measurement is also affected by the jet energy resolution (JER) [167, 168], where events from the processes $Z \to ee/\mu\mu$+jets and $\gamma \to ee$+jets are used to measure the detector resolution. One source, which shifts the individual jet energies in the simulation, is associated to the JER uncertainty. The last source that affects the jet measurement is the jet vertex tagger cut [136], this uncertainty is obtained by varying the applied cut.

- b-tagging: The systematic uncertainty is estimated for three jet flavours independently, the b-quark tagging efficiency, the efficiency with which jets originating from c-quarks pass the b-tag requirement (c-quark tagging efficiency) and the rate at which light-flavour jets are tagged (misidentified tagging efficiency) [142, 169, 170]. The uncertainties are decomposed into several uncorrelated components using the eigenvector method: 30, 15 and 80 eigenvectors for b-, c-, and light-flavour jet uncertainties, respectively. The systematic uncertainties are evaluated using factors used to correct the differences between simulations and data in each of the flavours.

- Missing transverse momentum: As the missing transverse momentum is calculated using the vector sum of several objects (Equation 4.7), the uncertainties on these objects are propagated to the $E_{\mathrm{T}}^{\mathrm{miss}}$ uncertainty. The systematic uncertainty of the soft-term scale is estimated by comparing the ratio of simulation to data. The systematic uncertainty of the soft-term resolution is estimated by evaluating the level of agreement between data and simulation in the E_x^{miss} and E_y^{miss} resolution. Both, the scale and resolution of the soft term, are varied to study their impact on the measurement.

The relative difference of each shifted $t\bar{t}\gamma$ reconstructed distribution compared to the nominal one is shown in Appendix F. The shifted samples are obtained from the nominal simulation, and therefore, the differences are considered to be dominantly due to the studied variation, and differences due to statistical variations are negligible.

6.8 Results

A likelihood fit to the distribution of the event level discriminator is performed in data, in the fiducial phase space. The normalisation of each background is fixed to its corresponding estimate of number of events. This number is obtained from simulation, with the exception of the hadronic-fake background, which is scaled by a data-driven scale factor. The number of signal events is extracted from the fit and consequently the fiducial cross section is measured. A total of 902 data candidate events are observed, with an expected background of 129 ± 56 events, in the dilepton channel. The event yield for the signal and background processes is presented in Table 6.11.

Process	$t\bar{t}\gamma$	Hadronic fakes	$e \to \gamma$ fake	$Z\gamma$ + jets	Other	Data
Event yield	783 ± 51	56 ± 43	1.8 ± 1.2	41 ± 18	18 ± 7	902

Table 6.11: The post-fit event yields for the signal and background processes for the fiducial cross-section measurement in the dilepton channel. The category “ Other ” includes contributions from single-top and diboson processes. The statistical and systematic uncertainties are shown.

The signal strength and the fiducial cross section in the dilepton channel are measured to be

$$\mu(\sigma_{t\bar{t}\gamma}^{\mathrm{fid}}/\sigma_{t\bar{t}\gamma}^{\mathrm{SM}}) = 1.10^{+0.08}_{-0.07},$$

$$\sigma_{t\bar{t}\gamma}^{\mathrm{fid}} = 69.35\ ^{+2.65}_{-2.59}\ (\mathrm{stat.})\ ^{+3.42}_{-3.20}\ (\mathrm{syst.})\ \mathrm{fb},$$

in agreement with the SM prediction at NLO within uncertainties, as shown in Figure 6.26.

The differential cross section is measured by unfolding the observed data, after subtracting the expected backgrounds, shown in Figure 6.27. The iterative Bayesian method is employed and three iterations are used. The measured differential cross sections are compared to prediction in Figure 6.28, and summarised in Table 6.12 in photon p_{T} bins. The results in $|\eta|$ bins are shown in Figure 6.29 and Table 6.13. For

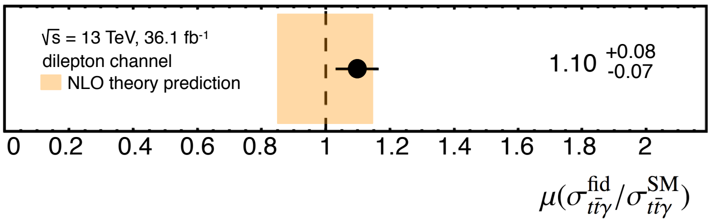

Figure 6.26: The fiducial cross-section measurement in the dilepton channel. The total statistical and systematic uncertainties are shown.

the minimum $\Delta R(\ell,\gamma)$, the results are described by Figure 6.30 and Table 6.14. The results for $\Delta\eta(\ell,\ell)$ are shown in Figure 6.31 and Table 6.15. Finally, the results for $\Delta\phi(\ell,\ell)$ are shown in Figure 6.32 and Table 6.16.

The observed data is found to be in agreement with simulation within uncertainties. The uncertainties on the cross section are dominated by the statistical uncertainty, ranging between 8 and 22% in p_{T} bins, 11 and 17% in $|\eta|$ bins, 10 and 28% in minimum $\Delta R(\ell,\gamma)$ bins, 8 and 22% in $\Delta\eta(\ell,\ell)$ bins, and 9 – 25% in $\Delta\phi(\ell,\ell)$ bins. The systematic uncertainty has also a sizeable impact on the measurement. The dominant systematic uncertainties on the measured cross sections arise from several sources. The leading uncertainty is caused by the background modelling, which is mainly due to the modelling of the $t\bar{t}$ process. Its impact on the cross section reaches values up to 10 – 13%, and varies from bin to bin. This variation is related to the statistical fluctuations of the hadronic-fake background. The second source of uncertainty, which has a notable effect in some bins, stems from the choice of the generator used for the signal parton showering, and for the initial and final state radiation to a smaller extent. The third dominant source is due to the luminosity estimation. It results in an uncertainty of 2% in all bins. The impact of the several sources of the systematic uncertainty on the measured cross section in each bin of the five differential distributions are given in Tables 6.17 – 6.21 for the photon p_{T}, the photon η, the minimum $\Delta R(\ell,\gamma)$, $\Delta\eta(\ell,\ell)$ and $\Delta\phi(\ell,\ell)$, respectively.

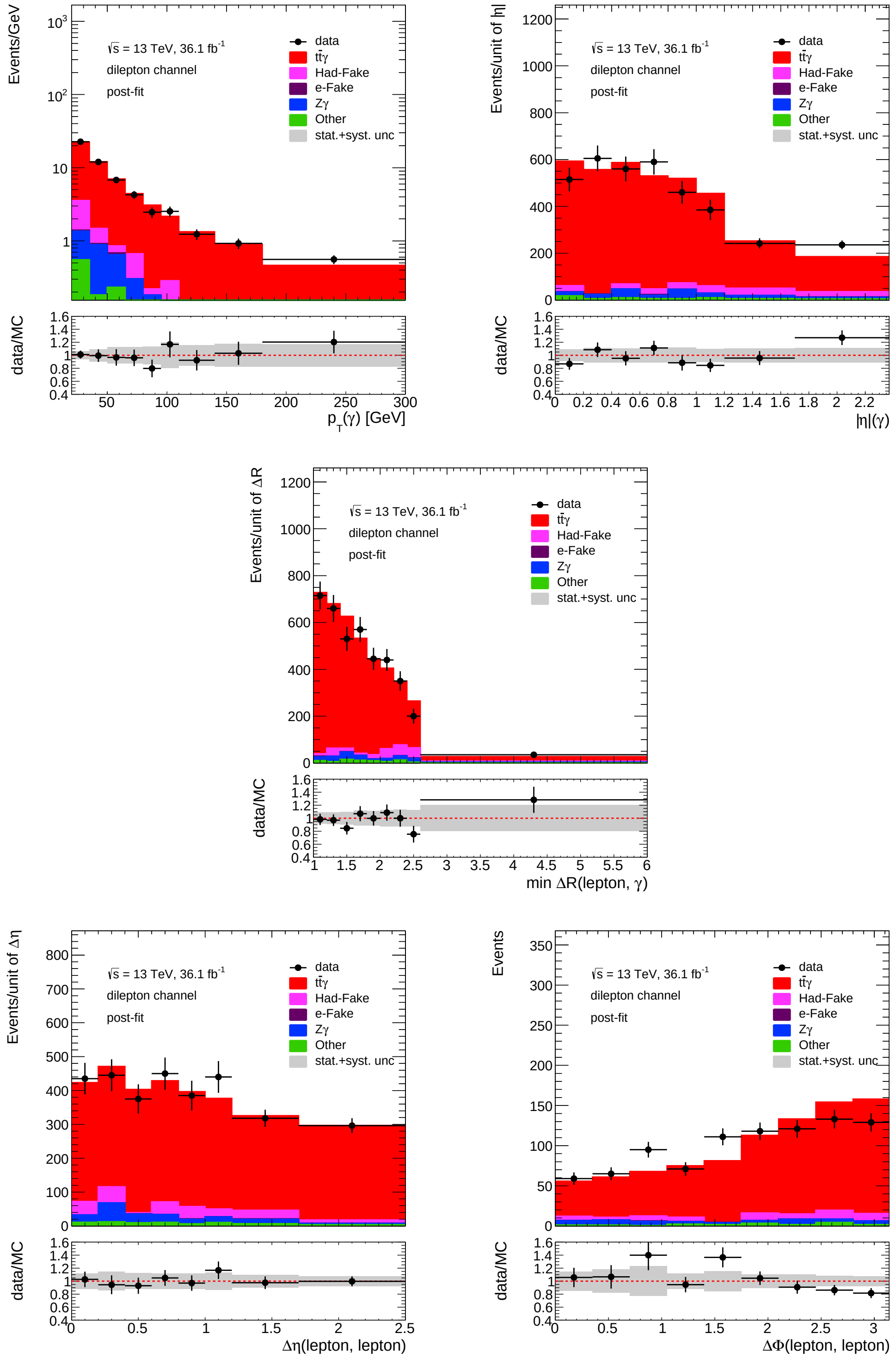

Figure 6.27: The post-fit distributions of the photon p_{T} (top-left), the photon $|\eta|$ (top-right), the minimum $\Delta R(\ell, \gamma)$ (centre), the $\Delta\eta(\ell, \ell)$ (bottom-left), and the $\Delta\phi(\ell, \ell)$ (bottom-right), in the dilepton channel. The category “ Other ” includes contributions from single top and diboson processes. The gray band includes both, the statistical and the systematic uncertainties .

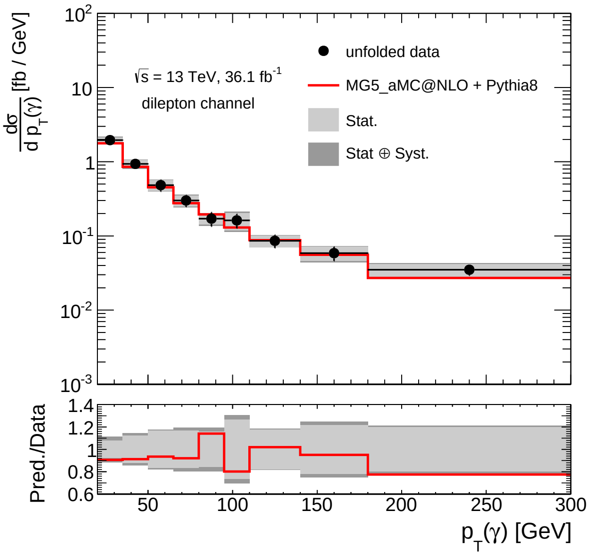

Figure 6.28: The differential cross section (black dots) as a function of the photon p_T, compared to the prediction (red line), in the dilepton channel.

Table 6.12: The differential cross section in photon p_T bins, obtained using the iterative Bayesian method, in the dilepton channel. The first and second associated uncertainties are the statistical and the systematic uncertainty respectively.

p_T bin	σ [fb]
20 - 35	29.33 ± 2.27 ± 2.46
35 - 50	14.03 ± 1.72 ± 1.06
50 - 65	7.25 ± 1.21 ± 0.47
65 - 80	4.50 ± 0.75 ± 0.46
80 - 95	2.56 ± 0.40 ± 0.30
95 - 110	2.43 ± 0.64 ± 0.38
110 - 140	2.58 ± 0.46 ± 0.14
140 - 180	2.34 ± 0.51 ± 0.29
180 - 300	4.20 ± 0.83 ± 0.33

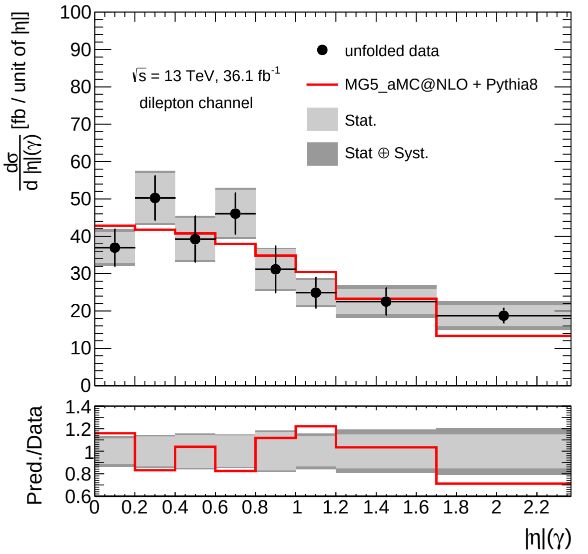

Figure 6.29: The differential cross section (black dots) as a function of the photon $|\eta|$, compared to the prediction (red line), in the dilepton channel.

Table 6.13: The differential cross section in photon $|\eta|$ bins, obtained using the iterative Bayesian method, in the dilepton channel. The first and second associated uncertainties are the statistical and the systematic uncertainty respectively.

$\|\eta\|$ bin	σ [fb]
0.0 - 0.2	7.39 ± 0.83 ± 0.57
0.2 - 0.4	10.05 ± 1.33 ± 0.58
0.4 - 0.6	7.85 ± 1.14 ± 0.49
0.6 - 0.8	9.21 ± 1.27 ± 0.51
0.8 - 1.0	6.23 ± 1.06 ± 0.44
1.0 - 1.2	4.98 ± 0.67 ± 0.41
1.2 - 1.7	11.26 ± 1.69 ± 1.34
1.7 - 2.37	12.56 ± 1.88 ± 1.80

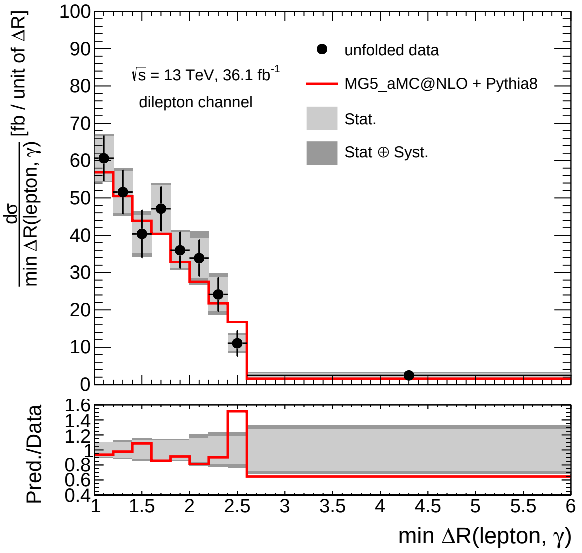

Figure 6.30: The differential cross section (black dots) as a function of the minimum $\Delta R(\ell, \gamma)$, compared to the prediction (red line), in the dilepton channel.

Table 6.14: The differential cross section in minimum $\Delta R(\ell, \gamma)$ bins, obtained using the iterative Bayesian method, in the dilepton channel. The first and second associated uncertainties are the statistical and the systematic uncertainty respectively.

min $\Delta R(\ell, \gamma)$ bin	σ [fb]
1.0 - 1.2	12.13 ± 1.18 ± 0.53
1.2 - 1.4	10.31 ± 1.12 ± 0.62
1.4 - 1.6	8.07 ± 1.01 ± 0.71
1.6 - 1.8	9.42 ± 1.28 ± 0.49
1.8 - 2.0	7.20 ± 0.95 ± 0.48
2.0 - 2.2	6.77 ± 1.07 ± 0.93
2.2 - 2.4	4.83 ± 0.90 ± 0.66
2.4 - 2.6	2.21 ± 0.42 ± 0.31
2.6 - 6.0	8.33 ± 2.29 ± 1.42

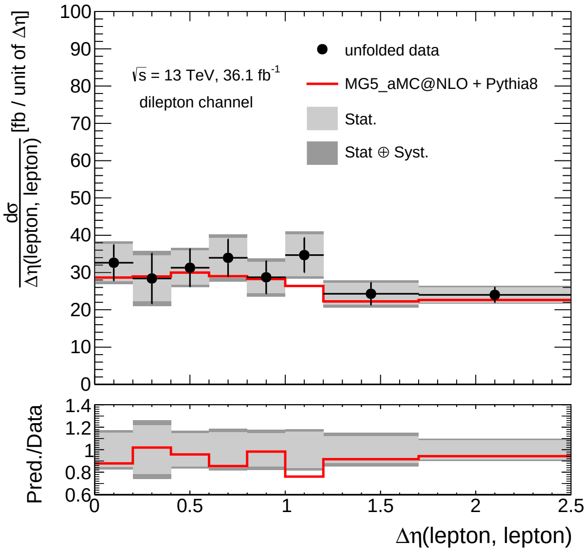

Figure 6.31: The differential cross section (black dots) as a function of the $\Delta\eta(\ell, \ell)$, compared to the prediction (red line), in the dilepton channel.

Table 6.15: The differential cross section in $\Delta\eta(\ell, \ell)$ bins, obtained using the iterative Bayesian method, in the dilepton channel. The first and second associated uncertainties are the statistical and the systematic uncertainty respectively.

$\Delta\eta(\ell, \ell)$ bin	σ [fb]
0.0 - 0.2	6.52 ± 1.00 ± 0.55
0.2 - 0.4	5.68 ± 1.23 ± 0.83
0.4 - 0.6	6.26 ± 0.92 ± 0.50
0.6 - 0.8	6.79 ± 1.06 ± 0.69
0.8 - 1.0	5.75 ± 0.84 ± 0.58
1.0 - 1.2	6.94 ± 1.12 ± 0.59
1.2 - 1.7	12.15 ± 1.45 ± 1.09
1.7 - 2.5	19.21 ± 1.62 ± 1.00

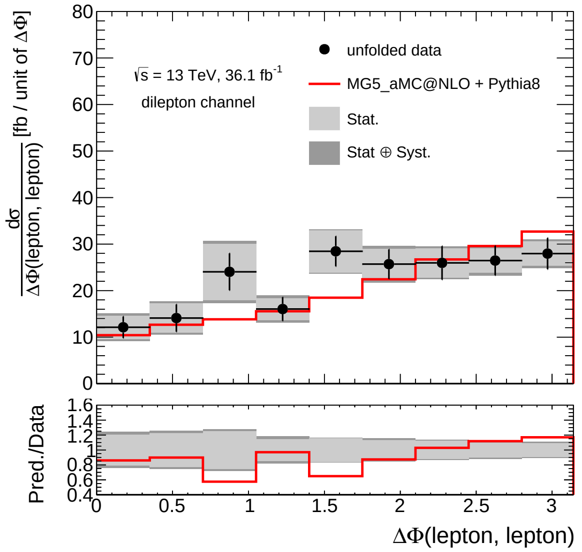

Figure 6.32: The differential cross section (black dots) as a function of the $\Delta\phi(\ell, \ell)$, compared to the prediction (red line), in the dilepton channel.

Table 6.16: The differential cross section in $\Delta\phi(\ell, \ell)$ bins, obtained using the iterative Bayesian method, in the dilepton channel. The first and second associated uncertainties are the statistical and the systematic uncertainty respectively.

$\Delta\phi(\ell, \ell)$ bin	σ [fb]
0.0 - 0.35	4.24 ± 0.87 ± 0.56
0.35 - 0.7	4.93 ± 1.11 ± 0.59
0.7 - 1.05	8.41 ± 2.11 ± 1.02
1.05 - 1.40	5.61 ± 0.82 ± 0.63
1.4 - 1.75	9.96 ± 1.60 ± 0.45
1.75 - 2.10	8.99 ± 1.16 ± 0.75
2.10 - 2.45	9.09 ± 1.11 ± 0.53
2.45 - 2.80	9.26 ± 0.91 ± 0.67
2.8 - 3.14	9.51 ± 0.88 ± 0.58

$p_T(\gamma)$ [Gev]	20 - 35	35 - 50	50 - 65	65 - 80	80 - 95	95 - 110	110 - 140	140 - 180	180 - 300
Source	systematic uncertainty (%)								
Signal Scale Variation	±0.75	±0.33	±0.10	±0.16	±0.29	±0.82	±1.14	±1.56	±2.71
Parton Distribution Function	±0.0	±0.0	±0.0	±0.0	±0.0	±0.0	±0.0	±0.0	±0.0
Signal ISR/FSR Setting	±0.72	±3.70	±3.74	±2.09	±5.14	±2.54	±3.57	±4.28	±0.0
Signal Parton Showering	±0.72	±1.59	±0.73	±1.14	±5.85	±11.24	±0.09	±3.08	±2.94
Background Modelling	±7.25	±5.10	±3.82	±9.30	±7.93	±9.80	±2.10	±10.37	±5.99
Luminosity	±2.09	±2.09	±2.09	±2.09	±2.09	±2.09	±2.09	±2.09	±2.09
Pileup Effects	±1.70	±1.67	±1.57	±1.43	±1.31	±1.17	±0.98	±0.86	±0.84
Photon Scale Factors	±1.27	±1.03	±0.84	±0.68	±0.67	±0.64	±0.72	±1.26	±1.45
Lepton Identification and Reconstruction	±1.09	±1.09	±1.10	±1.09	±1.15	±1.16	±1.17	±1.12	±1.27
E/Gamma Resolution and Scale	±0.27	±0.36	±0.42	±0.46	±0.51	±0.55	±0.55	±0.55	±0.55
Jet Identification and Reconstruction	±2.29	±2.15	±1.92	±1.64	±1.44	±1.35	±1.27	±1.25	±1.25
b-tagging	±0.78	±0.90	±0.76	±0.94	±0.97	±1.25	±0.98	±0.74	±0.65
Missing Transverse Momentum Reconstruction	±0.12	±0.11	±0.12	±0.12	±0.13	±0.22	±0.38	±0.49	±0.50
Total systematics	±8	±8	±7	±10	±12	±16	±5	±12	±8
Data statistics	±8	±12	±17	±17	±16	±26	±18	±22	±20
Total uncertainty	±11	±14	±18	±20	±20	±31	±19	±25	±21

Table 6.17: Summary of the sources of uncertainty on the absolute differential cross section for $p_T(\gamma)$ at particle level, presented as a percentage of the measured cross section in each bin in the dilepton channel. Entries of 0.0 are uncertainties that are less than 0.005 in magnitude.

$\lvert\eta\rvert(\gamma)$	0.0 - 0.2	0.2 - 0.4	0.4 - 0.6	0.6 - 0.8	0.8 - 1.0	1.0 - 1.2	1.2 - 1.7	1.7 - 2.37
Source	systematic uncertainty (%)							
Signal Scale Variation	±0.03	±0.09	±0.13	±0.04	±0.17	±0.05	±0.09	±0.34
Parton Distribution Function	±0.0	±0.0	±0.0	±0.0	±0.0	±0.0	±0.0	±0.0
Signal ISR/FSR Setting	±0.77	±0.75	±0.72	±0.17	±2.13	±2.77	±1.15	±0.16
Signal Parton Showering	±1.30	±4.25	±0.36	±0.42	±3.20	±2.22	±1.67	±4.93
Background Modelling	±6.66	±1.35	±5.09	±4.00	±4.50	±6.54	±11.11	±12.9
Luminosity	±2.09	±2.09	±2.09	±2.09	±2.09	±2.09	±2.09	±2.09
Pileup Effects	±1.59	±1.58	±1.57	±1.51	±1.42	±1.38	±1.40	±1.45
Photon Scale Factors	±0.72	±0.73	±0.73	±1.14	±1.13	±1.10	±1.31	±1.56
Lepton Identification and Reconstruction	±1.11	±1.11	±1.08	±1.10	±1.13	±1.11	±1.12	±1.16
E/Gamma Resolution and Scale	±0.14	±0.15	±0.20	±0.31	±0.45	±0.57	±0.61	±0.63
Jet Identification and Reconstruction	±1.87	±1.85	±1.88	±1.93	±1.95	±1.97	±1.98	±1.99
b-tagging	±0.80	±0.87	±0.78	±0.93	±0.81	±0.83	±0.83	±0.76
Missing Transverse Momentum Reconstruction	±0.11	±0.10	±0.10	±0.09	±0.10	±0.12	±0.13	±0.13
Total systematics	±8	±6	±6	±5	±7	±8	±12	±14
Data statistics	±11	±13	±15	±14	±17	±13	±15	±15
Total uncertainty	±14	±14	±16	±15	±18	±16	±19	±21

Table 6.18: Summary of the sources of uncertainty on the absolute differential cross section for $\lvert\eta\rvert(\gamma)$ at particle level, presented as a percentage of the measured cross section in each bin in the dilepton channel. Entries of 0.0 are uncertainties that are less than 0.005 in magnitude.

min $\Delta R(\ell,\gamma)$	1.0 - 1.2	1.2 - 1.4	1.4 - 1.6	1.6 - 1.8	1.8 - 2.0	2.0 - 2.2	2.2 - 2.4	2.4 - 2.6	2.6 - 6.0
Source	systematic uncertainty (%)								
Signal Scale Variation	±0.09	±0.12	±0.15	±0.07	±0.03	±0.25	±0.11	±0.50	±0.12
Parton Distribution Function	±0.0	±0.0	±0.0	±0.0	±0.0	±0.0	±0.0	±0.0	±0.0
Signal ISR/FSR Setting	±0.71	±0.85	±0.24	±0.29	±1.76	±3.39	±1.97	±1.11	±2.64
Signal Parton Showering	±0.65	±3.30	±7.03	±2.29	±1.34	±2.39	±0.85	±4.22	±5.09
Background Modelling	±2.43	±3.46	±3.67	±2.69	±4.84	±12.56	±12.96	±12.84	±15.64
Luminosity	±2.09	±2.09	±2.09	±2.09	±2.09	±2.09	±2.09	±2.09	±2.09
Pileup Effects	±1.17	±1.21	±1.43	±1.79	±1.98	±1.86	±1.58	±1.39	±1.35
Photon Scale Factors	±1.03	±1.02	±1.03	±1.01	±1.04	±1.07	±1.06	±1.09	±1.15
Lepton Identification and Reconstruction	±1.11	±1.14	±1.15	±1.11	±1.10	±1.10	±1.11	±1.08	±1.10
E/Gamma Resolution and Scale	±0.47	±0.41	±0.37	±0.35	±0.35	±0.35	±0.35	±0.35	±0.35
Jet Identification and Reconstruction	±1.80	±1.81	±1.87	±1.96	±2.02	±2.06	±2.05	±2.02	±2.00
b-tagging	±0.81	±0.81	±0.90	±0.92	±0.81	±0.85	±0.79	±0.61	±0.78
Missing Transverse Momentum Reconstruction	±0.17	±0.13	±0.09	±0.10	±0.12	±0.13	±0.13	±0.13	±0.13
Total systematics	±4	±6	±9	±5	±7	±14	±14	±14	±17
Data statistics	±10	±11	±12	±14	±13	±16	±19	±19	±28
Total uncertainty	±11	±12	±15	±15	±15	±21	±23	±24	±32

Table 6.19: Summary of the sources of uncertainty on the absolute differential cross section for $\Delta R(\ell,\gamma)$ at particle level, presented as a percentage of the measured cross section in each bin in the dilepton channel. Entries of 0.0 are uncertainties that are less than 0.005 in magnitude.

$\Delta\eta(\ell,\ell)$	0.0 - 0.2	0.2 - 0.4	0.4 - 0.6	0.6 - 0.8	0.8 - 1.0	1.0 - 1.2	1.2 - 1.7	1.7 - 2.5
Source	systematic uncertainty (%)							
Signal Scale Variation	±0.80	±1.07	±0.70	±0.65	±0.58	±0.18	±0.17	±1.14
Parton Distribution Function	±0.0	±0.0	±0.0	±0.0	±0.0	±0.0	±0.0	±0.0
Signal ISR/FSR Setting	±0.69	±0.42	±0.32	±1.52	±0.98	±0.72	±0.10	±0.50
Signal Parton Showering	±1.28	±2.17	±6.39	±1.25	±4.30	±0.72	±4.29	±3.11
Background Modelling	±7.13	±13.70	±2.55	±9.14	±8.29	±7.71	±7.05	±1.83
Luminosity	±2.09	±2.09	±2.09	±2.09	±2.09	±2.09	±2.09	±2.09
Pileup Effects	±1.65	±1.92	±2.05	±2.06	±1.91	±1.64	±1.28	±0.91
Photon Scale Factors	±1.06	±1.06	±1.06	±1.04	±1.09	±1.08	±1.04	±1.01
Lepton Identification and Reconstruction	±1.08	±1.09	±1.10	±1.12	±1.10	±1.12	±1.10	±1.15
E/Gamma Resolution and Scale	±0.40	±0.40	±0.40	±0.40	±0.40	±0.39	±0.37	±0.35
Jet Identification and Reconstruction	±2.85	±2.68	±2.24	±1.75	±1.43	±1.37	±1.61	±1.98
b-tagging	±0.76	±0.96	±0.83	±0.61	±0.82	±0.66	±0.85	±0.86
Missing Transverse Momentum Reconstruction	±0.07	±0.06	±0.05	±0.05	±0.06	±0.09	±0.14	±0.22
Total systematics	±8	±15	±8	±10	±10	±9	±9	±5
Data statistics	±15	±22	±15	±16	±15	±16	±12	±8
Total uncertainty	±17	±26	±17	±19	±18	±18	±15	±10

Table 6.20: Summary of the sources of uncertainty on the absolute differential cross section for $\Delta\eta(\ell,\ell)$ at particle level, presented as a percentage of the measured cross section in each bin in the dilepton channel. Entries of 0.0 are uncertainties that are less than 0.005 in magnitude.

$\Delta\phi(\ell,\ell)$	0.0 - 0.35	0.35 - 0.7	0.7 - 1.05	1.05 - 1.4	1.4 - 1.75	1.75 - 2.1	2.1 - 2.45	2.45 - 2.8	2.8 - 3.14
Source	systematic uncertainty (%)								
Signal Scale Variation	±0.88	±0.65	±0.45	±0.45	±0.20	±0.08	±0.25	±0.38	±0.42
Parton Distribution Function	±0.0	±0.0	±0.0	±0.0	±0.0	±0.0	±0.0	±0.0	±0.0
Signal ISR/FSR Setting	±0.34	±2.20	±0.49	±2.55	±0.76	±2.38	±0.26	±1.27	±2.11
Signal Parton Showering	±1.25	±7.58	±4.41	±2.66	±1.39	±0.87	±0.86	±0.40	±1.37
Background Modelling	±12.65	±8.17	±10.59	±9.93	±2.43	±7.12	±4.48	±6.04	±3.94
Luminosity	±2.09	±2.09	±2.09	±2.09	±2.09	±2.09	±2.09	±2.09	±2.09
Pileup Effects	±2.09	±2.06	±1.96	±1.70	±1.38	±1.20	±1.20	±1.31	±1.49
Photon Scale Factors	±1.08	±1.05	±1.06	±1.04	±1.03	±1.05	±1.03	±1.04	±1.05
Lepton Identification and Reconstruction	±1.07	±1.01	±1.02	±1.04	±1.08	±1.09	±1.13	±1.18	±1.24
E/Gamma Resolution and Scale	±0.42	±0.41	±0.41	±0.39	±0.37	±0.36	±0.36	±0.36	±0.36
Jet Identification and Reconstruction	±1.63	±1.59	±1.65	±1.70	±1.83	±1.96	±2.04	±2.09	±2.14
b-tagging	±0.91	±0.77	±0.88	±0.75	±0.55	±0.96	±0.95	±0.83	±0.85
Missing Transverse Momentum Reconstruction	±0.11	±0.11	±0.10	±0.08	±0.08	±0.11	±0.13	±0.15	±0.18
Total systematics	±13	±12	±12	±11	±5	±8	±6	±7	±6
Data statistics	±20	±22	±25	±15	±16	±13	±12	±10	±9
Total uncertainty	±24	±25	±28	±18	±17	±15	±14	±12	±11

Table 6.21: Summary of the sources of uncertainty on the absolute differential cross section for $\Delta\phi(\ell,\ell)$ at particle level, presented as a percentage of the measured cross section in each bin in the dilepton channel. Entries of 0.0 are uncertainties that are less than 0.005 in magnitude. Any asymmetric systematic uncertainties have been symmetrised.

CHAPTER 7

Constraining new physics using Effective Field Theory

The model-independent effective field theory approach is employed in order to constrain new physics and quantify the effect of possible deviations from the SM prediction. In this approach, new models are described by the addition of new higher-dimensional operators to the SM Lagrangian, with corresponding coefficients (see Equation 2.30). Three EFT operators affect the $t\bar{t}\gamma$ production [16]: the O_{tB} and O_{tW} operators which create electroweak dipole moments, and the O_{tG} operator which creates chromomagnetic dipole moments. The operators are described in Equation 2.32 and Feynman diagrams are shown in Figure 2.7.

In this study, each new operator is tested independently, and the interference between two different operators is not considered. The effect of the operators on the inclusive cross section is given by

$$\sigma = \sigma_{\mathrm{SM}} + \frac{C_i}{\Lambda^2}\sigma_i^{(1)} + \frac{C_i^2}{\Lambda^4}\sigma_i^{(2)}, \tag{7.1}$$

where σ_{SM} is the SM cross section, $\sigma_i^{(1)}$ is the cross section of the interference between diagrams with operator O_i vertex and SM diagrams, $\sigma_i^{(2)}$ is the cross section of the quadratic term of the operator O_i, C_i is the coefficient associated to the operator O_i, and Λ is the cut-off in TeV units.

7.1 EFT samples

For each operator, two samples are generated with the customised Lagrangian described in Equation 2.30, with a positive or negative coefficient value, which is chosen to be close to the corresponding current limits [171–173]. For consistency, the SM sample is generated with the same tool with all coefficients set to values close to zero. It has been verified that this SM sample is equivalent to what can be obtained from the usual SM generation setting (see Appendix G). In total, seven samples are generated, with all coefficients set to zero except for the one of interest. Considering only one operator at a time neglects the possible cancellation from contributions of different EFT operators. The cut-off Λ is set to 1 TeV for all samples.

The samples are generated using the MadGraph5_aMC@NLO generator, and Pythia 8 for parton showering. The generation is performed at NLO, and it includes only photons emitted from the initial partons or off-shell top quarks. Photons radiated from the decay products of the top quark are not accessible in MadGraph5_aMC@NLO at NLO, due to technical difficulties in computing these processes.

The selections at generator level are described in the following. At least one lepton and one photon are required. Leptons, photons and jets are required to have transverse momenta larger than 15 GeV and $|\eta| < 5.0$. The NNPDF3.0 set [88] is used. A dynamic scale defined as the sum of the transverse mass of all the final state particles divided by two, is applied. The list of the samples is given in Table 7.1. The positive and negative variations of the coefficients are used to extract $\sigma_i^{(1)}$ and $\sigma_i^{(2)}$ by means of the following equations:

$$\sigma_i^{(1)} = \frac{\sigma_i^{(+)} - \sigma_i^{(-)}}{2C_i}, \tag{7.2}$$

$$\sigma_i^{(2)} = \frac{\sigma_i^{(+)} + \sigma_i^{(-)} - 2 \times \sigma_{\text{SM}}}{2C_i^2}, \tag{7.3}$$

where $\sigma_i^{(+)}$ and $\sigma_i^{(-)}$ are the cross sections obtained by setting the coefficient C_i to its positive and negative value, respectively. The cross-section value for each coefficient variation is given in Table 7.1. The extracted cross sections, $\sigma_i^{(1)}$ and $\sigma_i^{(2)}$, are shown in Table 7.2 and compared to the SM. It can be observed that the additional contributions due to the quadratic term of the O_{tB} and O_{tW} operators are larger than their interference term, whereas the interference term dominates over the quadratic term for the O_{tG} operator. These contributions are enhanced when a fiducial region is defined, as discussed in Section 7.2.

EFT operator	Cross section [pb]
σ_{SM}	2.652 ± 0.013
$C_{tB}/\Lambda^2 = +5\ \text{TeV}^{-2}$	3.005 ± 0.013
$C_{tB}/\Lambda^2 = -5\ \text{TeV}^{-2}$	2.807 ± 0.013
$C_{tG}/\Lambda^2 = +0.3\ \text{TeV}^{-2}$	2.914 ± 0.014
$C_{tG}/\Lambda^2 = -0.3\ \text{TeV}^{-2}$	2.469 ±0.012
$C_{tW}/\Lambda^2 = +2\ \text{TeV}^{-2}$	2.757 ± 0.015
$C_{tW}/\Lambda^2 = -2\ \text{TeV}^{-2}$	2.670 ± 0.013

Table 7.1: The expected NLO cross section for each different C_i, generated one at a time. Only the statistical uncertainty is shown.

Cross section	O_{tB}	O_{tG}	O_{tW}
σ_{SM}	2.652	2.652	2.652
$C_i\sigma^{(1)}$	0.099	0.222	0.022
$C_i^2\sigma^{(2)}$	0.254	0.040	0.023
$C_i\sigma^{(1)}/\sigma_{\text{SM}}$	0.037	0.084	0.016
$C_i^2\sigma^{(2)}/\sigma_{\text{SM}}$	0.096	0.015	0.023

Table 7.2: The interference and quadratic cross-section terms due to the new operators at the generator level. The results are in pb.

7.2 Study in the fiducial region

The object definitions and the event selections defined for the fiducial region of the dilepton channel and introduced in Section 6.5.1 are implemented in a Rivet routine [174], and used for this study. The results of the inclusive fiducial cross sections are summarised in Table 7.3. The quadratic term of the O_{tB} operator has a larger impact on the cross section than the interference term, while the interference terms of the other two operators, O_{tG} and O_{tW}, contribute more to the cross section than their corresponding quadratic terms. The differential cross sections in photon p_{T} and the invariant mass of the photon and the hardest jet are compared to the SM cross section, and shown in Figure 7.1. The enhancement due to the O_{tB} operator gets larger with the increase of the photon p_{T} or the invariant mass. This is due to the amount of energy that enters the EFT vertex. The O_{tW} operator shows a similar behaviour as O_{tB}, but with a smaller impact on the SM cross section. For the last operator, O_{tG}, the effect is rather independent of the p_{T} or invariant mass bins.

Cross section	O_{tB}	O_{tG}	O_{tW}
σ_{SM}	0.646	0.646	0.646
$C_i\sigma^{(1)}$	0.023	0.057	0.013
$C_i^2\sigma^{(2)}$	0.065	-0.008	0.003
$C_i\sigma^{(1)}/\sigma_{\mathrm{SM}}$	0.036	0.087	0.020
$C_i^2\sigma^{(2)}/\sigma_{\mathrm{SM}}$	0.100	0.012	0.005

Table 7.3: The interference and quadratic cross-section terms due to the new operators, and their effect on the fiducial cross section in the dilepton channel. The results are in pb.

7.2.1 The fit

Constraints on the EFT operators can be studied by performing likelihood fits [19], within the RooFit/RooStats framework [144, 145]. The fit is performed to both, the observed data and Asimov datasets. In this search, the observed limits are obtained from the observed data, which is unfolded employing the iterative Bayesian method, as explained in Section 6.6. The Asimov datasets are obtained from the expected data, and can be treated as the observed data. Consistently, the Asimov dataset, used to compute the expected limits, is unfolded in the same way. The likelihood function of the SM measurement is modified with a new model including the additional terms due to the new operators. In the fit, the EFT coefficients are left as free parameters, and the SM cross section is fixed to the nominal one. The additional terms to the SM cross section are estimated using only photons radiated from the top-quark production, as explained in Section 7.1, whereas both, the radiative top production and the radiative top decay, are simulated in the nominal $t\bar{t}\gamma$ sample. Therefore, the total number of photons observed in the SM case should be transformed to correspond to the amount from the radiative top production only. This can be achieved, in a first approximation, with the help of the fractions of the radiative top production estimated in the fiducial region using the SM $t\bar{t}\gamma$ sample. Hence, the number of additional photons radiated from the

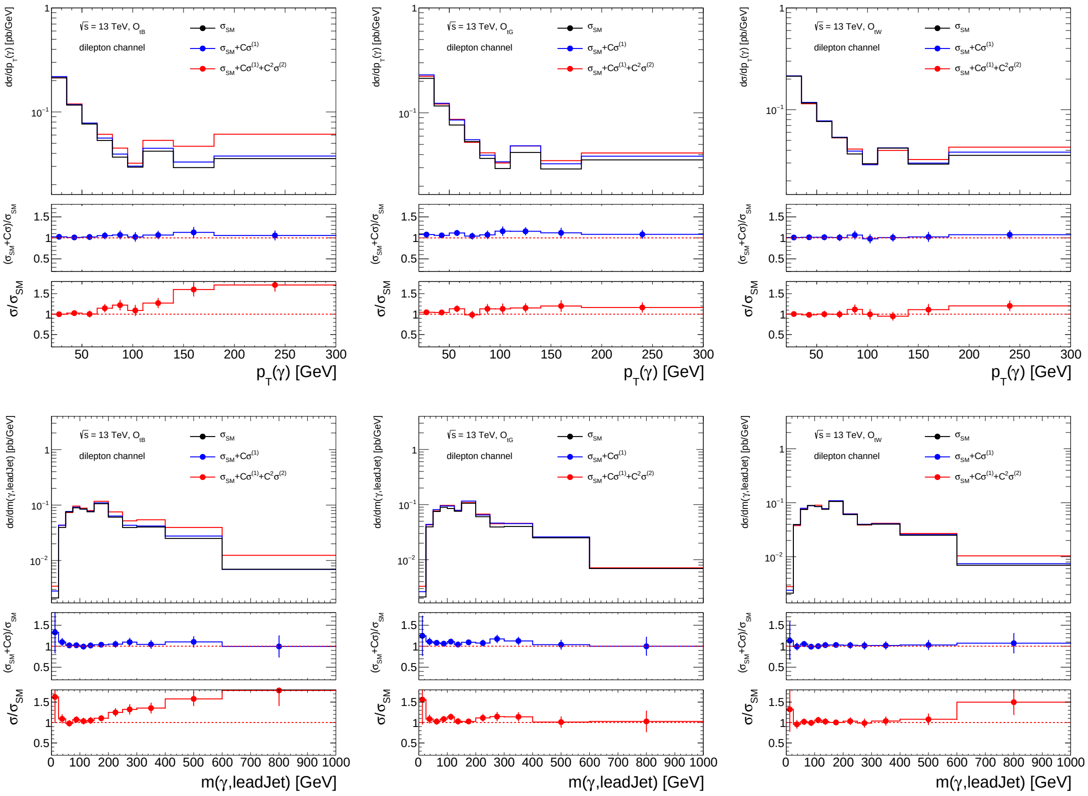

Figure 7.1: The effect of the EFT operators O_{tB} (left) O_{tG} (middle), and O_{tW} (right) on the $t\bar{t}\gamma$ dilepton fiducial cross section as a function of the photon p_{T} (top) and invariant mass of the photon and the hardest jet (bottom), for values of $C_{tB} = \pm 5$, $C_{tG} = \pm 0.3$ and $C_{tW} = \pm 2$. The SM differential cross section is shown in black, the effect of the interference term in blue, the effect of both, interference and quadratic terms in red.

top-quark due to the interference and the quadratic terms of a given EFT operator can be calculated by

$$N_i^{\sigma^{(1)}} = \frac{\sigma_i^{(1)}}{\sigma_{\mathrm{SM},i}} \cdot N_{\mathrm{tot},i}^{\mathrm{SM}} \cdot \mathrm{FR}_{\mathrm{prod},i}^{\mathrm{SM}}, \tag{7.4}$$

$$N_i^{\sigma^{(2)}} = \frac{\sigma_i^{(2)}}{\sigma_{\mathrm{SM},i}} \cdot N_{\mathrm{tot},i}^{\mathrm{SM}} \cdot \mathrm{FR}_{\mathrm{prod},i}^{\mathrm{SM}}, \tag{7.5}$$

where $\sigma_i^{(1)}/\sigma_{\mathrm{SM},i}$ and $\sigma_i^{(2)}/\sigma_{\mathrm{SM},i}$ are given in Table 7.3 and shown differentially in Figure 7.1, $N_{\mathrm{tot},i}^{\mathrm{SM}}$ is the total number of photons in the SM sample, including both, the radiative top production and the radiative top decay, in a given bin i of the photon p_{T} spectrum, and $\mathrm{FR}_{\mathrm{prod},i}^{\mathrm{SM}}$ is the fraction of photons emitted from the top quark or the initial-state partons. These fractions are shown in Figure 7.2 in photon p_{T} bins, where the effect of the EFT operators on the radiative top decay is neglected. On the other hand, if both types of radiation are assumed to be equally affected by the presence of the EFT operators, the fractions are set to one, and thus $\sigma_i^{(1,2)}/\sigma_{\mathrm{SM},i}$ is considered to be the same for the radiative top production and decay. The above calculated numbers, and the number of unfolded Asimov (observed) data are used as inputs to the fit.

The results of the fits are presented in Table 7.4. It can be seen that, with respect to the initial coefficient

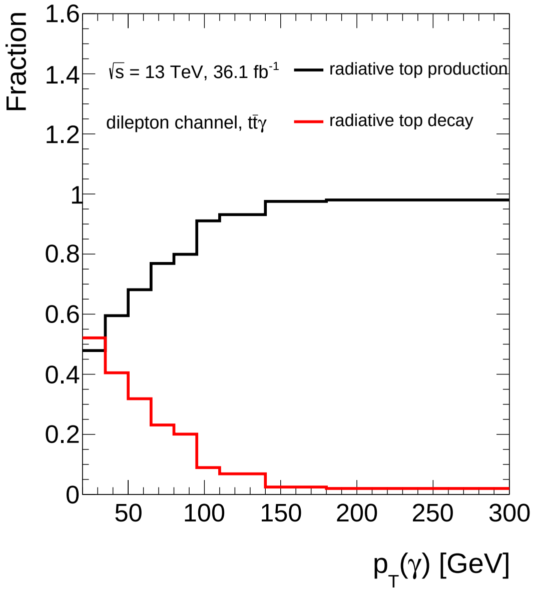

Figure 7.2: The fraction of photons radiated from the top-quark production or from its decay products as a function of the photon p_{T}, estimated in the fiducial region using the $t\bar{t}\gamma$ sample, in the dilepton channel.

values used in the simulation and corresponding to the current limits, the two coefficients C_{tB} and C_{tG} are close to improve the current limits, whereas the C_{tW} is only loosely constrained. As expected, if the new operators are assumed to affect the radiative top decay contribution as much as the radiative top production contribution, stronger constraints are obtained than when assuming that the new operators only affect the radiative top production contribution. The constraints are stronger in the observed case than in the expected case.

		init. C_{tB}	exp. C_{tB}	Obs. C_{tB}	init. C_{tG}	exp. C_{tG}	Obs. C_{tG}	init. C_{tW}	exp. C_{tW}	Obs. C_{tW}
Photon type	radiative top production	±5.00	±7.70	± 7.00	±0.30	±0.35	±0.32	±2.00	±6.00	±5.60
	radiative top production and decay	±5.00	±7.10	±6.50	±0.30	±0.32	±0.30	±2.00	±5.60	±5.20

Table 7.4: The constraints on the EFT coefficients, obtained by performing inclusive fits to the Asimov and observed data, in the fiducial region of the $t\bar{t}\gamma$ dilepton channel. “init.” is the initial value of the coefficient used in the simulation,“exp.” is the limit obtained when fitting the Asimov data, and “Obs.” is the limit obtained when fitting the observed data

CHAPTER 8

Summary and outlook

The production cross section of a top-quark pair in association with a photon is measured using 20.2 fb^{-1}of proton–proton collision data at $\sqrt{s} = 8$ TeV, and 36.1 fb^{-1}of data at $\sqrt{s} = 13$ TeV, collected by the ATLAS detector.

The first analysis is performed in the single-lepton channel (electron or muon). Data-driven techniques are employed to estimate the main backgrounds from events with hadronic-fake or $e \rightarrow \gamma$ fake objects, and also from the smaller background contribution of QCD multijet events. The remaining background sources with prompt photons are directly estimated from simulation. The fiducial cross section is measured by minimising the profile-likelihood ratio. A tracking isolation variable that efficiently discriminates between prompt photons and hadronic-fake candidates, is employed in the likelihood fit. The differential cross section as a function of the photon p_{T} and $|\eta|$, is also measured. The cross sections are found to be in agreement with their theoretical predictions at next-to-leading order. The measurements are dominated by systematic uncertainties stemming from the hadronic-fake and $e \rightarrow \gamma$ fake templates.

The second analysis is performed in the dilepton channel. With the higher luminosity of 36.1 fb^{-1}and the increased centre-of-mass energy, a first cross-section measurement in the dilepton channel, was possible. This channel has small background contributions. The main background arises from Z+γ events in the same-flavour channel, and from hadronic fakes in the different-flavour channels. A neural network discriminator, the ELD, is reconstructed from the kinematics of the selected events. The kinematics are mainly related to jet quantities and the missing transverse momentum. The likelihood fit uses the ELD distribution in the combined dilepton channel as a discriminator. The measured spectrum is unfolded to the particle level by inverting the migration matrix, which is a mapping between particle-level and reconstructed-level objects, selected in the fiducial region. The matrix is inverted by employing the iterative Bayesian method. The differential cross section is then extracted from the unfolded distributions, in bins of photon p_{T}, photon $|\eta|$, minimum ΔR between the photon and the leptons, and the difference in the η and ϕ angles between the two leptons. The measured cross section is found to be dominated by the statistical uncertainty. The systematic uncertainty has also a significant impact: the dominant effects are due to the background modelling, the luminosity estimation and the signal modelling.

A first search for possible top-photon anomalous coupling following the effective field theory approach, in the $t\bar{t}\gamma$ fiducial region, is presented. The search involves three operators, two electroweak dipole operators, O_{tB} and O_{tW}, and one chromomagnetic operator, O_{tG}. The differential distributions of the modified cross sections due to those operators suggests that constraints on the operators can be set, especially in high photon p_{T} regions. First inclusive limits are estimated. The results show that EFT operators are only loosely constrained. However, the limits can be improved if extracted differentially, to benefit from the sensitivity of the full distributions. Moreover, the study presented includes only photons radiated from the top-quark production. As a first approximation, fractions of the radiative top-quark production, which are estimated in the SM signal sample, are used to include photons from the decay products of top quarks to the EFT samples. The additional contributions from these photons indicate that tighter constraints can be achieved. A study that properly includes the radiative top decay could further enhance the sensitivity to the electroweak dipole operator O_{tW}.

The cross section can also be measured differentially for other observables, which might be more sensitive to the EFT operators: for example, the transverse momentum of leptons, or top-related quantities such as the top-quark p_{T} and the invariant mass of the top-quark pair.

Bibliography

[1] CDF Collaboration, *Observation of top quark production in $\bar{p}p$ collisions*, Phys. Rev. Lett. **74** (1995) 2626, arXiv: `hep-ex/9503002`.

[2] DØ Collaboration, *Observation of the top quark*, Phys. Rev. Lett. **74** (1995) 2632, arXiv: `hep-ex/9503003`.

[3] ATLAS Collaboration, *The ATLAS Experiment at the CERN Large Hadron Collider*, JINST **3** (2008) S08003.

[4] CMS Collaboration, *The CMS experiment at the CERN LHC*, JINST **3** (2008) S08004.

[5] L. Evans and P. Bryant, *LHC Machine*, JINST **3** (2008) S08001.

[6] ATLAS Collaboration, *Observation of a new particle in the search for the Standard Model Higgs boson with the ATLAS detector at the LHC*, Phys. Lett. **B716** (2012) 1, arXiv: `1207.7214 [hep-ex]`.

[7] CMS Collaboration, *Observation of a new boson at a mass of 125 GeV with the CMS experiment at the LHC*, Phys. Lett. **B716** (2012) 30, arXiv: `1207.7235 [hep-ex]`.

[8] ATLAS and CMS Collaborations, *Combined Measurement of the Higgs Boson Mass in pp Collisions at $\sqrt{s} = 7$ and 8 TeV with the ATLAS and CMS Experiments*, Phys. Rev. Lett. **114** (2015) 191803, arXiv: `1503.07589 [hep-ex]`.

[9] U. Baur et al., *Probing electroweak top quark couplings at hadron colliders*, Phys. Rev. **D71** (2005) 054013, arXiv: `hep-ph/0412021`.

[10] U. Baur et al., *Probing electroweak top quark couplings at hadron and lepton colliders*, Nucl. Phys. Proc. Suppl. **160** (2006) 17, arXiv: `hep-ph/0606264`.

[11] M. Schulze and Y. Soreq, *Pinning down electroweak dipole operators of the top quark*, Eur. Phys. J. **C76** (2016) 466, arXiv: `1603.08911 [hep-ph]`.

[12] J. A. Aguilar-Saavedra, *A Minimal set of top anomalous couplings*, Nucl. Phys. **B812** (2009) 181, arXiv: `0811.3842 [hep-ph]`.

[13] C. Degrande et al., *Effective Field Theory: A Modern Approach to Anomalous Couplings*, Ann. Phys. **335** (2013) 21, arXiv: `1205.4231 [hep-ph]`.

[14] A. Buckley et al., *Constraining top quark effective theory in the LHC Run II era*, JHEP **04** (2016) 015, arXiv: `1512.03360 [hep-ph]`.

[15] N. Greiner, S. Willenbrock and C. Zhang, *Effective Field Theory for Nonstandard Top Quark Couplings*, Phys. Lett. **B704** (2011) 218, arXiv: `1104.3122 [hep-ph]`.

[16] O. Bessidskaia Bylund et al., *Probing top quark neutral couplings in the Standard Model Effective Field Theory at NLO in QCD*, JHEP **05** (2016) 052, arXiv: `1601.08193 [hep-ph]`.

[17] ATLAS Collaboration, *Measurement of the $t\bar{t}\gamma$ production cross section in proton-proton collisions at $\sqrt{s} = 8$ TeV with the ATLAS detector*, JHEP **11** (2017) 086, arXiv: `1706.03046 [hep-ex]`.

[18] B. Batool et al., *Measurement of the $t\bar{t}\gamma$ production cross-section in pp collision at $\sqrt{s} = 13$ TeV with the ATLAS detector*, ATL-COM-PHYS-2017-673, URL: `https://cds.cern.ch/record/2266485`.

[19] G. Cowan et al., *Asymptotic formulae for likelihood-based tests of new physics*, Eur. Phys. J. **C71** (2011) 1554, arXiv: `1007.1727 [physics.data-an]`.

[20] D. J. Griffiths, *Introduction to elementary particles*, John Wiley & Sons, 1987.

[21] F. Halzen and A. D. Martin, *Quarks and leptons : an introductory course in modern particle physics*, Wiley, 1984.

[22] G. 't Hooft and M. J. G. Veltman, *Regularization and Renormalization of Gauge Fields*, Nucl. Phys. **B44** (1972) 189.

[23] S. L. Glashow, *Partial Symmetries of Weak Interactions*, Nucl. Phys. **22** (1961) 579.

[24] S. Weinberg, *A Model of Leptons*, Phys. Rev. Lett. **19** (1967) 1264.

[25] A. Salam and J. C. Ward, *Gauge theory of elementary interactions*, Phys. Rev. **136** (1964) B763.

[26] C. Patrignani et al. (Particle Data Group), *Review of Particle Physics*, Chin. Phys. **C40** (2016) 100001.

[27] F. Englert and R. Brout, *Broken Symmetry and the Mass of Gauge Vector Mesons*, Phys. Rev. Lett. **13** (1964) 321.

[28] P. W. Higgs, *Broken Symmetries and the Masses of Gauge Bosons*, Phys. Rev. Lett. **13** (1964) 508.

[29] P. W. Higgs, *Spontaneous Symmetry Breakdown without Massless Bosons*, Phys. Rev. **145** (1966) 1156.

[30] J. Ellis, G. Fogli and E. Lisi, *Indirect bounds on the Higgs boson mass from precision electroweak data*, Phys. Rev. Lett. **318** (1993) 148.

[31] DØ Collaboration, *Measurement of the differential cross sections for isolated direct photon pair production in $p\bar{p}$ collisions at $\sqrt{s}$ = 1.96 TeV*, Phys. Lett. **B725** (2013) 6, arXiv: `1301.4536 [hep-ex]`.

[32] ATLAS Collaboration, *Measurements of integrated and differential cross sections for isolated photon pair production in pp collisions at $\sqrt{s} = 8$ TeV with the ATLAS detector*, Phys. Rev. **D95** (2017) 112005, arXiv: `1704.03839 [hep-ex]`.

[33] ATLAS Collaboration, *Measurement of the cross section for isolated-photon plus jet production in pp collisions at $\sqrt{s} = 13$ TeV using the ATLAS detector*, arXiv: `1801.00112 [hep-ex]`.

[34] ATLAS, CDF, CMS and DØ Collaborations, *First combination of Tevatron and LHC measurements of the top-quark mass*, arXiv: `1403.4427 [hep-ex]`.

[35] ATLAS Collaboration, *Measurement of the production cross-section of a single top quark in association with a Z boson in proton–proton collisions at 13 TeV with the ATLAS detector*, arXiv: `1710.03659 [hep-ex]`.

[36] M. Czakon, P. Fiedler and A. Mitov,
Total Top-Quark Pair-Production Cross Section at Hadron Colliders Through $O(\alpha_S^4)$,
Phys. Rev. Lett. **110** (2013) 252004, arXiv: `1303.6254 [hep-ph]`.

[37] M. Czakon and A. Mitov,
NNLO corrections to top pair production at hadron colliders: the quark-gluon reaction,
JHEP **01** (2013) 080, arXiv: `1210.6832 [hep-ph]`.

[38] M. Czakon and A. Mitov, *NNLO corrections to top-pair production at hadron colliders: the all-fermionic scattering channels*, JHEP **12** (2012) 054, arXiv: `1207.0236 [hep-ph]`.

[39] M. Czakon and A. Mitov,
Top++: A Program for the Calculation of the Top-Pair Cross-Section at Hadron Colliders,
Comput. Phys. Commun. **185** (2014) 2930, arXiv: `1112.5675 [hep-ph]`.

[40] M. Cacciari et al., *Top-pair production at hadron colliders with next-to-next-to-leading logarithmic soft-gluon resummation*, Phys. Lett. **B710** (2012) 612,
arXiv: `1111.5869 [hep-ph]`.

[41] ATLAS Collaboration, *Measurement of the* $t\bar{t}$ *production cross-section using* $e\mu$ *events with b-tagged jets in pp collisions at* $\sqrt{s} = 13$ *TeV with the ATLAS detector*,
Phys. Lett. **B761** (2016) 136, arXiv: `1606.02699 [hep-ex]`.

[42] CMS Collaboration, *Measurement of the* $t\bar{t}$ *production cross section using events in the* $e\mu$ *final state in pp collisions at* $\sqrt{s} = 13$ *TeV*, Eur. Phys. J. **C77** (2017) 172,
arXiv: `1611.04040 [hep-ex]`.

[43] LHC Top Physics Working Group, *LHCTopWG Summary Plots, 2017*,
URL: `https://twiki.cern.ch/twiki/bin/view/LHCPhysics/LHCTopWGSummaryPlots`.

[44] M. Antola et al., *Minimal Super Technicolor*, Eur. Phys. J. **C71** (2011) 1784,
arXiv: `1001.2040 [hep-ph]`.

[45] CMS Collaboration,
Measurement of the semileptonic $\mathrm{t\bar{t}} + \gamma$ *production cross section in pp collisions at* $\sqrt{s} = 8$ *TeV*,
JHEP **10** (2017) 006, arXiv: `1706.08128 [hep-ex]`.

[46] ATLAS Collaboration, *Measurement of the* $t\bar{t}Z$ *and* $t\bar{t}W$ *production cross sections in multilepton final states using* $3.2\,fb^{-1}$ *of pp collisions at* $\sqrt{s} = 13$ *TeV with the ATLAS detector*,
Eur. Phys. J. **C77** (2017) 40, arXiv: `1609.01599 [hep-ex]`.

[47] CMS Collaboration, *Measurement of the cross section for top quark pair production in association with a W or Z boson in proton-proton collisions at* $\sqrt{s} = 13$ *TeV*,
arXiv: `1711.02547 [hep-ex]`.

[48] ATLAS Collaboration, *Evidence for the associated production of the Higgs boson and a top quark pair with the ATLAS detector*, arXiv: `1712.08891 [hep-ex]`.

[49] CMS Collaboration, *Evidence for associated production of a Higgs boson with a top quark pair in final states with electrons, muons, and hadronically decaying* τ *leptons at* $\sqrt{s} = 13$ *TeV*,
arXiv: `1803.05485 [hep-ex]`.

[50] B. Grzadkowski and M. Misiak,
Anomalous Wtb coupling effects in the weak radiative B-meson decay,
Phys. Rev. **D78** (2008) 077501, arXiv: `0802.1413 [hep-ph]`.

[51] J. Brod et al., *Probing anomalous* $t\bar{t}Z$ *interactions with rare meson decays*, JHEP **02** (2015) 141.

[52] ATLAS Collaboration,
Measurement of the top quark charge in pp collisions at $\sqrt{s} = 7$ *TeV with the ATLAS detector*,
JHEP **11** (2013) 031, arXiv: `1307.4568 [hep-ex]`.

[53] K. Melnikov, M. Schulze and A. Scharf,
QCD corrections to top quark pair production in association with a photon at hadron colliders,
Phys. Rev. **D83** (2011) 074013, arXiv: `1102.1967 [hep-ph]`.

[54] P.-F. Duan et al., *QCD corrections to associated production of* $t\bar{t}\gamma$ *at hadron colliders*,
Phys. Rev. D **80** (2009) 014022.

[55] W. T. Giele, Z. Kunszt and K. Melnikov, *Full one-loop amplitudes from tree amplitudes*,
JHEP **04** (2008) 049, arXiv: `0801.2237 [hep-ph]`.

[56] R. K. Ellis et al., *Masses, fermions and generalized D-dimensional unitarity*,
Nucl. Phys. **B822** (2009) 270, arXiv: `0806.3467 [hep-ph]`.

[57] M. Cacciari, G. P. Salam and G. Soyez, *The Anti-*k_t *jet clustering algorithm*,
JHEP **04** (2008) 063, arXiv: `0802.1189 [hep-ph]`.

[58] M. Schulze, *Private communication*.

[59] CDF Collaboration, *Evidence for* $t\bar{t}\gamma$ *Production and Measurement of* $\sigma_{t\bar{t}\gamma}/\sigma_{t\bar{t}}$,
Phys. Rev. **D84** (2011) 031104, arXiv: `1106.3970 [hep-ex]`.

[60] ATLAS Collaboration, *Measurement of the inclusive* $t\bar{t}\gamma$ *cross section with the ATLAS detector*,
ATLAS-CONF-2011-153, URL: `https://cds.cern.ch/record/1398197`.

[61] ATLAS Collaboration,
Observation of top-quark pair production in association with a photon and measurement of the $t\bar{t}\gamma$ *production cross section in pp collisions at* $\sqrt{s} = 7$ *TeV using the ATLAS detector*,
Phys. Rev. **D91** (2015) 072007, arXiv: `1502.00586 [hep-ex]`.

[62] J. Papavassiliou and C. Parrinello,
Gauge invariant top quark form-factors from e^+e^- *experiments*, Phys. Rev. **D50** (1994) 3059,
arXiv: `hep-ph/9311284`.

[63] S. D. Rindani, *Effect of anomalous tbW vertex on decay lepton distributions in* $e^+e^- \to t\bar{t}$ *and CP violating asymmetries*, Pramana **54** (2000) 791, arXiv: `hep-ph/0002006`.

[64] C. Lefèvre, *The CERN accelerator complex. Complexe des accélérateurs du CERN*,
URL: `https://cds.cern.ch/record/1260465`.

[65] C. Patrignani et al., *Review of Particle Physics*, Chin. Phys. **C40** (2016) 100001.

[66] C. Grupen and I. Buvat, eds., *Handbook of particle detection and imaging, vol. 1 and vol. 2*,
Springer, Berlin Germany, 2012.

[67] S. Tavernier, *Experimental Techniques in Nuclear and Particle Physics*,
Springer, Berlin Germany, 2010.

[68] D. H. Perkins, *Introduction to high energy physics; 4th ed.* Cambridge Univ. Press, 2000.

[69] C. W. Fabjan and F. Gianotti, *Calorimetry for particle physics*, Rev. Mod. Phys. **75** (2003) 1243.

[70] ATLAS Collaboration,
dE/dx measurement in the ATLAS Pixel Detector and its use for particle identification,
ATLAS-CONF-2011-016, URL: `https://cds.cern.ch/record/1336519`.

[71] C Kourkoumelis and S Vourakis, *HYPATIA—an online tool for ATLAS event visualization*, Phys.Educ **49** (2014) 21.

[72] *Magnetic filed system at ATLAS detector*, URL: `http://www.jetgoodson.com/images/thesisImages/magnetSystems.png`.

[73] M. Capeans et al., *ATLAS Insertable B-Layer Technical Design Report*, 2010, URL: `https://cds.cern.ch/record/1291633`.

[74] ATLAS Collaboration, *Track Reconstruction Performance of the ATLAS Inner Detector at* $\sqrt{s} = 13$ *TeV*, ATL-PHYS-PUB-2015-018, URL: `https://cds.cern.ch/record/2037683`.

[75] F. Hügging, *The ATLAS Pixel Insertable B-layer (IBL)*, Nucl. Instr. Meth. **A650** (2011) 45, arXiv: `1012.2742 [physics.ins-det]`.

[76] T. Cornelissen et al., *The new ATLAS track reconstruction (NEWT)*, J. Phys. Conf. Ser. **119** (2008) 032014.

[77] R. Frühwirth, *Application of Kalman filtering to track and vertex fitting*, Nucl. Instrum. Meth. **A262** (1987) 444.

[78] T. Cornelissen et al., *The global* χ^2 *track fitter in ATLAS*, J. Phys. Conf. Ser. **119** (2008) 032013.

[79] A. Flórez et al., *Searching for New Heavy Neutral Gauge Bosons using Vector Boson Fusion Processes at the LHC*, Phys. Lett. **B767** (2017) 126, arXiv: `1609.09765 [hep-ph]`.

[80] ATLAS Collaboration, *Luminosity Public Results for Run1*, URL: `https://twiki.cern.ch/twiki/bin/view/AtlasPublic/LuminosityPublicResults`.

[81] ATLAS Collaboration, *RunStatsPublicResults*, URL: `https://twiki.cern.ch/twiki/bin/view/AtlasPublic/RunStatsPublicResults`.

[82] ATLAS Collaboration, *Luminosity PublicResults for Run2*, URL: `https://twiki.cern.ch/twiki/bin/view/AtlasPublic/LuminosityPublicResultsRun2`.

[83] J. Pumplin et al., *New generation of parton distributions with uncertainties from global QCD analysis*, JHEP **07** (2002) 012, arXiv: `hep-ph/0201195`.

[84] M. A. Dobbs et al., *Les Houches guidebook to Monte Carlo generators for hadron collider physics*, arXiv: `hep-ph/0403045`.

[85] A. D. Martin et al., *Parton distributions for the LHC*, Eur. Phys. J. **C63** (2009) 189, arXiv: `0901.0002 [hep-ph]`.

[86] R. D. Ball et al., *Parton distributions with LHC data*, Nucl. Phys. **B867** (2013) 244, arXiv: `1207.1303 [hep-ph]`.

[87] H.-L. Lai et al., *New parton distributions for collider physics*, Phys.Rev. **D82** (2010) 074024, arXiv: `1007.2241 [hep-ph]`.

[88] R. D. Ball et al., *Parton distributions for the LHC Run II*, JHEP **04** (2015) 040, arXiv: `1410.8849 [hep-ph]`.

[89] J. Butterworth et al., *PDF4LHC recommendations for LHC Run II*, J. Phys. **G43** (2016) 023001, arXiv: `1510.03865 [hep-ph]`.

[90] M. L. Mangano et al.,
ALPGEN, a generator for hard multiparton processes in hadronic collisions,
JHEP **07** (2003) 001, arXiv: `hep-ph/0206293`.

[91] T. Stelzer and W. F. Long, *Automatic generation of tree level helicity amplitudes*,
Comput. Phys. Commun. **81** (1994) 357, arXiv: `hep-ph/9401258`.

[92] J. Alwall et al., *The automated computation of tree-level and next-to-leading order differential cross sections, and their matching to parton shower simulations*, JHEP **07** (2014) 079,
arXiv: `1405.0301 [hep-ph]`.

[93] J. Alwall et al., *MadGraph 5 : Going Beyond*, JHEP **06** (2011) 128,
arXiv: `1106.0522 [hep-ph]`.

[94] J. Alwall et al., *MadGraph/MadEvent v4: the new web generation*, JHEP **0709** (2007) 028,
arXiv: `hep_ph/0706.2334`.

[95] T. Gleisberg et al., *Event generation with SHERPA 1.1*, JHEP **02** (2009) 007,
arXiv: `0811.4622 [hep-ph]`.

[96] S. Frixione, P. Nason and C. Oleari,
Matching NLO QCD computations with parton shower simulations: the POWHEG method,
JHEP **11** (2007) 070, arXiv: `0709.2092 [hep-ph]`.

[97] S. Alioli et al., *A general framework for implementing NLO calculations in shower Monte Carlo programs: the POWHEG BOX*, JHEP **06** (2010) 043, arXiv: `1002.2581 [hep-ph]`.

[98] T. Sjöstrand, S. Mrenna and P. Skands, *PYTHIA 6.4 physics and manual*, JHEP **05** (2006) 026,
arXiv: `hep-ph/0603175`.

[99] T. Sjostrand, S. Mrenna and P. Z. Skands, *A Brief Introduction to PYTHIA 8.1*,
Comput. Phys. Commun. **178** (2008) 852, arXiv: `0710.3820 [hep-ph]`.

[100] T. Sjöstrand et al., *An Introduction to PYTHIA 8.2*, Comput. Phys. Commun. **191** (2015) 159,
arXiv: `1410.3012 [hep-ph]`.

[101] E. Barberio and Z. Was,
PHOTOS: A universal Monte Carlo for QED radiative corrections: version 2.0,
Comput. Phys. Commun. **79** (1994) 291.

[102] P. Golonka and Z. Was,
PHOTOS Monte Carlo: a precision tool for QED corrections in Z and W decays,
Eur. Phys. J. **45** (2006) 97, arXiv: `hep-ph/0506026`.

[103] ATLAS Collaboration, *Summary of ATLAS Pythia 8 tunes*, ATL-PHYS-PUB-2012-003,
URL: `https://cds.cern.ch/record/1474107`.

[104] S. Agostinelli et al., *GEANT4: A Simulation toolkit*, Nucl. Instrum. Meth. **A506** (2003) 250.

[105] F. Maltoni and T. Stelzer, *MadEvent: Automatic event generation with MadGraph*,
JHEP **02** (2003) 027, arXiv: `hep-ph/0208156`.

[106] H. Murayama, I. Watanabe and K. Hagiwara,
HELAS: HELicity amplitude subroutines for Feynman diagram evaluations,
URL: `http://inspirehep.net/record/336604/`.

[107] N. D. Christensen and C. Duhr, *FeynRules - Feynman rules made easy*,
Comput. Phys. Commun. **180** (2009) 1614, arXiv: `0806.4194 [hep-ph]`.

[108] C. Degrande et al., *UFO - The Universal FeynRules Output*, Comput. Phys. Commun. **183** (2012) 1201, arXiv: `1108.2040 [hep-ph]`.

[109] P. de Aquino et al., *ALOHA: Automatic Libraries Of Helicity Amplitudes for Feynman Diagram Computations*, Comput. Phys. Commun. **183** (2012) 2254, arXiv: `1108.2041 [hep-ph]`.

[110] ATLAS Collaboration, *The ATLAS Simulation Infrastructure*, Eur. Phys. J. **C70** (2010) 823, arXiv: `1005.4568 [physics.ins-det]`.

[111] ATLAS Collaboration, *Measurements of top-quark pair differential cross-sections in the $e\mu$ channel in pp collisions at $\sqrt{s} = 13$ TeV using the ATLAS detector*, Eur. Phys. J. **C77** (2017) 292, arXiv: `1612.05220 [hep-ex]`.

[112] M. Czakon, D. Heymes and A. Mitov, *Dynamical scales for multi-TeV top-pair production at the LHC*, JHEP **04** (2017) 071, arXiv: `1606.03350 [hep-ph]`.

[113] P. Z. Skands, *Tuning Monte Carlo Generators: The Perugia Tunes*, Phys. Rev. **D82** (2010) 074018, arXiv: `1005.3457 [hep-ph]`.

[114] ATLAS Collaboration, *ATLAS Run 1 Pythia8 tunes*, ATL-PHYS-PUB-2014-021, URL: `https://cds.cern.ch/record/1966419`.

[115] G. Corcella et al., *HERWIG 6: an event generator for hadron emission reactions with interfering gluons (including supersymmetric processes)*, JHEP **01** (2001) 010, arXiv: `hep-ph/0011363`.

[116] J. M. Butterworth, J. R. Forshaw and M. H. Seymour, *Multiparton interactions in photoproduction at HERA*, Z. Phys. C **72** (1996) 637, arXiv: `hep-ph/9601371`.

[117] J. Bellm et al., *Herwig 7.0/Herwig++ 3.0 release note*, Eur. Phys. J. **C76** (2016) 196, arXiv: `1512.01178 [hep-ph]`.

[118] S. Alioli et al., *NLO single-top production matched with shower in POWHEG: s- and t-channel contributions*, JHEP **09** (2009) 111, arXiv: `0907.4076 [hep-ph]`.

[119] E. Re, *Single-top Wt-channel production matched with parton showers using the POWHEG method*, Eur. Phys. J. **C71** (2011) 1547, arXiv: `1009.2450 [hep-ph]`.

[120] N. Kidonakis, *NNLL resummation for s-channel single top quark production*, Phys. Rev. **D81** (2010) 054028, arXiv: `1001.5034 [hep-ph]`.

[121] N. Kidonakis, *Next-to-next-to-leading-order collinear and soft gluon corrections for t-channel single top quark production*, Phys. Rev. **D83** (2011) 091503, arXiv: `1103.2792 [hep-ph]`.

[122] N. Kidonakis, *Two-loop soft anomalous dimensions for single top quark associated production with a W- or H-*, Phys. Rev. **D82** (2010) 054018, arXiv: `1005.4451 [hep-ph]`.

[123] ATLAS Collaboration, *Electron reconstruction and identification efficiency measurements with the ATLAS detector using the 2011 LHC proton-proton collision data*, Eur. Phys. J. **C74** (2014) 2941, arXiv: `1404.2240 [hep-ex]`.

[124] ATLAS Collaboration, *Electron efficiency measurements with the ATLAS detector using 2012 LHC proton–proton collision data*, Eur. Phys. J. **C77** (2017) 195, arXiv: `1612.01456 [hep-ex]`.

[125] ATLAS Collaboration, *Electron efficiency measurements with the ATLAS detector using the 2015 LHC proton–proton collision data*, ATLAS-CONF-2016-024, URL: `https://cds.cern.ch/record/2157687`.

[126] ATLAS Collaboration, *Measurement of the muon reconstruction performance of the ATLAS detector using 2011 and 2012 LHC proton–proton collision data*, Eur. Phys. J. **C74** (2014) 3130, arXiv: `1407.3935 [hep-ex]`.

[127] ATLAS Collaboration, *Muon reconstruction performance of the ATLAS detector in proton–proton collision data at $\sqrt{s}$ =13 TeV*, Eur. Phys. J. **C76** (2016) 292, arXiv: `1603.05598 [hep-ex]`.

[128] ATLAS Collaboration, *Object selection and calibration, background estimations and MC samples for the Winter 2013 Top Quark analyses with 2012 data*, ATL-COM-PHYS-2013-088, URL: `https://cds.cern.ch/record/1509562`.

[129] K. Rehermann and B. Tweedie, *Efficient identification of boosted semileptonic top quarks at the LHC*, JHEP **03** (2011) 059, arXiv: `1007.2221 [hep-ph]`.

[130] J.-B. De Vivie De Regie et al., *ATLAS electron, photon and muon isolation in Run 2*, ATL-COM-PHYS-2017-290, URL: `https://cds.cern.ch/record/2256658`.

[131] ATLAS Collaboration, *Measurement of the photon identification efficiencies with the ATLAS detector using LHC Run-1 data*, Eur. Phys. J. **C76** (2016) 666, arXiv: `1606.01813 [hep-ex]`.

[132] ATLAS Collaboration, *Photon identification in 2015 ATLAS data*, ATL-PHYS-PUB-2016-014, URL: `https://cds.cern.ch/record/2203125`.

[133] W. Lampl et al., *Calorimeter Clustering Algorithms: Description and Performance*, ATL-LARG-PUB-2008-002, URL: `https://cds.cern.ch/record/1099735`.

[134] ATLAS Collaboration, *Jet energy measurement with the ATLAS detector in proton–proton collisions at $\sqrt{s} = 7$ TeV*, Eur. Phys. J. C **73** (2013) 2304, arXiv: `1112.6426 [hep-ex]`.

[135] ATLAS Collaboration, *Performance of pile-up mitigation techniques for jets in pp collisions at $\sqrt{s} = 8$ TeV using the ATLAS detector*, Eur. Phys. J. **C76** (2016) 581, arXiv: `1510.03823 [hep-ex]`.

[136] ATLAS Collaboration, *Tagging and suppression of pileup jets with the ATLAS detector*, ATLAS-CONF-2014-018, URL: `https://cds.cern.ch/record/1700870`.

[137] ATLAS Collaboration, *Performance of b-Jet Identification in the ATLAS Experiment*, JINST **11** (2016) P04008, arXiv: `1512.01094 [hep-ex]`.

[138] V. Kostyukhin, *Secondary vertex based b-tagging*, ATL-PHYS-2003-033, URL: `http://inspirehep.net/record/1195848`.

[139] ATLAS Collaboration, *Secondary vertex finding for jet flavour identification with the ATLAS detector*, ATL-PHYS-PUB-2017-011, URL: `https://cds.cern.ch/record/2270366`.

[140] ATLAS Collaboration,
Optimisation of the ATLAS b-tagging performance for the 2016 LHC Run,
ATL-PHYS-PUB-2016-012, URL: `https://cds.cern.ch/record/2160731`.

[141] P. C. Bhat, *Multivariate Analysis Methods in Particle Physics*,
Ann. Rev. Nucl. Part. Sci. **61** (2011) 281.

[142] ATLAS Collaboration, *Expected performance of the ATLAS b-tagging algorithms in Run-2*,
ATL-PHYS-PUB-2015-022, URL: `https://cds.cern.ch/record/2037697`.

[143] ATLAS Collaboration, *Performance of missing transverse momentum reconstruction for the ATLAS detector in the first proton-proton collisions at at $\sqrt{s}$= 13 TeV*,
ATL-PHYS-PUB-2015-027, URL: `https://cds.cern.ch/record/2037904`.

[144] W. Verkerke and D. Kirkby, *The RooFit toolkit for data modeling*, arXiv: `physics/0306116`.

[145] L. Moneta et al., *The RooStats Project*, arXiv: `1009.1003 [physics.data-an]`.

[146] ATLAS Collaboration, *Measurement of the top quark-pair production cross section with ATLAS in pp collisions at $\sqrt{s} = 7$ TeV*, Eur. Phys. J. **C71** (2011) 1577, arXiv: `1012.1792 [hep-ex]`.

[147] M. J. Oreglia, *A study of the reactions $\psi' \to \gamma\gamma\psi$*, SLAC-R-236, 1980,
URL: `http://www.slac.stanford.edu/cgi-wrap/getdoc/slac-r-236.pdf`.

[148] N. B. Atlay et al., *Measurement of the $t\bar{t}\gamma$ production cross section at $\sqrt{s} = 8\ TeV$ in 20.3fb^{-1} of pp collision data collected with the ATLAS detector*, ATL-COM-PHYS-2015-1524,
URL: `https://cds.cern.ch/record/2114747`.

[149] F.A. Berends et al., *On the production of a W and jets at hadron colliders*,
Nucl. Phys. **B357** (1991) 32.

[150] ATLAS Collaboration, *Jet energy measurement and its systematic uncertainty in proton–proton collisions at $\sqrt{s} = 7$ TeV with the ATLAS detector*, Eur. Phys. J. C **75** (2015) 17,
arXiv: `1406.0076 [hep-ex]`.

[151] ATLAS Collaboration,
Luminosity determination in pp collisions at $\sqrt{s} = 8$ TeV using the ATLAS detector at the LHC,
Eur. Phys. J. **C76** (2016) 653, arXiv: `1608.03953 [hep-ex]`.

[152] ATLAS Collaboration,
Electron and photon energy calibration with the ATLAS detector using LHC Run 1 data,
Eur. Phys. J. C **74** (2014) 3071, arXiv: `1407.5063 [hep-ex]`.

[153] ATLAS Collaboration, *Performance of the ATLAS Trigger System in 2015*,
Eur. Phys. J. **C77** (2017) 317, arXiv: `1611.09661 [hep-ex]`.

[154] S. Heer, *Modeling and measuring the $t\bar{t}\gamma$ process with the ATLAS detector at 8 TeV*,
Master thesis, Bonn University, 2015, URL: `https://cds.cern.ch/record/2146397`.

[155] M. Cacciari, G. P. Salam and G. Soyez, *The Catchment Area of Jets*, JHEP **04** (2008) 005,
arXiv: `0802.1188 [hep-ph]`.

[156] M. Cacciari and G. P. Salam, *Pileup subtraction using jet areas*, Phys. Lett. **B659** (2008) 119,
arXiv: `0707.1378 [hep-ph]`.

[157] F. Chollet et al., *Keras*, `https://github.com/fchollet/keras`.

[158] D. H. Guest et al., *lwtnn/lwtnn: Release for Athena v21*,
URL: `https://doi.org/10.5281/zenodo.290682`.

[159] V. Blobel, *An Unfolding method for high-energy physics experiments*, arXiv: hep-ex/0208022.

[160] F. Spanò, *Unfolding in particle physics: a window on solving inverse problems*, URL: http://inspirehep.net/record/1344095/.

[161] G. D'Agostini, *Improved iterative Bayesian unfolding*, arXiv: 1010.0632 [physics.data-an].

[162] A. Höcker and V. Kartvelishvili, *SVD approach to data unfolding*, Nucl. Instrum. Meth. **A372** (1996) 469, arXiv: hep-ph/9509307.

[163] *RooUnfold package*, URL: http://hepunx.rl.ac.uk/~adye/software/unfold/RooUnfold.html.

[164] A. Kalogeropoulos and J. Alwall, *The SysCalc code: A tool to derive theoretical systematic uncertainties*, arXiv: 1801.08401 [hep-ph].

[165] W. Buttinger, *Using Event Weights to account for differences in Instantaneous Luminosity and Trigger Prescale in Monte Carlo and Data*, ATL-COM-SOFT-2015-119, URL: https://cds.cern.ch/record/2014726.

[166] ATLAS Collaboration, *Electron and photon energy calibration with the ATLAS detector using data collected in 2015 at* $\sqrt{s}$ = 13 TeV, ATL-PHYS-PUB-2016-015, URL: https://cds.cern.ch/record/2203514.

[167] ATLAS Collaboration, *Jet energy scale measurements and their systematic uncertainties in proton-proton collisions at* $\sqrt{s}$ = 13 *TeV with the ATLAS detector*, Phys. Rev. **D96** (2017) 072002, arXiv: 1703.09665 [hep-ex].

[168] ATLAS Collaboration, *Jet Calibration and Systematic Uncertainties for Jets Reconstructed in the ATLAS Detector at* $\sqrt{s}$ = 13 *TeV*, ATL-PHYS-PUB-2015-015, URL: https://cds.cern.ch/record/2037613.

[169] ATLAS Collaboration, *Calibration of b-tagging using dileptonic top pair events in a combinatorial likelihood approach with the ATLAS experiment*, ATLAS-CONF-2014-004, URL: http://cds.cern.ch/record/1664335.

[170] ATLAS Collaboration, *Calibration of the performance of b-tagging for c and light-flavour jets in the 2012 ATLAS data*, ATLAS-CONF-2014-046, URL: http://cds.cern.ch/record/1741020.

[171] A. Tonero and R. Rosenfeld, *Dipole-induced anomalous top quark couplings at the LHC*, Phys. Rev. D **90** (2014) 017701, arXiv: 1404.2581 [hep-ex].

[172] Ranzosi, Diogo Buarque and Zhang, Cen, *Probing the top-quark chromomagnetic dipole moment at next-to-leading order in QCD*, Phys. Rev. D **91** (11 2015) 114010, arXiv: 1503.08841 [hep-ex].

[173] J. A. Aguilar-Saavedra, B. Fuks and M. L. Mangano, *Pinning down top dipole moments with ultraboosted tops*, Phys. Rev. D **91** (2015) 094021, arXiv: 1412.6654 [hep-ph].

[174] A. Buckley et al., *Rivet user manual*, Comput. Phys. Commun. **184** (2013) 2803, arXiv: 1003.0694 [hep-ph].

APPENDIX A

Single secondary vertex finding algorithm

In proton–proton collisions, there are many sources of track vertices, such as: b- and c-hadron decays, photon conversions, V^0 decays, hadronic interactions with the detector materials or fake vertices. The latter are more often produced in environments with large track multiplicity. The Secondary Vertex Finder (SVF) algorithm is used to reconstruct a displaced vertex of the b-hadron decay inside a jet (see Figure 4.8). The algorithm results in a list of reconstructed secondary vertices (SVs) and their information, which are taken by the SV-based b-tagging algorithm [137]. The vertexing and the relative b-tagging algorithms were successfully exploited by the ATLAS collaboration for data analysis in Run I. The SVF algorithm was first presented in Ref. [138]. Since then it underwent several performance improvements. The working principle of the SVF algorithm and its Run II upgrades are discussed in Ref. [139], and are summarised in this appendix. The information provided by the SVF algorithm are fed to an ATLAS combined b-tagging algorithm based on multi-variate techniques [140–142] which provides the best separation between the different jet flavours.

One of the operation modes of the SVF algorithm is the Single Secondary Vertex Finder (SSVF). The SSVF tries to reconstruct a single secondary vertex per jet. For a b-jet containing both b- and c-hadron decay vertices, the SSVF merges these vertices into a common single vertex if they are close, or reconstructs the vertex with the largest track multiplicity if they are far apart. The resolution of the ATLAS tracking detector does not allow to resolve reliably the cascade decays of b- and c-hadrons in every jet. Quite often either b- or c-vertex contains only one reconstructed track and cannot be reconstructed alone. Therefore, the search for a single secondary vertex in a b-jet is justified and the found vertex should preserve most of the information necessary for the b-tagging. The general idea of the single vertex finding algorithm works as follows:

1. A list of tracks within a jet are provided to the algorithm. The list undergoes strict quality requirements (Section A.2).

2. Find all two-track vertices from the above selected tracks (Section A.3).

3. Identify and reject as many two-track vertices as possible, that are unrelated to the b-/c-hadron vertex (Section A.3.1).

4. Convert the cleaned two-track vertex set into a multi-track vertex set by merging the two-track vertices which are close in space (Section A.4).

A.1 Samples

The results in this appendix are obtained using simulated $pp \to t\bar{t}$ events at a centre-of-mass energy of $\sqrt{s} = 13$ TeV, generated using the Powheg-Box [96, 97] generator interfaced to Pythia 6 [98] for parton showering and hadronisation, with the Perugia 2012 tune [113].

Jets are reconstructed using the anti-k_t algorithm [57]. A cone of size 0.4 is used to associate tracks to jets. Jets are required to have a transverse momentum of $p_T > 40$ GeV to suppress contribution of jets produced in pile-up interactions. These jets are flavour labelled by matching jets to the truth-level weakly decaying b- and c-hadrons. If a b-hadron is found within a ΔR cone of 0.4, then the jet is labelled as a b-jet. If no b-hadron is found, the search is repeated for c-hadrons, if a c-hadron is found and no τ leptons are found, the jet is then labelled as a c-jet. If no match is found for c, b, or τ, the jet is labelled as a light-flavour jet.

A.2 Track selection

The SSVF algorithm receives a user-prepared set of tracks as an input. Out of those, the algorithm selects the tracks within a jet volume of $\Delta R = 0.4$[1] and fulfilling the basic quality requirements presented in Table A.1. These requirements are designed to select well-reconstructed tracks, rejecting tracks from material interactions, photon conversions, long-lived particle (K^0_S, Λ) decays, pile-up events, etc.

Each track is required to have at least seven silicon hits (sum of SCT and Pixel hits, see Section 3.3.3 for detector description), and at most one hit is shared between tracks. A track quality fit (χ^2 per degree of freedom) > 3 is imposed. To reduce the influence of hadronic interactions in the ID material, the track transverse impact parameter is required to fulfill $|d_0| < 5$ mm, where d_0 (see Figure 4.8) is the transverse distance of the track to the primary vertex (PV) of the event. The longitudinal impact parameter is required to be $|z_0| < 25$ mm, z_0 is the z-coordinate of the track at the primary vertex. The error in measuring $|d_0|$ and z_0 distances is required to be less than 1 mm and 5 mm respectively.

High p_T jets ($\gtrsim 300$ GeV) suffer from increasing multiplicity of tracks produced in jet fragmentation. Jets in the high $|\eta| > 1.5$ region suffer from the increasing amount of detector material leading to worse resolution and increased hadronic interaction rate [74]. Additional track cleaning is required for these jets to mitigate the negative influence on the secondary vertex finding efficiency (extra selections in Table A.1).

- High η region: Due to the new insertable B-layer in the inner detector [73–75], the minimal number of requested hits in the silicon detectors is increased by one for the tracks in the detector end-caps. This allows to reduce the SV fake rate caused by the detector material.

- Jets with high track multiplicity: The increase of the track multiplicity increases the probability to reconstruct fake vertices. To reduce the number of fakes, tracks are ordered according to their p_T and at most the 25 tracks with largest p_T are accepted and used in the secondary vertex search. This requirement mainly affects tracks in high p_T jets which have high track multiplicities.

- Pile-up tracks: Tracks with low transverse impact significance σ_d[2], and high longitudinal impact significance σ_z[3] are classified as pile-up tracks. Those tracks are removed to reduce the number of fake vertices.

---

[1] Value 0.4 can be changed by a user.

[2] The transverse distance of the track from the transverse position of the primary vertex divided by its error.

[3] The z-coordinate for the tracks with respect to the z-position of the primary vertex divided by its error.

- Track impact significance: To suppress tracks coming from the event primary vertex, a requirement on the 3D track impact significance $\sigma_{3D} = \sqrt{{\sigma_d}^2 + {\sigma_z}^2}$ is applied. In the signed σ_d and σ_z track significance plane, the tracks coming from b-hadron decays are present mostly in one quadrant with positive σ_d, σ_z. Therefore, to maximise an acceptance to the secondary tracks, the 3D significance requirement is made asymmetric $\sigma_{3D} = \sqrt{(\sigma_d - 0.6)^2 + (\sigma_z - 0.6)^2} > 2$. The tuning parameter 0.6 is obtained by maximising the amount of reconstructed vertices in b-jets with respect to the amount of fake vertices in light jets.

Variable	Description	Value
	Basic track quality requirements	
`SctHits`	Minimum allowed number of SCT hits	4
`PixelHits`	Minimum allowed number of Pixel hits	1
`SiHits`	Minimum allowed number of Pixel+SCT hits	7
`BlayHits`	Minimum allowed number of b-layer hits	0
`SharedHits`	Maximum allowed number of shared hits	1
`CutPt`	Minimum allowed p_{T}	700 MeV
`CutZVrt`	Maximum allowed longitudinal impact parameter z_0	25 mm
`Cutd0`	Maximum allowed transverse impact parameter d_0	5 mm
`CutChi2`	Maximum allowed χ^2	3
`ConeForTag`	Maximum allowed ΔR around the jet direction for track selection	0.4
`d0TrkErrorCut`	Maximum allowed d_0 error	1 mm
`ZTrkErrorCut`	Maximum allowed z_0 error	5 mm
	Extra track requirements	
`TrackInJetNumberLimit`	Maximum number of tracks in jet for vertex search (ordered by p_{T})	25
`AntiPileupSigRCut`	Maximum allowed σ_d significance for pileup tracks	2
`AntiPileupSigZCut`	Minimum allowed σ_z significance for pileup tracks	6
`TrkSigCut`	Minimum allowed significance of 3D distance between track and primary vertex	2

Table A.1: The basic and the extra improved track selections in the single secondary vertex finding algorithm. The variable name is mentioned as implemented in the SSVF tool, and will be used as in Figure A.1.

Figure A.1 illustrates the basic track selection described in Table A.1 as a function of jet η for both b-labelled and light-labelled jets. The requirements are added incrementally and the number of tracks passing the selections for each jet η is plotted as a profile plot (mean values). The following features are observed:

- The mean value of selected tracks is ~ 7 for light jets and ~ 9 for b-jets.
- The largest amount of tracks in a jet is removed by the z_0 requirement (in blue). This selection aims at removing pile-up tracks inside jets.

- A selection inefficiency is observed at $|\eta| \geq 1.5$ for b-jets due to the d_0 requirement (orange), while the number of selected tracks is expected to be independent of η (compare the orange with the remaining colours just below the orange).
- Other track quality requirements reduce in total the reconstructed-track yield in a jet by $\sim 15-20\%$

Figure A.2 illustrates the same basic track selection criteria but for tracks originating only from a b-/c-hadron decay inside a b-jet. Figure A.2 confirms that tracks stemming from b-/c-hadron decays are mostly not affected by the applied track selections, while tracks from other sources are removed as shown in Figure A.1.

Figure A.3 shows the transverse and the longitudinal track impact parameters significance (track impact parameter divided by its error) of the tracks passing all the requirements (in Table A.1) and used in the SV reconstruction. The long tail of the transverse impact significance in b-jets is due to the long lived b-hadrons inside the jets, and the b-hadron decays tend to have positive signed impact parameters.

A.3 Two-track vertex selection

The set of tracks passing the track selections (Table A.1) are used to form all possible two-track vertices. The sum of the two significances of the tracks in the two-track vertex is required to be larger than 2. An additional requirement is needed to further reduce pile-up; the three dimensional significance of the distance of the two-track vertex from the primary vertex is required to be larger than 3. Finally the χ^2 requirement of the fitted two-track vertex is made to be at most of 4.5.

A.3.1 Cleaning of two-track vertices

To additionally reduce fake vertices and material interaction, and to achieve higher purity for the final secondary vertex reconstruction, extra cleaning requirements are applied:

- Material rejection requirement: Hadronic interactions with the detector material are rejected based on a comparison of the vertex radius with radii of cylindrical material layers. The nuisance two-track vertices produced by hadronic interactions are identified by their radial positions and removed from further consideration if their radii are consistent within the detector material position. Figure A.4 demonstrates the radial distribution of the two-track vertices reconstructed in light jets. Peaks due to hadronic interactions are clearly visible at radii corresponding to the Pixel detector layers (~34 mm, ~51 mm, ~89 mm, ~123 mm) and beampipe wall (~25 mm) (see also Figure 3.7 for a schematic view of the detector).
- Environments with high track density (e.g. in the core of a jet or in events with very high pileup) suffer from the large fractions of fake vertices. Such fake vertices can be suppressed by exploiting the following observation: any secondary track should not have associated detector hits with radii smaller than the radius of the SV found by the algorithm. This observation is used to remove fake vertices by requiring that the hit patterns of the tracks associated to a two-track vertex are consistent with the position of the reconstructed secondary vertex inside the tracking detector.
- Some of the reconstructed two-track vertices are coming from K^0, Λ^0 decays and photon conversions. For a proper reconstruction of the $b-/c$-decays, these nuisance vertices have to be removed. V^0 decay vertices are identified by their masses. The masses of particles (proton, pion or electron) are assigned to the same set of tracks and the vertex invariant mass is then computed. In case of

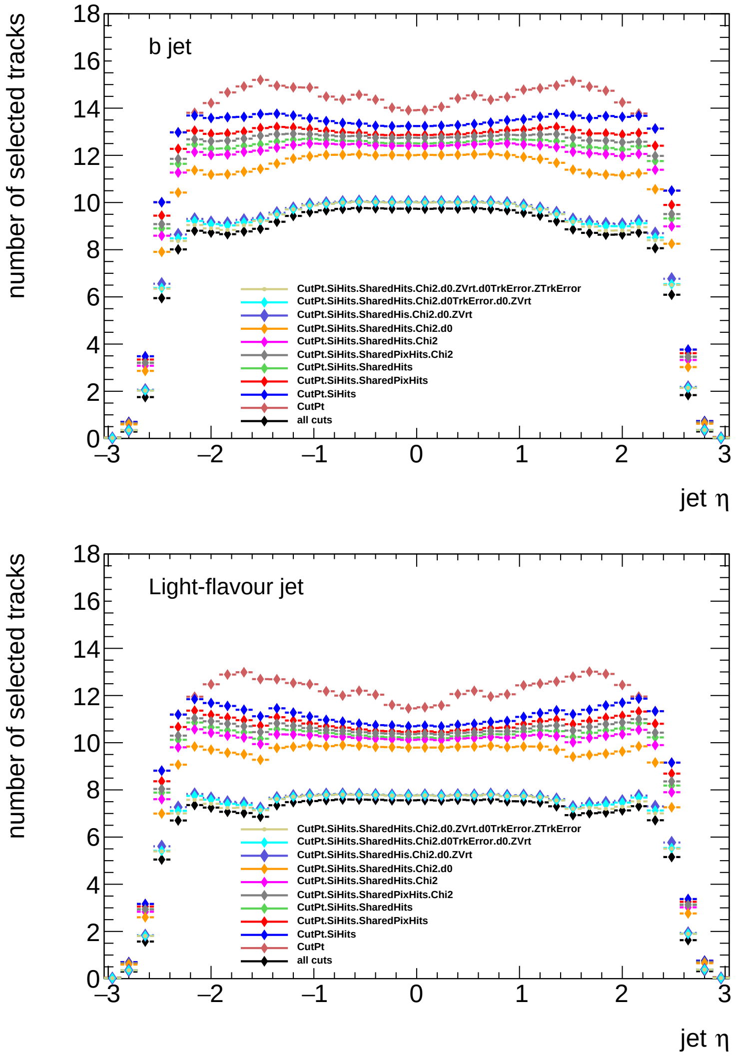

Figure A.1: The basic track selection requirements as a function of jet η for b-jets (top) and light jets (bottom). The applied values described in Table A.1 are used incrementally, starting with the p_T requirement (brown), and adding the silicon hits (dark blue), shared pixel hits (red), shared hits (green), χ^2 (gray, pink), d_0 (orange), z_0 (purple), d_0 track error (light blue), z_0 track error (dark green) requirement and all basic requirements in Table A.1 (black).

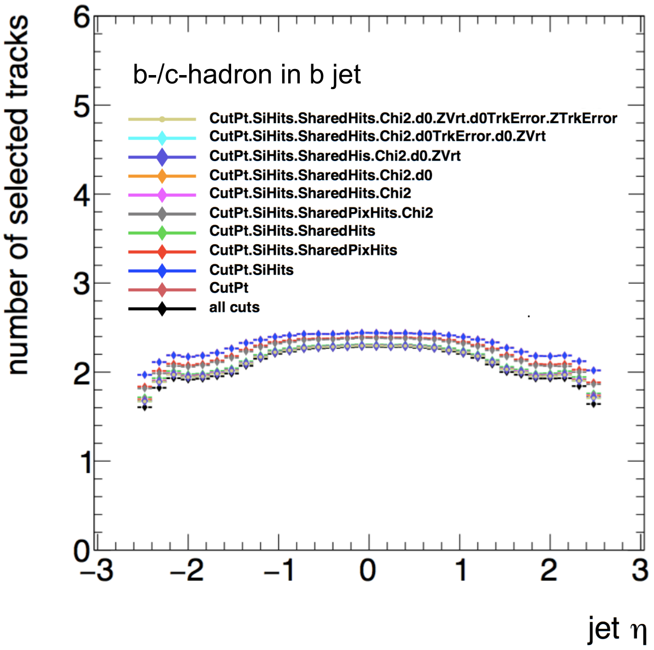

Figure A.2: The basic track selection requirements as a function η for b-jets. The selections are applied to tracks coming from b-/c-hadron decay. The applied values described in Table A.1 are used incrementally, starting with the p_T requirement (brown), and adding the silicon hits (dark blue), shared pixel hits (red), shared hits (green), χ^2 (gray, pink), d_0 (orange), z_0 (purple), d_0 track error (light blue), z_0 track error (dark green) requirement and all basic requirements in Table A.1 (black).

the $p\pi$ hypothesis the proton mass is assigned to the track with the highest p_T, while the pion mass is assigned to the lowest p_T-track. Conversion vertices are identified as a low mass peak assuming the e^+e^- track hypothesis. Figure A.5 shows the invariant mass distributions of $\pi^+\pi^-$ with a peak of K^0 decay, $p\pi$ with a peak of Λ^0 decays and e^+e^- with a conversion peak. The impact parameters to event primary vertex of the obtained combined V^0 tracks are calculated. If the obtained impact parameter of the V^0 track is small, the two charged tracks coming from this vertex are marked as bad tracks and do not participate in the subsequent combined vertex search.

- The SSVF is specially designed to look for b- and c-hadron decays, therefore any two-track vertex with an invariant mass larger than 6 GeV is removed.

The effects of the removal of material interactions and the cleaning of V^0 as a function of the radial distance between the final reconstructed secondary vertices and the nearest material layer (see Figure A.4) are shown in Figure A.6. Different combinations of the two requirements are shown in the figure: none of the requirement is applied, only the material rejection is applied, only the V^0 cleaning is required, and finally both of the material rejection and the vertex cleaning requirements are imposed. Hadronic interaction vertices are concentrated at the low end of these distributions, as can be clearly seen in the light-flavour jet plot, where a contribution of such vertices is significant. The vertices in b-jets are practically unaffected by the combined vertex cleaning procedure, while number of the reconstructed vertices (mainly fake ones) in the light jets is significantly reduced.

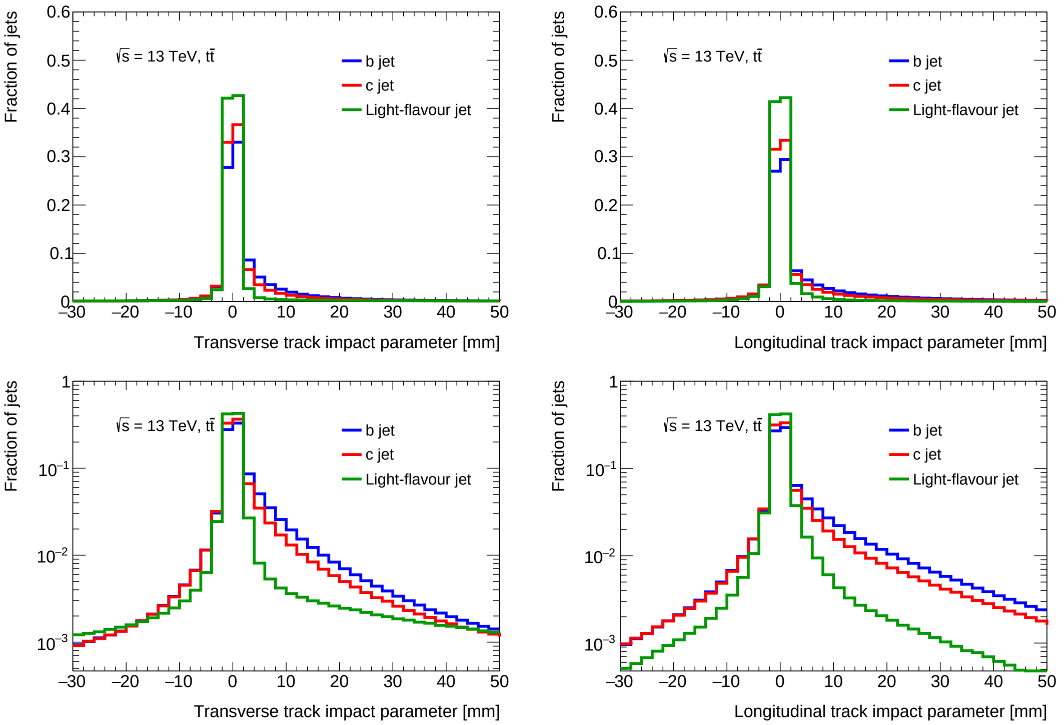

Figure A.3: The distributions of the transverse (left) and longitudinal (right) track impact significance of the tracks used in the final reconstructed inclusive SV, if found. Bottom panels are the same distributions but using a log scale for the y-axis. The distributions are normalised to one.

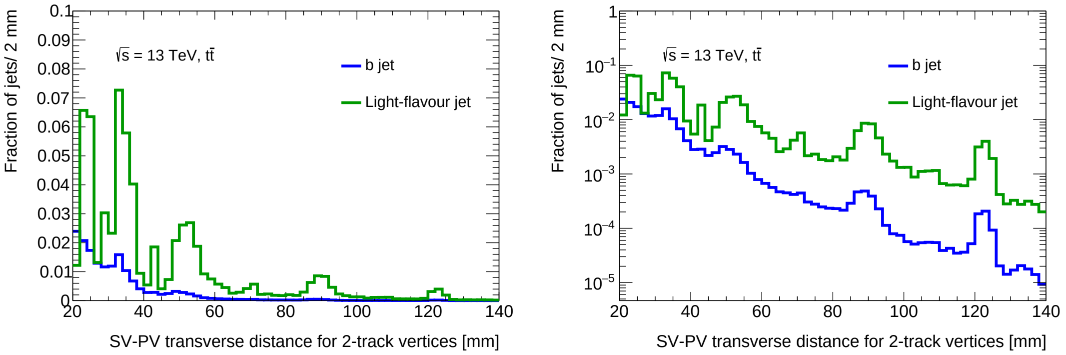

Figure A.4: The radial distribution of the reconstructed two-track vertices (left) in *b*-jets (blue) and light-flavour jets (green) with peaks due to hadronic interactions in the Pixel detector layers and beampipe wall. Panel (right) shows the same distribution in a log scale for better visibility of the peaks. The distributions are normalised to one.

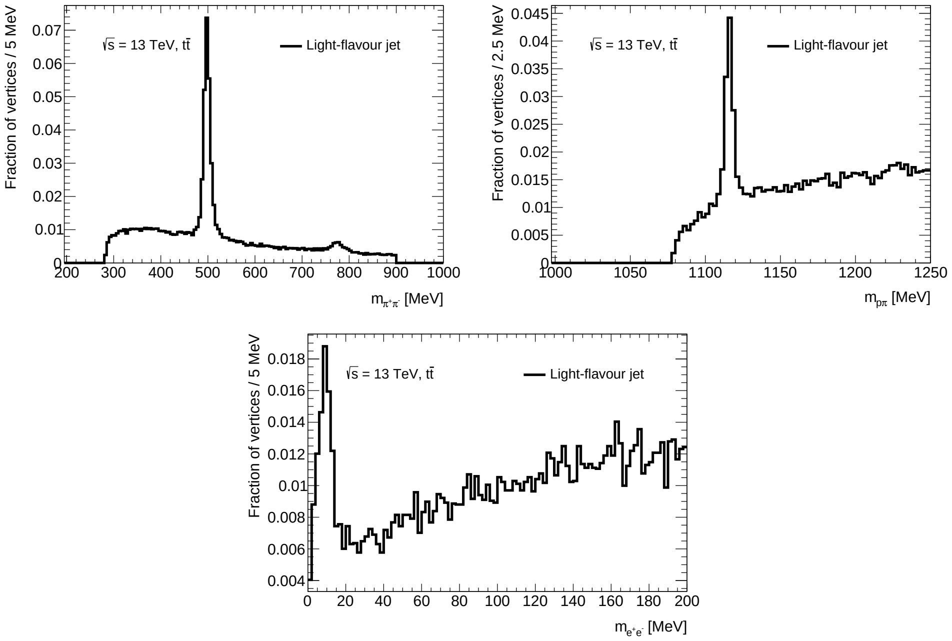

Figure A.5: The invariant mass spectra of $\pi^+\pi^-$ (top-left), $p\pi$ (top-right) and e^+e^- coming from photon conversions (bottom) in light jets. The distributions are normalised to one.

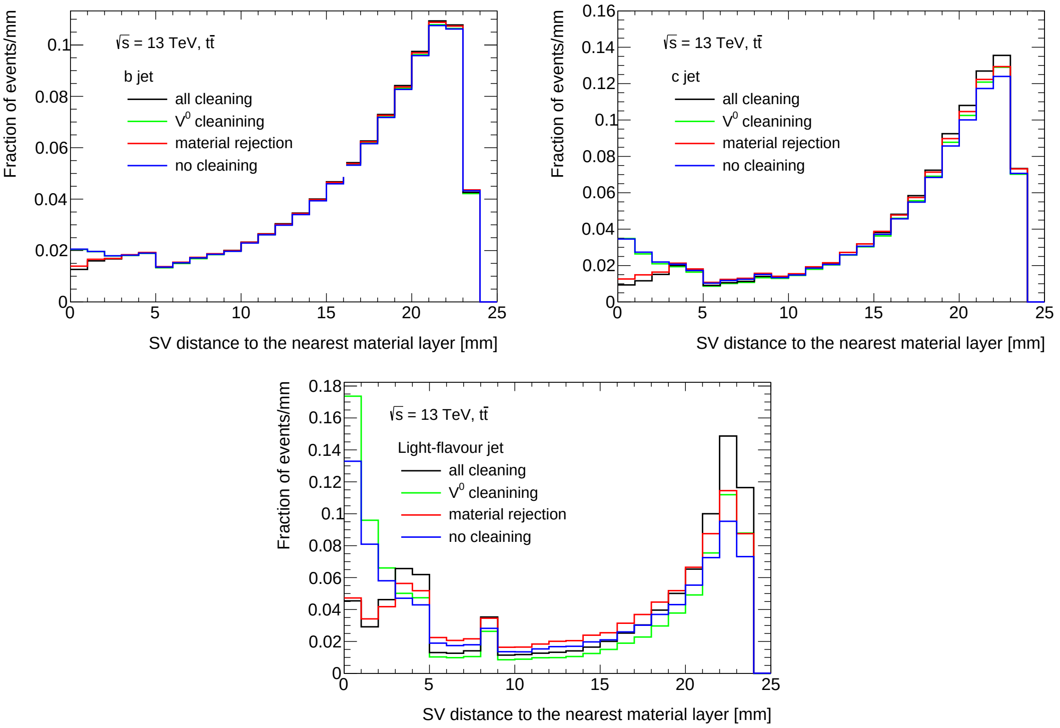

Figure A.6: The distance to nearest material layer distributions for different selections in b-jets (top-left), c-jets (top-right), light jets (bottom), with applying the material rejection and vertex cleaning (black), the vertex cleaning only (green), the material rejection only (red), or none of the requirements (blue). The distributions are normalised to one.

A.4 Single secondary vertex search

All tracks contributing to the cleaned two-track vertices (Section A.3) are combined into one list of selected tracks. This track list is supplied to the vertex fitter. The vertex fitter runs iteratively on all the tracks in the list; trying to fit one secondary vertex (SV) out of all these tracks. In each iteration the track with the largest χ^2 of the track-vertex association is removed and the vertex fit is re-done until an acceptable vertex χ^2 and a vertex invariant mass < 6 GeV are obtained.

Finally all tracks in the jet, that passed the selections listed in Table A.1 but not included into the reconstructed SV, are tested for compatibility with the secondary vertex. The χ^2 of the track-secondary vertex association should be small enough and smaller than the χ^2 of the corresponding track-primary vertex association. If such a track is found, it is included into the secondary vertex.

If the obtained vertex after the iterative fit procedure contains only two tracks, the vertex cleaning (see Section A.3.1) is applied again, this step reduces considerably the fake rate of the SSVF.

A.5 Properties of secondary vertices

Several variables are computed by the SSVF algorithm for the final secondary vertices. Some of these interesting variables are introduced in this section.

The normalised distributions of the SV properties are shown in Figure A.7; the SV mass, the number of two-track vertices, the energy ratio of the tracks contributing to the SV to the sum of energies of all the tracks in the jet, the ΔR of the flight direction with respect to the jet axis, the 3D SV-PV distance divided by its error (3D decay length significance) and the SV transverse distance to the primary vertex. These properties are an important input to the multivariate b-tagging algorithm MV2 [140, 142]. Some of those variables are used as inputs to the SV based b-tagging algorithms, those particular ones are shown in Figure A.8. Figure A.8 shows the profile distribution (the mean value) of the SV properties, as a function of jet η and p_T. The parameters are chosen due to being relatively independent of jet η. However, the number of two-track vertices reaches a maximum value in the central η region inside b-jets. On the other hand, the reconstructed secondary vertex mass, the energy fraction and the SV distance to material layers are independent of jet η. The mean values of the same variables are also shown as a function of jet p_T in the same Figure A.8. The distributions illustrate one of the challenges faced by SV reconstruction in high p_T jets. The higher jet p_T causes a higher track multiplicity and more reconstruction of two-track vertices. Many of these two-track vertices are fakes, merging them into one secondary vertex gives a fake vertex. This effect increases significantly at high jet p_T, and the SV properties are becoming less discriminating as shown in the figure.

A.6 Performance of the single secondary vertex finder

The reconstructed secondary vertices inside a jet are retrieved, and the reconstruction efficiency of the SV is plotted as a function of jet p_T and η. The new settings of the SSVF (extra selections described in Table A.1 and Section A.3.1) are compared to the old settings for light-flavour and b-jets in Figure A.9. The upgrade of the SSVF has increased significantly its rejection power to remove fake vertices, and also improved its reconstruction efficiency in b-jets, especially in the high p_T regions.

The SV reconstruction efficiencies in the three jet flavours as a function of jet η were shown in Figure 4.9. An average of ~ 80% reconstruction efficiencies is achieved in b-jets, in the central region of the detector, and a drop of the reconstruction efficiency is observed at $|\eta| \geq 1.5$ inside b- and c-jets. The probability to have fake secondary vertices in light jets shows very low values in the central region but an

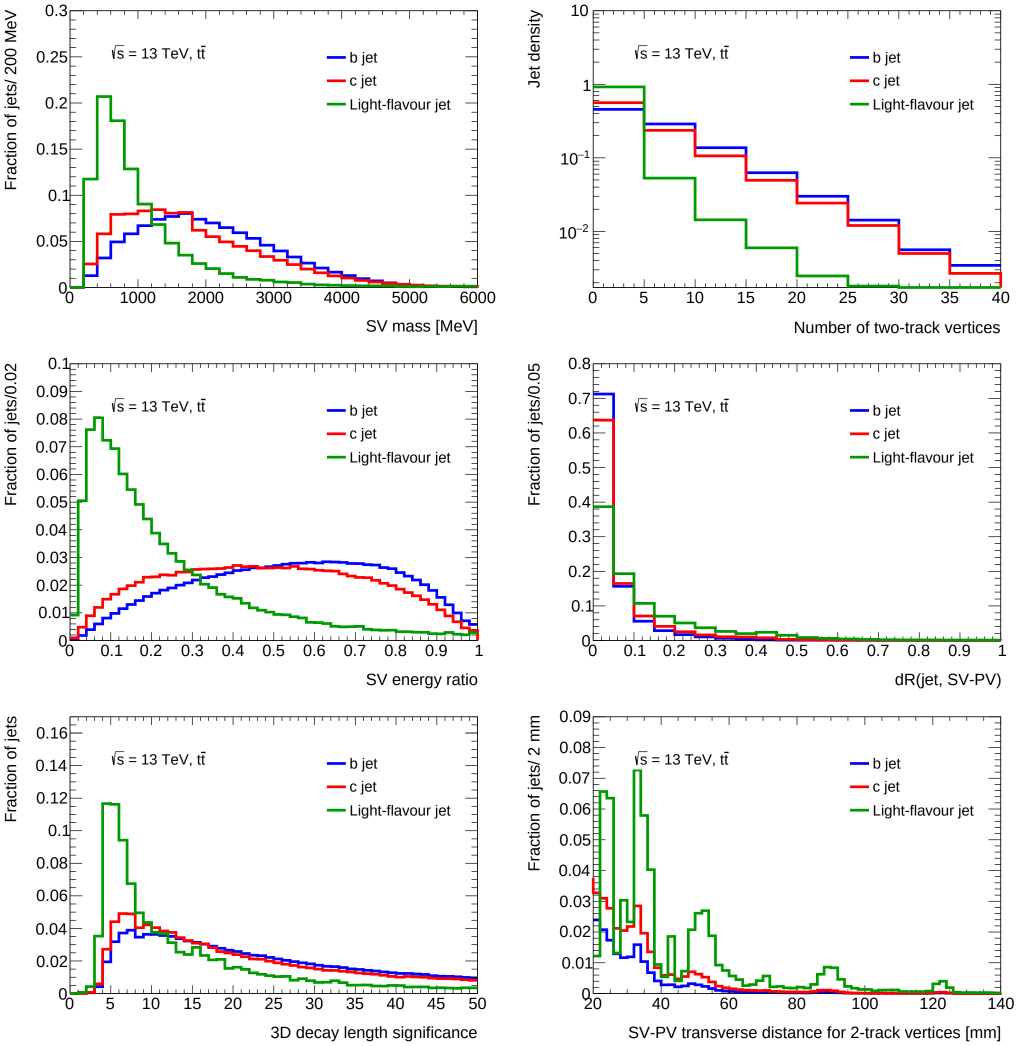

Figure A.7: The distributions of the secondary vertex properties for *b*-jet (blue), *c*-jet (red) and light-flavour jet (green). The distributions are normalised to one.

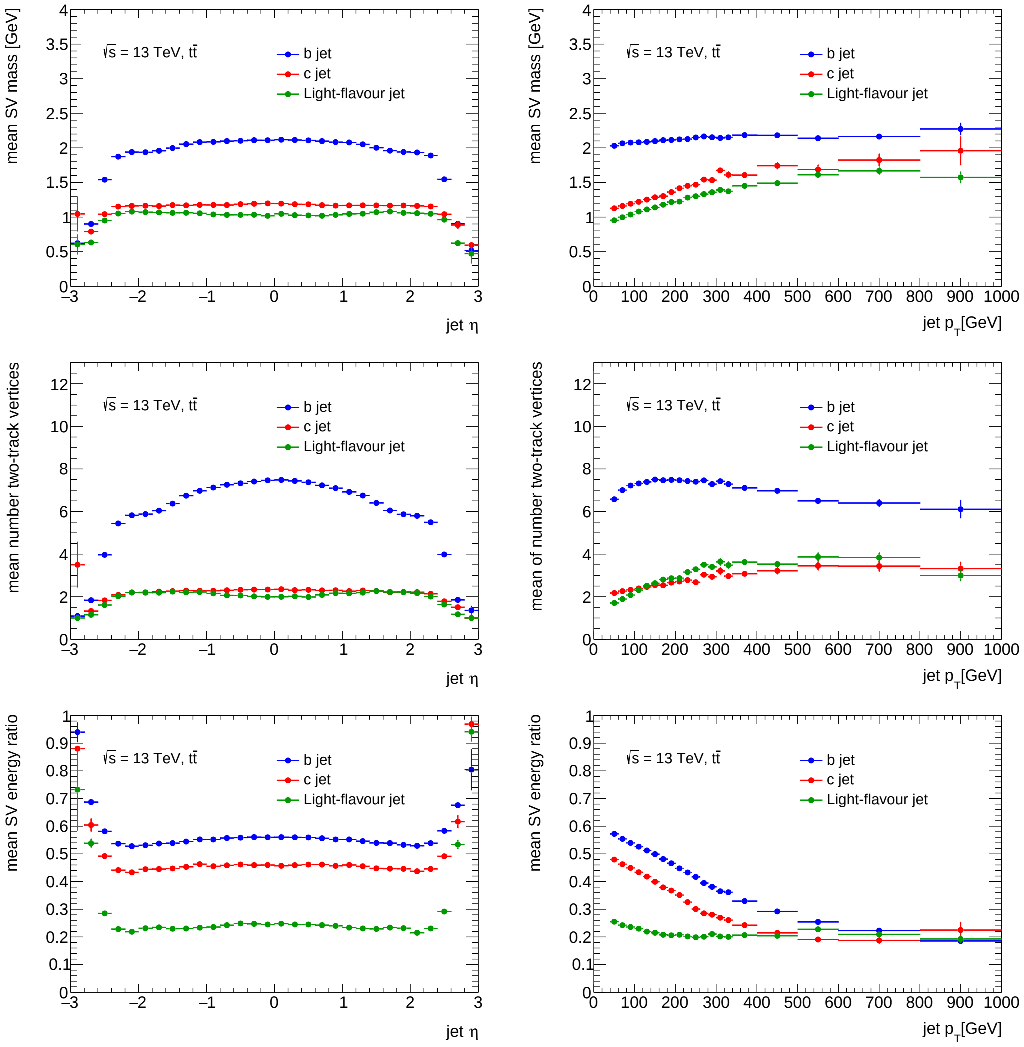

Figure A.8: The mean values of secondary vertex properties as a function of jet η (left column) and jet p_{T} (right column) for b-jet (blue), c-jet (red), light-flavour jet (green).

increase at high η regions, due to pile-up and large number of material interactions. On average, the c-jet and light-jet efficiencies are found to be 30% and <5%, respectively.

The SV reconstruction efficiencies as a function of the jet p_T were also shown in the same Figure 4.9. The increase of tracks from fragmentation in high p_T jets is a more likely reason for the performance degradation. As shown in the figure, the number of fake vertices is increasing with jet p_T in light jets, while the SV reconstruction efficiencies slightly decrease with jet p_T.

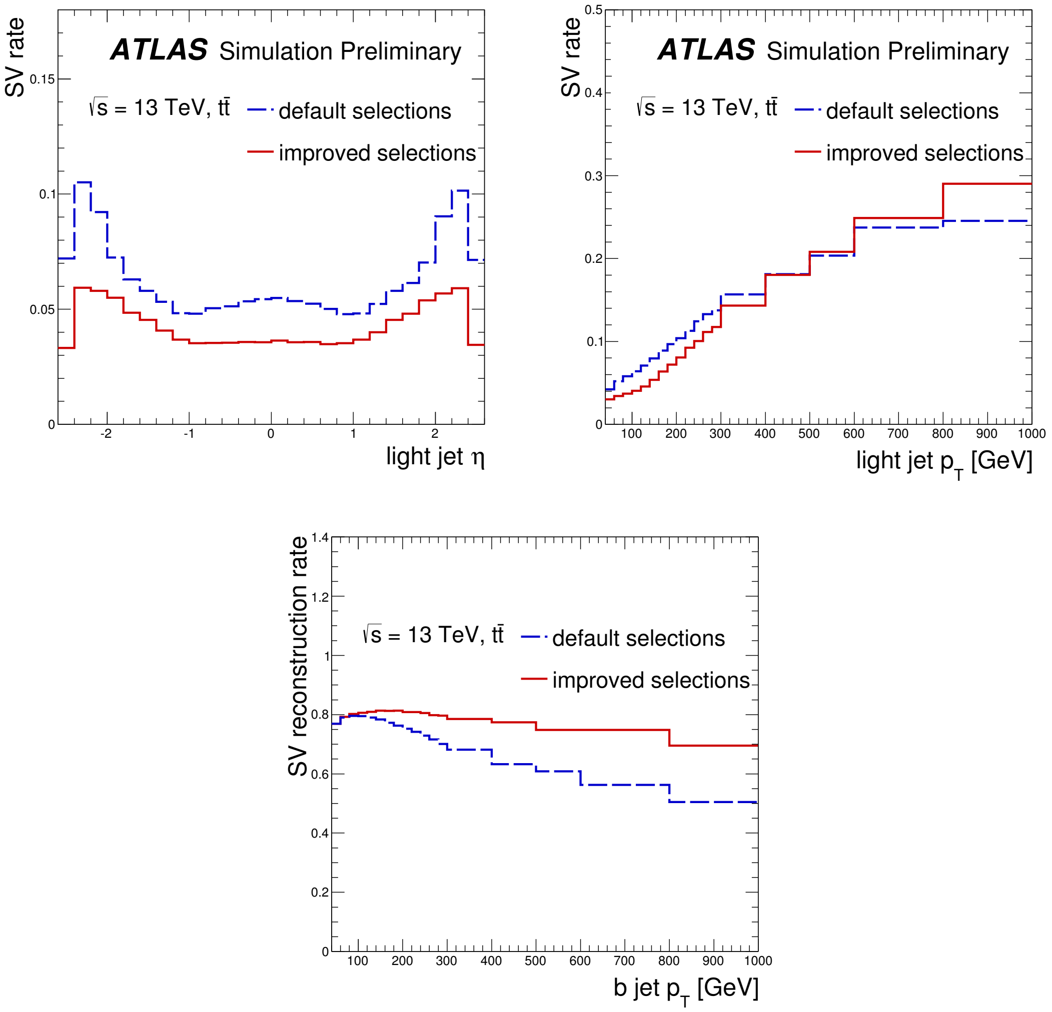

Figure A.9: The fraction of fake vertices in light-flavour jets, as a function of the jet η (top-left), and the jet p_T (top-right) [140], the plots compare the initial settings of the SSVF in blue to the improved settings in red. The bottom panel shows the same comparison in b-jets as a function of the jet p_T.

APPENDIX B

Z+γ validation region

A selection of distributions in the Z+γ validation region VR1, as defined in Section 6.3.1, is shown in Figure B.1 and Figure B.2 for the ee and $\mu\mu$ channels, respectively.

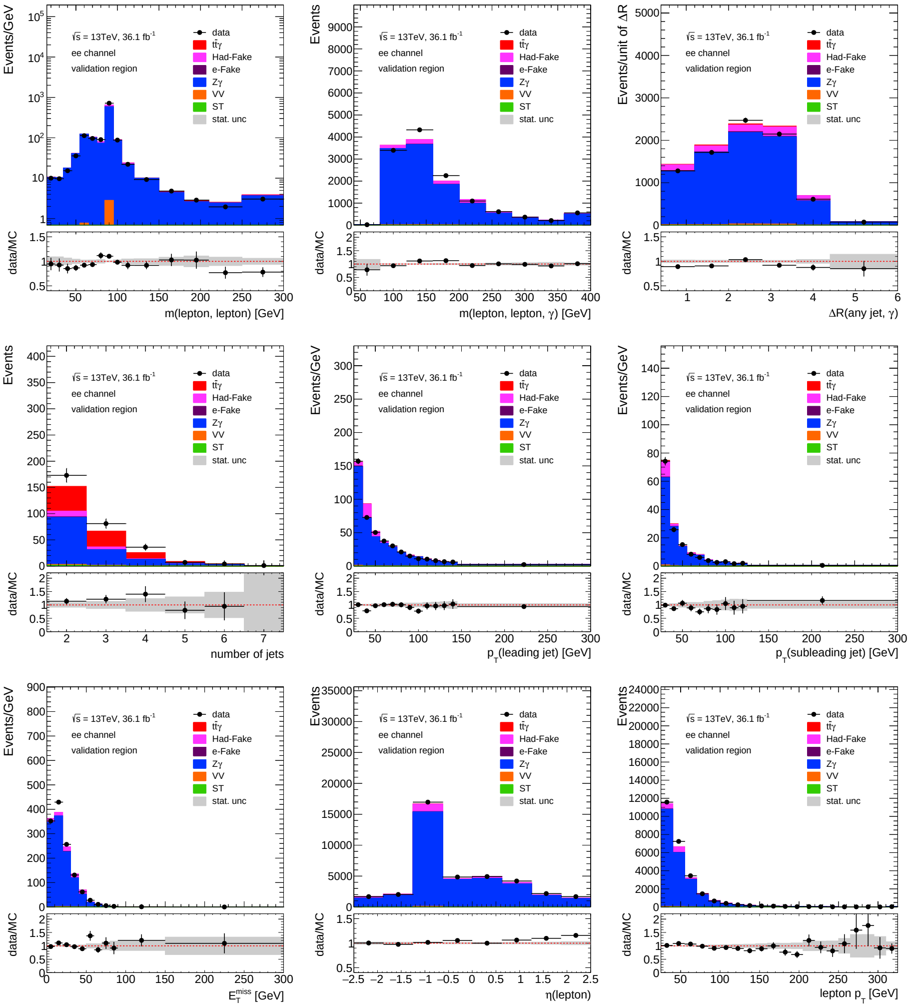

Figure B.1: A selection of pre-fit distributions in Z+γ VR1 for the *ee* channel. Only statistical uncertainties are shown.

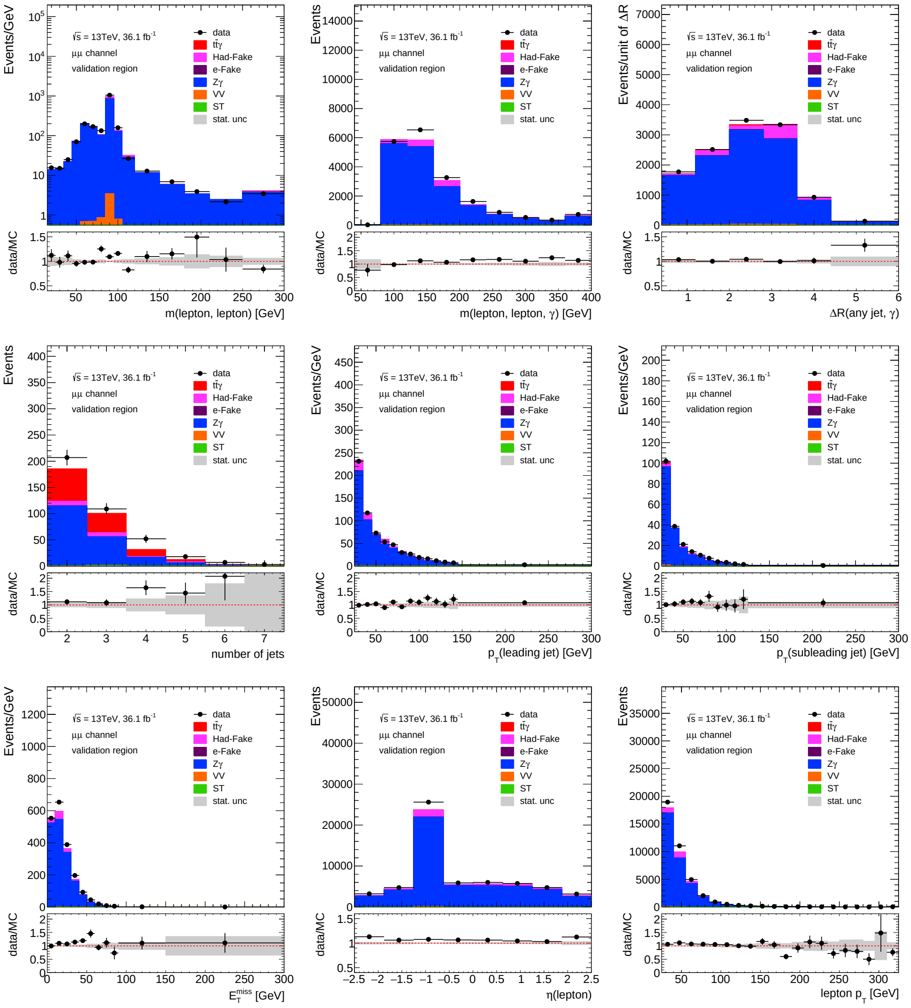

Figure B.2: A selection of pre-fit distributions in the Z+γ VR1 for the $\mu\mu$ channel. Only statistical uncertainties are shown.

APPENDIX C

Pre-fit distributions in the three dilepton channels

A selection of pre-fit distributions in the $e\mu$, ee and $\mu\mu$, and combined dilepton channels is shown in Figures C.1, C.2, C.3 and C.4, respectively.

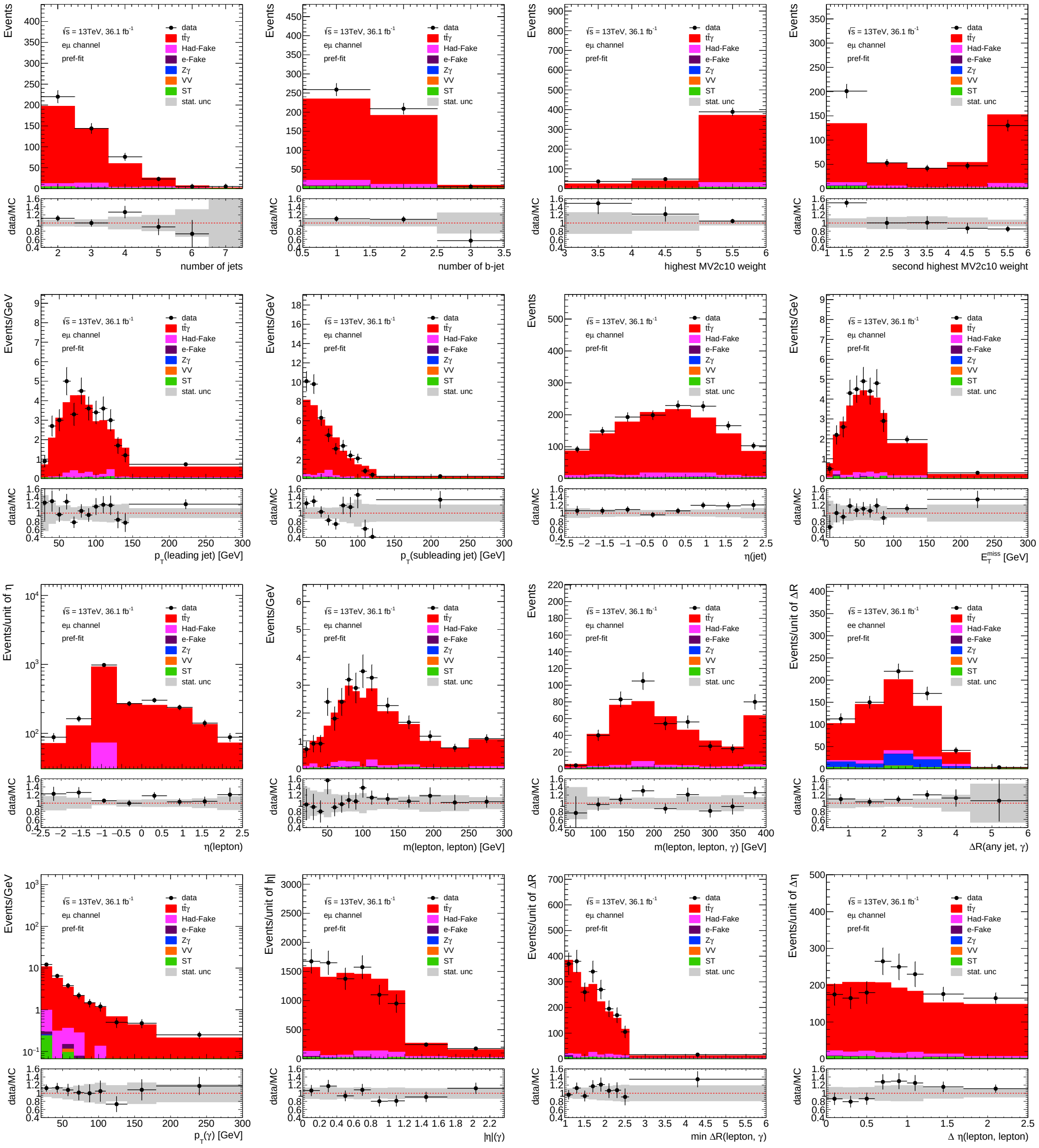

Figure C.1: A selection of pre-fit distributions in the $e\mu$ channel. All background processes are estimated based on simulations and are described in Section 6.3. Only statistical uncertainties are shown.

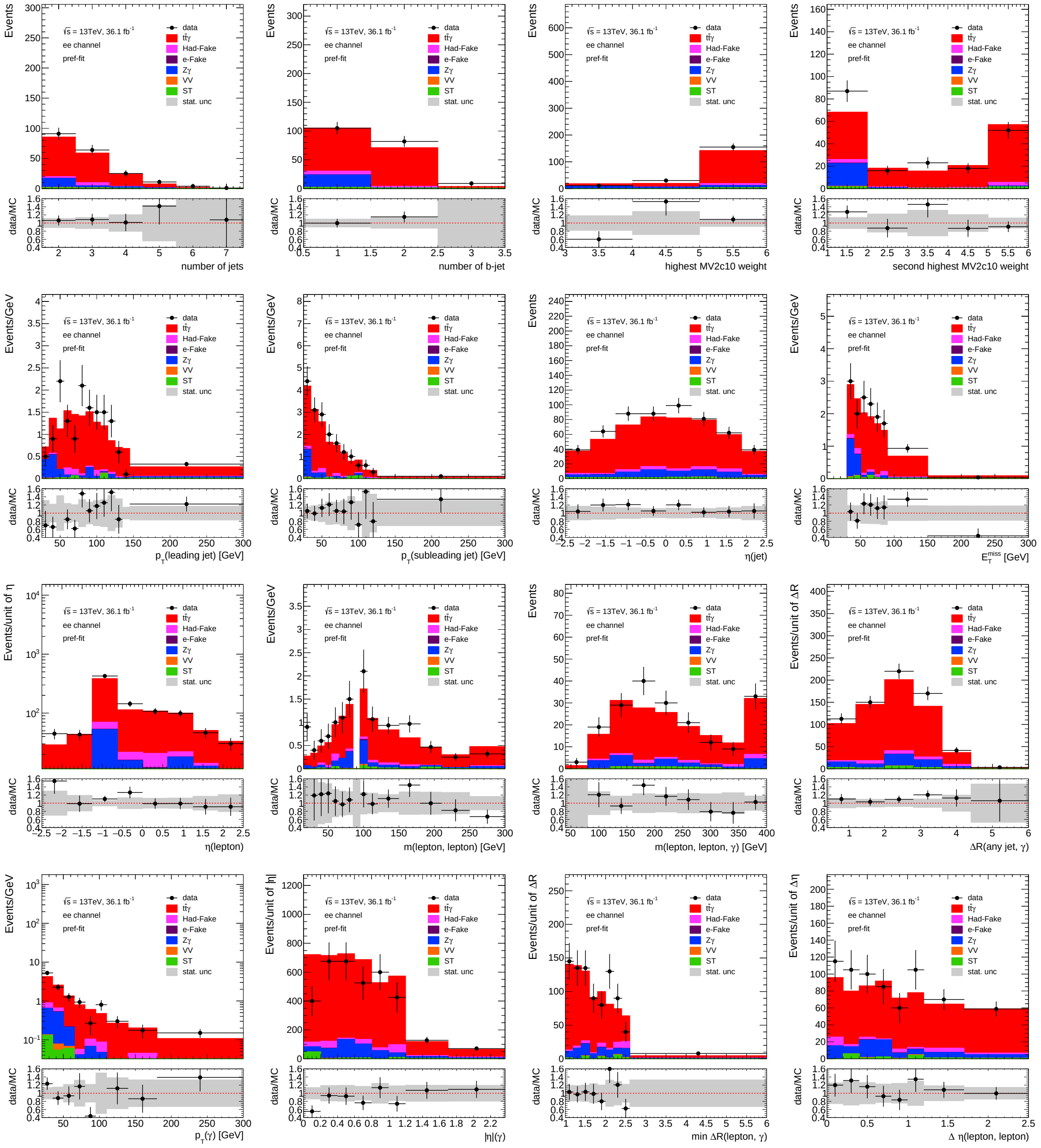

Figure C.2: A selection of pre-fit distributions in the *ee* channel. All background processes are estimated based on simulations and are described in Section 6.3. Only the statistical uncertainties are shown.

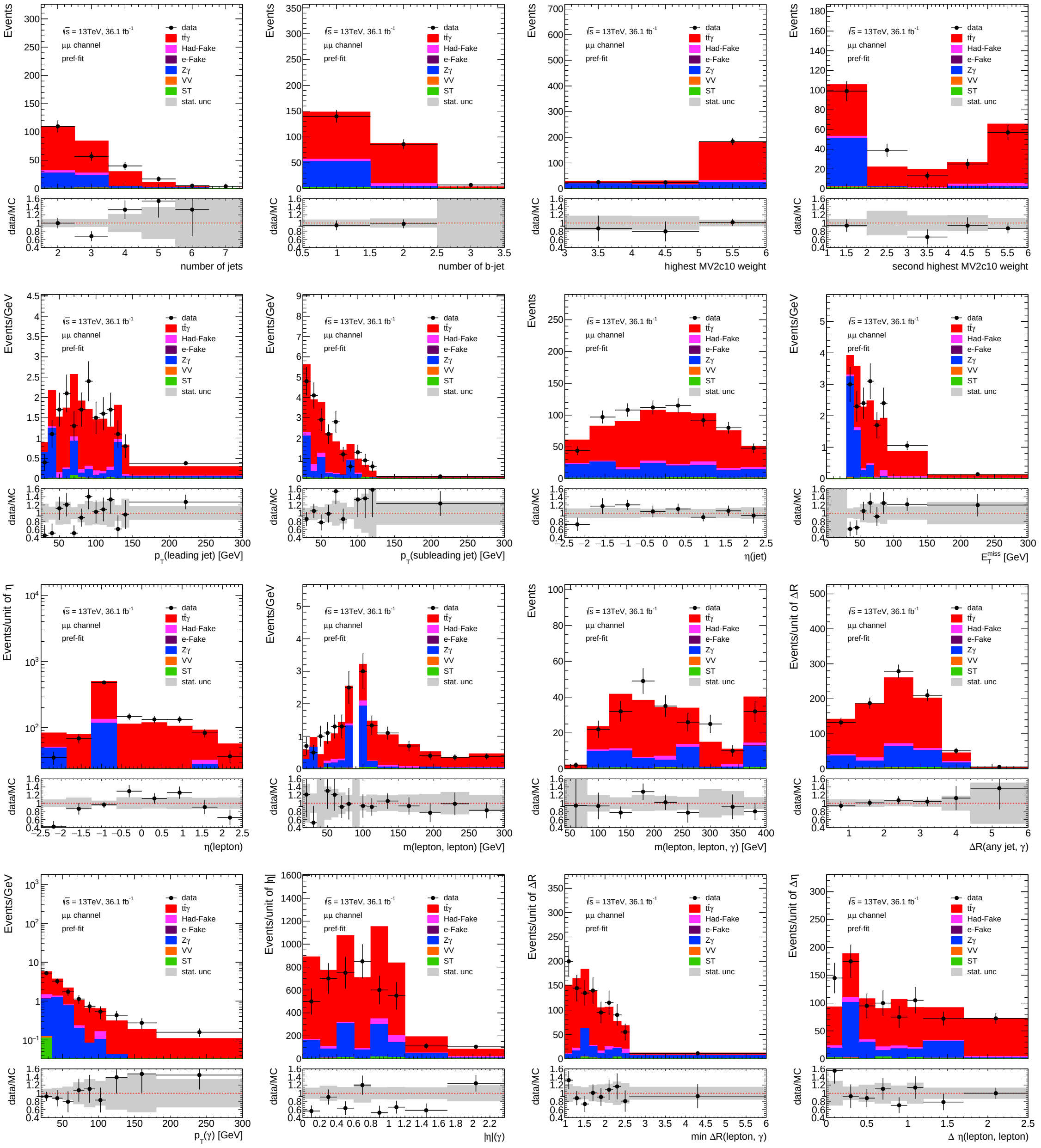

Figure C.3: A selection of pre-fit distributions in the $\mu\mu$ channel. All background processes are estimated based on simulations and are described in Section 6.3. Only statistical uncertainties are shown.

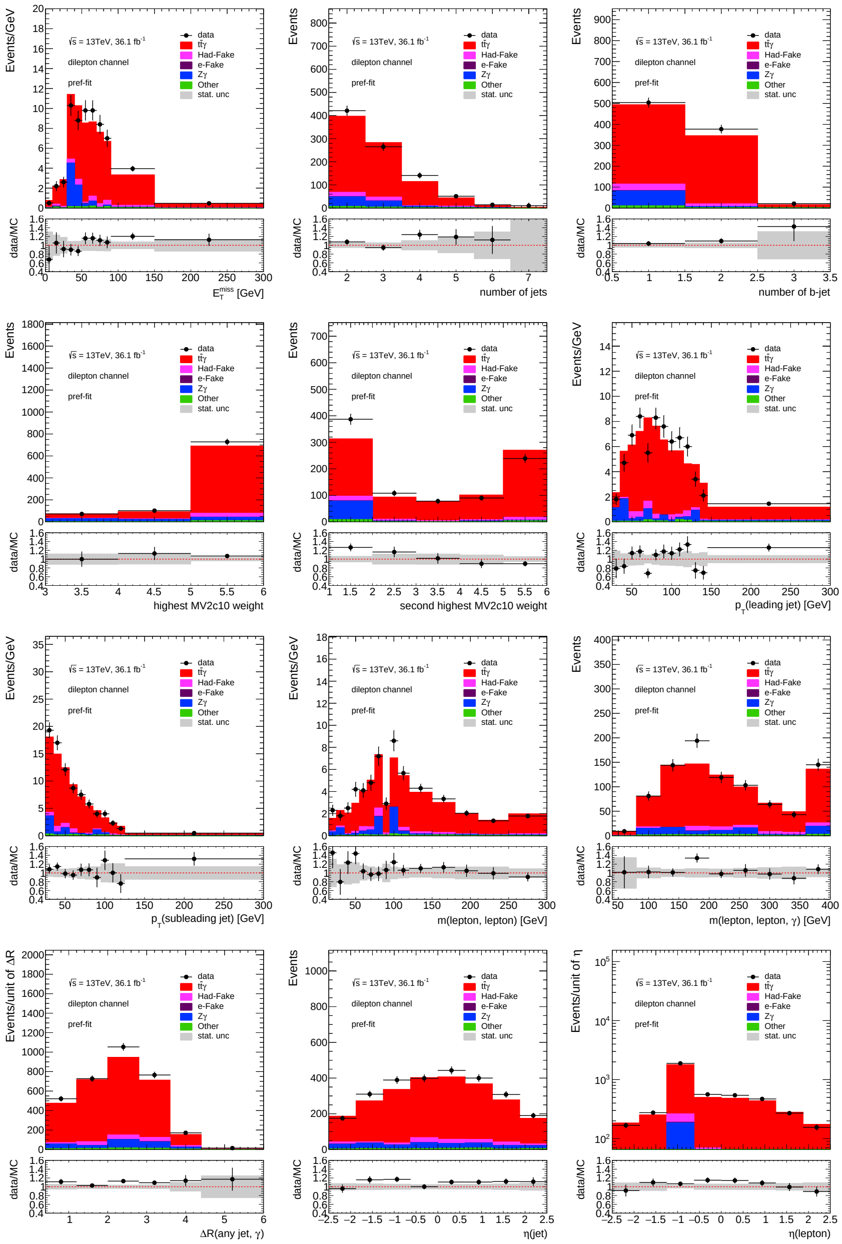

Figure C.4: A selection of pre-fit distributions in the dilepton channel. All background processes are estimated based on simulations and are described in Section 6.3. Only statistical uncertainties are shown.

APPENDIX D

RMS test

The 20 RMS distributions, which are obtained for the first photon p_T bin and after 20 different numbers of iterations, are shown in Figure D. The 100 pseudo-datasets described in Section 6.6.1 are used in each distribution. Gaussian fit are shown in red. The mean value of the fit is presented as a function of the number of iterations in the first distribution in Figure 6.17 (top-left). Similar 20 distributions are produced for each of the other seven bins in photon p_T but are not shown here.

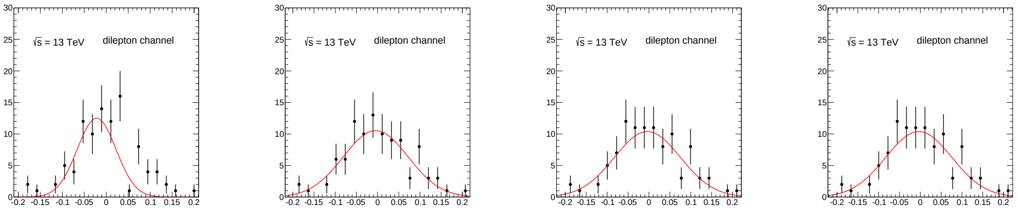

RMS of bin 1 ($p_T(\gamma)$) at iteration 1

RMS of bin 1 ($p_T(\gamma)$) at iteration 2

RMS of bin 1 ($p_T(\gamma)$) at iteration 3

RMS of bin 1 ($p_T(\gamma)$) at iteration 4

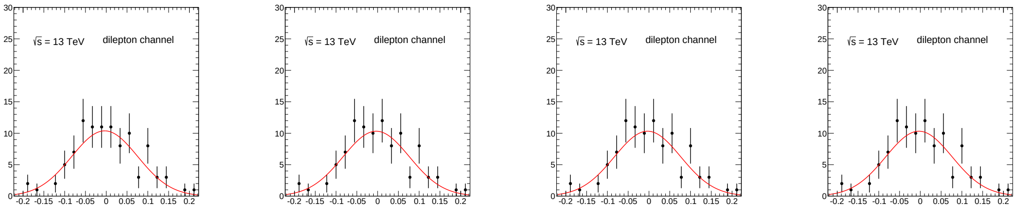

RMS of bin 1 ($p_T(\gamma)$) at iteration 5

RMS of bin 1 ($p_T(\gamma)$) at iteration 6

RMS of bin 1 ($p_T(\gamma)$) at iteration 7

RMS of bin 1 ($p_T(\gamma)$) at iteration 8

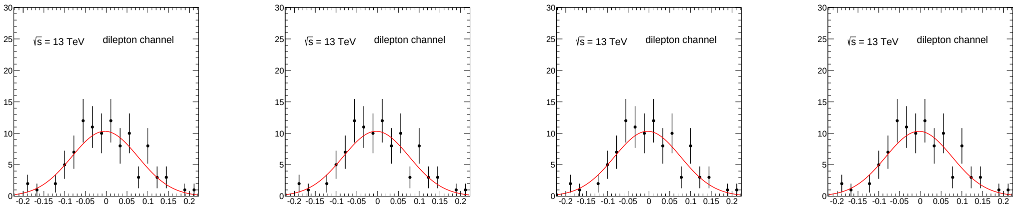

RMS of bin 1 ($p_T(\gamma)$) at iteration 9

RMS of bin 1 ($p_T(\gamma)$) at iteration 10

RMS of bin 1 ($p_T(\gamma)$) at iteration 11

RMS of bin 1 ($p_T(\gamma)$) at iteration 12

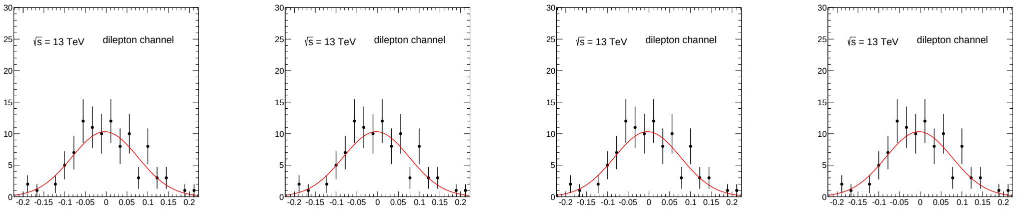

RMS of bin 1 ($p_T(\gamma)$) at iteration 13

RMS of bin 1 ($p_T(\gamma)$) at iteration 14

RMS of bin 1 ($p_T(\gamma)$) at iteration 15

RMS of bin 1 ($p_T(\gamma)$) at iteration 16

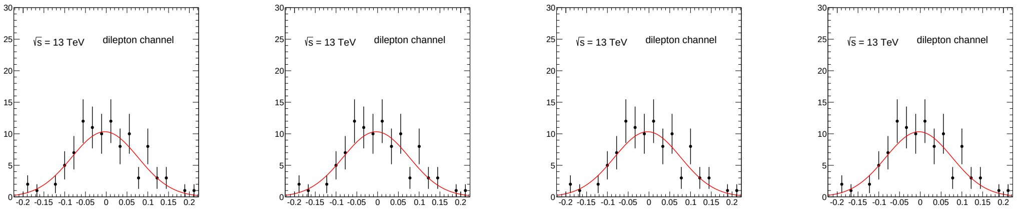

RMS of bin 1 ($p_T(\gamma)$) at iteration 17

RMS of bin 1 ($p_T(\gamma)$) at iteration 18

RMS of bin 1 ($p_T(\gamma)$) at iteration 19

RMS of bin 1 ($p_T(\gamma)$) at iteration 20

Figure D.1: The RMS distributions of the first photon p_T bin, in the dilepton channel.

APPENDIX E

Pull study

The distributions of the pulls calculated per bin using Equation 6.22, are shown in photon p_T bins in Figure E.1, in $|\eta|$ bins in Figure E.2, in minimum $\Delta R(\ell, \gamma)$ bins in Figure E.3, in $\Delta\eta(\ell, \ell)$ bins in Figure E.4, and in $\Delta\phi(\ell, \ell)$ bins in Figure E.5. Gaussian fits are shown in red. A mean value of zero and width of one is obtained, and shown in Section 6.6.4 as a function of each variable.

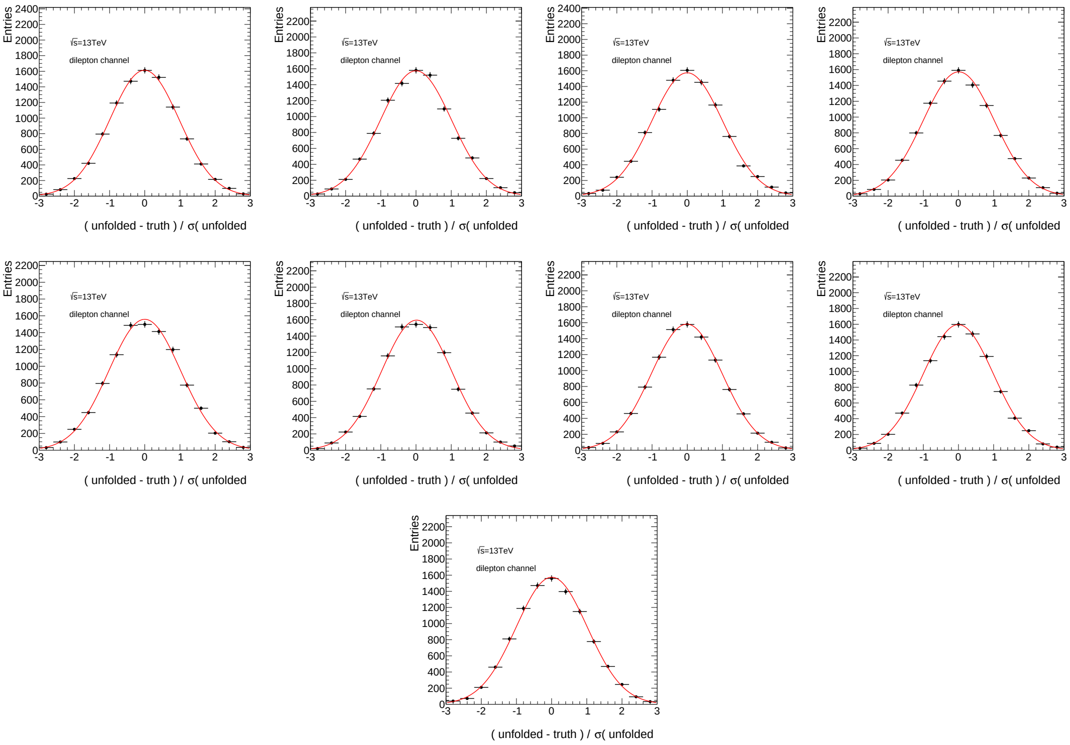

Figure E.1: The distributions of the pull in each bin of p_T (black dots) in the dilepton channel. The Gaussian fits are shown in red.

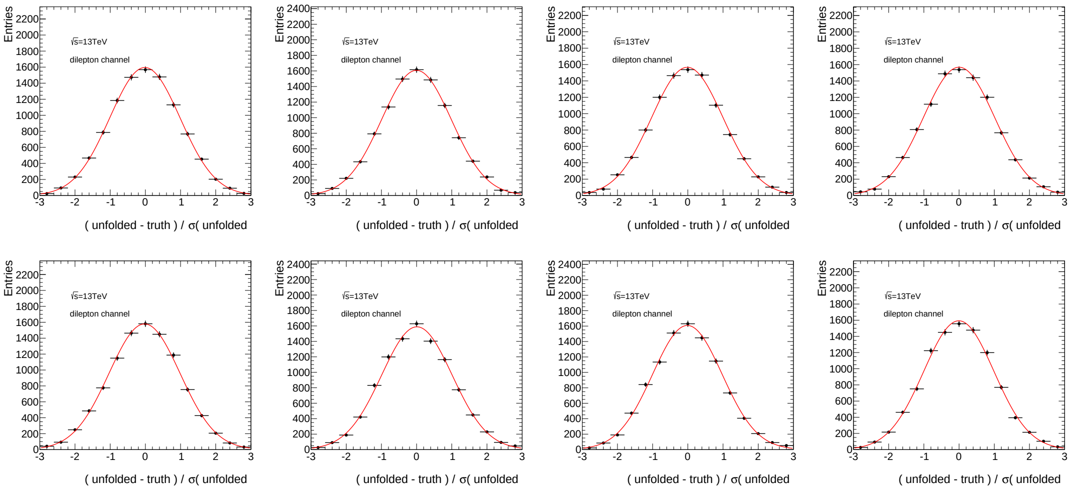

Figure E.2: The distributions of the pull in each bin of $|\eta|$ (black dots) in the dilepton channel. The Gaussian fits are shown in red.

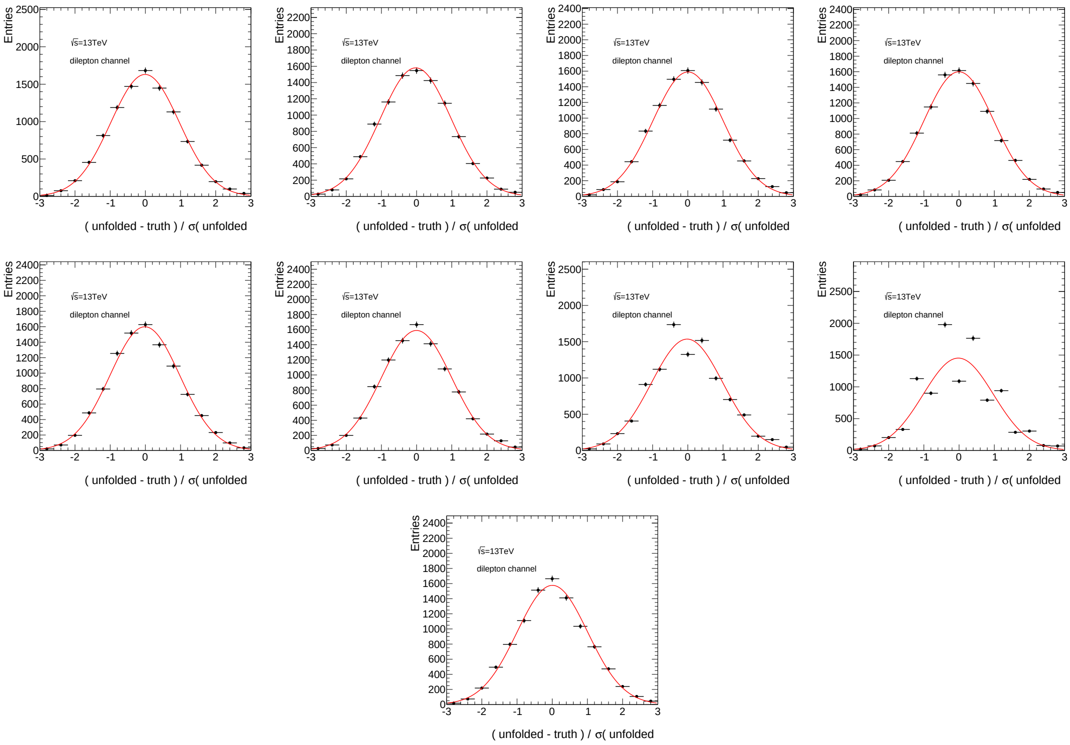

Figure E.3: The distributions of the pull in each bin of minimum $\Delta R(\ell, \gamma)$ (black dots) in the dilepton channel. The Gaussian fits are shown in red.

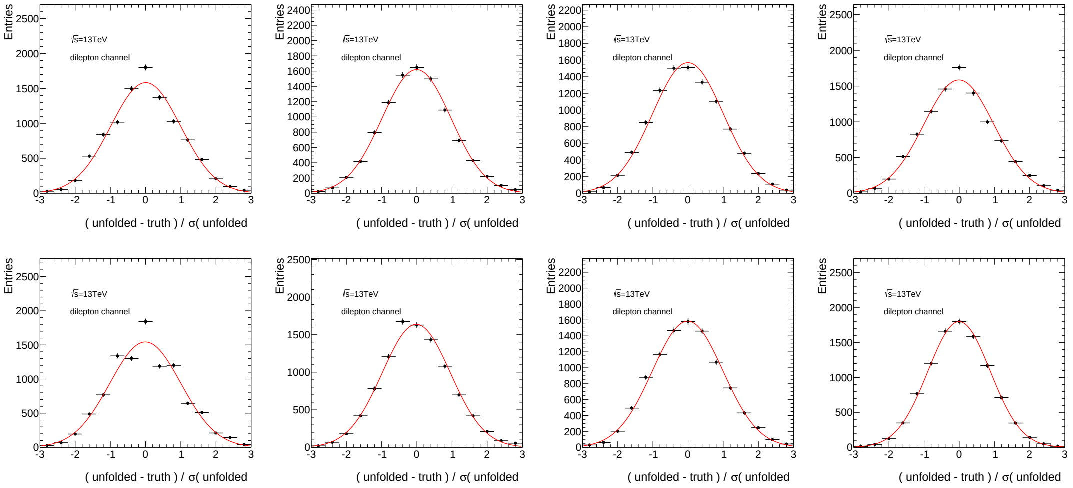

Figure E.4: The distributions of the pull in each bin of $\Delta\eta(\ell,\ell)$ (black dots) in the dilepton channel. The Gaussian fits are shown in red.

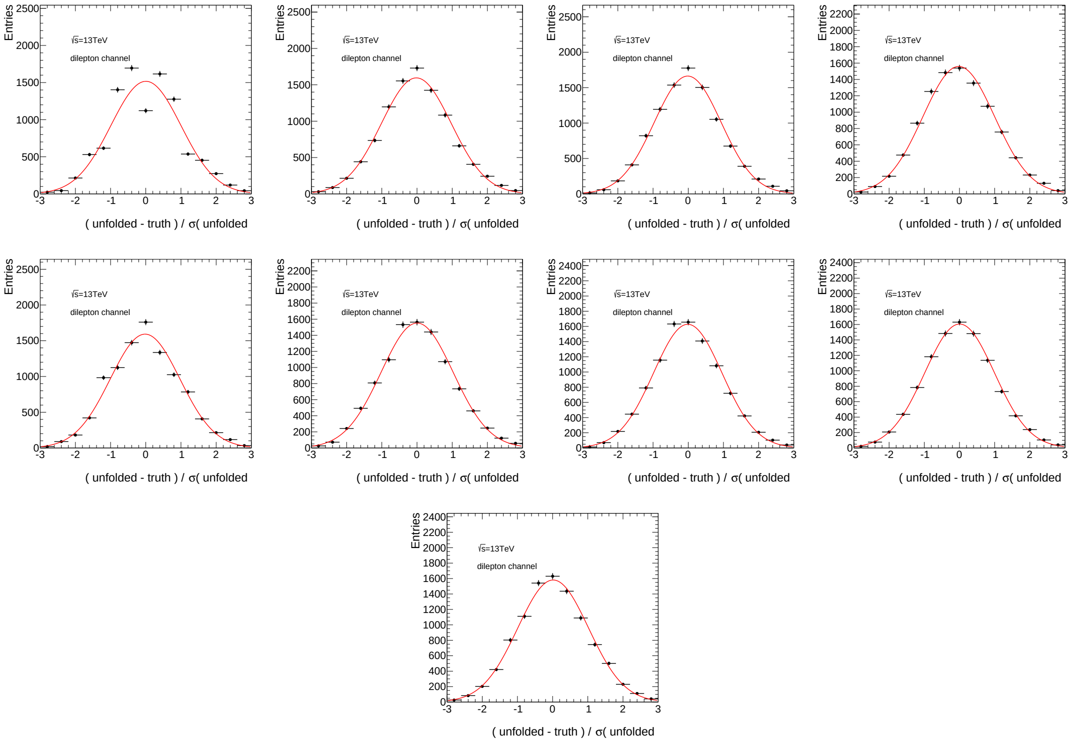

Figure E.5: The distributions of the pull in each bin of $\Delta\phi(\ell,\ell)$ (black dots) in the dilepton channel. The Gaussian fits are shown in red.

APPENDIX F

Breakdown of systematic uncertainties

The size of the shifted $t\bar{t}\gamma$ reconstructed distribution due to the luminosity estimation, the choice of the parton shower generator of the signal sample and the pile-up scale factor, is compared to the nominal distribution and shown in Figure F.1 in bins of p_{T}, $|\eta|$, minimum $\Delta R(\text{lepton}, \gamma)$, $\Delta\eta(\ell, \ell)$ and $\Delta\phi(\ell, \ell)$ of the reconstructed object. It can be seen that the number of events in the shifted samples is mostly the same as the nominal sample, and therefore the majority of differences due to systematic shifts are expected to be significant.

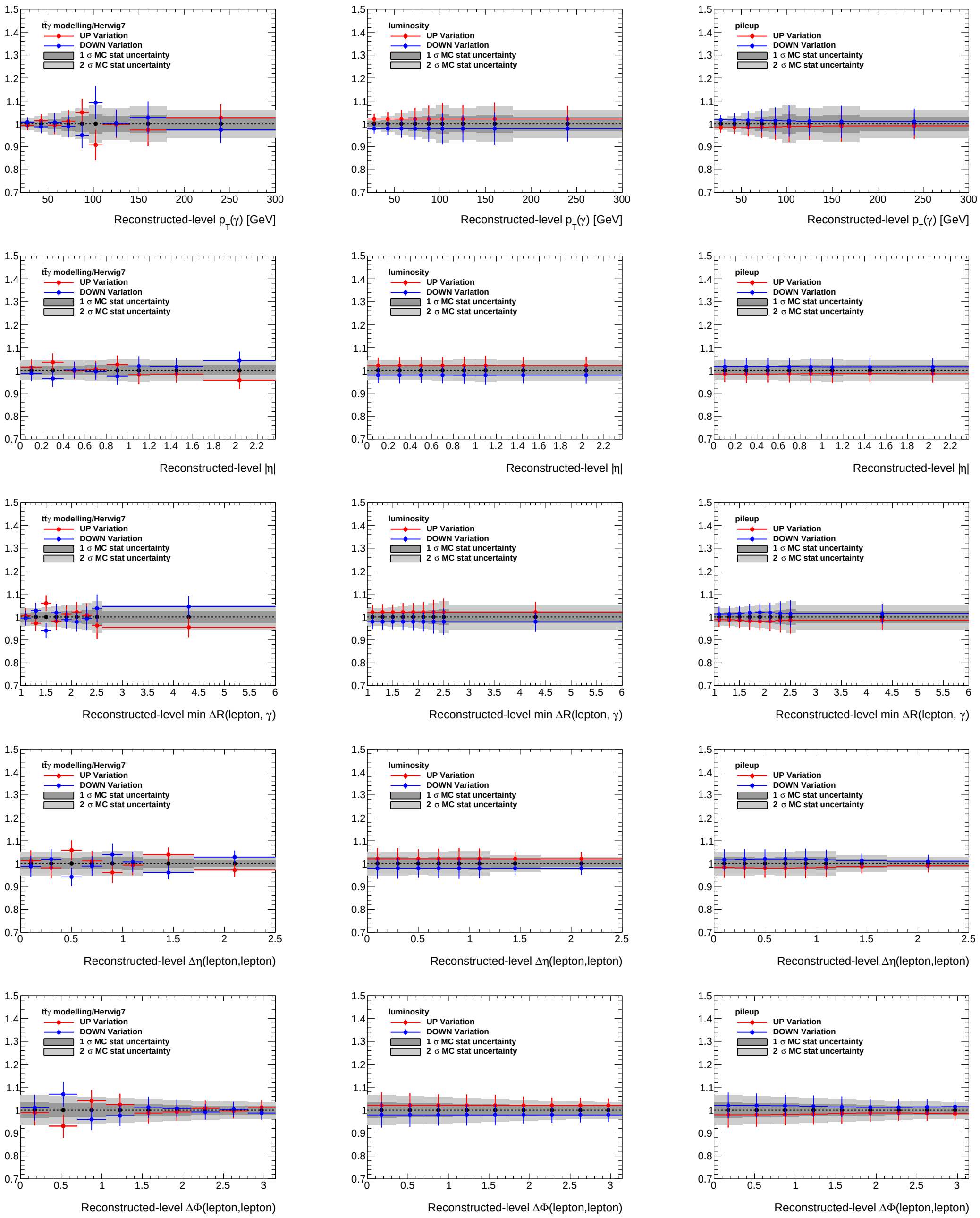

Figure F.1: Reconstructed-level distributions of the size of the relative systematic shifts due to signal modelling (left), luminosity (centre) and pile-up (right), in bins of p_{T} (first row), $|\eta|$ (second row), minimum $\Delta R(\ell, \ell)$ (third row), $\Delta\eta(\ell, \ell)$ (fourth row) and $\Delta\phi(\ell, \ell)$ in the dilepton channel.

APPENDIX G

Validation of EFT samples

A validation is performed in order to confirm that the EFT model performs similarly to the SM, if the EFT coefficients are set very close to zero; in this case the process is referred as SM-like. The coefficients are not set exactly to zero to avoid divergences in the calculations of the amplitudes in the EFT model. The validation is done by generating two samples, one is using the SM, and the other is using the EFT model with coefficients ≈ 0, at LO. Similarly, two samples are generated at NLO. The differential cross section as a function of the photon's observables are checked and found to behave very similarly in the two samples, as shown in Figure G.1 for the LO process, and Figure G.2 for the NLO process.

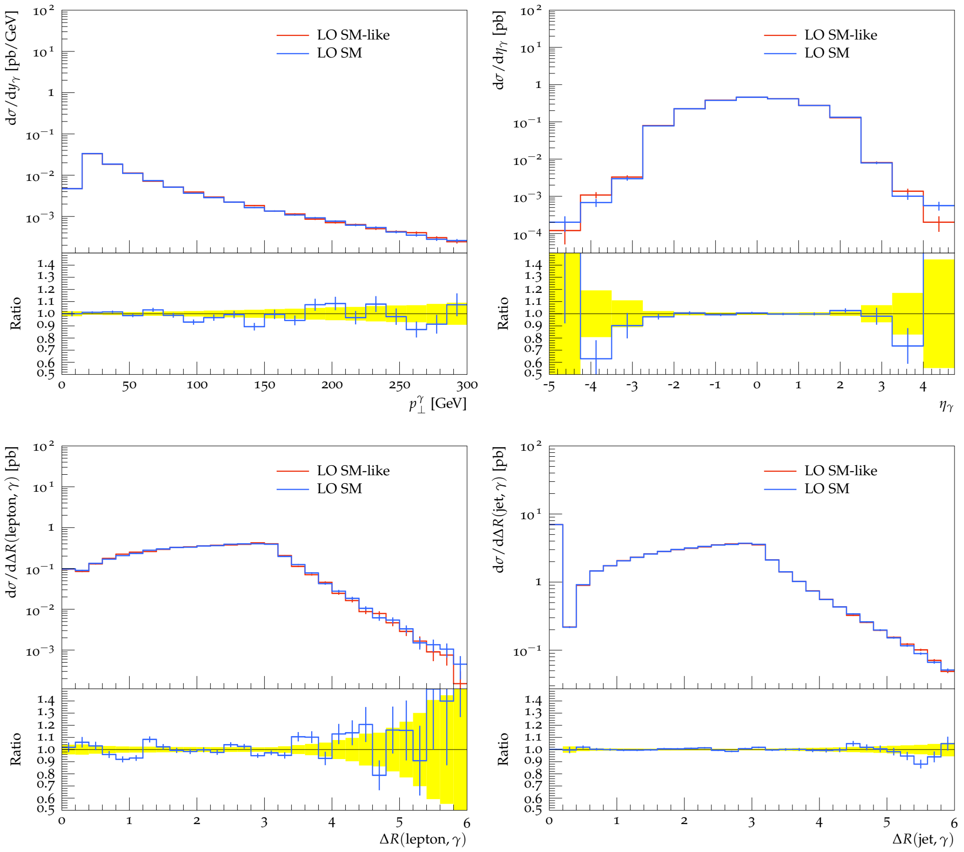

Figure G.1: A comparison between generating a small sample using the SM, shown in blue, and using the EFT model with its coefficients are set very close to zero, shown in red. Both are generated at LO.

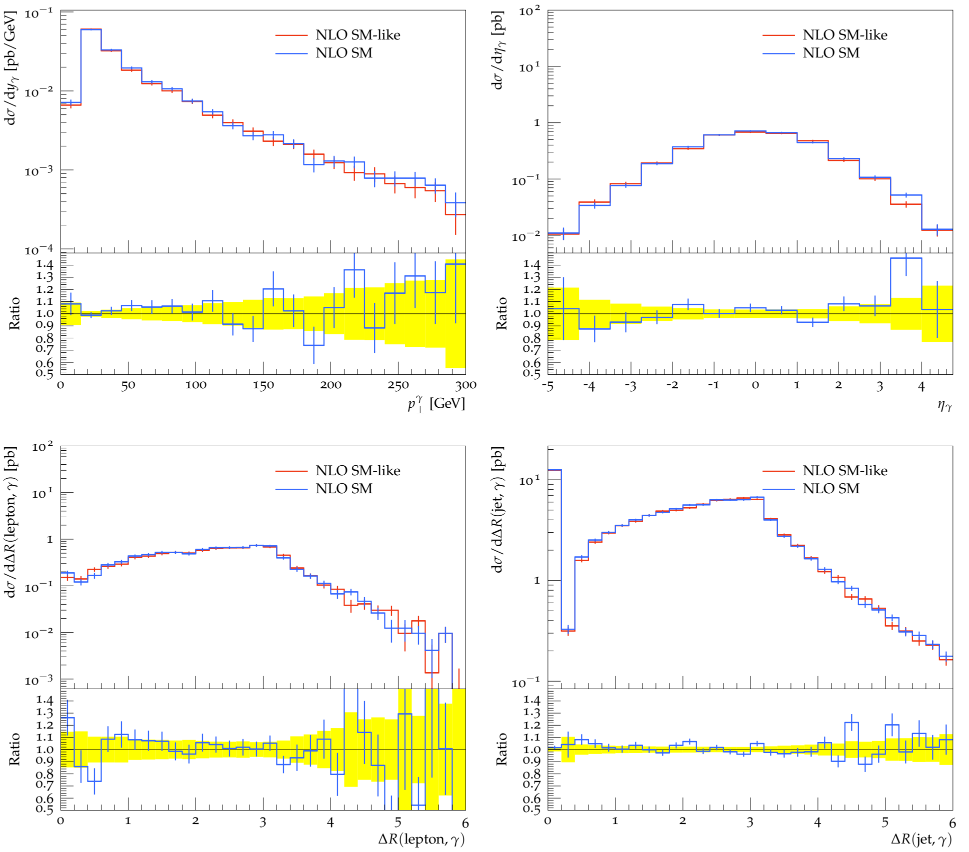

Figure G.2: A comparison between generating a small sample using the SM, shown in blue, and using the EFT model with its coefficients are set very close to zero, shown in red. Both are generated at NLO.